## *Star formation and stellar mass assembly in galaxy formation models*

MITCHELL, PETER,DANIEL

# Star formation and stellar mass assembly in galaxy formation models

Peter Mitchell

## Abstract

We use the semi-analytic galaxy formation model, GALFORM, to explore the implications of results from multi-wavelength galaxy surveys within the context of the hierarchical structure formation paradigm. Specific topics which we investigate include (i): the biases that can be introduced by using spectral energy distribution fitting to infer stellar masses from broad-band photometry, (ii) the reasons why galaxy formation models struggle to reproduce the exponential drop with time in star formation rates of star-forming galaxies inferred from a wide range of observations, (iii) the physical processes that control the evolution in the median relationship between stellar mass and halo mass predicted by galaxy formation models. We show that stellar masses of compact dusty star-forming galaxies could be underestimated by SED fitting as a result of assuming a uniform foreground dust screen geometry. We explain how the standard implementation of supernova feedback and gas reincorporation within galaxy formation models results in flat predicted star formation histories for star forming galaxies. We show that this is inconsistent with observational data which imply that these star formation histories should instead be peaked at intermediate redshift. We also show how the supernova feedback and gas reincorporation implementations within standard galaxy formation models result in a baryon conversion efficiency within haloes that is roughly independent of cosmic time at fixed halo mass. Consequently, the median stellar mass versus halo mass relationship is predicted by these models to not evolve significantly.

# Star formation and stellar mass assembly in galaxy formation models

by Peter Mitchell

A thesis submitted to the University of Durham
in accordance with the regulations for
admittance to the Degree of Doctor of Philosophy.

Department of Physics
University of Durham
March 2015

# Contents

# List of Figures

# List of Tables

# Declaration

The work described in this thesis was undertaken between 2011 and 2015 while the author was a research student under the supervision of Dr. Cedric Lacey, Prof. Shaun Cole and Prof. Carlton Baugh in the Department of Physics at the University of Durham. This work has not been submitted for any other degree at the University of Durham or any other University.

Chapters 3 and 4 have been published in the form of a paper in Monthly Notices of the Royal Astronomical Society,

- *How well can we really estimate the stellar masses of galaxies from broad-band photometry?*
  Mitchell P. D., Lacey C. G., Baugh C. M., Cole S., 2013, MNRAS, 435, 87

- *The evolution of the star-forming sequence in hierarchical galaxy formation models*
  Mitchell P. D., Lacey C. G., Cole S., Baugh C. M., 2014, MNRAS, 444, 2637

Chapter 5 will be submitted soon in the form of a paper to Monthly Notices of the Royal Astronomical Society.

# Acknowledgements

For their guidance throughout (and before starting) my Phd, I thank my supervisors Cedric Lacey, Shaun Cole and Carlton Baugh. Cedric, for his seemingly endless repository of knowledge on all things astrophysics. Shaun, for his exceptional listening skills and uncanny ability to translate many of my poorly articulated ideas to the other two. Carlton, for his understanding of how to make what might otherwise be niche research appeal to a wider audience. I would also like to thank Richard Bower for his enthusiasm in discussions, Claudia Lagos for her sage advice and John Helly for quickly fixing just about every technical problem I ever encountered.

Of course, I should mention my former and current office companions, Peter, Charles, Rachel, Steve & James, who have persevered alongside me to overcome compiler errors, numpy broadcasting rules, matplotlib idiosyncrasies and much more. Outside of work, my former and current band mates, George, Lizzie, Danielle, Alasdair and James have shared my perfectionism while keeping my guitarists ego (mostly) in check. Special thanks to George for slowly but surely improving my sense of time. My other friends that I haven't yet mentioned, Tamsyn, Michelle, Violeta, Will, Ewan, Alex, Mathilde, Flora and Matthieu have also been instrumental in keeping me going.

Finally, I would like to thank my family for their support, cross-country taxi service and gardening expertise.

This work was supported by the Science and Technology Facilities Council [grant numbers ST/J501013/1, ST/F001166/1].

# Chapter 1 | *Introduction*

## 1.1 Cosmic inventory

At present, the Lambda Cold Dark Matter ($\Lambda$CDM) model represents our best guess for describing both the contents and expansion history of the Universe after inflation (Komatsu et al., 2011; Planck Collaboration et al., 2014a). In this model, the energy density of the Universe at the present day is dominated by cold dark matter (CDM) and a cosmological constant ($\Lambda$). According to the most recent analysis of measurements of the cosmic microwave background (CMB) performed by the Planck collaboration, these components make up $95\%$ of the energy density at the present day, with CDM contributing $\Omega_c = 0.26$ and $\Lambda$ contributing $\Omega_\Lambda = 0.69$ (Planck Collaboration et al., 2015). This leaves the contribution from baryons at $5\%$ of the total energy density at the present day. However, unlike the components of the dark sector ($\Lambda$ and CDM), astronomers can directly observe a small fraction of these baryons by observing light from extragalactic sources across the electromagnetic spectrum.

Baryons can be subdivided into several categories, each distinct in their contribution to extragalactic light. By far the most important contributors to the energy density of photons that reach us from local extragalactic sources are stars, gravitationally collapsed structures with mass densities in their cores that are typically $\sim 10^{31}$ times larger than the cosmic mean. In turn, the vast majority of stars are observed to reside within much larger structures referred to as galaxies, with mean densities typically $\sim 10^7$ greater than the cosmic mean. By integrating the differential number density of galaxies as a function of luminosity and wavelength, one finds that stars are the source of $\approx 97\%$ of the luminosity density in photons that are emitted by baryons in the local Universe (Somerville et al., 2012). Of this $97\%$,

$\approx 53\%$ can be observed as direct starlight, while the remaining $44\%$ is absorbed by dust that resides within the interstellar medium (ISM) of galaxies (Somerville et al., 2012). This absorbed starlight can then be observed through thermal emission of this dust.

While stars dominate as contributors to the luminosity density of photons emitted in the local Universe, they are thought to contribute only $\sim 3.5\%$ of the mass density in baryons today (Li & White, 2009). Galaxies also contain gas and super massive black holes (SMBHs), contributing $\sim 2\%$ and $\sim 0.008\%$ respectively to the mass density of baryons in the local Universe (Keres et al., 2003; Fukugita & Peebles, 2004; Hopkins et al., 2007; Martin et al., 2010). Photons emitted by gas accreting onto SMBHs make up the majority of the remaining luminosity density in photons emitted locally ($\sim 2.9\%,$ Hopkins et al., 2007). In comparison, gas in the ISM of galaxies provides only a minimal contribution to this photon luminosity density (excluding thermal reprocessing of starlight by dust grains). Integrating the $21\,\mathrm{cm}$ luminosity function reveals that neutral atomic gas contributes a meager $\sim 10^{-7}\%$ of the energy in photons emitted in the local Universe (Martin et al., 2010). Integrating carbon monoxide luminosity functions for different transitions reveals that molecular hydrogen contributes $\sim 10^{-3}\%$ of the locally emitted luminosity density (Lagos et al., 2012) [1]. Integrating emission line luminosity functions sourced by partially ionised gas in the ISM of local galaxies gives a contribution of $\sim 0.21\%$ (Hogg et al., 1998; Nakamura et al., 2004; Cowie et al., 2010; Swinbank et al., 2012; Pirzkal et al., 2013).

Adding this together, galaxies are thought contribute $\sim 99.96\%$ of the locally emitted luminosity density in photons while only contributing $\sim 5\%$ to the mass density of baryons. The remaining $95\%$ of the baryonic mass density is thought to be located in ionised gas both in extended haloes around galaxies (circum galactic medium, CGM) and in the wider intergalactic medium (IGM). For the massive galaxy groups and clusters, halo gas is heated to temperatures high enough to emit

[1] Carbon monoxide is used as a tracer for molecular hydrogen because it is easily observed and forms under similar ISM conditions as molecular hydrogen

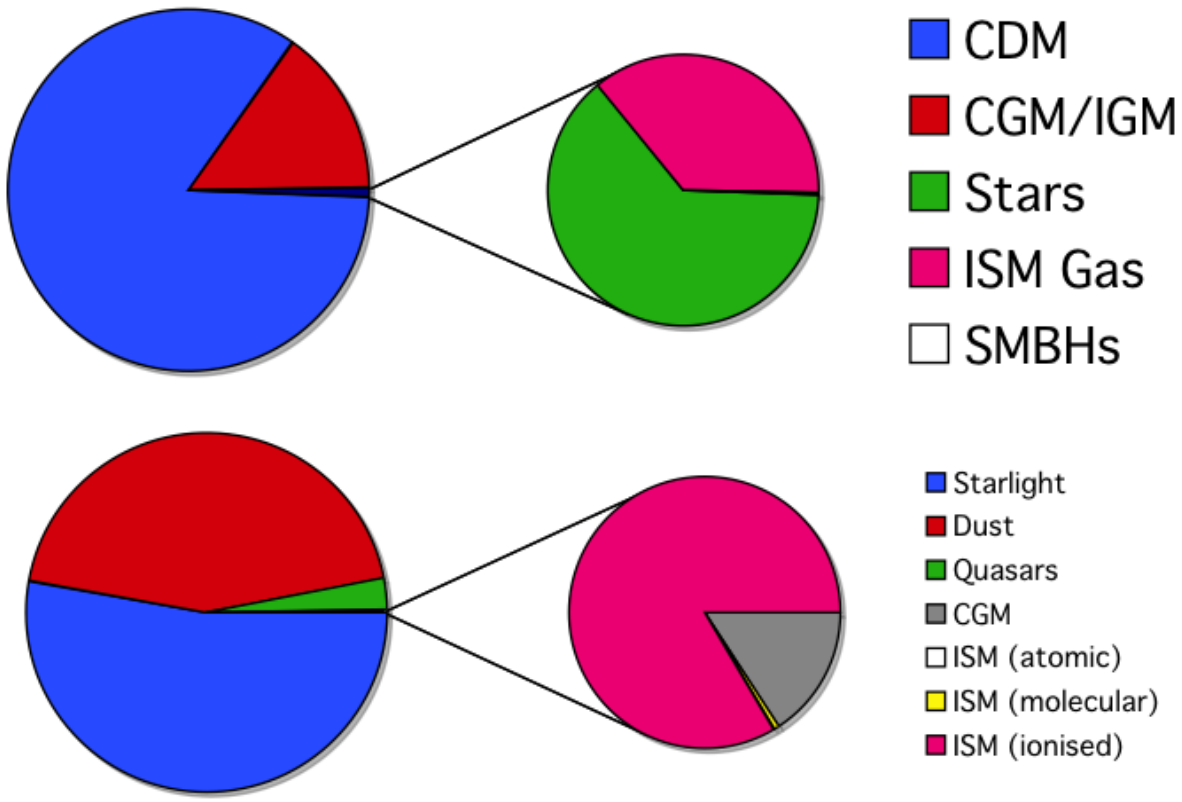


Figure 1.1: Top: Mass density of the present day Universe, split into cold dark matter, the circum-galactic medium, stars, the interstellar medium within galaxies, and supermassive black holes. Bottom: Luminosity density of the present day Universe, split into directly observed starlight, reprocessed dust emission, quasars, the circum-galactic medium in galaxy clusters, and the interstellar medium split into atomic, molecular and partially ionised gas.

thermal Bremsstrahlung radiation, accounting for the final $\sim 0.04\%$ of the luminosity density in photons emitted locally (Böhringer et al., 2014). The remaining baryons in ionised gas are, in general, too faint to be detected in emission. To summarise, the mass density and energy density of photons emitted by sources at the present day are presented in Fig. 1.1.

The dominant role of stars and black holes in emitting photons means that galaxies and quasars (exceptionally bright accreting SMBHs) are the two main cosmological tracers used by cosmologists to study how the observable Universe evolved after the time of last scattering (when the cosmic microwave background (CMB) decoupled from baryons at $z \sim 1100$). However, if the power spectrum of density fluctuations in the galaxy distribution is compared to the power spectrum of the CMB evolved forwards using linear theory, one finds that galaxies and quasars are biased tracers of the overall mass distribution. Over several decades, the need to understand the implications of this bias for cosmology measurements has been one of the major motivations for building a theoretical framework for understanding the formation and evolution of galaxies and SMBHs.

## 1.2 Constraining the ΛCDM cosmological model

Taken at face value, it seems bizarre that cosmologists would arrive at the cosmic inventory presented in Section 1.1, given how little of it can be directly observed. However, evidence supporting the ΛCDM model has built up over several decades through many independent lines of inquiry.

Perhaps the most important piece of evidence came with the discovery of large scale fluctuations in the temperature map of the CMB made by the COBE satellite (Smoot et al., 1992). These primordial fluctuations are consistent with inflationary models and provide sufficient anisotropy to explain the growth of structure through gravitational instability in a universe that contains dark matter. On smaller angular scales, where density fluctuations can enter the sound horizon before the epoch of recombination, gravity and pressure from the baryon-radiation fluid can

affect these primordial fluctuations, producing a pattern of acoustic peaks in the CMB temperature power spectrum. These acoustic peaks correspond to modes of oscillations in the baryon-photon fluid that were at extrema in density at the epoch of recombination. Measuring the positions and shapes of these peaks give cosmologists a great deal of information about the contents of the Universe at that time. The first peak at angular wavenumber, $l \sim 200$ corresponds to the fundamental mode of sound waves that had precisely the correct amount of time to oscillate to a single compression or rarefaction between the time of entering the sound horizon and the epoch of recombination (Hu & Dodelson, 2002). The position of this peak has been measured to an extremely high level of precision by various experiments over the last two decades (de Bernardis et al., 2000; Hanany et al., 2000; Planck Collaboration et al., 2014a). These measurements (combined with information from higher order peaks to constrain the sound speed) confirm that the Universe is extremely close to being spatially flat on large scales. The second acoustic peak corresponds to sound waves that have had just enough time to undergo a single compression/rarefaction cycle before recombination. Roughly speaking, the ratio between the amplitudes of the first and second peaks gives information on how much inertia is in the photon-baryon fluid at recombination, constraining the density of baryons at that time. Higher order acoustic peaks constrain the extent to which dark matter acts against the tendency for density fluctuations to decay in a radiation dominated Universe. Measuring the amplitudes of these peaks therefore directly constrains the amount of dark matter present in the Universe (Hu & Dodelson, 2002).

Another cornerstone of the $\Lambda$CDM model is that at the present day, $68.5\%$ of the energy density of the Universe is in the form of a cosmological constant. The CMB alone can constrain $\Lambda$ from the combination of the first and higher order peaks constraining the geometry, baryonic and dark matter densities. However, the first observational evidence for $\Lambda$ that became widely accepted came instead from supernovae data. Measurements of standard candles that constrain how the luminosity distance varies with redshift give strong constraints on both the cosmological constant. Type 1a Supernovae (SNe) turn out to be suitably bright standard candles

for this purpose and give strong evidence that the rate of expansion of the Universe has been increasing at late times (Riess et al., 1998; Perlmutter et al., 1999; Hicken et al., 2009).

As well as acoustic peaks in the CMB temperature power spectrum, the aftermath of oscillations in the baryon-radiation fluid before recombination also leave an observable signature in the matter power spectrum. This signature, referred to as Baryon Acoustic Oscillations (BAO), has been observed in the clustering of galaxies (Cole et al., 2005; Eisenstein et al., 2005; Anderson et al., 2014) the Lyman alpha forest (Slosar et al., 2013) and the cross correlation between quasars and the Lyman alpha forest (Font-Ribera et al., 2014). The position of the BAO feature, combined with CMB constraints, provides a precise measurement of the angular diameter distance and the Hubble parameter at a given redshift. As well as the BAO peak at a characteristic scale, galaxy clustering can be used to provide additional cosmological constraints. The clustering of galaxies has been precisely measured for large spectroscopic samples using luminous red galaxies as tracers of the halo population (Reid et al., 2010). Once galaxy bias, non linear evolution of the matter power spectrum and redshift space distortions are taken into account, these clustering measurements have been shown to be consistent with the $\Lambda$CDM parameters inferred from other cosmological probes.

Strong gravitational lensing of variable sources (such as quasars) provides another test of $\Lambda$CDM. By measuring the time delays between variability of multiple images, the distance to the lens can be determined. This constrains the Hubble parameter (e.g. Refsdal, 1964; Fadely et al., 2010; Suyu et al., 2010). Weak gravitational lensing can also be employed to constrain cosmological parameters (e.g. Massey et al., 2007; Schrabback et al., 2010). In this case, galaxy surveys with high image quality are used to measure, statistically, the distorted shapes of galaxies caused by cosmic shear. For a given set of cosmological parameters, theoretical predictions for the matter power spectrum can be used to predict the expected statistical shear signal. A likelihood analysis can then be employed to constrain cosmological parameters (e.g. Massey et al., 2007).

Another method used to constrain cosmological parameters comes from observations of galaxy clusters. Clusters are spatially associated groups of galaxies that are thought to reside within the most massive dark matter haloes. The most massive galaxy clusters at a given epoch correspond to the largest scale fluctuations that undergo non linear evolution and collapse. Therefore, the massive end of the halo mass function is sensitive to cosmological parameters, particularly $\Omega_{\mathrm{M}}$ and $\sigma_8$, the rms linear fluctuation amplitude at $8\,\mathrm{Mpc}h^{-1}$ (Eke et al., 1996). Cluster masses can be estimated using X-ray data (e.g. Henry et al., 2009) and weak gravitational lensing (e.g. Mantz et al., 2015). Calibrations between X-ray data and Sunyaev-Zeldovich effect data have also been used to estimate the cluster mass function from number counts of Sunyaev-Zeldovich selected clusters (Sehgal et al., 2011; Benson et al., 2013; Planck Collaboration et al., 2014b). Consistency between the cluster mass function predicted by the ΛCDM model constrained by measurements of the Hubble parameter (Freedman et al., 2001) and the CMB normalisation with this observational data provides powerful evidence for the ΛCDM cosmological model.

While precision tests for ΛCDM cannot be undertaken on the scale of galaxies, ΛCDM still makes predictions on these scales that are consistent with observational data. The most obvious of these is that dark matter should dominate the gravitational potential in and around galaxies. Measurements of galaxy rotation curves, velocity dispersions (both of stars within galaxies and of galaxies in groups/clusters), peculiar velocities and lensing signals all unanimously indicate that there is significant amount of the mass around galaxies that is not directly observable (Zwicky, 1933; Oort, 1940; Kahn & Woltjer, 1959; Rubin & Ford, 1970; Rubin et al., 1980, 1985). Dark matter is therefore consistent with the observational evidence for missing mass on small scales. The most powerful evidence of this type comes from galaxy clusters, where the high gas temperature of intracluster gas makes it, in principle, possible to account for almost all of the baryons within a given cluster. Comparing the mass inferred in this way to the mass implied by the galaxy dynamics, hydrostatic modelling or lensing tests whether or not the baryon

fraction from ΛCDM is consistent (White et al., 1993). At present, there is evidence that this consistency has been achieved, within systematic uncertainties (Gonzalez et al., 2013). Insights on dark matter using galaxy clusters can be extended further using lensing measurements of colliding galaxy clusters, which support the theory that dark matter is collisionless (Clowe et al., 2004; Markevitch et al., 2004).

Putting this all together, the current status is that by combining together different observations that are sensitive to cosmological parameters in different ways, the observational data are perfectly consistent with a ΛCDM model with little evidence of a need for additional physics (Komatsu et al., 2011; Planck Collaboration et al., 2014a). However, these are all observations that are made on large scales, where theoretical predictions can made using a combination of simple linear perturbation theory and non linear effects can be accounted for using numerical simulations without baryons. Testing ΛCDM on smaller scales, where baryonic physics becomes important, is much more difficult. In this regime, understanding how radiative cooling, hydrodynamics, star formation and feedback processes shape the distribution of mass within (and outside of) haloes becomes paramount. At present, it is not possible to take a given cosmological model and make predictions for properties of the galaxy population entirely from first principles. Therefore, while ΛCDM has not been falsified for failing to predict a realistic galaxy population, galaxy formation models and simulations have thus far been of little use for differentiating between cosmological parameter combinations (e.g. Guo et al., 2013a) (although they can be used to constrain the dark matter particle mass for the case of warm dark matter, Kennedy et al., 2014).

On the other hand, the precise observational constraints that exist for ΛCDM model parameters mean that from the point of view of trying to understand galaxy formation, the initial conditions and background expansion of the Universe are known with a high degree of accuracy. This significantly simplifies the complex problem of using theoretical modelling to try to understand, and in particular quantify, how galaxies form and evolve.

## 1.3 Structure formation and dark matter haloes

Modern galaxy formation theory is constructed upon a theoretical framework for the hierarchical growth of structure. Within this framework, linear fluctuations in the matter density field grow by gravitational instability until they become sufficiently overdense with respect to the background expansion that they collapse through gravity. These collapsed overdensities in the dark matter, referred to as haloes, stabilise into virial equilibrium and are supported by velocity dispersion against further collapse. The shape of the matter power spectrum (which can be inferred from the CMB and galaxy clustering measurements) is such that the variance of fluctuations ($\approx P(k)k^3$) is larger on smaller scales. Consequently, small scale fluctuations are able to collapse first and larger scale fluctuations collapse at later times, accreting smaller haloes in the process. In practice, this means that haloes generally form through merging of smaller haloes and each halo defined at a given time will have a merger tree of progenitors. Given that galaxies are thought to form within dark matter haloes, an essential input for any galaxy formation model is the statistics of both the abundance and merging histories of haloes. Two distinct methods for predicting these statistics have been developed.

The first is a framework that combines the statistics of smoothed Gaussian fluctuation fields with linear theory. In this framework, the probability that the smoothed density field at an arbitrary point space is above some density threshold is calculated (Press & Schechter, 1974). The threshold is chosen to correspond to the critical overdensity for gravitational collapse, which has been computed using the spherical collapse model (and more complex variants, e.g. Sheth et al., 2001). The probability to be above the threshold can then be associated with the fraction of mass elements that would have collapsed to form dark matter haloes above a given scale (Press & Schechter, 1974). An extension of the formalism introduced by Press & Schechter (1974) exploits the linear and Gaussian properties of the fluctuation field to trace how haloes grow by using the variance in the density field smoothed as a function of scale (Bond et al., 1991; Lacey & Cole, 1993). This process turns

out to be equivalent to solving a diffusion equation with a barrier to represent the collapse threshold.

The second method to predict the statistics of haloes is to directly simulate the evolution of the collisionless dark matter fluid using N-body simulation codes (Press & Schechter, 1974; White, 1976; Frenk et al., 1983; Springel, 2005). In dark matter only simulations, the mass density field is discretely sampled with Lagrangian particles. The initial configuration is set so that these particles are first uniformly distributed uniformly over a box and are then perturbed so that the particles exhibit the density fluctuations calculated from linear theory. Simple newtonian gravity is then used to predict the forces between particles and periodic boundary conditions are employed to ensure that the box behaves as a homogeneous and isotropic region of the Universe. With the advent of powerful parallel computing resources and sophisticated algorithms to reduce the cost of computing the gravitational forces, it has been possible for over two decades to use simulations to produce populations of dark matter haloes that are cosmologically representative (Springel et al., 2005; Klypin et al., 2011). A key advantage of using numerical simulations to generate halo populations is that the simulation also contains all of the positional and velocity information of the haloes, allowing the clustering of haloes in real or redshift space to be predicted. A powerful piece of evidence to support the $\Lambda$CDM model comes from the fact that if observed galaxies are statistically associated with a simulated halo population, the predicted galaxy clustering is in very good agreement with observed galaxy clustering (Conroy et al., 2006).

Numerical simulations have also been used to learn a great deal about the internal structure of dark matter haloes. One of the most important numerical results in this area is that the radial density profiles of dark matter haloes have a characteristic shape which can be described by a single parameter in the fitting function advocated by (Navarro et al., 1996). To good approximation, the internal structures of dark matter haloes are therefore completely specified by the halo mass and the halo concentration of this so-called, Navarro, Frenk and White (NFW) profile. In turn, halo concentrations have been shown to be closely connected with the halo

mass and time of formation (Navarro et al., 1997; Bullock et al., 2001; Eke et al., 2001). Another important result obtained from numerical simulations is that the central regions of dark matter haloes which are accreted onto a larger halo can survive as distinct, gravitationally bound structures, referred to as satellite subhaloes (Ghigna et al., 1998; Springel et al., 2008). Gravitational tidal forces strip the least gravitationally bound mass from these satellite subhaloes, leaving only the dense inner part of the original halo intact. Despite being composed of collisionless dark matter, satellite subhaloes can dissipate their orbital energy through dynamical friction, the process of dragging a wake behind the satellite as the satellite moves through the smooth halo component of the host.

Although haloes are thought to be supported through velocity dispersion rather than rotation, they are expected to acquire some amount of angular momentum through interaction with their larger scale environment in the stages prior to collapse (Hoyle, 1949; Peebles, 1969; Doroshkevich, 1970; White, 1984). This turns out to be very important for galaxies to exhibit the structure that we observe. The theoretical expectation is that the interaction of proto-haloes with the tidal field of their neighbours leads to torques that are the source of this angular momentum build-up. In a similar vein to the universal halo densities profiles advocated by Navarro et al. (1996), numerical simulations show that all haloes share a common probability distribution function for their total angular momentum content, approximately independent of halo mass and cosmology (Cole & Lacey, 1996).

## 1.4 Galaxy formation within haloes

Galaxies are thought to form at the bottom of the gravitational potential wells associated with individual dark matter haloes (White & Rees, 1978). To a good approximation, the first haloes are thought to form by accreting both primordial gas and dark matter such that the baryon fraction within these haloes is equal to the cosmic mean. Subsequent haloes that form from accretion of smaller haloes will also accrete satellite galaxies and their associated gas haloes. The internal gas struc-

ture within dark matter haloes is expected to be significantly different with respect to the structure of the dark matter component. On the one hand, gas feels the same gravitational forces as the dark matter and the dark matter will dominate the gravitational potential. On the other hand, gas is both collisional and dissipative, meaning that gas experiences thermal pressure and can dissipate energy through radiative cooling.

In the traditional galaxy formation framework outlined by White & Rees (1978), gas accreted onto haloes would shock at the virial radius, upon encountering hotter gas at the virial temperature of the halo that was already present. In this picture, dark matter haloes contain quasi-hydrostatic gas haloes that are balanced against gravitational collapse by pressure support. This gas is expected to have similar specific angular momentum to the parent dark matter halo. Over time, these hot gas haloes are expected to cool through radiative process and therefore contract towards the bottom of the gravitational potential, forming a disk. A simplified explanation for this is the following. While radiative cooling can be efficient at dissipating energy, photons do not carry significant angular momentum. The minimum energy configuration of gas with a radially aligned angular momentum distribution is a thin disk. Therefore, disk galaxies are thought to be a natural consequence of tidally torqued material that can dissipate energy through radiative cooling.

Once a gas disk has formed at the centre of a dark matter halo, it must form stars to be consistent with the galaxies that are observed. While the formation of gas disks can be described in terms of simple physics, the physics of star formation is more complex and is not particularly well understood, partly because of the immense dynamic range involved. What is well established is that there is an empirical relationship between the integrated star formation rate surface density and the integrated surface density of gas within galaxies. This empirical relationship is referred to as the Kennicutt-Schmidt law (Kennicutt, 1998). A more modern take on the relationship is that the star formation rate surface density is actually better correlated with the surface density of molecular hydrogen, rather than that of the total gas content (Kennicutt et al., 2007; Bigiel et al., 2008). Although a complete theo-

retical explanation for this relationship has not been agreed upon, the correlation makes sense given that stars are known to form in dense giant molecular clouds. While the Kennicutt-Schmidt relationship does not represent a predictive theory of star formation, it does prove to be very convenient for modelling galaxy formation and for numerical simulations that do not resolve the detailed small scale structure of the ISM.

Once populations of stars have formed from the cold ISM in galaxies, their subsequent evolution is fairly well understood thanks to many years of observational and theoretical work undertaken to study stars in the Milky Way and other nearby galaxies. Perhaps the most critical aspect of stellar evolution for galaxy formation is that the most massive stars in a given stellar population are known to inject huge amounts of energy into the ISM through supernova (SNe) explosions. If this energy can be efficiently coupled to surrounding gas with low radiative losses, SNe explosions provide, in principle, a mechanism to drive gas out of galaxies in outflowing winds. Such winds are observed in actively star forming galaxies that are expected to host recent SNe activity (Heckman et al., 2000; Shapley et al., 2003; Weiner et al., 2009). Given that higher levels of star formation activity result in more SNe explosions per unit time, star formation is expected to be self-regulating. For example, if there is a larger than normal gas reservoir in a galaxy of a given size, it is expected that this will lead to an elevated star formation rate (SFR) because of the Kennicutt-Schmidtt relation. A larger SFR results in a higher rate of SNe explosions which are expected to eject gas from the reservoir, driving the system back to an equilibrium configuration. This process of ejecting gas from galaxies to regulate star formation is referred to as SNe feedback. It has been known for many years that SNe (or something that behaves in the same way) must be operating in galaxies to explain the global inefficiency of star formation implied by the cosmic inventory presented in Section 1.1 (e.g. White & Rees, 1978; White & Frenk, 1991). A well established theoretical prediction for how much gas should be driven out of galaxies by SNe feedback has yet to be achieved, with the dynamic range of the problem effectively providing an insurmountable obstacle. However, idealised calculations have been

performed to derive expected scalings (Creasey et al., 2013; Lagos et al., 2013).

The scaling that is generally agreed upon for SNe feedback, both on theoretical grounds and through indirect observational evidence, is that SNe feedback is probably most effective in smaller galaxies with shallow gravitational potential wells. For massive galaxies, it has been recognised since the cosmological baryon fraction was constrained by primordial deuterium measurements (O'Meara et al., 2001) that SNe feedback alone would be most likely be insufficient to explain the lack of efficiency of star formation in massive haloes (Benson et al., 2003). An alternative mechanism that acts as an explanation for inefficient star formation in massive haloes is feedback from active galactic nuclei (AGN). It is well established observationally that almost all galaxies are expected to host supermassive black holes at their centres (Kormendy & Richstone, 1995; Magorrian et al., 1998). To have reached the black hole masses that are inferred from observations, this SMBH population must have accreted large amounts of gas, releasing large amounts of gravitational potential energy in the process. Indeed, while the bolometric luminosity of sources locally is dominated by starlight, the luminosity per unit mass of SMBHs is larger than that of starlight by over a factor of ten (Hopkins et al., 2007). Provided the energy output of SMBHs can be efficiently coupled to gas inside galaxy haloes, AGN feedback provides an extremely promising mechanism to reduce star formation in massive galaxies (Bower et al., 2006; Croton et al., 2006). Observational evidence for this feedback mechanism comes from X-ray cavities observed in the hot ionised intracluster gas that are associated with radio jets originating from SMBHs located in brightest cluster galaxies (Rafferty et al., 2006; Bîrzan et al., 2008).

## 1.5 Results from galaxy surveys

The complexity and dynamic range of the physical processes that govern galaxy formation precludes the formulation of a galaxy formation theory from first principles that makes a complete prediction for the observed properties of the galaxy

population. Instead, researchers in this area are forced to calibrate models and simulations against observational constraints (e.g. Cole et al., 2000; Schaye et al., 2015). Once any model parameters are constrained, the model can then be tested against other observational constraints that were not included in the calibration process. Inevitably, as observational constraints change and improve with time, galaxy formation models are often forced to evolve to explain new observational results.

The advent of large spectroscopic and multi-wavelength photometric galaxy surveys has dramatically increased the range of observational constraints that galaxy formation models can be tested against (York et al., 2000; Giavalisco et al., 2004; Scoville et al., 2007). Some examples of important observational results that should be reproduced by galaxy formation models include the shape and normalisation of the luminosity function of galaxies, as a function of wavelength environment and redshift (e.g. Loveday et al., 2012; Marchesini et al., 2012; McNaught-Roberts et al., 2014), the clustering of galaxies as a function of luminosity, redshift and colour (Norberg et al., 2001, 2002; Coil et al., 2004; Zehavi et al., 2004) and the colour bimodality between red sequence and blue cloud galaxies (Baldry et al., 2006; Strateva et al., 2001).

To extract more information from multi-wavelength galaxy surveys, stellar population synthesis models that provide the spectral energy distributions (SEDs) of simple stellar populations of a given age, metallicity and stellar initial mass function (IMF) are used to infer the intrinsic properties of large samples of galaxies (e.g. Papovich et al., 2001; Ilbert et al., 2010). Using this approach, it is now routine for observational studies to infer the stellar masses of galaxies using SED fitting. Consequently, stellar mass functions have, arguably, replaced luminosity functions as the fundamental diagnostic of choice to characterise the galaxy population at a given epoch.

Alongside the rise in popularity of stellar mass estimation, emission from UV, mid-infrared (MIR), FIR, radio and nebula lines are now routinely used to estimate the SFRs of star forming galaxies (Kennicutt, 1998). Combining stellar mass and SFR estimates for common samples, observers infer that there are two distinct

populations of galaxies in the SFR versus stellar mass plane, analogous to the blue cloud and red sequence (Brinchmann et al., 2004; Salim et al., 2007). These two populations are made up of a star forming sequence where star formation rates are tightly correlated to stellar mass, and a much broader distribution of passive galaxies with negligible SFRs compared to their current stellar mass. An important result that has emerged from these studies is that the characteristic star formation rate of star forming galaxies at fixed stellar mass is inferred to drop by over an order of magnitude between a redshift, $z = 2$, and now (e.g. Rodighiero et al., 2010; Karim et al., 2011). This result is echoed by observational estimates of the integrated star formation rate density per unit comoving volume (e.g. Hopkins & Beacom, 2006).

As the size and resolution of dark matter simulations has improved over the last decade, interest has grown in empirically relating stellar mass functions inferred from observational data with the predicted halo population. Several methods have been employed that attempt to infer the distribution of stellar mass as a function of halo mass. Two of the most prominent of these include halo occupation distribution modelling (Berlind & Weinberg, 2002) and more recently, subhalo abundance matching (Conroy et al., 2006; Behroozi et al., 2010; Moster et al., 2010). The popularity of this approach has seen the median stellar mass to halo mass (SHM) relationship emerge as a key diagnostic of the galaxy population.

This thesis explores several of these key observational results using a theoretical galaxy formation model. The numerical implementations and underlying physics of the model are described in Chapter 2. In Chapter 3, the impact of using SED fitting to infer stellar masses is explored by applying the same observational techniques to simulated galaxies. In Chapter 4, the implications of the observational result that the SFRs of star forming galaxies have dramatically declined over cosmic time are examined. Chapter 5 presents an analysis of the evolution of the median stellar mass versus halo mass relation predicted by a galaxy formation model. Chapter 6 presents a summary of the conclusions from this thesis and outlines possible directions for future work.

# Chapter 2

# *Modelling galaxy formation*

## Overview

With the establishment of ΛCDM as a working cosmological model that predicts properties for a population of dark matter haloes, a natural question to ask is "how exactly was the galaxy population that we observe assembled within these haloes?". An obvious way to try and answer this question involves direct numerical simulation, including baryons as well as dark matter. Given that the relevant physics and initial conditions are thought to be known, the only barrier to this approach is numerical resolution. Unfortunately, it is thought that small scale physical processes, such as SNe explosions that take place in the cores of stars (with densities $\approx 10^{31}$ times the cosmic mean), can affect the larger scale properties of gas in galaxies. This creates a dynamic range problem which cannot be overcome without implementing models that account for sub-resolution physical effects. The state-of-the-art in this area is that a galaxy population that gives reasonable agreement with a variety of observational constraints can be simulated using sub-resolution physical prescriptions for star formation, SNe explosions and AGN energy injection into the ISM (Vogelsberger et al., 2014; Schaye et al., 2015). These sub-resolution physical prescriptions have to be tuned in order to achieve this agreement (Crain et al., 2015). Higher resolution simulations of smaller samples of haloes have also been claimed to match observational constraints but without this tuning process (e.g. Hopkins et al., 2014). However, these zoom simulation suites currently lack the statistical power to prove whether this is truly the case.

An alternative methodology for trying to understand galaxy formation is to

try to simplify the physical processes that are thought to be relevant in order to construct a galaxy formation model. A large range of different types of models exists, each designed to explain a different set of observed galaxy properties within a simple theoretical framework. These models range in complexity from simple chemical evolution models that are used to explain observed stellar abundances in nearby galaxies (e.g. Larson, 1972; Pagel & Patchett, 1975), all the way up to fully fledged hierarchical galaxy formation models that attempt to predict almost all of the observable integrated properties of galaxies (e.g. Kauffmann et al., 1993; Cole et al., 2000). In this thesis, all of the scientific analysis will be performed using a specific model of the latter type, the Durham semi-analytic model (SAM) referred to as GALFORM (Cole et al., 2000). In this Chapter, we introduce the semi-analytic modelling approach, focussing on aspects of the modelling that are relevant to the following Chapters in this thesis.

## 2.1 Compartmentalization

The starting point for semi-analytic galaxy formation models is that the mass content of galaxies and their surroundings can be compartmentalized into a discrete set of components. This compartmentalization is motivated by observations which show that galaxies consist of spatially and kinematically distinct components. For example, the stellar components of galaxies can be decomposed into a rotationally supported disk and a velocity dispersion supported bulge/spheroid component. Galaxy stellar disks can be described by a simple exponential density profile, given by

$$\rho_{\star,D}(r,z) = \rho_{\star,\mathrm{D},0}\ \exp(-r/r_{\mathrm{s}})\ \exp(-z/h_{\mathrm{s}}), \tag{2.1}$$

where $r_{\mathrm{s}}$ is the radial scalelength and $h_{\mathrm{s}}$ is the vertical scale height. Cold gas in galaxies is typically observed to follow a similar exponential disk profile, with the exception of gas associated with nuclear starbursts. Disk galaxy rotation curves are observed to be fairly flat as a function of radius (e.g. Rubin et al., 1980).

The projected density profiles of galaxy spheroids can be simply described by a spherically symmetric $r^{1/4}$ density profile, which approximately corresponds in deprojection to

$$\rho_{\star,B}(r) = \rho_{\star,\mathrm{B},0} \left(\frac{r}{r_\mathrm{s}}\right)^{-0.855} \exp\left[-\left(\frac{r}{r_\mathrm{s}}\right)^{1/4}\right] \tag{2.2}$$

where $r_\mathrm{s}$ is the radial scalelength (de Vaucouleurs, 1948; Mellier & Mathez, 1987). In this scheme, a galaxy spheroid can refer either to an elliptical galaxy (if there is a negligible disk component) or to a bulge embedded within a galaxy disk.

The remaining stellar, gas and dark matter components of galaxies can be simply described by spherically symmetric density profiles. These halo components are thought to be much more spatially extended than galaxy disks and spheroids. As described in Chapter 1, dark matter halo density profiles can be described by an NFW profile (Navarro et al., 1996), given by

$$\rho_\mathrm{DM}(r) = \frac{4\rho_\mathrm{s}}{x\,(1+x)^2}, \quad x \equiv r/r_\mathrm{s}, \tag{2.3}$$

where $r_\mathrm{s}$ is the scale radius.

For halo gas, observations of x-ray emitting gas in groups and clusters, as well as numerical simulations, indicate that in massive haloes, there is a hot, diffuse gas component. This hot gas halo is both observed and predicted to be less centrally concentrated than the dark matter, with a density profile that can be simply described by a $\beta$-model, given by

$$\rho_\mathrm{g}(r) = \frac{\rho_{\mathrm{g},0}}{\left[1+(r/r_\mathrm{core})^2\right]^{3\beta/2}}, \tag{2.4}$$

where $r_\mathrm{core}$ is a characteristic core radius and $\beta = 2/3$. The $\beta$ profile can be physically motivated under the assumption that the hot gas halo is isothermal and that the underlying mass distribution follows a King profile (Cavaliere & Fusco-Femiano, 1976). The specific value of $\beta = 2/3$ is motivated by dissipationless hydrodynamic simulations (Eke et al., 1998). Observationally, it thought that hot gas haloes are not, in general, isothermal for the galaxy cluster population, leading to

more complex parametrisations being proposed in the literature (e.g. Patej & Loeb, 2015). However, the $\beta$ profile broadly captures the differences between the spatial distributions of hot gas and dark matter in clusters and simplicity of the parametrisation makes it an attractive choice for galaxy formation models.

For the purposes of modelling galaxy formation, the $\beta$ profile can be extrapolated down to much smaller galaxies. However, in this regime there is no definitive observational evidence for quasi-hydrostatic hot gas profiles (e.g. Benson et al., 2000; Bogdán et al., 2013). The original theoretical expectation was that all haloes (or at least those unaffected by photoionization heating from reionization) would contain quasi-hydrostatic profiles as a result of shock heating of gas as it was accreted at the virial radius (White & Frenk, 1991). However, high resolution hydrodynamical simulations indicate that a substantial fraction of the gas in smaller haloes does not shock at the virial radius (e.g. Fardal et al., 2001; Kereš et al., 2005). On the other hand, this problem will not necessarily have an adverse effect on galaxy formation models that continue to assume that a hot gas profile is present in all haloes (Benson & Bower, 2011). This is because these models limit infall rates when the radiative cooling timescale is shorter than the freefall timescale (see 2.3.1).

Observations of the Milky Way and nearby galaxies reveal that in addition to diffuse dark matter and gas components, there is also a stellar halo (see Helmi, 2008, for a review). However, this component is thought to be completely subdominant in mass for most galaxies. For simplicity, this component can therefore be neglected. It should be noted that this is not a good approximation for galaxy clusters where the intracluster light can comprise a significant fraction of the total stellar mass in the system (Burke et al., 2012; Guennou et al., 2012).

Putting this all together, a given galaxy in a semi-analytic model is compartmentalized into a dark matter halo, a hot gas halo, a disk and a spheroid. An illustration of the assumed density profiles for a typical Milky-Way like galaxy in such a model is shown in Fig. 2.1. This compartmentalization approach greatly simplifies the numerical implementation of the model. On the other hand, the simplification obviously comes at the expense of having to assume idealised spatial

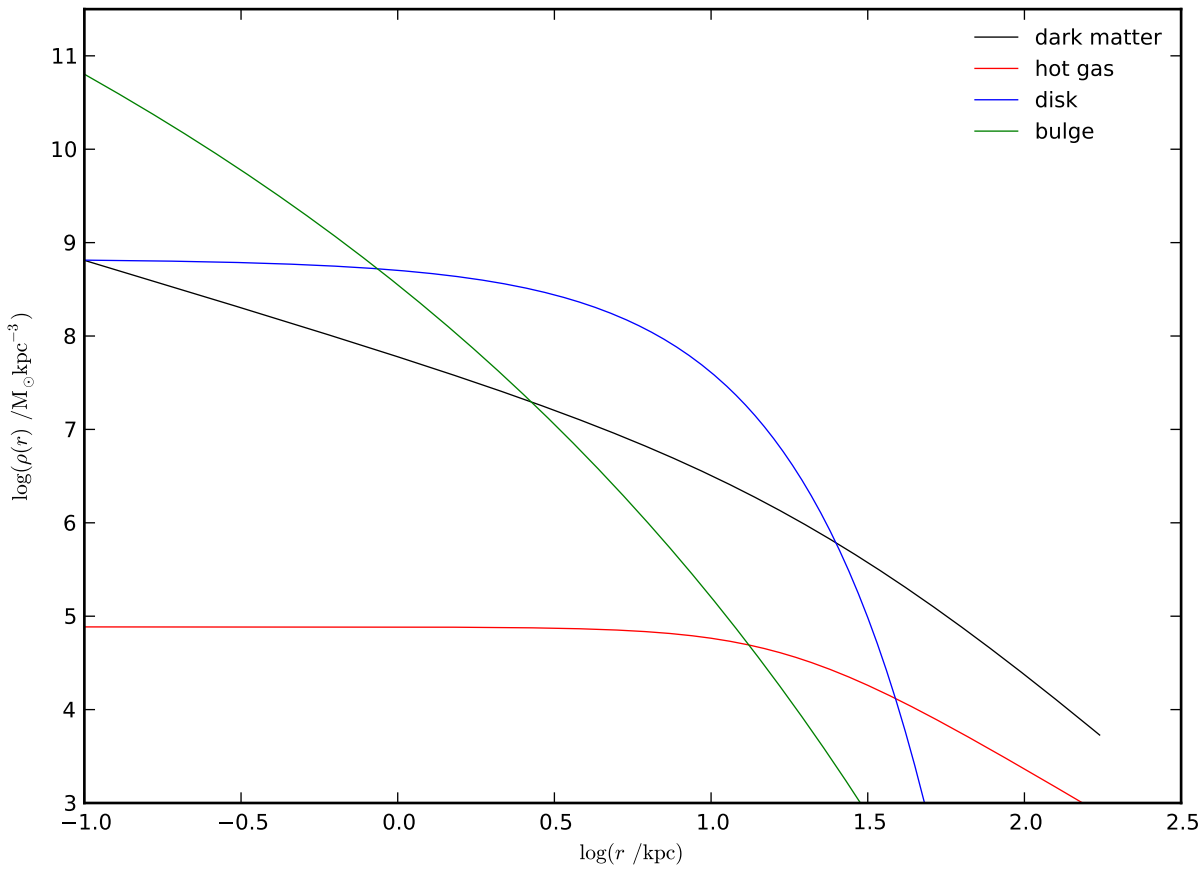


Figure 2.1: Radial density profiles of different components for a Milky-Way like galaxy. The black line shows the dark matter profile, which follows an NFW profile. The red line shows the hot gas profile, which follows a $\beta$ profile. The blue line shows the disk profile in the mid-plane of the disk, which follows an exponential profile. A ratio of the radial to vertical disk scalelength of $f_\star = 7.3$ was assumed (Kregel et al., 2002). The green line shows the bulge profile, which follows a deprojected $R^{1/4}$ profile.

and kinematic distributions.

## 2.2 A simple galaxy formation model

With the compartmentalization of galaxies into a dark matter and hot gas halo, a cold gas and stellar disk, and a cold gas and stellar bulge/spheroid, the next step in building a semi-analytic galaxy formation model is to consider how mass is exchanged between these different components. With this compartmentalization scheme in hand, a fairly general galaxy formation model can be written as a simple set of coupled differential equations. To illustrate this, we consider a simplified model where spheroid components are not included. We also neglect the hierarchical assembly process (no satellite galaxies). This simplified model can be written as

$$\begin{pmatrix} \dot{M}_{\rm DM} \\ \dot{M}_{\rm hot} \\ \dot{M}_{\rm cold} \\ \dot{M}_{\star} \\ \dot{M}_{\rm res} \end{pmatrix} = \begin{pmatrix} 0 & 0 & 0 & 0 & 0 \\ 0 & 0 & 0 & 0 & \frac{1}{\tau_{\rm ret}} \\ 0 & 0 & \frac{-1(1-R+\beta)}{\tau_{\star}} & 0 & 0 \\ 0 & 0 & \frac{(1-R)}{\tau_{\star}} & 0 & 0 \\ 0 & 0 & \frac{\beta}{\tau_{\star}} & 0 & \frac{-1}{\tau_{\rm ret}} \end{pmatrix} \begin{pmatrix} M_{\rm DM} \\ M_{\rm hot} \\ M_{\rm cold} \\ M_{\star} \\ M_{\rm res} \end{pmatrix} + \begin{pmatrix} (1-f_{\rm B})\dot{M}_{\rm H} \\ f_{\rm B}\dot{M}_{\rm H} - \dot{M}_{\rm infall} \\ \dot{M}_{\rm infall} \\ 0 \\ 0 \end{pmatrix}. \quad (2.5)$$

In this system of equations, there are five mass reservoirs. $M_{\rm DM}$ represents mass in the dark matter halo halo, $M_{\rm hot}$ represents mass in the hot gas halo, $M_{\rm cold}$ represents mass in the cold gas disk, $M_{\star}$ represents mass in the stellar disk and $M_{\rm res}$ represents mass in an additional reservoir.

The remaining terms in Eqn 2.5 represent the effects of physical processes on the mass in each reservoir. $\dot{M}_{\rm H}$ represents cosmological accretion of mass onto the halo. $f_{\rm B}$ is the cosmological baryon fraction, $f_{\rm B} \equiv \Omega_{\rm B}/\Omega_{\rm M}$. $\dot{M}_{\rm infall}$ is the rate of infall of gas from the hot gas halo onto the cold gas disk. $\tau_{\star}$ is a characteristic star formation timescale. Note that throughout the rest of this Chapter, we use $\Psi$ to represent the instantaneous star formation rate, which for the linear star formation law adopted in Eqn 2.5, is given by $\Psi = M_{\rm cold}/\tau_{\rm star}$. $R$ is the fraction of star forming

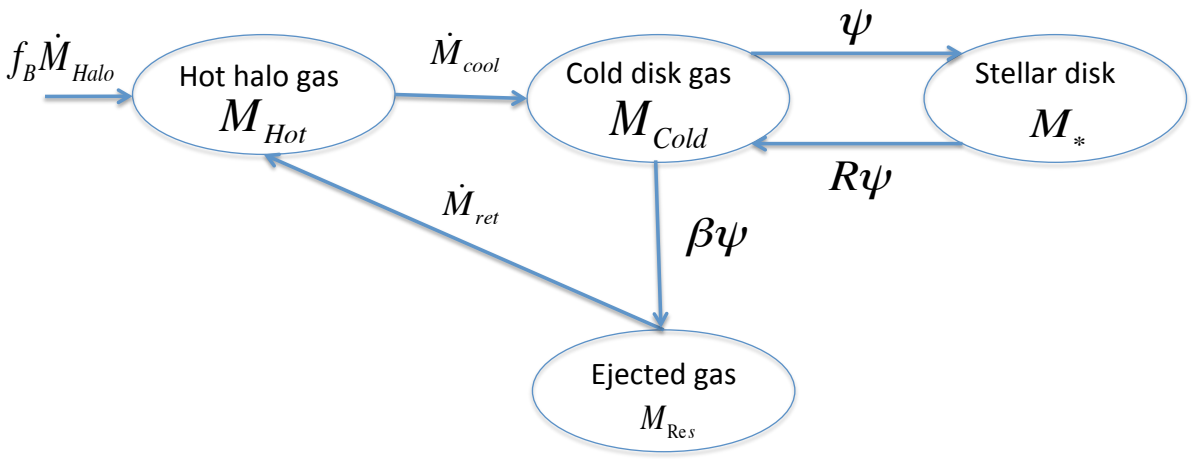


Figure 2.2: Schematic of a simple galaxy formation model. Mass enters the system through cosmological accretion, is cycled through a halo by feedback until finally reaching the stellar disk.

gas that is recycled back into the ISM as a result of stellar evolution. $\beta$ is the mass loading factor, which represents the effects of SNe feedback in ejecting gas from the cold gas disk. The resulting mass ejection rate is given by $\dot{M}_{\rm ej} = \beta\Psi$. This ejected gas is placed into a reservoir, $M_{\rm res}$, from which it is reincorporated into the hot gas halo over a characteristic timescale, $\tau_{\rm ret}$.

The set of equations listed in Eqn 2.5 is strongly coupled, and no simple analytical solution exists, even in the limit of a fixed cosmological accretion rate [1]. However, the behaviour of the system is fairly intuitive, as illustrated by the schematic shown in Fig. 2.2. A tracer gas particle that enters the hot gas halo through cosmological accretion will be statistically cycled a number of times before finally settling into the stellar disk. This statistical cycling time is controlled by a combination of the mass loading factor and the timescales for infall, disk depletion and gas reincorporation. In the regime where one of these timescales is significantly longer than than the others, the behaviour of the system for a given cosmological accretion rate will be entirely determined by a combination of that timescale and the

[1] An analytic solution does exist for the model presented in Cole et al. (2000), where the ejected gas reservoir was not considered.

mass loading factor. This is a point which we will return to in Chapter 4.

## 2.3 Infall, star formation, stellar evolution and feedback

Having set set up a simple set of equations that describe how mass is exchanged between different galaxy components, we now consider how to calculate the various terms that appear in Eqn 2.5.

### 2.3.1 Infall

The first term which we consider is the infall term, $\dot{M}_{\rm infall}$, which is the rate with which mass leaves the hot gas reservoir and enters the cold gas reservoir. Physically, this can either correspond to gas undergoing radiative cooling to settle at the centre of a quasi-hydrostatic hot gas halo, or to gas freefalling towards the centre of the gravitational potential of the halo. Semi-analytic galaxy formation models typically distinguish between these two regimes by calculating which one provides the limiting infall timescale. As a rule of thumb, gas infall is limited by the freefall timescale at early times when the radiative cooling timescale is short [2]. This situation is then reversed at late times as gas densities drop and the virial temperature rises, such that the radiative loss timescale limits the infall rate.

To calculate the dynamical freefall timescale, consider a test particle placed at a radius, $r_{\rm ff}$, within a NFW density profile. If the test particle starts at rest, energy conservation implies that

$$\frac{1}{2}(\dot{r}')^2 + \Phi(r') = \Phi(r_{\rm ff}), \tag{2.6}$$

where $\Phi(r')$ is the potential of a NFW profile at a radius, $r'$, given by

[2]Incidentally, this is the reason that infall rates in semi-analytic galaxy formation models do not dramatically disagree with modern hydrodynamical simulations, despite assuming all cosmological accreted gas is shock heated at the virial radius (Benson & Bower, 2011).

$$\Phi(r') = -16\pi G\rho_{\rm s} r_{\rm s}^2 \ln(1 + r'/r_{\rm s})\frac{r_{\rm s}}{r'}, \tag{2.7}$$

where $r_{\rm s}$ is the scale radius of a NFW profile (Chapter 2.2 Binney & Tremaine, 2008). Eqn 2.6 can be rearranged to give

$$\mathrm{d}t = \frac{1}{\sqrt{2}}[\Phi(r_{\rm ff}) - \Phi(r')]^{-1/2}\,\mathrm{d}r'. \tag{2.8}$$

The freefall time, $t_{\rm ff}$, for a test particle to fall from a radius, $r_{\rm ff}$, to the centre of the halo is obtained through integration, yielding

$$t_{\rm ff} = \frac{1}{\sqrt{2}}(16\pi G\rho_0)^{-1/2} pI(p), \quad p \equiv \frac{r_{\rm ff}}{r_{\rm s}}, \tag{2.9}$$

where

$$I(p) = \int_1^0 \left[\ln(1+px)\frac{1}{px} - \ln(1+p)\frac{1}{p}\right]^{-1/2} \mathrm{d}x, \quad x \equiv \frac{r'}{r_{\rm ff}}. \tag{2.10}$$

Eqn 2.9 can be expressed in terms of the halo dynamical time, $t_{\rm dyn} \equiv r_{\rm H}/V_{\rm H} = GM/V_{\rm H}^3$, as

$$t_{\rm ff} = \frac{1}{\sqrt{2}}\, t_{\rm dyn}\, a^3 f(a)\, pI(p), \quad a \equiv \frac{r_{\rm s}}{r_{\rm H}} = \frac{1}{c}, \quad f(a) \equiv \ln\left(1 + \frac{1}{a}\right) - \frac{1}{1+a}, \tag{2.11}$$

where $r_{\rm H}$ is the halo virial radius and $c$ is the NFW halo concentration.

To calculate the radiative cooling timescale for gas at a given density, it is typically assumed that the hot gas halo that surrounds a galaxy is in collisional ionization equilibrium, and is isothermal. In this case, we define the radiative cooling timescale, $\tau_{\rm cool}$, as the ratio of the thermal energy, $U$, to the radiative luminosity of the cooling gas, $L_{\rm cool}$. The internal energy is given by

$$U = \frac{3}{2}\frac{k_{\rm B}T}{\mu m_{\rm p}}, \tag{2.12}$$

where $T$ is the gas temperature and $\mu m_{\rm p}$ is the mean molecular weight of the gas. The cooling luminosity can be recast in the form of the cooling function, $\Lambda(T, Z)$, as

$$L_{\rm cool} = \frac{n_{\rm H}^2 \, \Lambda(T, Z)}{\rho}, \tag{2.13}$$

where $\rho$ is the gas density, $n_{\rm H}$ is the number density of hydrogen ions and $\Lambda(T, Z)$ has been normalised to unit number density of hydrogen nuclei. The cooling time can therefore be written as

$$\tau_{\rm cool} = \frac{3}{2} \frac{k_{\rm B} T}{\mu m_{\rm p}} \frac{\rho}{n_{\rm H}^2 \Lambda(T, Z)}. \tag{2.14}$$

The temperature of the hot gas is calculated assuming that the gas is shock heated to the virial temperature, which is given by

$$T = \frac{1}{2} \frac{\mu m_{\rm p}}{k_{\rm B}} V_H^2, \tag{2.15}$$

where $V_H$ is the circular velocity of the halo at the virial radius.

For a given hot gas and halo density profile, Eqns 2.14 and 2.11 can be used to compare the radiative cooling and freefall timescales at an arbitrary radius, $r$, within the halo. In practice, semi-analytic models calculate the infall rate by inverting these equations to calculate the radius within which gas would have had time to cool/freefall after some formation time, $t_{\rm form}$. These limiting radii define the cooling radius, $r_{\rm cool}$, and the freefall radius, $r_{\rm ff}$. The distinction for gas infall being limited by cooling or by freefall is then encapsulated by the limiting infall radius, $r_{\rm infall} = \min(r_{\rm cool}, r_{\rm ff})$. The infall rate is then simply given by

$$\dot{M}_{\rm infall} = 4\pi r_{\rm infall}^2 \rho(r_{\rm infall}) \dot{r}_{\rm infall}. \tag{2.16}$$

A more detailed explanation of how Eqn 2.16 is actually calculated in practice within GALFORM is not included in this thesis. Different cooling models with different methods for implementing Eqn 2.16 are described in Cole et al. (2000), Bower et al. (2006) and Benson & Bower (2010). The central problem is the question of how to calculate the hot gas density profile, $\rho(r)$, as hot gas cools out of the centre of the profile into the disk while fresh gas is added to the hot gas profile through

cosmological accretion and gas reincorporation. This has lead to the implementation of notional profiles that represent the hot gas density profile in the absence of infall from cooling or freefall. Other complications include the choice of how to calculate of $t_{\rm form}$ and $\dot{r}_{\rm infall}$. The majority of the results in this thesis use the Bower et al. (2006) scheme. In some cases (which are noted in each relevant Chapter), we present results using the Benson & Bower (2010) scheme.

To illustrate the difference between the cooling and freefall regimes, Fig. 2.3 shows the two characteristic timescales as a function of halo mass and formation redshift. Depending on the formation redshift, infall within haloes switches from being limited by the freefall timescale to being limited by cooling timescale at a halo mass, $\log(M_{\rm H}/{\rm M}_{\odot}) \approx 12$.

### 2.3.2 Star formation

In the simple galaxy formation model laid out in Eqn 2.5, we assumed a linear star formation law of the form

$$\Psi = \frac{M_{\rm cold}}{\tau_{\star}}, \tag{2.17}$$

where $\Psi$ is the instantaneous star formation rate, $M_{\rm cold}$ is the total gas mass of the galaxy disk, and $\tau_{\star}$ is a characteristic star formation timescale. As an example of how $\tau_{\star}$ can be calculated, Cole et al. (2000) proposed that

$$\tau_{\star} = \frac{\tau_{\rm disk}}{\epsilon_{\star}} \left( \frac{V_{\rm disk}}{200\,{\rm kms}^{-1}} \right)^{\alpha_{\star}}, \tag{2.18}$$

where $\tau_{\rm disk}$ is the disk dynamical timescale, $V_{\rm disk}$ is the circular velocity of the disk at the half-mass radius, and both $\epsilon_{\star}$ and $\alpha_{\star}$ are considered model parameters. For the case of $\alpha_{\star} = 0$, this star formation law corresponds to a Kennicutt law, which has empirical support from observations (e.g. Kennicutt, 1998).

While a linear SF law is very convenient for writing a set of simple of equations like Eqn 2.5, more recent versions of the GALFORM semi-analytic model instead use the empirically motivated non-linear star formation law described in Lagos

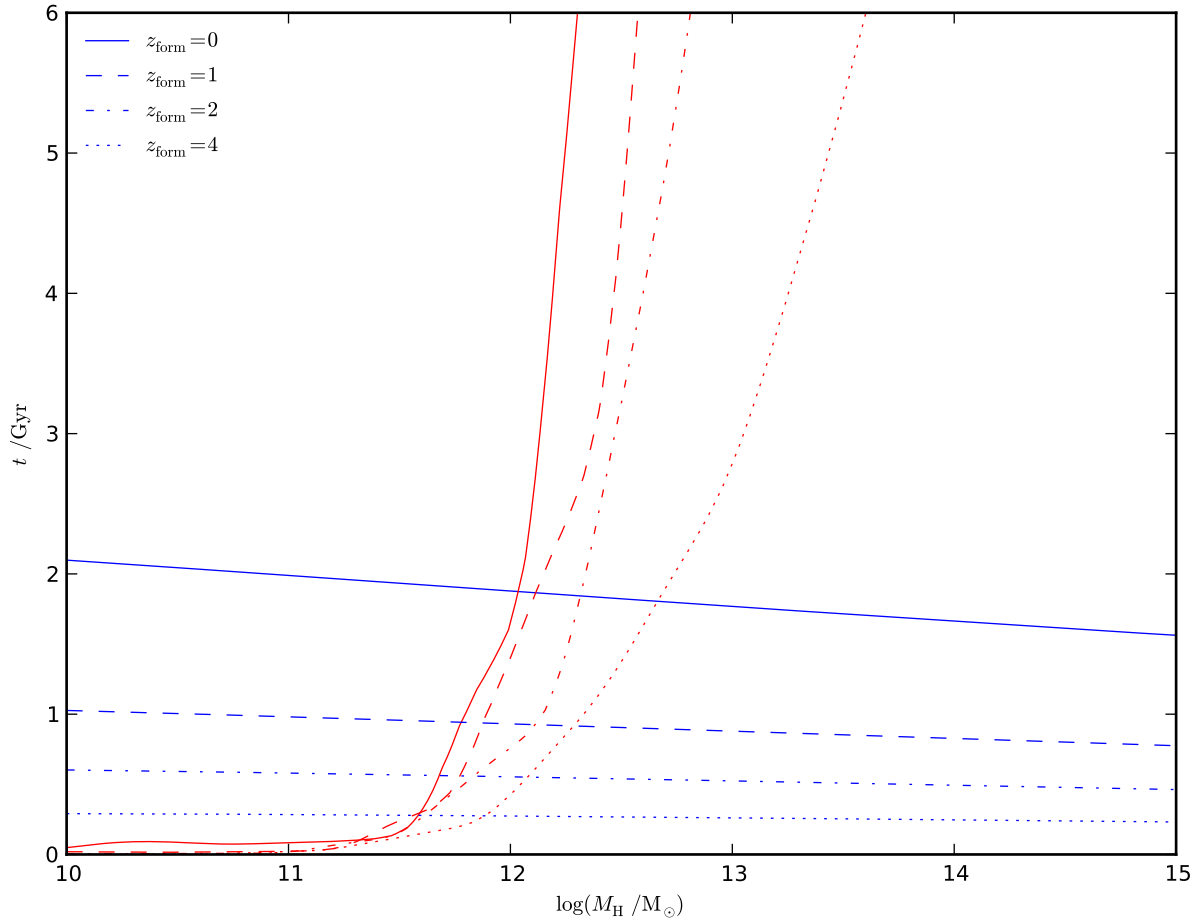


Figure 2.3: Cooling (red) and freefall (blue) timescales plotted as a function of halo mass. Different line styles show the timescales for different formation redshifts, as labelled. The formation redshift determines the halo circular velocity and the halo concentration. Red lines show the cooling timescale for gas at the mean density of the hot gas halo. Here the hot gas halo follows a $\beta$ profile with core radius, $r_{\rm core} = 0.1 r_{\rm H}$. The mass of the hot gas halo is set to $M_{\rm hot} = f_{\rm b} M_{\rm H}$, and the metallicity is set to $Z_{\rm hot} = 0.1\,{\rm Z}_\odot$. Blue lines show the freefall timescale for a particle placed at the virial radius of the halo.

et al. (2011b). Almost all models in subsequent Chapters of this thesis will use this non-linear SF law. Specifically, the SF law from Lagos et al. (2011b) that we use is based upon the empirical law introduced by Blitz & Rosolowsky (2006). The Blitz & Rosolowsky (2006) SF law is linear in the molecular gas surface density, $\Sigma_{\rm mol}$, and is given by

$$\Sigma_{\rm SFR} = \nu_{\rm SF} \Sigma_{\rm mol}, \tag{2.19}$$

where $\Sigma_{\rm SFR}$ is the star formation rate surface density and $\nu_{\rm SF}$ is a coefficient set to $0.5\,{\rm Gyr}^{-1}$, based on observations from Leroy et al. (2008).

To implement this SF law into a semi-analytic galaxy formation model, it is necessary to first calculate the fraction of gas that is in the molecular phase, as a function of radius within the galaxy disk. Following Blitz & Rosolowsky (2006) this is determined using

$$R_{\rm mol} \equiv \frac{\Sigma_{\rm mol}}{\Sigma_{\rm atomic}} = \left( \frac{P_{\rm ext}}{P_0} \right)^{\alpha}, \tag{2.20}$$

where $\Sigma_{\rm atomic}$ is the surface density of atomic hydrogen, $P_{\rm ext}$ is the hydrostatic pressure of the disk at the mid plane, and $P_0$ and $\alpha$ are parameters that, again, can be constrained by observational data (Blitz & Rosolowsky, 2006; Leroy et al., 2008). $P_{\rm ext}$ can be calculated following the approach of Elmegreen (1993), as

$$P_{\rm ext} \approx \frac{\pi}{2} G \Sigma_{\rm gas} \left[ \Sigma_{\rm gas} + \left( \frac{\sigma_{\rm g}}{\sigma_\star} \right) \Sigma_\star \right], \tag{2.21}$$

where $\Sigma_{\rm gas}$ is the total gas surface density, $\Sigma_\star$ is the surface density of stars, and $\sigma_{\rm g}$ and $\sigma_\star$ are the vertical velocity dispersions in gas and stars respectively. This relationship is implemented into GALFORM assuming that $\sigma_{\rm g} = 10\,{\rm km s}^{-1}$ and $\sigma_\star = \max(\sigma_{\rm g}, \sqrt{\pi G h_{\rm s} \Sigma_\star})$. The vertical disk scale height can be approximated as $h_{\rm s} \approx r_{\rm s}/7.3$, where $r_{\rm s}$ is the radial scale length of the disk (Kregel et al., 2002).

Putting this all together, the Blitz & Rosolowsky (2006) SF law allows $\Sigma_{\rm sfr}$ to be calculated at a given radius within the disk once values for the stellar disk mass, $M_\star$, the total gas mass, $M_{\rm cold}$, and the radial scale length, $r_{\rm s}$, are specified. The total

star formation rate is then determined by integrating over radius in the disk. This integral has be calculated numerically within the model and the final star formation rate is not linear in the total gas mass.

### 2.3.3 Stellar evolution and feedback

Once gas has collapsed to form stars, it is expected that some of the gas will be returned to the ISM as a result of stellar evolution. Typically, semi-analytic models deal with this gas recycling using the instantaneous recycling approximation (IRA). Under the IRA, a constant recycled fraction, $R$, of gas that forms stars is immediately returned to the ISM. In this case, the stellar mass assembly rate is related to the star formation rate by $\dot{M}_\star = (1 - R)\Psi$ (in the absence of feedback).

In addition to this mass recycling, it is also thought that the feedback from massive stars (the dominant mechanism typically thought to be SNe explosions) can drive gas in the ISM from galaxies in powerful outflows. This process is represented in semi-analytic models by assuming that the outflow rate, $\dot{M}_{\rm ej}$, is directly linked to the instantaneous star formation rate, $\Psi$, by the mass loading factor, $\beta$ such that

$$\dot{M}_{\rm ej} = \beta\,\Psi. \tag{2.22}$$

Linking the mass ejection rate to the instantaneous star formation rate in this way is effectively another application of the IRA. This assumption can be justified in this context because the lifetimes of massive stars are short ($\approx 10\,\mathrm{Myr}$) compared to other typical timescales in semi-analytic models.

The complexity and dynamic range involved in tracing how energy and momentum injected into the ISM by SNe drive outflowing winds means that the mass loading factor represents one of the most uncertain aspects of semi-analytic models. Historically, these models have resorted to a phenomenological approach where a simple parametrisation of the mass loading factor is adopted that allows the model to reproduce the inefficient stellar mass assembly that is implied by the shape of the

local luminosity function for low mass galaxies. In GALFORM, the parametrisation adopted is

$$\beta = \left( \frac{V_{\rm disk}}{V_{\rm hot}} \right)^{-\alpha_{\rm hot}}, \tag{2.23}$$

where $V_{\rm disk}$ is the circular velocity of the disk at the disk half-mass radius, and $V_{\rm hot}$ and $\alpha_{\rm hot}$ are model parameters. To explain the global inefficiency of star formation, $V_{\rm hot}$ and $\alpha_{\rm hot}$ are typically set such that the mass loading factor $\beta$, is greater than unity for galaxies with ongoing star formation. To reproduce the shallow slope of the luminosity function below the knee, $\alpha_{\rm hot}$ is typically set to $\approx 3$, reflecting the need for stronger feedback in low mass galaxies. The parametrisation of $\beta$ with circular velocity is crudely justified because the $V_{\rm disk}$ traces the depth of the gravitational potential close to the galaxy. In practice, the mass loading factor is expected to be determined in part by the detailed properties of the ISM in the vicinity of SNe explosions, although it might be reasonably expected that the relevant global ISM properties would correlate with galaxy circular velocity to some degree (Creasey et al., 2013; Lagos et al., 2013).

Once gas has been ejected from a galaxy by SNe feedback, there is then an open question as to what the fate of that gas will be as it propagates through the larger scale halo. There are various considerations that need to be taken into account. Firstly, the outflowing gas will not be in thermal or dynamical equilibrium with the surrounding hot gas for some time after being ejected, so it seems inappropriate to place ejected gas directly back into the hot gas reservoir with no delay. A second consideration is whether the gas will actually leave the halo entirely. Physically, the fate of the outflowing gas will depend on the interplay between gravity and hydrodynamical interaction with the larger scale gas halo. In principle, hydrodynamical simulations can be used to study this process. In practice, however, the dynamics of outflowing gas in these simulations will depend sensitively on the uncertain implementation of sub-grid modelling for the energy injection into the ISM from SNe feedback.

For the simple galaxy formation model described by Eqn 2.5, a straight forward

scheme has been adopted in which gas ejected from the disk by feedback is placed into an additional reservoir, $M_{\rm res}$ [3]. This ejected gas is then reincorporated from $M_{\rm res}$ into the hot gas halo over a characteristic timescale, $t_{\rm ret}$. This reincorporation timescale is parametrised in GALFORM as

$$\tau_{\rm ret} = \frac{t_{\rm dyn}}{\alpha_{\rm reheat}}, \tag{2.24}$$

where $t_{\rm dyn}$ is the halo dynamical timescale and $\alpha_{\rm reheat}$ is a model parameter, typically set roughly to unity. The assumption that gas ejected by feedback returns to the hot gas halo over a dynamical timescale effectively corresponds to assuming that the gas is ejected ballistically to the virial radius of the halo, before being reincorporated into the hot gas halo. There are various reasons why this scenario is probably overly simplistic. For example, it might be expected that gas would be ejected with velocities significantly greater than the escape velocity for smaller haloes. On the other end of the mass spectrum, neglecting the hydrodynamical interaction between outflowing gas and the hot gas coronae that are known to be present in galaxy groups and clusters could also be problematic.

## 2.4 Chemical enrichment & angular momentum

The simple model outlined in Section 2.2 considered only how mass was exchanged between different components. We now extend this scheme to also consider the exchange of angular momentum and metals. The primary purpose of tracking angular momentum in GALFORM is to calculate the sizes and circular velocities of galaxy disks, a calculation which we describe in Section 2.5.2. The purpose of tracking metals is firstly to allow to the radiative cooling timescale, given by Eqn 2.14, to be computed self consistently. In addition, tracking both the mass assembly and chemical enrichment histories of galaxies in the model allows predictions for observable SEDs, a step which we describe in Section 2.9.

[3] It should be noted that unlike the other mass reservoirs in the model (the disk and the halo), this reservoir of ejected gas does not have a defined spatial, kinematic or thermal distribution.

Following the same compartmentalization scheme as Eqn 2.5, an equivalent set of equations for metals can be written as

$$\begin{pmatrix} \dot{M}_{Z,\mathrm{hot}} \\ \dot{M}_{Z,\mathrm{cold}} \\ \dot{M}_{Z,\star} \\ \dot{M}_{Z,\mathrm{res}} \end{pmatrix} = \begin{pmatrix} 0 & 0 & 0 & \frac{1}{\tau_{\mathrm{ret}}} \\ 0 & \frac{-1(1-R+\beta)}{\tau_\star} & 0 & 0 \\ 0 & \frac{(1-R)}{\tau_\star} & 0 & 0 \\ 0 & \frac{\beta}{\tau_\star} & 0 & \frac{-1}{\tau_{\mathrm{ret}}} \end{pmatrix} \begin{pmatrix} M_{\mathrm{Z,hot}} \\ M_{\mathrm{Z,cold}} \\ M_{\mathrm{Z},\star} \\ M_{\mathrm{Z,res}} \end{pmatrix} + \begin{pmatrix} f_{\mathrm{B}} Z_{\mathrm{BB}} \dot{M}_{\mathrm{H}} - \dot{M}_{Z,\mathrm{infall}} \\ \dot{M}_{Z,\mathrm{infall}} + \frac{pM_{\mathrm{cold}}}{\tau_\star} \\ 0 \\ 0 \end{pmatrix}, \tag{2.25}$$

where $M_{\mathrm{Z,hot}}$ is the mass in metals in the hot gas halo, $M_{\mathrm{Z,cold}}$ corresponds to the cold gas disk, $M_{\mathrm{Z},\star}$ corresponds to metals locked in disk stars and $M_{\mathrm{Z,res}}$ corresponds to the ejected gas reservoir. Compared to Eqn 2.5, Eqn 2.25 contains two additional terms: the metal yield, $p$, and the metallicity of primordial gas, $Z_{\mathrm{BB}}$. In practice, the mass in metals accreted from the primordial IGM is negligible relative to the metals injected by stellar evolution. As for the recycled fraction, $R$, the instantaneous recycling approximation can be adopted for chemical enrichment, such that $p$ is a constant.

As for angular momentum, a final extension to Eqns 2.5 and 2.25 can be written as

$$\begin{pmatrix} \dot{J}_{\mathrm{DM}} \\ \dot{J}_{\mathrm{hot}} \\ \dot{J}_{\mathrm{cold}} \\ \dot{J}_\star \\ \dot{J}_{\mathrm{res}} \end{pmatrix} = \begin{pmatrix} 0 & 0 & 0 & 0 & 0 \\ 0 & 0 & 0 & 0 & \frac{1}{\tau_{\mathrm{ret}}} \\ 0 & 0 & \frac{-1(1-R+\beta)}{\tau_\star} & 0 & 0 \\ 0 & 0 & \frac{(1-R)}{\tau_\star} & 0 & 0 \\ 0 & 0 & \frac{\beta}{\tau_\star} & 0 & \frac{-1}{\tau_{\mathrm{ret}}} \end{pmatrix} \begin{pmatrix} J_{\mathrm{DM}} \\ J_{\mathrm{hot}} \\ J_{\mathrm{cold}} \\ J_\star \\ J_{\mathrm{res}} \end{pmatrix} + \begin{pmatrix} (1-f_{\mathrm{B}})\dot{J}_{\mathrm{H}} \\ f_{\mathrm{B}}\dot{J}_{\mathrm{H}} - \dot{J}_{\mathrm{infall}} \\ \dot{J}_{\mathrm{infall}} \\ 0 \\ 0 \end{pmatrix}, \tag{2.26}$$

where $J_{\mathrm{DM}}$ is the angular momentum of the dark matter halo, $J_{\mathrm{hot}}$ corresponds to the hot gas halo, $J_{\mathrm{cold}}$ corresponds to the cold gas disk, $J_\star$ corresponds to the stellar disk and $J_{\mathrm{res}}$ corresponds to the ejected gas reservoir. Additional terms that appear in Eqn 2.26 compared to Eqn 2.5 include the cosmological angular momentum accretion rate, $\dot{J}_{\mathrm{H}}$, and the infall rate of angular momentum from the hot gas halo into the cold gas disk, $\dot{J}_{\mathrm{infall}}$. Here, angular momentum, $J_i$, refers to the total scalar an-

gular momentum content within a galaxy component (for example, the dark matter halo) around an axis that crosses the centre of the halo, and is perpendicular to the disk plane.

Built into Eqn 2.26 is a series of assumptions which we now discuss. The first of these is that the specific angular momentum[4] of gas accreted onto haloes is identical to that of the dark matter. The second is that the angle of the angular momentum vector of accreted gas remains constant over the lifetime of a galaxy (this assumption is implicit in the model because we track angular momentum as a scalar quantity). The third is that angular momentum exactly traces mass through star formation, stellar evolution and feedback processes. In other words, it is assumed that the specific angular momentum of a galaxy disk remains constant through these processes.

In GALFORM, a final assumption is adopted that the hot gas halo always has total scalar specific angular momentum content,

$$J_{\rm hot} = \frac{M_{\rm hot}}{M_{\rm B}} f_{\rm B} J_{\rm H}, \tag{2.27}$$

where $M_{\rm B}$ is the total baryonic mass of the halo. In effect, this means that the angular momentum of gas reincorporated from the ejected gas reservoir, $J_{\rm res}$, is adjusted such that the hot gas halo always has the same specific angular momentum as the dark matter halo. Taking this step violates (scalar) angular momentum conservation but has has the significant upside in that it significantly reduces the scheme of angular momentum transfer equations to

$$\begin{pmatrix} \dot{J}_{\rm DM} \\ \dot{J}_{\rm hot} \\ \dot{J}_{\rm disk} \end{pmatrix} = \begin{pmatrix} (1-f_{\rm B})\dot{J}_{\rm H} \\ f_{\rm B}\dot{J}_{\rm H} - \dot{J}_{\rm infall} \\ \dot{J}_{\rm infall} \end{pmatrix}, \tag{2.28}$$

where the cold gas and stellar disks have been grouped together into a single angular momentum reservoir, $J_{\rm disk}$.

To compute the cosmological accretion of angular momentum, $\dot{J}_{\rm H}$, GALFORM

[4] angular momentum per unit mass

exploits results from numerical simulations which show that the dimensionless halo spin parameter, $\lambda_{\rm H}$, is roughly independent of mass and cosmological parameters (Barnes & Efstathiou, 1987; Efstathiou et al., 1988; Warren et al., 1992; Cole & Lacey, 1996; Kauffmann et al., 1999). $\lambda_{\rm H}$ is given by

$$\lambda_{\rm H} = \frac{J_{\rm H}|E_{\rm H}|^{1/2}}{GM_{\rm H}^{5/2}}, \tag{2.29}$$

where $E_{\rm H}$ is the total energy content of the halo. A value for $\lambda_{\rm H}$ is assigned to each halo by sampling from a log-normal probability distribution function (PDF) (Cole et al., 2000).

Under the assumption that the rotational velocity, $V_{\rm rot}$ of concentric shells of dark matter is independent of radius, and that these rotating shells are aligned, the total scalar angular momentum of a spherically symmetric halo is obtained by integrating over surface elements as

$$J_{\rm H} = V_{\rm rot} \int_0^{\pi} \sin(\theta)^2 \, {\rm d}\theta \int_0^{2\pi} {\rm d}\phi \int_0^{r_{\rm H}} \rho(r') r'^3 {\rm d}r', \tag{2.30}$$

which reduces to

$$J_{\rm H} = \pi^2 V_{\rm rot} \int_0^{r_{\rm H}} \rho(r') r'^3 {\rm d}r'. \tag{2.31}$$

Therefore, calculating the angular momentum of the dark matter halo with a given density profile only requires the rotation velocity, $V_{\rm rot}$ to be calculated. An expression for $V_{\rm rot}$ was obtained by Cole et al. (2000) assuming that dark matter haloes obey effective hydrostatic equilibrium with isotropic velocity dispersion. Under this assumption, the kinetic and potential energies of the system can be calculated to obtain $E_{\rm H}$ (see Appendix A of Cole et al., 2000). Combining an expression for $E_{\rm H}$ with Eqn 2.29 and Eqn 2.30 yields

$$V_{\rm rot} = A(a_{\rm NFW}) \lambda_{\rm H} V_{\rm H}, \; a_{\rm NFW} = \frac{r_{\rm s}}{r_{\rm H}} = \frac{1}{c} \tag{2.32}$$

where $V_{\rm H}$ is the circular velocity at the virial radius and $A(a_{\rm NFW})$ is a dimensionless coefficient that is a weak function of the NFW halo concentration, $c$ (Cole et al.,

2000).

To calculate the rate of angular momentum exchange from the hot gas halo onto the disk, $\dot{J}_{\rm infall}$, the angular momentum of the hot gas halo at the infall radius, $r_{\rm infall}$ is determined, analogous to the calculation of the mass infall rate. To calculate the angular momentum of the hot gas halo at a given radius, it is necessary to calculate a rotation velocity, $V_{\rm rot}^{\rm gas}$, for the hot gas halo such that the specific angular momentum of the hot gas halo is equal to that of the dark matter halo. Once $V_{\rm rot}$ has been calculated for the dark matter, $V_{\rm rot}^{\rm gas}$ can be determined by evaluating Eqn 2.31 for both the hot gas and the dark matter haloes.

## 2.5 Galaxy sizes

The primary purpose of tracking angular momentum in a model like GALFORM is for calculating galaxy sizes and circular velocities. These quantities are then fed back into the parametrisation for the mass loading factor, given by Eqn 2.23, such that the size calculation is coupled with the rest of the model. Galaxy sizes are also used to obtain dust extinction corrections when computing observable SEDs.

### 2.5.1 Halo contraction

Galaxy sizes are computed within GALFORM using a contraction scheme such that the dark matter halo responds adiabatically to the gravitational potential of the disk and spheroid. A system of equations is constructed and solved such that the contracted halo, disk and spheroid are in dynamical equillibrium. In this configuration, the disk is assumed to be in centrifugal equilibrium and the spheroid in virial equilibrium. To compute the contraction of the halo, it is assumed that the pseudo specific angular momentum, $rV_{\rm c}(r)$, is conserved for each shell of the halo (Blumenthal et al., 1986). Under this assumption,

$$rV_{\rm c}(r) = r_0 V_{\rm c,0}(r_0), \tag{2.33}$$

where $V_{\rm c}$ is the circular velocity of the contracted halo at a radius $r$. $V_{\rm c,0}$ is the circular velocity at a radius $r_0$ that the halo would have if no galaxy had formed. We refer to this latter configuration as the uncontracted halo. Here, the "halo" refers collectively to the dark matter, hot gas, ejected gas and satellite components which have been grouped together. When considering this collective halo component in the scenario where no galaxy had formed, the halo is assumed to follow the same NFW density profile as the dark matter halo.

The density profiles of the contracted and uncontracted haloes are related by

$$M_{\rm H}(r) = f_{\rm H} M_{\rm H,0}(r_0), \tag{2.34}$$

where $M_{\rm H}(r)$ is the mass of the contracted halo interior to a radius, $r$, and $M_{\rm H,0}(r_0)$ is the corresponding mass of the uncontracted halo interior at a radius, $r_0$. $1 - f_{\rm H}$ is the fraction of mass that has condensed out of the uncontracted halo component to form the galactic disk and spheroid.

Under the approximation that the disk density profile is treated as being spherically symmetric, the circular velocity of the contracted halo is given by

$$V_{\rm c}^2(r) = G[M_{\rm H}(r) + M_{\rm D}(r) + M_{\rm B}(r)]/r, \tag{2.35}$$

where $M_{\rm D}(r)$ and $M_{\rm B}(r)$ are the mass of the disk and bulge respectively within a radius, $r$. The corresponding relationship for the uncontracted halo is

$$V_{\rm c,0}^2(r_0) = G[M_{\rm H,0}(r_0)]/r_0. \tag{2.36}$$

Combining Equations 2.33, 2.34, 2.35 and 2.36 together,

$$r_0 M_{\rm H,0}(r_0) = r[f_{\rm H} M_{\rm H,0}(r_0) + M_{\rm D}(r) + M_{\rm B}(r)]. \tag{2.37}$$

This relates the uncontracted halo profile to the disk and spheroid profiles. With the density profiles of the disk and spheroid defined in 2.1, all that remains is to solve for the half mass radii of the disk and bulge such that they are in dynamical

equilibrium with the contracted halo. Note that the contracted halo density profile is not explicitly calculated under this scheme.

### 2.5.2 Disk and spheroid sizes

#### Disk

To compute the centrifugal equilibrium configuration of the disk, we need to be able to relate the circular velocity of the disk at a given radius to the total angular momentum of the disk. These quantities can be related by

$$j_{\rm D} = k_{\rm D} r_{\rm D} V_{\rm D}(r_{\rm D}), \tag{2.38}$$

where $j_{\rm D}$ is the specific angular momentum of the disk and $V_{\rm D}(r_{\rm D})$ is the circular velocity of the disk in the disk plane at the half-mass radius, $r_{\rm D}$ [5]. $k_{\rm D}$ is a constant which for a flat rotation curve is given by $k_{\rm D} = 1.19$, a result that is straightforwardly obtained by integrating over the angular momentum profile of the disk.

The circular velocity of the disk at the half mass radius is related to the contracted halo and spheroid density profiles by

$$\begin{aligned} V_{\rm D}^2(r_{\rm D}) &= G[f_{\rm H} M_{\rm H,0}(r_{\rm D,0}) + M_{\rm D}(r_{\rm D}) + M_{\rm B}(r_{\rm D})]/r_{\rm D} \\ &= G[f_{\rm H} M_{\rm H,0}(r_{\rm D,0}) + \frac{1}{2} M_{\rm D} + M_{\rm B}(r_{\rm D})]/r_{\rm D}, \end{aligned} \tag{2.39}$$

where $M_{\rm D}$ is the total disk mass and $r_{\rm D,0}$ is the uncontracted radius of a halo shell that has contracted to radius, $r_{\rm D}$. Here, as in Eqn 2.35, the disk profile has been approximated to be spherically symmetric. To correct for this approximation, a factor $k_{\rm h} = 1.25$ can be introduced such that the circular velocity is computed for an exponential disk in the mid plane, yielding

$$V_{\rm D}^2(r_{\rm D}) = G[f_{\rm H} M_{\rm H,0}(r_{\rm D,0}) + \frac{1}{2} k_{\rm h} M_{\rm D} + M_{\rm B}(r_{\rm D})]/r_{\rm D}, \tag{2.40}$$

[5] For an exponential disk profile, $r_{\rm D}$ is related to the radial scalelength by $r_{\rm D} = 1.68 r_{\rm s}$.

(Cole et al., 2000; Binney & Tremaine, 2008). Combining Eqn 2.40 with Eqn 2.38, the specific angular momentum of the disk can be related to the spheroid and uncontracted halo profiles by

$$j_{\rm D}^2 = k_{\rm D}^2 G r_{\rm D}[f_{\rm H} M_{\rm H,0}(r_{\rm D,0}) + \frac{1}{2} k_{\rm h} M_{\rm D} + M_{\rm B}(r_{\rm D})]. \tag{2.41}$$

Finally, by combining Eqn 2.40 with Eqn 2.37 evaluated at $r_{\rm D}$ to cancel out the spheroid profile, the uncontracted halo profile can be related to $r_{\rm D}$ through

$$r_{\rm D,0} M_{\rm H,0}(r_{\rm D,0}) = \frac{j_{\rm D}^2}{k_{\rm D}^2 G} - \frac{1}{2}(k_{\rm h} - 1) r_{\rm D} M_{\rm D}. \tag{2.42}$$

In this equation, there are two unknowns: $r_{\rm D}$ and $r_{\rm D,0}$.

### Spheroid

For the spheroid, a pseudo-angular momentum, $j_{\rm B}$, can be defined as

$$j_{\rm B} = r_{\rm B} V_{\rm B}(r_{\rm B}), \tag{2.43}$$

where $V_{\rm B}(r_{\rm B})$ is the spheroid circular velocity at the deprojected half-mass radius, $r_{\rm B}$. At this stage, we have not described the model for spheroid formation that is implemented within GALFORM. We return to this topic in Section 2.6.3.

By employing exactly the same approach as was used to obtain Eqn 2.42, an equivalent relationship between the uncontracted halo profile and the spheroid profile at a radius, $r_{\rm B}$, can be obtained, yielding

$$r_{\rm B,0} M_{\rm H,0}(r_{\rm B,0}) = \frac{j_{\rm B}^2}{G}. \tag{2.44}$$

In this case, it has been assumed that the disk density profile is spherically symmetric, such that $k_{\rm h} = 1$.

Finally, to relate $r_{\rm B,0}$ to $r_{\rm B}$, we can make use of an intermediate step from obtaining Eqn 2.44 which relates $j_{\rm B}$ to the disk and uncontracted halo profiles, which is given by

$$j_{\rm B}^2 = G r_{\rm B}[f_{\rm H} M_{\rm H,0}(r_{\rm B,0}) + M_{\rm D}(r_{\rm B}) + \frac{1}{2} M_{\rm B}]. \quad (2.45)$$

By solving the coupled system of equations given by Equations 2.42, 2.40 and 2.45 with a root finding algorithm, the disk and spheroid half-mass radii can be computed.

## 2.6 Hierarchical galaxy formation and spheroid formation

In the preceding sections of this Chapter, we have described fully how to construct and compute the various terms within a set of equations that describe the formation of a galaxy disk within a dark matter halo. The only term that remains to be described from this set of equations is the cosmological mass accretion term, $\dot{M}_{\rm H}$, which is the rate with which mass (both gas and dark matter) is accreted at the virial radius of the halo. In some simple galaxy formation models, $\dot{M}_{\rm H}$ is obtained simply by calculating the average accretion rates of haloes for a given halo mass bin at $z = 0$ (Dutton et al., 2007; Bouché et al., 2010). For a full semi-analytic model such as GALFORM, the entire merging histories of dark matter haloes[6] are tracked through the hierarchical assembly process. In this case, the scheme of equations that we have described throughout this Chapter have to be coupled with the resulting dark matter halo merger trees. Furthermore, we now have to also consider the fate of galaxies that become of satellites of larger galaxies.

### 2.6.1 Merger trees

There are two methods which are commonly used to generate halo merger trees. The first is to use an algorithm based on the extended Press-Schecter (EPS) formalism which predicts merger rates as a function of mass and time (e.g. Lacey & Cole,

[6] down to some resolution limit

1993; Cole et al., 2000; Parkinson et al., 2008). By sampling from a halo mass function at the desired output time, these algorithms follow a given halo backwards in time, using the EPS formalism to predict how the halo splits into multiple progenitor haloes at each time step. The halo mass function can either be predicted using a Press-Schecter approach or by fitting results from simulations (Jenkins et al., 2001; Tinker et al., 2008). Given the statistical nature of the EPS formalism, these algorithms use a Monte-Carlo technique to generate random realisations of halo merger trees.

The alternative method to generate merger trees is to analyse the results of large dark matter only N-body simulations (e.g. Springel et al., 2005). In this case, algorithms are employed in post-processing to identify bound structures within the simulation box (e.g. Springel et al., 2001). This defines a population of haloes and subhaloes at a given output time of the simulation. By tracing particle identifiers between output times, an algorithm to trace the merging histories of dark matter haloes can be constructed, forming merger trees (Helly et al., 2003; Jiang et al., 2014a). Unlike the EPS merger trees generated using a Monte-Carlo approach, trees extracted from simulations suffer from various complications that arise from cases where structure finding algorithms give inconsistent results between pairs of output times. Also, cases where satellite subhaloes exit the virial radius of the host have to be considered, particularly when constructing a semi-analytic model.

Comparing the EPS and simulation methods for generating merger trees, there are advantages and disadvantages of both techniques. The advantage of EPS algorithms is that they are computationally inexpensive and that they have arbitrary resolution. The advantage of trees extracted from simulations are that the position and velocity information of haloes and subhaloes are predicted. The most obvious disadvantage of the EPS approach is that it is idealised and has to be tuned to agree with simulation results (which are believed to be more accurate within resolution limits, Parkinson et al., 2008). On the other hand, simulation trees suffer from finite resolution, although this problem can be partially overcome by combining results from simulations of differing sizes and resolutions (Guo et al., 2011). The majority

of the results presented in later Chapters of this thesis were obtained using merger trees generated from simulation output from the Millennium simulation (Springel et al., 2005), although some of the results in Chapter 3 were obtained using EPS trees and some of the results from Chapter 5 were obtained using an updated version of the Millennium simulation. We describe which method was used in each respective Chapter.

### 2.6.2 Satellite galaxies

To construct a galaxy formation model of the type described in this Chapter on top of a halo merger tree, the primary consideration is how to account for the presence of satellite galaxies embedded within subhaloes. For the dark matter, this is straightforward as the overall mass distribution is still assumed to follow an NFW profile. The mass of subhaloes that enter the virial radius of a larger host halo can simply be added to the mass of the host, along with any mass that is accreted from unresolved subhaloes or diffuse dark matter. For the density profiles of subhaloes, the relevant aspect for most galaxy formation calculations is the gravitational potential at the centre of the subhalo, which is not expected to be significantly affected by tidal stripping. Therefore, semi-analytic models typically assume that the satellite subhalo density profiles are preserved after infall onto a larger host.

As for gas, the baryon accretion rate must adjusted in the model such that the total baryon fraction within the halo (including ejected gas) is equal to the cosmic mean. With this constraint in place, the next consideration is that gas can be stripped from satellite subhaloes by hydrodynamical ram-pressure forces exerted by the hot gas halo of the host. Gravitational tidal stripping can also act to remove gas and stars from satellite haloes, although this effect is ignored within GALFORM. To represent the effects of ram-pressure stripping, the standard implementation within GALFORM is simply to assume that all hot gas in satellite subhaloes is instantly stripped at infall and is added to the hot gas profile of the host. Additionally, gas that is ejected from satellite galaxies by SNe feedback will be added to the ejected gas reservoir of the host. Instantaneous stripping is likely to be extreme

and is thought to cause problems in reproducing the observed properties of satellite galaxies (Guo et al., 2013a). An alternative implementation featuring delayed stripped was introduced by Font et al. (2008), although the results of this implementation still depend sensitively on the very uncertain fate of gas ejected from satellites by feedback. For the topics addressed in this thesis, the detailed properties of satellite galaxies are not a primary concern, so all results will be presented using the standard maximal stripping implementation.

The next theoretical consideration concerning satellite galaxies is that dynamical friction causes subhalo orbits to decay with time, such that the enclosed satellite galaxy will eventually merge with the central galaxy of the host. The merging timescale, $\tau_{\rm merge}$, for a subhalo's orbit to fully decay can be expressed, following Lacey & Cole (1993), as

$$\tau_{\rm merge} = f_{\rm df}\Theta_{\rm orbit}\tau_{\rm dyn}\frac{0.3722}{\ln(\Lambda_{\rm Coulomb})}\frac{M_{\rm H}}{M_{\rm sat}}, \tag{2.46}$$

where $M_{\rm H}$ is the mass of the host and $M_{\rm sat}$ is the mass of the satellite subhalo at infall. This expression was derived by modelling a point mass orbiting within an isothermal halo using the standard Chandrasekhar formula. $\ln(\Lambda_{\rm Coulomb})$ is the so-called Coulomb logarithm, which is taken to be given by $\ln(\Lambda_{\rm Coulomb}) = \ln(M_{\rm H}/M_{\rm sat})$ (Cole et al., 2000). $\Theta_{\rm orbit}$ is a factor which encapsulates the dependence of $\tau_{\rm merge}$ on the orbital parameters of the satellite (energy and angular momentum). Based on fitting to results from numerical simulations from Tormen (1997), Cole et al. (2000) found that $\Theta_{\rm orbit}$ could be determined for a given satellite at infall by sampling from a log normal PDF. Finally, $f_{\rm df}$ is a model parameter introduced to correct the merging timescale, primarily for the effects of subhalo mass loss through tidal stripping.

### 2.6.3 Spheroid formation

Thus far, we have only considered a set of equations that describe how disks form out of gas that condenses at the centres of dark matter haloes. Rather than extend-

ing this set of equations to include spheroid formation, semi-analytic models typically implement spheroid formation through discrete merging and disk instability events.

Within GALFORM, merging events occur when the time since infall for a satellite galaxy exceeds the dynamical friction timescale given by Eqn 2.46. For each discrete merging event, the resulting behaviour is determined by the baryonic mass (cold gas plus stars) ratio of the satellite and central galaxy. For the case that $M_{\rm sat}/M_{\rm central} >= f_{\rm ellip}$, all of the stars and cold gas from both the central and satellite galaxy are added to the spheroid of the central galaxy. Such an event is referred to as a major merger.

In the opposite case where $M_{\rm sat}/M_{\rm central} < f_{\rm ellip}$, stars from the satellite are added to the spheroid of the central galaxy. Such an event is referred to as a minor merger. The fate of the cold gas in minor mergers is determined by additional criteria. If $M_{\rm sat}/M_{\rm central} > f_{\rm burst}$ and the central galaxy gas fraction, $M_{\rm cold,c}/M_{\rm c} > f_{\rm gas,burst}$, then the cold gas from both the central and satellite galaxy is added to the central spheroid. If $M_{\rm sat}/M_{\rm central} \leq f_{\rm burst}$ or $M_{\rm cold,c}/M_{\rm c} \leq f_{\rm gas,burst}$, the cold gas from both the central galaxy and the satellite galaxy are combined into the disk of the central galaxy, conserving specific angular momentum of the central disk. Here, $f_{\rm ellip}$, $f_{\rm burst}$ and $f_{\rm gas,burst}$ are all regarded as model parameters.

The alternative channel for spheroid formation that is implemented within GALFORM is through disk instabilities. Strongly self-gravitating disks are expected to become unstable under the following criterion:

$$\frac{V_{\rm D}}{\sqrt{GM_{\rm D}/r_{\rm D}}} < \epsilon_{\rm disk}, \tag{2.47}$$

where $\epsilon_{\rm disk}$ is a model parameter expected to be $\approx 1.1$ (Efstathiou et al., 1982; Mo et al., 1998; Cole et al., 2000). If this criterion is met, the stellar and cold gas disk components are transferred to a galaxy spheroid.

As described in Section 2.5.2, to calculate the size of spheroids we need to calculate the pseudo-angular momentum $j_{\rm B} = V_{\rm B}(r_{\rm B})r_{\rm B}$. This quantity is reset after each disk instability or merging event. Following a merger, $r_{\rm B}$ is computed using

$$\frac{(M_1 + M_2)^2}{r_{\rm B}} = \frac{M_1^2}{r_1} + \frac{M_2^2}{r_2} + \frac{f_{\rm orbit}}{c}\frac{M_1 M_2}{r_1 + r_2}, \tag{2.48}$$

where $M_1$ and $M_2$ are the masses of the merging galaxy components. $r_1$ and $r_2$ are the half-mass radii of these components. $M_1$ and $M_2$ include contributions from twice the uncontracted dark matter halo enclosed within $r_1$ and $r_2$. Eqn 2.48 follows from energy conservation and virial equilibrium arguments (Cole et al., 2000). The form factor, $c$, and the constant, $f_{\rm orbit}$, are estimated from the binding energy and mutual orbital energy respectively. Both can be approximated as being constant (Cole et al., 2000).

For disk instabilities, $r_{\rm B}$ is again estimated following energy conservation and virial equilibrium arguments, yielding

$$\frac{c_{\rm B}(M_{\rm D,0} + M_{\rm B,0})^2}{r_{\rm B}} = \frac{c_{\rm B} M_{\rm B,0}^2}{r_{\rm B,0}} + \frac{M_{\rm D,0}^2}{r_{\rm D,0}} + \frac{f_{\rm int}}{c}\frac{M_{\rm B,0} M_{\rm D,0}}{r_{\rm B,0} + r_{\rm D,0}}, \tag{2.49}$$

where $M_{\rm D,0}$ and $M_{\rm B,0}$ are, respectively, the masses of the disk and spheroid before the instability. As for the merger calculation, $M_{\rm D,0}$ and $M_{\rm B,0}$ include contributions from twice the uncontracted dark matter halo enclosed within $r_{\rm D,0}$ and $r_{\rm B,0}$. $r_{\rm D,0}$ and $r_{\rm B,0}$ are the half-mass radii of these components. $c_{\rm B}$ and $c_{\rm D}$ are form factors calculated from the self-gravity of the two components and $f_{\rm int}$ is a constant calculated from the gravitational interaction energy between the disk and bulge (Cole et al., 2000).

Once $r_{\rm B}$ has been computed for the new spheroid, the circular velocity at the half-mass radius, $V_{\rm B}(r_{\rm B})$, is computed using $V_{\rm B}(r_{\rm B}) = G(M_1 + M_2)/2r_{\rm B}$ where $M_1$ and $M_2$ are equivalent to $M_1$ and $M_2$ in Eqn 2.48 for a merger and to $M_{\rm D,0}$ and $M_{\rm B,0}$ for a disk instability. Once $V_{\rm B}(r_{\rm B})$ and therefore $j_{\rm B}$ are determined after a merger/instability the system of adiabatic contraction equations are solved with $j_{\rm B}$ held constant, as described in 2.5.1. In practice, spheroids do not typically change significantly in size or circular velocity after the contraction procedure (Cole et al., 2000).

### 2.6.4 Starbursts

For disk instability, major merger or gas rich minor merger events in GALFORM, the gas that is transferred to the galaxy spheroid undergoes a starburst. Starburst events are modelled with a star formation parametrisation that is distinct from the parametrisation for star formation in galaxy disks described in Section 2.3.2. Specifically, the gas in the burst is converted into stars over a timescale, $\max(f_{\rm dyn}\tau_{\rm B}, \tau_{\rm B,min})$, where $\tau_{\rm B}$ is the bulge dynamical timescale and $f_{\rm dyn}$ and $\tau_{\rm B,min}$ are model parameters. An equivalent SNe feedback parametrisation to that used for disk star formation is also employed for starbursts, with the spheroid circular velocity $V_{\rm B}$ substituted for the disk circular velocity $V_{\rm D}$.

## 2.7 AGN and photoionization feedback

As the first light sources in the Universe after recombination reionize the IGM, the associated ionizing radiation field injects thermal energy into gas. It is thought that this heating has a significant effect on galaxy formation that takes place in small dark matter haloes, preventing gas both from infalling onto, and condensing within smaller haloes. This process is represented within GALFORM following a simple scheme where hot gas is not allowed to infall onto a disk in haloes with circular velocity $V_{\rm H} < V_{\rm cut}$ at redshifts $z < z_{\rm cut}$ where $V_{\rm cut}$ and $z_{\rm cut}$ are model parameters, typically set to $30\,{\rm kms}^{-1}$ and $10$ respectively. Photoionization feedback has minimal impact on the model galaxy populations which are analysed in this thesis.

A key aspect of modern galaxy formation models and simulations is that they include the effects of AGN feedback acting against radiative cooling by injecting thermal energy into the hot gas atmospheres of galaxy groups and clusters. GALFORM adopts a simple scheme, introduced in Bower et al. (2006), where cooling is suppressed in haloes that are in a quasi-hydrostatic cooling regime and host a super-massive black hole that is considered sufficiently luminous to balance the cooling luminosity of the hot gas halo, $L_{\rm cool}$. Black holes are tracked at the centres

of galaxies in the model and are assumed to grow by accreting a fraction of the gas associated with galaxy merger and disk instability events (Bower et al., 2006; Malbon et al., 2007). Haloes are taken to be in the quasi-hydrostatic cooling regime if $t_{\rm cool}(r_{\rm cool}) > t_{\rm ff}(r_{\rm cool})/\alpha_{\rm cool}$, where $t_{\rm cool}$ and $t_{\rm ff}$ are the radiative cooling and freefall timescales evaluated at a radius $r_{\rm cool}$, as described in Section 2.3.1. $\alpha_{\rm cool}$ is considered a model parameter and is typically set $\approx 1$.

## 2.8 Numerical implementation

In this Chapter, we have described the underlying equations and how the various terms within these equations are calculated within the semi-analytic model, GALFORM. Here, we provide a brief explanation of how these equations are solved within the GALFORM code.

### 2.8.1 Numerical integration

The starting point for any numerical scheme is the finite temporal resolution of halo merger trees, particularly for those extracted from numerical simulations. For example, there are $64$ output snapshots from the Millennium simulation, which is the source of merger trees for a significant fraction of the results presented in this thesis. The number of merger tree time steps sets the rate with which cosmological accretion rates can be updated. In GALFORM, halo masses are updated in discrete steps (i.e. halo mass is held constant over a timestep). In this scheme, halo masses are not defined continuously in time. Therefore, large changes in halo mass between time steps would lead to numerical errors when solving the other physical equations using a standard numerical integration scheme.

The original version of GALFORM presented in Cole et al. (2000) featured a linear SF law (given by Eqn 2.17) and did not include the reservoir of gas ejected by feedback, $M_{\rm res}$. In this version of the model, the constant halo mass between time steps is combined with the assumption that the infall rate onto galaxy disks is also constant. In this case, the galaxy formation equations for star formation, stellar

evolution and feedback can be solved analytically over the time step. Gas ejected by feedback was returned to the hot gas halo only at the start of a time step where the host halo had doubled in mass.

The model introduced in Bower et al. (2006) was the first version of GALFORM to implement the ejected gas reservoir, $M_{\rm res}$. Including continuous reincorporation from this reservoir couples the star formation and feedback calculations with the infall calculation. To retain the analytic solutions for the SF equations from Cole et al. (2000), Bower et al. (2006) introduced substeps between the main time step grid defined by the merger trees. In this scheme, halo mass was kept constant across the full time step but the gas reincorporation and infall rates were updated at the start of each substep. The infall rate was kept constant between substeps so that the analytic solutions from (Cole et al., 2000) could still be used.

The most recent change to the numerical scheme in GALFORM was introduced by Lagos et al. (2011b). Lagos et al. (2011b) introduced the non-linear SF law given by Eqn 2.19, which is incompatible with the analytic solutions to the SF equations from Cole et al. (2000). To solve this problem, Lagos et al. (2011b) introduced a 4th order Runge-Kutta adaptive integration scheme to solve the star formation and feedback equations. This scheme preserved the constant infall rates over substeps and discrete gas reincorporation at the start of each substep.

To summarise, the resulting numerical integration scheme used for the majority of the models presented in this thesis is therefore a hybrid of an effective first order scheme for cosmological accretion, gas infall and reincorporation, and a 4th order adaptive scheme for star formation and feedback.

### 2.8.2 Halo formation events

An important aspect of calculations in GALFORM involving hot gas or dark matter density profiles is the idea of halo formation events. These are defined as time steps in the merger tree where a given halo is either identified for the first time or doubles in mass with respect to the previous formation event. The time elapsed since the previous formation event is then used to calculate the cooling and freefall

radii by inverting the cooling and freefall timescale equations.

Halo formation events are also used as markers for deciding when to update the properties of a given halo. Specifically, the halo circular velocity, $V_{\rm H}$, and the halo NFW concentration, $c$, are updated for a given halo at each halo formation event.

## 2.9 Calculating observables

While the intrinsic star formation, merging, chemical enrichment and size growth histories of the galaxy population predicted by a model like GALFORM are interesting in their own right, these properties cannot be compared to direct observables. However, observables can be computed by coupling the output of galaxy formation models with stellar population synthesis (SPS) models that predict the SED, $l_\lambda(t, Z_\star)$ of a simple stellar population of a given age, initial mass function (IMF) and metallicity, $Z_\star$. Assuming a universal IMF, the intrinsic SED, $L_\lambda(t)$, of a galaxy is then given by the following convolution integral

$$L_\lambda(t) = \int_0^t l_\lambda(t - t', Z_\star(t'))\psi(t')\,{\rm d}t', \tag{2.50}$$

where $\psi(t)$ is the star formation rate of the galaxy at time, $t$.

To compare $L_\lambda(t)$ with observed SEDS, it is necessary to consider the effects of intervening gas and dust between a given galaxy and the observer. In general, the first consideration should be absorption and scattering by dust in the Milky Way galaxy, but in practice this is always corrected for in observational studies.

The next consideration is absorption and scattering of light as it propagates between the distant galaxy and the observer. Any dust that is present outside the ISM of galaxies is not thought to have a significant effect on observable galaxy SEDs. However, neutral hydrogen gas in the IGM gas can significantly affect the transmission of photons with rest-frame wavelengths shortward of the Lyman alpha line. This effect is included in GALFORM using the prescription from Madau (1995).

A more complicated problem is the question of how to model the effects of dust attenuation from within the ISM of an observed galaxy. The dust model adopted for the GALFORM models presented in this thesis employs a two component dust model. The first component represents diffuse dust that is thought to be present in galaxy disks and in spheroids undergoing bursts of star formation. The second component represents absorption from compact dust clouds that are observed to surround young stars and star forming regions. The total dust mass in a given galaxy is computed assuming a dust-to-metals ratio compatible with local ISM measurements (Savage & Mathis, 1979; Cole et al., 2000). This dust is then split between diffuse and cloud components, with the fraction in clouds given by a model parameter, $f_{\rm c}$.

To represent the diffuse dust component, GALFORM makes use of tabulated radiative transfer calculations from Ferrara et al. (1999). The assumed geometrical configuration is an exponential stellar disk and a Jaffe (1983) spheroid profile (which is very similar to an $r^{1/4}$ profile Cole et al., 2000). The diffuse dust is assumed to trace the same spatial distribution as the stellar disk. For the case of starbursts, the starburst is approximated as an exponential disk. The Ferrara et al. (1999) models are tabulated as a function of inclination, central optical depth and disk-to-bulge scalelength ratio. The solutions used in GALFORM employ a Milky Way extinction curve.

To represent the compact dust component, it is assumed that young stars are surrounded by uniform density dust clouds of a constant mass and radius. Stars are assumed to escape these clouds over a timescale, $t_{\rm esc}$, which is set to $1\,{\rm Myr}$ by default. Specifically, all of the light from stellar populations younger than $t_{\rm esc}$ are attenuated by the compact cloud component while none of the light from stellar populations older than $2t_{\rm esc}$ is attenuated. Between these ages, a fraction $2-t/t_{\rm esc}$ of stars of age, $t$, are assumed to be affected by the compact cloud component.

GALFORM also includes a model for the thermal reemission of starlight absorbed by dust. Given that we do not use this model for dust emission for any of the results presented in this thesis, we do not discuss it here.

## 2.10 Model parameters

A consequence of the semi-analytic modelling approach is that models such as GALFORM contain numerous model parameters. Some of these parameters can be considered as well constrained on the basis of theoretical expectation or from direct empirical evidence. For example, dynamical friction timescales can be reasonably well constrained from direct numerical simulation, while the molecular SF law introduced by Lagos et al. (2011b) is constrained by observational studies correlating star formation and molecular gas tracers in local galaxies.

On the other hand, parameters describing the effects of SNe feedback (both ejection efficiency and reincorporation timescale) are much less constrained on theoretical or direct empirical grounds. Instead, indirect evidence is used to constrain these parameters by exploring the model parameter space against observational constraints such as the local luminosity function. In this way, the model is tuned to reproduce robust local observational results. With the model parameters then fixed, the model can then be tested against observational datasets that were not used in the tuning process. As a general rule of thumb, most of the models presented in this thesis were originally tuned to reproduce primarily the local luminosity function in the $b_{\rm j}$ and $K$ photometric bands (Cole et al., 2000; Baugh et al., 2005; Bower et al., 2006; Lagos et al., 2011b, 2012). We defer more detailed discussion of any tuning to the relevant Chapters for each model considered.

## 2.11 The life and times of a Milky-Way halo

To summarise this Chapter and the introduction to semi-analytic modelling, we show in Fig. 2.4 an illustration of the evolution in different properties of a halo with mass, $\log(M_{\rm H}/{\rm M}_{\odot}) = 12.2$ at $z = 0$. The code used to generate this figure is very similar to GALFORM but uses a 4th order Runge-Kutta numerical integration scheme with fixed time steps to solve all of the differential equations in the model self-consistently. The model shown is simplified with respect to GALFORM in that it

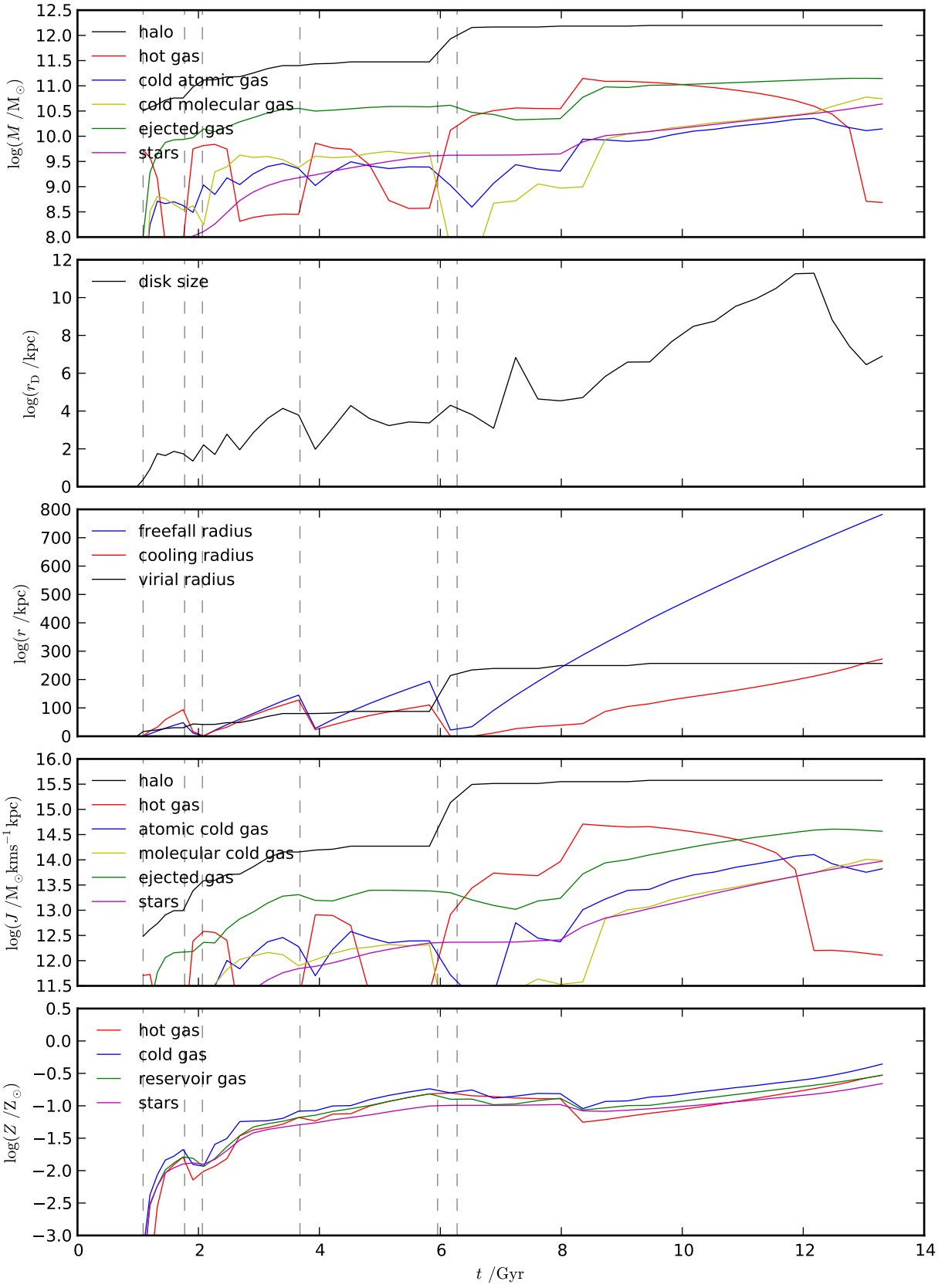
halo
hot gas
cold atomic gas
cold molecular gas
ejected gas
stars
$\log(M\ /\mathrm{M}_\odot)$
disk size
$\log(r_\mathrm{D}\ /\mathrm{kpc})$
freefall radius
cooling radius
virial radius
$\log(r\ /\mathrm{kpc})$
halo
hot gas
atomic cold gas
molecular cold gas
ejected gas
stars
$\log(J\ /\mathrm{M}_\odot\mathrm{kms}^{-1}\mathrm{kpc})$
hot gas
cold gas
reservoir gas
stars
$\log(Z\ /\mathrm{Z}_\odot)$
$t\ /\mathrm{Gyr}$

Figure 2.4: Evolution of a Milky-Way like halo in a simplified semi-analytic model. *Top:* Mass evolution. *Second:* Disk size evolution. *Third:* Halo virial, cooling and freefall radii evolution. *Fourth:* Angular momentum evolution. *Bottom:* Metallicity evolution. In each panel dashed vertical black lines indicate the times of halo formation events.

does not include spheroid formation, AGN or photoionization feedback. Also, all baryons from satellite galaxies are instantly merged onto the central galaxy upon subhalo infall.

Starting with the mass assembly history shown in the top panel of Fig. 2.4, we see the expected result that the majority of the baryons in the halo at $z = 0$ have not been converted into stars. Instead, the majority of the baryonic mass in the system is typically in the ejected reservoir component. This underlines the importance of the implementation of SNe feedback and gas reincorporation in controlling the stellar mass assembly history of the central galaxy. For the hot gas component, the importance of the location of specific halo formation events (dashed vertical lines) is apparent. In the second panel, we see that the size of the galaxy disk grows steadily over cosmic time. It is interesting to note that this evolution is not monotonic; the specific angular momentum of the disk can be sensitive to both the infall rate and the absolute position of the infall radius. In the third panel, the evolution of the cooling and freefall radii after each halo formation event demonstrates how radiative cooling is almost always the limiting timescale for gas infall for this halo mass. The fourth panel shows the angular momentum assembly process. It is apparent that this closely traces the mass assembly process in the model. The final panel shows the chemical enrichment history. In this case, SNe feedback is very efficient such that metals are well mixed between the different baryonic components.

To act as a point of comparison, we choose to also show the evolutionary histories of galaxies forming within a smaller and a larger halo. Fig. 2.5 shows the evolutionary history of a smaller $\log(M_{\rm H}/{\rm M}_{\odot}) = 11.3$ halo. Fig. 2.6 shows the evolutionary history of a larger $\log(M_{\rm H}/{\rm M}_{\odot}) = 13.1$. Comparing the smaller halo with the Milky-Way like halo shown in Fig. 2.4, it is apparent that the smaller halo spends a slightly larger fraction of time in the freefall limited regime for gas infall.

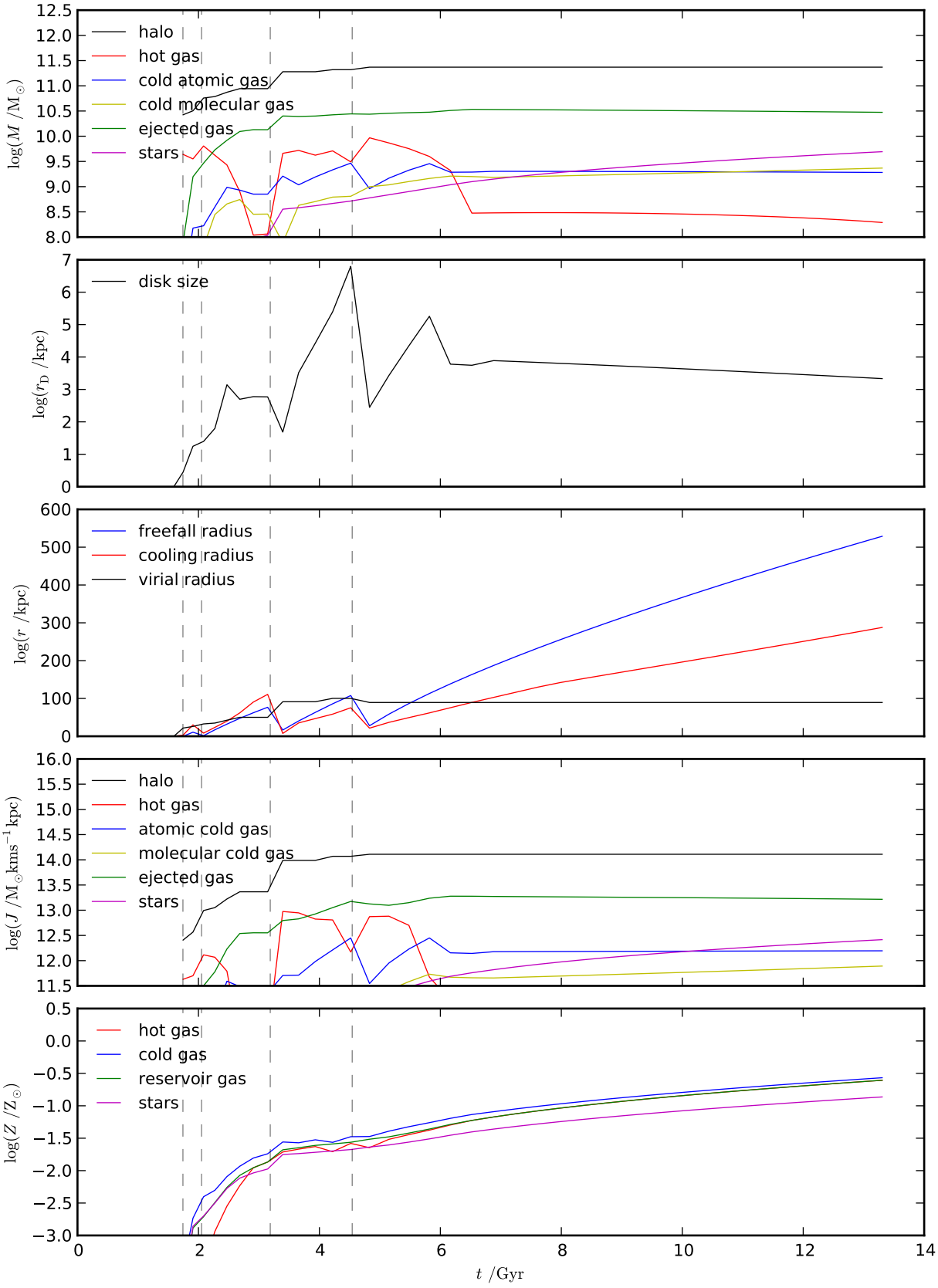
halo
hot gas
cold atomic gas
cold molecular gas
ejected gas
stars
log(M /M⊙)
disk size
log(rD /kpc)
freefall radius
cooling radius
virial radius
log(r /kpc)
halo
hot gas
atomic cold gas
molecular cold gas
ejected gas
stars
log(J /M⊙kms−1kpc)
hot gas
cold gas
reservoir gas
stars
log(Z /Z⊙)
t /Gyr

Figure 2.5: Evolution of a small ($\log(M_{\rm H}/{\rm M}_{\odot}) = 11.3$) halo in a simplified semi-analytic model. Formatting is identical to Fig. 2.4.

At late times, the infall radius has exceeded the halo virial radius so that the mass in the hot gas halo is negligible. The gas reincorporation timescale is very clearly the limiting timescale for this halo given that the vast majority of the baryons are in the ejected component.

For the larger, group mass halo shown in Fig. 2.6, the efficiency of SNe feedback has dropped significantly such that the majority of the baryons are in hot gas and stars. We note that the stellar mass of the galaxy is very large because we have not included the effects of AGN feedback. Again, gas infall is limited by the radiative cooling timescale. However, in this case, the cooling radius only reaches a small fraction of the halo virial radius at late times. It is interesting to note that the galaxy disk is much smaller for the group halo than for the other two haloes considered. The resulting non-monotonic relationship between mass and galaxy size disagrees with observational results and so represents a clear problem with either the angular momentum exchange rates or the adiabatic contraction model implemented within GALFORM. Other distinguishing features of the group mass halo are that the molecular to atomic cold gas ratio is large and that chemical enrichment is much more segregated between different galaxy/halo components. The chemical segregation occurs simply because SNe feedback is much less effective at ejecting gas out of the galaxy disk for the group mass halo.

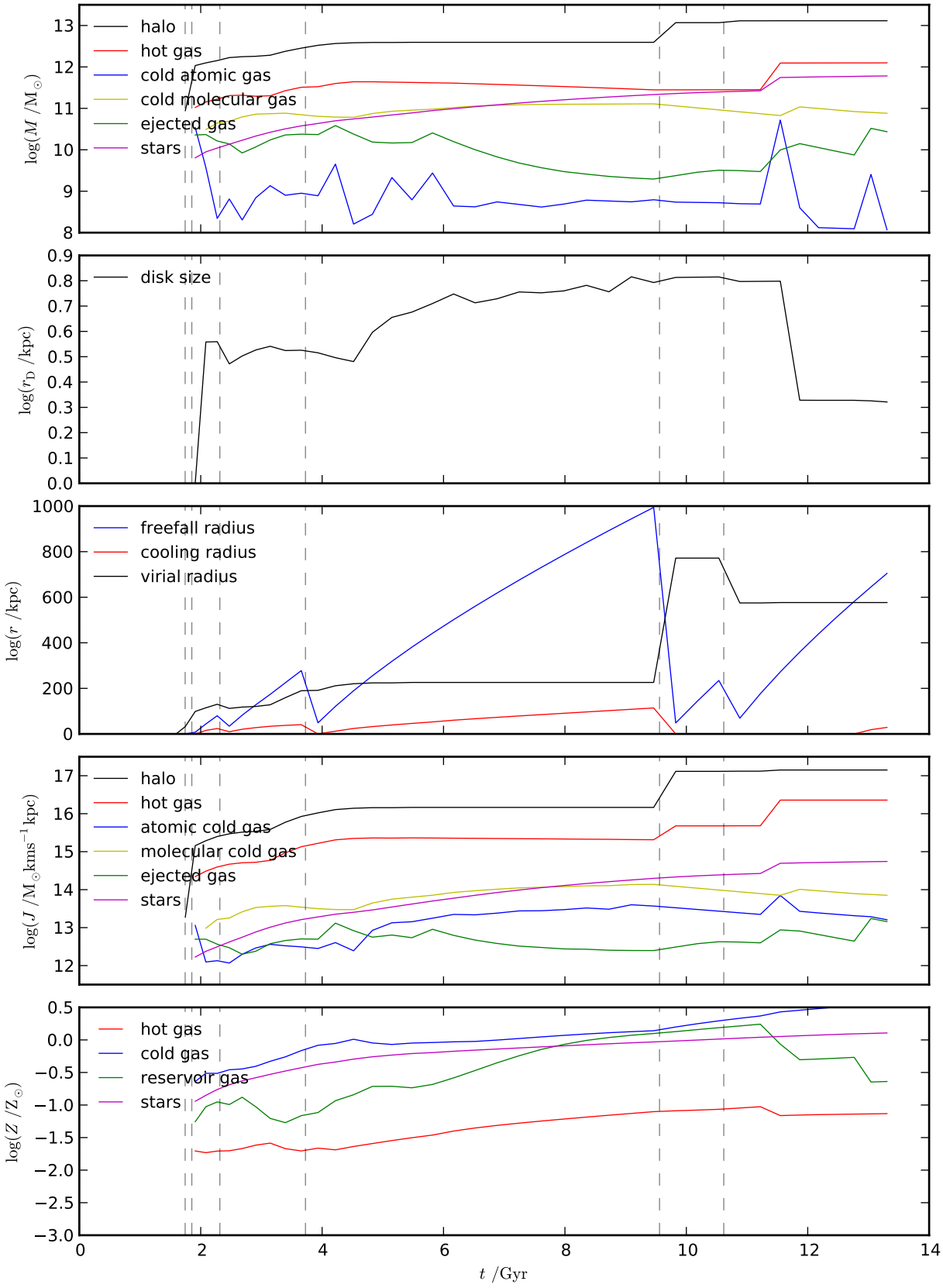
halo
hot gas
cold atomic gas
cold molecular gas
ejected gas
stars
log(M /M⊙)
disk size
log(rD /kpc)
freefall radius
cooling radius
virial radius
log(r /kpc)
halo
hot gas
atomic cold gas
molecular cold gas
ejected gas
stars
log(J /M⊙kms−1kpc)
hot gas
cold gas
reservoir gas
stars
log(Z /Z⊙)
t /Gyr

Figure 2.6: Evolution of a group sized ($\log(M_{\rm H}/{\rm M}_{\odot}) = 13.1$) halo in a simplified semi-analytic model. Formatting is identical to Fig. 2.4.

# Chapter 3

# *Estimating the stellar masses of galaxies from broad-band photometry*

## 3.1 Introduction

A successful theory of galaxy formation is essential for accurately connecting any underlying cosmological framework with the observable Universe. The vast dynamic range and overall complexity involved in the interplay between gas, stars and dark matter in galaxies strongly restricts what any model of galaxy formation can predict *a priori*. To make progress, it is necessary to use observational results to constrain galaxy formation models. Estimating the stellar masses of galaxies offers, in principle, a powerful method to characterize the galaxy population that can be compared directly to theoretical predictions. Unlike directly observable quantities, stellar mass is a derived quantity that can only be estimated from observational data through the application of a series of models and assumptions. It is therefore critical to understand how these assumptions affect the reliability of stellar mass estimates and how any uncertainties affect global diagnostics of the galaxy population, such as the stellar mass function.

The traditional approach for constraining parameters in theoretical galaxy formation models is to use directly observable properties of the galaxy population such as the luminosity function or the Tully-Fisher relation. This requires that the intrinsic physical properties of model galaxies calculated using either hydrodynamical simulations or semi-analytic models (SAMs) can be converted into directly

observable quantities. Stellar population synthesis (SPS) models (e.g. Bruzual & Charlot, 2003; Maraston, 2005) are combined with predicted star-formation and chemical enrichment histories of model galaxies to produce spectral energy distributions (SEDs) that can be compared with observational data. Uncertainties in the form of the initial mass function (IMF) of stars, the accuracy of SPS models and the manner in which dust attenuates the light emitted by stars make this process challenging (e.g. Conroy et al., 2009, 2010b). It can be difficult in some cases to be confident whether the comparison between model predictions and observational results does in fact show if a given model is successful in describing the underlying physics.

The estimation of the stellar masses of galaxies from observational data is typically achieved using the technique of broad-band SED fitting, which inverts the process of generating observables from intrinsic galaxy properties. The popularity of this technique can be attributed to the success of multi-wavelength surveys such as the Sloan Digital Sky Survey (SDSS; York et al., 2000), the Great Observatories Origins Deep Survey (GOODS; Giavalisco et al., 2004) and the Cosmological Evolution Survey (COSMOS; Scoville et al., 2007). These surveys quantify how the galaxy population evolves with look-back time by utilizing broad-band photometry from the UV to the NIR to obtain accurate photometric redshifts for much larger galaxy samples than would be possible using spectroscopy. The information and methods used to obtain accurate photometric redshifts by fitting stellar population models can readily be extended to also estimate stellar masses and other galaxy properties. Consequently, it has become standard practice to estimate these quantities whenever multi-wavelength photometry is available.

The same uncertainties associated with converting the intrinsic properties of model galaxies into observables also affect the accuracy of SED fitting applied to observational data. However, there are a number of additional assumptions that must be made to estimate the stellar masses of galaxies from observations. For example, unlike for the case of model galaxies, the star formation histories (SFHs) of real galaxies are not known. Instead, a prior for the SFHs of galaxies must be

adopted. Various studies have attempted to explore how stellar mass estimates depend on the different assumptions made in SED fitting (e.g. Papovich et al., 2001; Wuyts et al., 2007; Marchesini et al., 2009; Conroy et al., 2009; Maraston et al., 2010; Ilbert et al., 2010; Michałowski et al., 2012; Banerji et al., 2013; Moustakas et al., 2013; Schaerer et al., 2013). There is a general consensus that stellar mass estimates are more reliable compared to other quantities such as star-formation rates (SFRs) and galaxy ages that can be estimated using the same process. However, the reported level of uncertainty on stellar mass estimates can vary strongly, depending on the specific galaxy samples considered. Conroy et al. (2009) find that the stellar mass-to-light ($M/L$) ratios of star-forming galaxies at $z = 0$ can only be constrained to within $0.3\,\mathrm{dex}$ at a $95\%$ level of confidence when various uncertainties in SPS modelling are taken into account. This does not include the uncertainty associated with the choice of the IMF. Gallazzi & Bell (2009) find that, ignoring the uncertainties associated with SPS modelling and dust attenuation, it is possible to constrain $M/L$ ratios of galaxies with smooth SFHs to within $0.1\,\mathrm{dex}$ using spectral features or a single optical colour (see also Wilkins et al., 2013). Longhetti & Saracco (2009) consider the accuracy of stellar mass estimates of early-type galaxies, finding that the true stellar masses of mock galaxies can only be recovered to within a factor of $\approx 0.3 - 0.5\,\mathrm{dex}$, given the variations between different SPS models and metallicities. Marchesini et al. (2009) quantify how uncertainties associated with the assumptions made in SED fitting contribute to the error budget of the stellar mass function. They find that potential systematic errors associated with these assumptions can dominate over other error sources, such as photometric redshifts or galaxy photometry. They also find that the shape of the mass function, particularly at the low-mass end, is sensitive to, for example, the assumed metallicity and the adopted dust attenuation law.

We explore this topic from an alternative angle by applying the methods used in observational studies to estimate stellar masses from SEDs output by the semi-analytic galaxy formation model GALFORM (Cole et al., 2000). We focus on understanding the various random and systematic errors encountered when estimating

the stellar masses of individual galaxies and also study how these translate into errors in the stellar mass function. This exercise serves as a useful example of how the process of converting between observables and intrinsic galaxy properties can have an impact on global diagnostics of the galaxy population. Several studies have adopted a similar approach by combining SED fitting with galaxy formation models, aiming to understand the accuracy of SED fitting in different scenarios (Lee et al., 2009; Wuyts et al., 2009; Lee et al., 2010; Pforr et al., 2012). This method is useful because outside of the limited number of cases where additional data are available, it is difficult to test the accuracy of quantities estimated using SED fitting. Fitting mock galaxy SEDs provides a means to do this and theoretical galaxy formation models are, in principle, a useful tool for producing samples of mock galaxies with realistic star-formation and chemical enrichment histories. In the case of SAMs, model galaxy samples that represent the entire galaxy population over a range of redshifts can be generated rapidly. This allows us to isolate and understand different effects by considering variants of the underlying model.

Lee et al. (2009) use model galaxy SEDs from the Somerville & Primack (1999) SAM to explore the accuracy of SED fitting in recovering the physical properties of Lyman-break galaxies (LBGs). They find that stellar masses are, on average, well recovered for LBGs as they are underestimated, on average, by less than $0.1\,\mathrm{dex}$. They attribute this success to two competing factors. Younger stars can mask the presence of older stars in LBG SEDs in some cases, leading to an underestimate of the total stellar mass. However, they also find that there is a tendency for SED fitting to overestimate the age of LBGs. This typically leads to overestimating the stellar masses of some galaxies.

Pforr et al. (2012) combine SED fitting with the GalICS SAM (Hatton et al., 2003). They find that, in general, stellar masses are slightly underestimated when using standard exponentially declining SFHs in the SED fitting process. They demonstrate that this problem can be resolved by adopting exponentially increasing SFHs for star-forming galaxies. They conclude that stellar masses are recovered almost perfectly at redshifts $z \in 2, 3$, where the allowed distribution of galaxy ages is

fairly narrow. At lower redshifts, however, they find that the stellar masses of star-forming galaxies can be underestimated by up to $0.6\,\mathrm{dex}$ as a result of discrepancies between the estimated and true SFHs. They explain that this is caused by the larger range of possible ages at low redshift combined with degeneracies between age and dust. Finally, they also show that this problem can be circumvented by choosing to ignore dust reddening when estimating the stellar masses of star-forming galaxies at low redshift. This prevents the SED fitting procedure from fitting an unrealistically young age coupled with a large amount of dust reddening.

A key difference in our methodology compared to that of Pforr et al. and Lee et al. is that we use a physically motivated model for attenuation by dust. Pforr et al. and Lee et al. instead adopt empirical dust attenuation laws to calculate model galaxy SEDs, corresponding physically to a uniform foreground screen of dust placed between the galaxy and an observer. The difference between a foreground dust screen model and the physically motivated radiative transfer calculation performed in our analysis turns out to be very significant for our results on stellar mass estimation. It should also be noted that it is not our intent to follow Pforr et al. (2012) in attempting to quantify the exact level of random and systematic errors on stellar mass estimates for an exhaustive range of possible SED fitting configurations and filter sets. This is because any quantitative results derived from the approach of combining SED fitting with theoretical models may be sensitive to the degree to which a given model can represent the true galaxy population. Instead, we attempt to provide a detailed explanation of the different error sources we encounter when considering the overall galaxy population over a wide range of redshifts. This is achieved by isolating the different factors responsible for biasing stellar mass estimates in a specific set of idealized test cases.

The outline of this Chapter is as follows. In Section 3.2, we introduce broad-band SED fitting, explain some of the underlying assumptions that are involved in the process and outline the parameter choices we make in this study. Section 3.3 gives a brief overview of GALFORM and the specific models which we use in this study. We also explain how intrinsic galaxy properties are transformed into ob-

servables in the context of the assumptions made in SED fitting. In Section 3.4, we present results of performing SED fitting on model galaxies, focusing on exploring the systematics that affect the recovery of the stellar masses of individual galaxies. We present results for the stellar mass function over a range of redshifts in Section 3.5. Finally, we discuss and summarize our results in Section 3.6 and Section 3.7.

## 3.2 Broad-band SED fitting

We seek to understand the relationship between the stellar mass estimated from observations using SED fitting and the stellar mass predicted by theoretical models. Instead of using broad-band photometry from observed galaxies, we fit the broad-band magnitudes of model galaxies predicted by the semi-analytic model GALFORM. The precise details of the method used to perform SED fitting in different observational studies typically vary very little. Detailed descriptions and discussion of the method can be found in Bolzonella et al. (2000), Salim et al. (2007), Walcher et al. (2011) and Taylor et al. (2011). In this section we provide an overview of SED fitting as a method of estimating stellar mass. We also describe our parameter choices for the SED fitting procedure used in this study.

### 3.2.1 Overview

Broad-band SED fitting works by comparing a grid of template galaxy SEDs to observational data. Typically, a maximum-likelihood method is then used to decide which template best fits the data (although see Taylor et al., 2011; Salim et al., 2007, for a discussion of alternative statistical techniques). This is achieved by first minimizing $\chi^2$ for each template SED, then choosing the best-fitting template SED with the smallest associated $\chi^2$ value. This corresponds to choosing the mode of the likelihood distribution. $\chi^2$ is calculated by summing over all available photometric bands using

$$\chi^2 = \sum_n \left[ \frac{F_{\mathrm{galaxy},n} - s\, F_{\mathrm{temp},n}}{\sigma_n} \right]^2, \tag{3.1}$$

where $F_{\mathrm{galaxy},n}$ and $F_{\mathrm{temp},n}$ are the fluxes of the galaxy and template, respectively, in the $n$th band, $s$ is a normalization factor and $\sigma_n$ is the $1\sigma$ flux error associated with a galaxy in the $n$th band. The normalization factor $s$ is calculated such that $\chi^2$ is minimized for each template SED using

$$s = \frac{\sum_m \left[ \frac{F_{\mathrm{galaxy},m}\, F_{\mathrm{temp},m}}{\sigma_m^2} \right]}{\sum_m \left[ \frac{F_{\mathrm{temp},m}}{\sigma_m} \right]^2}, \tag{3.2}$$

where a choice can be made regarding which bands are included in the summation. We choose to follow standard practice by simply summing over all available photometric bands, as in Eq. 3.1. The stellar mass of each galaxy is then calculated by multiplying the stellar mass of the template by the normalization factor, $s$. This means that the stellar mass is estimated through normalization over the entirety of the observed galaxy SED, weighted by the error in each band.

Template galaxies SEDs are generated using publicly available SPS models (e.g. Bruzual & Charlot, 2003; Maraston, 2005; Conroy et al., 2009). SPS models predict the spectra of simple stellar populations (SSPs), a group of stars with the same age and metallicity and a distribution of initial masses given by the stellar initial mass function (IMF). These SSP spectra are then convolved with an assumed parametrization for the typical SFH of a galaxy. It is well established that various degeneracies make it very difficult to place strong constraints on galaxy SFHs from photometric data alone, unless strong priors are adopted (e.g. Maraston et al., 2010). It is therefore standard practice to assume a simple parametrization for the SFH which can represent a broad range of possible SFHs without creating a prohibitively large parameter space over which to search. By far the most common choice of parametrization used for the SFH of low and intermediate redshift galaxies is an exponentially declining SFH. It should be noted, however, that there are numerous studies which have advocated alternatives, particularly for high red-

shift galaxies (e.g. Lee et al., 2010; Michałowski et al., 2012; Pacifici et al., 2013). The exponentially declining SFH is parametrized by the time since the onset of star-formation, $t_{\rm age}$, and the $e$-folding time scale, $\tau$. SPS models also output the mass returned from a SSP back into the interstellar medium (ISM) as a function of age, which in turn is used to predict the $M/L$ ratio of each template galaxy. To reduce the size of the parameter space that needs to be searched over, it is typically assumed that all of the stars in each template galaxy have a single stellar metallicity, $Z_{\star}$. Furthermore, the number of metallicity points in the parameter grid is usually very small due to the sparse metallicity grid made available for publicly available SPS models. For example, there are only 5 metallicities available for the Bruzual & Charlot (2003) (BC03) SPS model. Unlike what is done in theoretical models, it is not standard practice to interpolate between metallicities in SED fitting.

### 3.2.2 Dust attenuation

Observed galaxy SEDs are a product of the intrinsic galaxy SED produced by stellar emission which is then attenuated according to radiative transfer through intervening gas and dust. It is standard practice in SED fitting to account for absorption by neutral hydrogen in the IGM using the prescription from Madau (1995). This is adopted in both GALFORM and in the SED fitting procedure used in this study. Attenuation by dust in the ISM of galaxies is a substantially more complex radiative transfer problem. Dust in galaxies can be concentrated around young stars or distributed diffusely throughout regions of the ISM. Given the lack of information available on the relative spatial distribution of stars and dust in distant galaxies, attenuation by dust it usually accounted for in SED fitting using the empirical Calzetti dust attenuation law (Calzetti et al., 1994, 2000). The Calzetti attenuation law has a fixed shape which is different from the dust extinction curve in the local ISM. The star-dust geometry that is implicitly assumed when applying the Calzetti law corresponds physically to a uniform, foreground dust screen placed between the observer and the stellar populations in a given galaxy. Making this assumption has the advantage for SED fitting in that the Calzetti is consequently only character-

ized by only a single parameter, the reddening $E(B-V)$, defined as the difference between the observed and intrinsic $B-V$ colour. The shape of the Calzetti law was derived from a sample of 30 local starbursts (Calzetti et al., 1994) and the normalization was derived from a sub-sample of only 4 local starbursts (Calzetti et al., 2000).

A number of studies have attempted to assess how well the Calzetti law can reproduce the attenuation curves of different galaxy types. At low redshift, Wild et al. (2011) apply a pair-matching technique to study the shape of the attenuation curves of SDSS spirals. They find evidence that the shape of the optical dust attenuation curves of local star-forming galaxies is strongly dependent on galaxy inclination. Specifically, they show that face-on spirals have steeper optical attenuation curves than the Calzetti law, whereas edge-on spirals are consistent with the Calzetti law. They also find that the slopes of the near-infrared (NIR) attenuation curves are consistent with Milky-Way extinction or Calzetti law attenuation curves, independent of inclination. In the UV, they find evidence for a bump in the attenuation curve of spirals at $2175$ Å (see also Conroy et al., 2010a). This feature is absent from the Calzetti law and could have a significant impact on the interpretation of the properties of high redshift galaxies (Gonzalez-Perez et al., 2013).

Another method that is used to investigate the dust attenuation properties of galaxies involves measuring how the ratio of far-infrared (FIR) to ultraviolet (UV) flux, IRX, varies as a function of the UV spectral slope, $\beta$ (Bell, 2002; Goldader et al., 2002; Howell et al., 2010; Murphy et al., 2011; Penner et al., 2012, e.g.). The position of galaxies on the IRX-$\beta$ plane can then be compared with the relationship derived for local starbursts (Meurer et al., 1999; Overzier et al., 2011). The Meurer et al. (1999) relation was derived from the same galaxy sample used to derive the Calzetti law and so this comparison tests whether the Calzetti law is applicable to objects other than modestly starbursting local galaxies. Bell (2002) was the first to show that local star-forming galaxies lie below this relation such that there is less UV attenuation for a given value of $\beta$. Goldader et al. (2002) were the first to show that local ultraluminous infrared galaxies lie above this relation such that the

Calzetti law underestimates the total UV attenuation for these objects.

Various studies have also applied this method to high redshift star-forming galaxy samples (e.g. Murphy et al., 2011; Buat et al., 2012; Reddy et al., 2012; Penner et al., 2012). This exercise is difficult because FIR SEDs are typically available only for the most extreme dusty galaxies at higher redshifts, although a stacking analysis can ameliorate this problem (Reddy et al., 2012). There is evidence for consistency between the high redshift and local IRX-$\beta$ relations (e.g. Reddy et al., 2010, 2012), although it has also been argued that specific object classes can be offset from the local relation (e.g. Murphy et al., 2011; Penner et al., 2012). Buat et al. (2012) apply a different approach and analyse a sample of 751 UV-selected galaxies at $z \in 1, 2$, fitting the full UV-FIR SEDs using a SED fitting procedure that features a generalized form of the Calzetti law (Noll et al., 2009). They find evidence for a steeper attenuation curve in the UV than the canonical Calzetti law for $20\%$ of their sample, and also a UV bump.

### 3.2.3 Filter and parameter choices

The final step in producing template SEDs involves convolving with the broad-band filters used in given observational data set. Deep multi-wavelength surveys such as GOODS have many photometric bands available, spanning all the way from the UV through to the radio. Wide-area surveys on the other hand such as SDSS typically have only optical broad-band photometry available. For simplicity, we use a single filter set across a wide range of redshifts with the exception of Section 3.5.1 where we consider LBG samples. Filters blueward of the Lyman limit at $912$Å in the rest frame are excluded from the fitting process. We do not include artificial redshift or flux errors, setting $\sigma_n$ in Eq. 3.1 to $10\%$ of the model galaxy flux $F_{\mathrm{galaxy},n}$ for each band. These error sources become important at high redshift but can be understood without the need for a theoretical model and are not particularly relevant for understanding errors in stellar mass estimates associated with the assumptions made in SED fitting. However, ignoring them entirely means that any quantification of the errors in stellar mass estimates given in this Chapter should

be considered as lower limits. We do consider the effect of artificially perturbing model fluxes when exploring LBG samples in Section 3.5.1, where it becomes important to include detection criteria in order to robustly compare model predictions with observational data.

In this study we use two filter and SED fitting parameter sets, as outlined in Table 3.1. A common feature of both sets is that we use Bruzual & Charlot (2003) SPS models and the Calzetti law for SED fitting. $t_{\rm age}$ is always constrained to be less than the age of the Universe at the given redshift. We refer to the first parameter set as the standard parameter grid because it is designed to be broadly representative of the choices made in observational studies of low to intermediate redshift galaxies where Spitzer IRAC imaging between $3.6\mu{\rm m}$ and $8\mu{\rm m}$ is often available (e.g. Ilbert et al., 2010; Santini et al., 2012; Mortlock et al., 2011). It uses the exponentially declining SFH typically used for galaxies at low and intermediate redshift and is therefore characterized by $t_{\rm age}$, $\tau$, $Z_\star$ and $E(B-V)$. We use a Salpeter IMF for this parameter set despite the fact that the GALFORM models we consider typically use a Kennicutt IMF to demonstrate how the systematic uncertainty on the IMF compares against other sources of error in stellar mass estimation. We modify this choice of IMF in the templates to a Chabrier IMF in Section 3.5 where we consider model predictions of the stellar mass function. This choice is made so that the stellar masses of model galaxies estimated from SED fitting are consistent with the observational studies with which we compare.

We also use a second parameter set, deliberately constructed to closely resemble the choices made by Lee et al. (2012), who use SED fitting to estimate the stellar masses of LBGs at $z = 4$ and $z = 5$. We refer to this parameter set as the LBG parameter grid and use it in Section 3.5.1. It uses an exponentially declining SFH, including the limit of $\tau \to \infty$, corresponding to a constant SFH. When considering LBGs, it is important to consider both the effect of photometric errors and non-detections where galaxies drop below the sensitivity limit of the survey. Instead of setting $\sigma_n$ in Eq. 3.1 to $10\%$ of the model galaxy flux $F_{{\rm galaxy},n}$, in this case we use the 5-sigma limiting magnitudes listed in Table 1 of Lee et al. (2012) to determine

| Standard Parameter Grid | |
|---|---|
| Filters | $B_{435}$, $V_{606}$, $R$, $i_{775}$, $z_{850}$, $J$, $H$, $K$, 3.6, 4.5, 5.8, 8.0$\mu$m |
| IMF | Salpeter |
| $t_{\rm age}$/Gyr | 0.1, 0.11, 0.13, 0.14, 0.16, 0.18, 0.2, 0.23, ... |
| $\tau$/Gyr | 0.1, 0.3 0.6, 1, 2, 3, 4, 5 7, 9, 13, 15, 30 |
| $Z_\star$/Z$_\odot$ | 2.5, 1, 0.4, 0.2, 0.02 |
| $E(B-V)$ | 0, 0.03, 0.06, 0.1, 0.15, 0.2, 0.25, 0.3, ... 1 |
| Lyman-Break Galaxy Parameter Grid | |
| Filters | $B_{435}$, $V_{606}$, $i_{775}$, $z_{850}$, $J$, $H$, $K$, 3.6, 4.5, 5.8$\mu$m |
| IMF | Chabrier |
| $t_{\rm age}$/Gyr | 0.1, 0.11, 0.13, 0.14, 0.16, 0.18, 0.2, 0.23, ... |
| $\tau$/Gyr | 0.1, 0.2 0.3, 0.4, 0.6, 0.8, 1.0 , $\infty$ |
| $Z_\star$/Z$_\odot$ | 1, 0.2 |
| $E(B-V)$ | 0, 0.025, 0.05, 0.075 ... 0.95 |

Table 3.1: Parameter grids for SED fitting. The top section outlines the standard parameter grid we use for the majority of our results. The bottom section outlines the parameter grid used in Section 3.5.1 for exploring LBG sample selection. $t_{\rm age}$ is the time since the onset of star-formation and $\tau$ is the $e$-folding time-scale for an exponentially decreasing SFH. $Z_\star$ is the stellar metallicity and $E(B-V)$ is the colour excess which characterizes the Calzetti dust attenuation law.

$\sigma_n$. We also consider the effect of artificially perturbing fluxes using a Gaussian distribution with $\sigma$ again taken from Table 1 in Lee et al. (2012). To facilitate a self-consistent comparison, we follow the same procedure for non-detections described in Lee et al. (2012), where non-detected bands are used as upper limits in Eq. 3.1 if $s\,F_{{\rm temp},n}$ exceeds the upper limit in that band. We use the LBG dropout selection criteria (both colour and $S/N$ selection) given by Equations 1-13 in Stark et al. (2009). These criteria select $B_{435}$, $V_{606}$ and $i_{775}$ dropouts to create samples of LBGs at $z = 4, 5$ and $6$ respectively. We use a Chabrier IMF for this parameter set. The allowed parameter values for both parameter sets are listed in Table 3.1.

## 3.3 Modelling hierarchical galaxy formation

In this section we provide a brief description of the aspects of the GALFORM semi-analytic model which are relevant to this work. An introduction to the model and the associated underlying physics can be found in Cole et al. (2000), Baugh (2006) and Benson (2010). Briefly, GALFORM connects the properties of galaxies to a given cosmological model by coupling dark matter halo merger trees to a set of continuity equations that describe the exchange of baryons accreted on to dark matter haloes between stellar, cold disk gas and hot halo gas components. The physical processes that determine the form of these continuity equations include shock heating and subsequent radiative cooling of accreted gas onto galaxy disks, quiescent star-formation in galaxy disks, chemical enrichment of the ISM, the ejection of cold gas and metals by supernova feedback, the suppression of gas cooling by AGN and photoionization feedback and disk instabilities and galaxy mergers that can trigger both spheroid formation and bursts of star-formation. It is important to note that various versions of GALFORM have appeared in the literature which we refer to as separate models. These models are distinct from each other in that they all use different choices for model parameters and in some cases actually include physical processes which do not appear in other models.

### 3.3.1 The Lagos12 and Lacey13 models

We adopt the recently developed model described in Lagos et al. (2012) (hereafter Lagos12) as the fiducial model to explore in this study. The Lagos12 model is the most recent version of the model described in Lagos et al. (2011b), which in turn is a development of the model originally described in Bower et al. (2006) (hereafter Bower06). The Bower06 model was the first variant of GALFORM to include the effects of AGN feedback shutting down gas cooling in massive haloes. The Lagos12 model is distinct from the Bower06 model in that it includes an alternative star formation law for galaxy disks based on an empirical relationship connecting the star formation rate in a galaxy to the molecular-phase gas density. The molecular

gas fraction is, in turn, related to the mid-plane pressure in the galaxy disk (Blitz & Rosolowsky, 2006). This new law is observationally motivated and is characterized by parameters which are constrained by observations, greatly reducing the available parameter space in the model. Other changes with respect to Bower06 include longer time scales for both the minimum and total duration of starbursts and different reionization parameters. These changes were made to reconcile the model predictions with observations of LBGs (Lacey et al., 2011). The model uses SPS files from a 1999 private release of the Bruzual & Charlot model family (BC99) and assumes a Kennicutt IMF (Kennicutt, 1983). The BC99 SPS models represent an intermediate step between the public model releases from Bruzual & Charlot (1993) and Bruzual & Charlot (2003) and are found to be very similar to the BC03 SPS models. Compared to the $x = 1.35$ Salpeter IMF used in the SED fitting procedure, the Kennicutt IMF used in the Lagos12 model has the same mass range ($m_\star \in 0.1, 100\,\mathrm{M}_\odot$) but has a steeper slope of $x = 1.5$ and a break in the power law at $m_\star = 1\mathrm{M}_\odot$, below which the slope is $x = 0.4$. The IMF slope $x$ is defined by $\frac{\mathrm{d}N(m)}{\mathrm{d}\ln m} \equiv m^{-x}$. The lack of a power law break at $0.1\,\mathrm{M}_\odot$ means that the Salpeter IMF has an overabundance of low-mass stars compared to the Kennicutt IMF, resulting in higher $M/L$ ratios.

To help explore if certain aspects of our results are model dependent, we also consider the model presented in Lacey et al. (in preparation) (hereafter Lacey13). The Lacey13 model is a hybrid of the Bower06 model family and the model from Baugh et al. (2005). It includes AGN feedback, starburst events triggered by disk instabilities and galaxy mergers, the star formation law described in Lagos et al. (2011b) and a non-universal IMF. We choose this model as a comparison to the Lagos12 model because of several differences between the models which are relevant for SED fitting. The non-universal IMF used in the Lacey13 model consists of a Kennicutt IMF for star formation in disks and a top-heavy IMF with slope $x = 1$ in starbursts. It should be noted that the slope of the top-heavy IMF used in the Lacey13 model is less extreme than the $x = 0$ top-heavy IMF required in Baugh et al. to match the number counts of submillimetre galaxies. The Lacey13 model

generates SEDs using the Maraston (2005) (hereafter MA05) SPS model. There has been a considerable amount of debate in the literature as to whether the luminosity of thermally-pulsating asymptotic giant (TP-AGB) stars featured in the MA05 model is accurate (e.g. Kriek et al., 2010; Zibetti et al., 2013). This has potentially important consequences for the stellar mass inferred from SED fitting, potentially changing the $M/L$ at NIR wavelengths by as much as $50\%$ for a stellar population of age $\approx 1\mathrm{Gyr}$ (Maraston et al., 2006; Michałowski et al., 2012). Although we do not explore this issue in any detail, the debate surrounding the contribution from TP-AGB stars makes the Lacey13 model a useful comparison to our fiducial model.

### 3.3.2 Calculating intrinsic galaxy SEDs

The SED fitting procedure described in Section 3.2 relies on the accuracy of SPS modelling to provide realistic SEDs for simple stellar populations. The same is true for GALFORM which uses SPS modelling to predict model galaxy SEDs from the star formation and chemical enrichment history of each galaxy, as calculated by the model. Compared to SED fitting, which has to assume a parametric form for galaxy SFHs and a single metallicity for all of the stars in a given galaxy, GALFORM self-consistently generates complex assembly histories for galaxies which include chemical evolution (see Baugh, 2006, for examples). There are only a small number of metallicities available for publicly released SPS models. Therefore, in order to actually use the chemical enrichment history of each galaxy in GALFORM, the model performs linear interpolation in $\log(Z_\star)$ between the tabulated SSPs. This approach is not applied in standard SED fitting procedures which instead use a discrete metallicity grid. Another difference between GALFORM and SED fitting is that galaxies in GALFORM are divided into disk and bulge components. The net SED of each model galaxy predicted by GALFORM is therefore the sum of two composite stellar populations, each with its separate star formation and chemical enrichment history. Finally, it should also be noted that GALFORM uses a different choice with respect to SED fitting regarding the treatment of the recycling of mass and metals. SPS models typically provide estimates of the amount of mass a SSP recycles back

to the ISM as a function of age. This information is used in SED fitting to calculate the best-fitting stellar mass. For reasons of numerical efficiency, theoretical galaxy formation models, including GALFORM, typically do not use this information and instead apply the instantaneous recycling approximation where mass and metals are instantly returned to the ISM. The amount of mass and metals returned per unit mass of stars formed are both fixed parameters in GALFORM and are therefore independent of the age of a galaxy. The exact recycled fractions and yields are calculated, for a given IMF, from the output of a SSP with solar metallicity at an age of $10\,\mathrm{Gyr}$. This has a direct impact on how stellar mass is calculated in GALFORM and it is expected that this will lead to a small, redshift-dependent disagreement with the non-instantaneous recycling scheme employed in SED fitting.

### 3.3.3 Dust attenuation

The SED fitting procedure and GALFORM both use the same Madau (1995) prescription for absorption and scattering of UV photons by neutral hydrogen in the IGM. However, there are important differences in the way attenuation by dust is treated. The SED fitting procedure uses the Calzetti law which includes the assumption of a star-dust geometry corresponding to a uniform, foreground dust screen, as discussed in Section 3.2.2. GALFORM performs a more physical calculation of radiative transfer for a realistic geometry of the stars and dust. It models dust as a two phase medium separated into diffuse dust in the ISM and compact dust clouds that enshroud star-forming regions (Silva et al., 1998). For a detailed description of this dust attenuation model, see Lacey et al. (2011) and references therein and also Lacey, Baugh & Frenk (in preparation). We provide a qualitative overview of the model here, focusing on aspects of the modelling that are particularly relevant to our analysis. We use the standard terminology whereby extinction curves describe the absorption and scattering out of the sightline to a single star and attenuation curves describe the total absorption and scattering both into and out of all sightlines to an extended stellar distribution on the sky. We characterize attenuation curves with the effective optical depth, $\tau_{\mathrm{eff}}$, as a function of wavelength

$\lambda$. The effective optical depth, $\tau_{\mathrm{eff},\lambda}$, is defined by

$$\tau_{\mathrm{eff},\lambda} = -\ln(F_{\mathrm{atten},\lambda}/F_{\mathrm{intrin},\lambda}), \tag{3.3}$$

where $F_{\mathrm{atten},\lambda}$ and $F_{\mathrm{intrin},\lambda}$ are, respectively, the attenuated and intrinsic galaxy fluxes at a given wavelength and $F_{\mathrm{atten},\lambda}$ is calculated from a radiative transfer model.

The starting point for the dust model used in GALFORM is to calculate the total dust mass in each galaxy. This is calculated by assuming that the ratio of mass in dust to metals in the cold gas is a constant and that this ratio follows the value inferred for the local ISM (Savage & Mathis, 1979). Dust is then divided into diffuse and compact birth cloud components. The relative fraction of dust mass in each component is a model parameter. The fraction in diffuse dust, $f_{\mathrm{diffuse}}$, is set to $0.75$ in the Lagos12 model and $0.5$ in the Lacey13 model. Both dust components use an input Milky-Way extinction curve as a starting point to calculate the resultant attenuation curves of each galaxy by radiative transfer. It is important to realise that inclination and geometric effects can lead to total attenuation curves which are very different from the input extinction curve (e.g. Gonzalez-Perez et al., 2013).

The spatial distribution of diffuse dust is assumed to follow an exponential disk profile that traces the stellar disk, both in radial and vertical scale-length. The effective optical depth associated with diffuse dust is calculated by interpolating between the tabulated radiative transfer calculations performed by Ferrara et al. (1999). Ferrara et al. (1999) calculate the effective optical depth of disk-bulge systems as a function of wavelength, galaxy inclination, face-on extinction optical depth in the $V$-band, $\tau_{V0}$, and disk-to-bulge scale-length ratio. $\tau_{V0}$ is calculated directly from the density of dust at the centre of the disk, using the local ISM dust to metals ratio, and so scales with the surface density of diffuse dust in the galaxy disk as

$$\tau_{V0} \propto f_{\mathrm{diffuse}} M_{\mathrm{cold}} Z_{\mathrm{cold}} / {r_{\mathrm{disk}}}^2, \tag{3.4}$$

where $M_{\mathrm{cold}}$ and $Z_{\mathrm{cold}}$ are the mass and metallicity of cold gas in the galaxy disk and $r_{\mathrm{disk}}$ is the radius of the galaxy disk. It should be noted that no allowance is

made in the modelling of diffuse dust for any differences in the relative spatial distributions of young and old stars in the galaxy disk, although this is accounted for with the second, compact dust cloud component. It is normally assumed that there is no dust in galaxy bulges. An exception is made, however, for diffuse dust associated with gas forming stars in starbursts triggered by mergers or disk instabilities. In these starbursting systems, the attenuation by diffuse dust is approximated by temporarily treating the bulge as a disk when using the results from the Ferrara et al. (1999) radiative transfer calculations. We discuss some of the advantages and potential problems associated with the way that diffuse dust is modelled in GALFORM, in the context of our results, in Section 3.6.

The second dust component in GALFORM represents dust in dense molecular clouds enshrouding star-forming regions. As such, it generally affects the light emitted only by young stars which in turn are assumed to escape the dense dust clouds over a fixed time scale, which is a model parameter. The cloud component is therefore more significant in actively star-forming galaxies and starbursts where very young stellar populations can dominate large parts of the overall galaxy SED. The escape time is set to $1\,\mathrm{Myr}$ for the Lagos12 model and $1\,\mathrm{Myr}$ for the Lacey13 model. The clouds are modelled as being spherically symmetric with uniform density and a mass of $10^6\mathrm{M}_\odot$ and a radius of $16\mathrm{pc}$. The enshrouded stars are placed at the centre. Attenuation from this simple geometry can be evaluated analytically. For a more detailed description of this aspect of the calculation, see Lacey, Baugh & Frenk (in preparation).

The resultant combination of the diffuse and compact dust components attenuating the overall galaxy SED increases the level of physical realism beyond what is represented by the Calzetti law used in SED fitting. We pay particular attention to this in Section 3.4.5 but it should be noted that a full exploration of how the dust modelling used in GALFORM compares to the empirical relations used in observational studies is beyond the scope of this Chapter. For more information, see Gonzalez-Perez et al. (2013) for a discussion of how model predictions derived using this dust modelling approach compare with observations of LBGs.

## 3.4 Stellar mass recovery

In this section we first examine how accurately SED fitting can recover the stellar masses of a volume limited sample of model galaxies predicted by the Lagos12 model at a selection of redshifts. We then attempt to isolate and explain the various different effects which affect the accuracy of stellar mass estimation. In this section, we use the standard SED fitting parameter grid and filter set described in the top half of Table 3.1. The number of model galaxies considered at each redshift is of the order of $10^5$, such that the galaxy population is well represented.

### 3.4.1 Overview

Fig. 3.1 shows the ratio of the stellar mass estimated using SED fitting, $M_\star[\mathrm{fit}]$ to the true stellar mass in the Lagos12 model, $M_\star[\mathrm{model}]$, plotted as a function of $M_\star[\mathrm{model}]$ for a selection of redshifts. We choose to show individual galaxies colour coded by the density of points at a given position on the plane. We also show the 10, 50 and 90 percentile ranges of the distribution. This approach shows the broad trends in the overall distribution whilst still highlighting the presence of any unusual features or outliers. We quantify the distributions in each panel using two simple statistics in order to facilitate a rough quantitative comparison with other results presented in this section. We define $\mu$ as the mean value of the median offset in $\log_{10}(M_\star[\mathrm{fit}]/M_\star[\mathrm{model}])$ calculated for each bin in $M_\star[\mathrm{model}]$. We define $\sigma$ as half of the mean value of the 68% range in $\log_{10}(M_\star[\mathrm{fit}]/M_\star[\mathrm{model}])$ calculated for each bin in $M_\star[\mathrm{model}]$. If there is no dependence of the scatter and median offset on $M_\star[\mathrm{model}]$, then $\mu$ and $\sigma$ quantify exactly the average systematic and random errors which affect the stellar mass estimation.

At face value, the results shown in Fig. 3.1 indicate that the accuracy of the stellar masses estimated using SED fitting is very poor, particularly at high redshift. It should be noted, however, that we have deliberately chosen to assume a Salpeter IMF in our SED fitting procedure despite the fact that the Lagos12 model uses a Kennicutt IMF. The difference in $M/L$ ratio between the Salpeter and Kennicutt

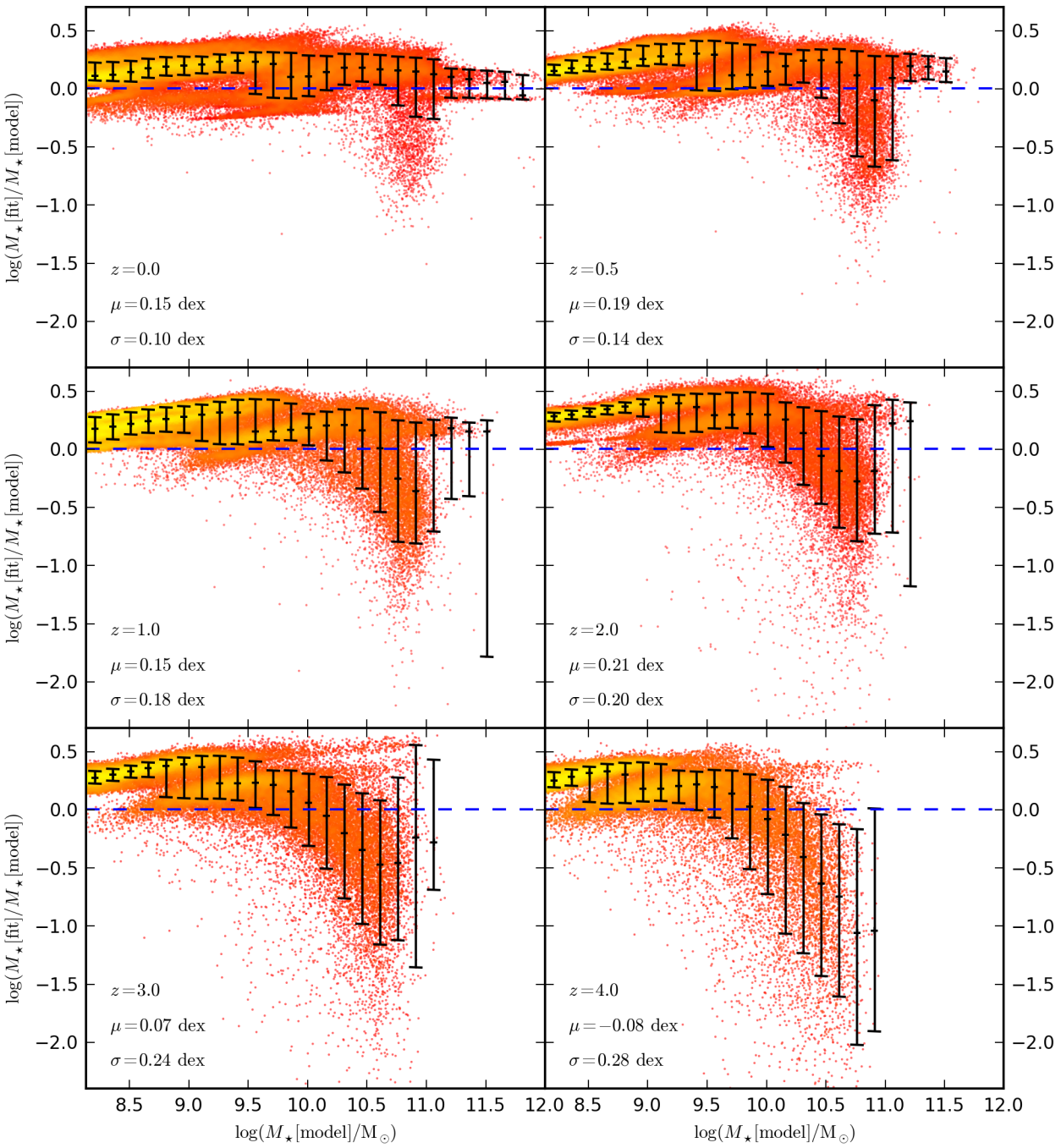


Figure 3.1: Caption continued on following page.

Figure 3.1: The log of the ratio of the stellar mass estimated using SED fitting to the true stellar mass in the Lagos12 model, plotted as a function of the true stellar mass. Each panel corresponds to a different redshift as labelled. The coloured points represent individual model galaxies. The point colours are scaled logarithmically with the local point density in the panel, from red at low density to yellow at high density. The black points and corresponding error bars show the median, $10$ and $90$ percentiles of the distribution in bins of true stellar mass. $\mu$ is the mean median offset and $\sigma$ is half the mean $68\%$ range of the distribution. For reference, the blue dashed line shows the locus of equality between estimated and true stellar mass.

IMFs can account for the systematic offset in $M_\star[\mathrm{fit}]/M_\star[\mathrm{model}]$ seen for low mass galaxies. However, the IMF mismatch cannot explain the behaviour displayed for massive galaxies, particularly at high redshift. These galaxies display a huge scatter in $M_\star[\mathrm{fit}]/M_\star[\mathrm{model}]$. Specifically, there seems to be a population of massive galaxies where the stellar mass is significantly underestimated. The medians and percentiles of the overall distribution show that this is an outlying population at low redshift. However, at high redshift, it is apparent that the stellar masses of almost all of the most massive model galaxies is significantly underestimated. In the most extreme individual cases, the stellar mass can be underestimated by factors greater than a hundred. Finally, the distributions display a level of bimodal behaviour which can be seen by eye from the point density distribution indicated by the colour scheme. This is easier to see in the higher redshift panels. The two peaks of the bimodal feature are typically offset in $\log_{10}(M_\star[\mathrm{fit}]/M_\star[\mathrm{model}])$ by $\approx 0.25\,\mathrm{dex}$. This is significant and clearly undesirable.

There are a number of different factors in the SED fitting calculation that could combine to produce the behaviour shown in Fig. 3.1. Therefore, it is useful to modify the SED fitting procedure and GALFORM in order to isolate how each factor of the calculation contributes to this overall behaviour. In Fig. 3.2, we show how the distribution of estimated over true stellar mass changes with the inclusion or exclusion of these factors for the Lagos12 model. We adopt a fiducial redshift of $z = 2$ for this exercise. Fig. 3.2a shows the case where GALFORM and the SED fitting proce-

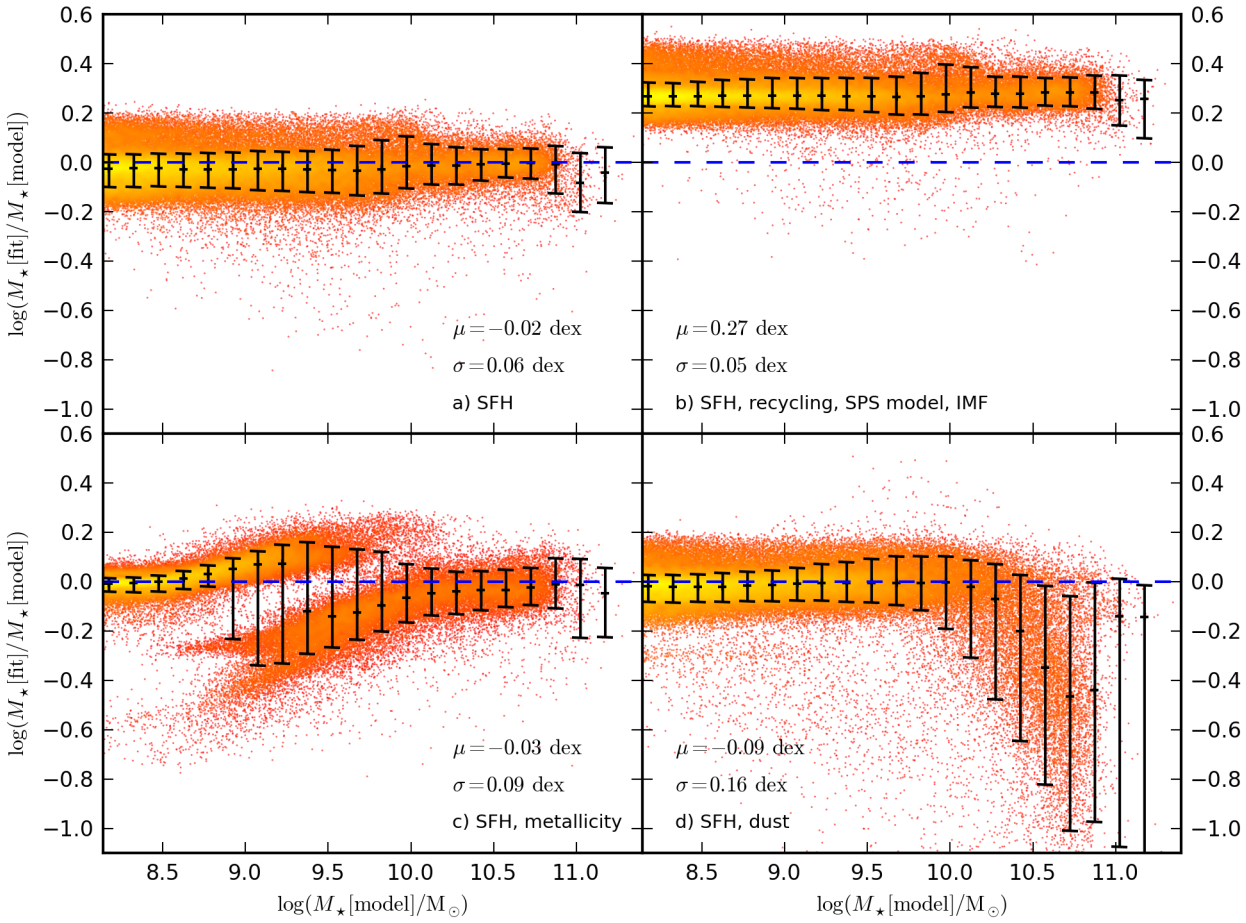


Figure 3.2: The log of the ratio in the stellar mass estimated using SED fitting to the true stellar mass in the Lagos12 model at $z = 2$, plotted as a function of the true stellar mass. Formatting of points and symbols is the same as in Fig. 3.1. The different panels show the distribution for different variations of both SED fitting and GALFORM. *a)* The SFHs of galaxies are the only factor which can vary in the SED fitting process. No dust extinction is applied to model galaxy SEDs in GALFORM and $E(B-V) = 0$ is applied as a constraint in the SED fitting procedure. $Z_\star = Z_\odot$ is applied as a constraint in both GALFORM and the SED fitting. The SPS model used by GALFORM is changed to BC03 with a Salpeter IMF (in order to be consistent with the SED fitting) and the instantaneous recycling approximation is used in the SED fitting procedure (to be consistent with GALFORM). *b)* SFHs, recycling, SPS models and the IMF are the only factors in the SED fitting process. Dust and metallicity related effects are removed as in Panel *a)*. *c)* SFHs and metallicity are the only factors in the SED fitting process. Dust, recycling, SPS models and IMF related effects are removed as in Panel *a)*. *d)* SFHs and dust are the only factors in the SED fitting process. Metallicity, recycling, SPS model and IMF related effects are removed as in Panel *a)*.

dure have been stripped down to the point where effectively only the SFH is being fit for each model galaxy. This is achieved by removing all of the effects associated with dust attenuation, chemical enrichment, recycling and the choice of SPS model and IMF. SPS model, recycling and IMF related effects are removed simply by making the two calculations consistent. Specifically, the SPS model used by GALFORM is changed to BC03 with a Salpeter IMF and the instantaneous recycling approximation is adopted in the SED fitting procedure. We remove chemical enrichment effects by forcing SED calculations in both GALFORM and the SED fitting procedure to use solar metallicity. Dust effects are removed by setting $E(B-V)=0$ as a constraint in the SED fitting procedure and by using the unattenuated fluxes for model galaxies from GALFORM. From this simplified case, the other panels show how the distribution changes with the reintroduction of the various aspects of the calculation that were removed in Fig. 3.2a. Each aspect is reintroduced in isolation.

The remainder of this section is outlined as follows. In Section 3.4.2, we discuss the role of SFHs, SPS models, recycling and the choice of IMF on the inferred stellar mass. In Section 3.4.3, we explore how our results are affected by wavelength coverage. Section 3.4.4 and Section 3.4.5 discuss the impact of metallicity and dust respectively. In Section 3.4.6, we extend our analysis to the Lacey13 model to explore the model dependence of our results.

### 3.4.2 SFHs, recycling, SPS models and the IMF

As discussed earlier, the case presented in Fig. 3.2a is simplified to the extent where the only difference between SED calculations performed by GALFORM and the fitting procedure is in the form of the galaxy SFHs. The SED fitting procedure assumes an exponentially declining SFH characterized by the time since the onset of star-formation, $t_{\rm age}$, and the $e$-folding time scale, $\tau$, whereas GALFORM self-consistently calculates the SFH of each model galaxy. None of the concerning features and trends seen in Fig. 3.1 are present in Fig. 3.2a, which instead shows a smooth distribution with a small scatter almost centered around the locus of equality between estimated and true stellar mass. The distribution can be completely

| z | 0 | 0.5 | 1 | 2 | 3 | 4 |
|---|---|---|---|---|---|---|
| GALFORM: BC03 SPS, Salpeter / SED fitting: BC03 SPS, Salpeter, IRA | | | | | | |
| $\mu$/dex | -0.01 | -0.01 | -0.03 | -0.02 | -0.01 | -0.01 |
| $\sigma$/dex | 0.01 | 0.03 | 0.04 | 0.06 | 0.05 | 0.05 |
| GALFORM: BC03 SPS, Salpeter / SED fitting: BC03 SPS, Salpeter, NIRA | | | | | | |
| $\mu$/dex | -0.01 | -0.01 | -0.01 | 0.01 | 0.04 | 0.05 |
| $\sigma$/dex | 0.01 | 0.03 | 0.04 | 0.05 | 0.05 | 0.05 |
| GALFORM: BC99 SPS, Salpeter / SED fitting: BC03 SPS, Salpeter, NIRA | | | | | | |
| $\mu$/dex | -0.03 | -0.01 | -0.02 | 0.00 | 0.03 | 0.06 |
| $\sigma$/dex | 0.04 | 0.04 | 0.05 | 0.05 | 0.05 | 0.05 |
| GALFORM: BC99 SPS, Kennicutt / SED fitting: BC03 SPS, Salpeter, NIRA | | | | | | |
| $\mu$/dex | 0.26 | 0.26 | 0.26 | 0.27 | 0.30 | 0.31 |
| $\sigma$/dex | 0.03 | 0.05 | 0.05 | 0.05 | 0.05 | 0.05 |

Table 3.2: The mean median offset $\mu$ and half the mean $68\%$ range, $\sigma$, of distributions in $\log(M_\star[\mathrm{fit}]/M_\star[\mathrm{model}])$ against $M_\star[\mathrm{model}]$. All values listed are for the Lagos12 model in the case where dust effects are ignored, both in the model and in the SED fitting procedure. Metallicity effects are also removed by forcing both the model and the SED fitting procedure to use $Z_\star = \mathrm{Z}_\odot$. Each column corresponds to a different redshift. Each pair of rows corresponds to a different combination of choices made regarding SPS modelling, the IMF and recycling in GALFORM and the SED fitting procedure. The top pair of rows corresponds to the simplified case where GALFORM and the SED fitting procedure both use BC03 SPS models, instantaneous recycling (IRA) and a Salpeter IMF. The second pair of rows corresponds to the case where the SED fitting procedure is changed back to using default non-instantaneous recycling (NIRA). The third pair of rows corresponds to the case where the Lagos12 model is changed back to using default BC99 SPS models and the SED fitting procedure uses NIRA. The final pair of rows corresponds to the default case where GALFORM uses BC99 SPS models, IRA and a Kennicutt IMF. The corresponding default SED fitting procedure uses BC03 SPS models, a Salpeter IMF and NIRA.

characterized by the mean offset $\mu = -0.02\,\mathrm{dex}$ and the mean spread $\sigma = 0.06\,\mathrm{dex}$ in this idealized case. It is perhaps surprising that, on average, the SED fitting works so well given the diversity of SFHs which can be predicted in GALFORM, and it is interesting then to see whether this result is reproduced at other redshifts. We list the $\mu$ and $\sigma$ values for this simplified case for other redshifts in the top pair of rows in Table 3.2. It is interesting to see that, averaged over the entire galaxy population, the assumption of an exponentially declining SFH has almost no impact on the accuracy of the stellar mass estimation at $z = 0$ ($\mu = -0.01\,\mathrm{dex}$ and $\sigma = 0.01\,\mathrm{dex}$). In addition, the small scatter seen in Fig. 3.2a at $z = 2$ does not increase for higher redshifts. Comparing this level of scatter with that seen in Fig. 3.1 implies that, for our analysis, the assumption of an exponentially declining SFH has a negligible impact on stellar mass estimation.

To explore this further, we show the average SFHs of galaxies from the Lagos12 model as a function of redshift and stellar mass in Fig. 3.3. The average is performed over 100 galaxies in each mass bin. It should be noted that for a large value of $\tau$, an exponential declining SFH resembles a constant SFH. With this in mind, it can be seen that, qualitatively, an exponentially decreasing SFH will provide an adequate fit to all of the average SFHs shown at lower redshifts. Even at $z = 4$, the bulk of the stellar mass growth still occurs at a relatively constant star-formation rate such that an exponentially declining SFH fit to the data could recover the stellar mass if a large value of $\tau$ were chosen.

We strongly emphasize, however, that these findings only apply to the average over all model galaxies with $M_\star \geq 1.4 \times 10^8\,\mathrm{M}_\odot$. The extremely small scatter seen in Fig. 3.2a. does not imply that the SFHs of individual galaxies are well recovered on an object-by-object basis. We have explored how well the SED fitting procedure recovers the mass-weighted mean age of model galaxies from the Lagos12 model and find a larger scatter (typically $\sigma \approx 0.2\,\mathrm{dex}$) between estimated and true mass-weighted age than is shown for the mass recovery in Fig. 3.2a. Furthermore, a closer inspection of Fig. 3.2a reveals that there are outliers to the overall distribution where the stellar mass is underestimated by almost an order of mag-

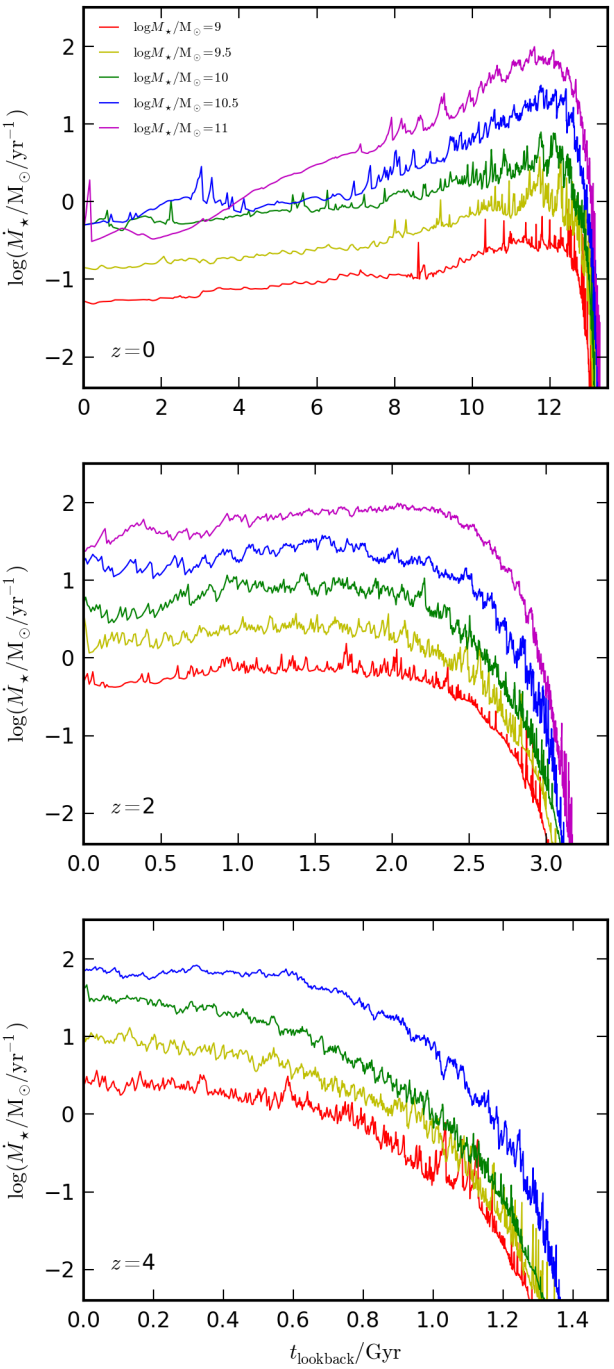


Figure 3.3: Average SFHs of model galaxies in the Lagos12 model, plotted as a function of look-back time from the redshift labelled. Each curve represents the average SFH of 100 galaxies of a given stellar mass at the redshift corresponding to each panel, as indicated by the key.

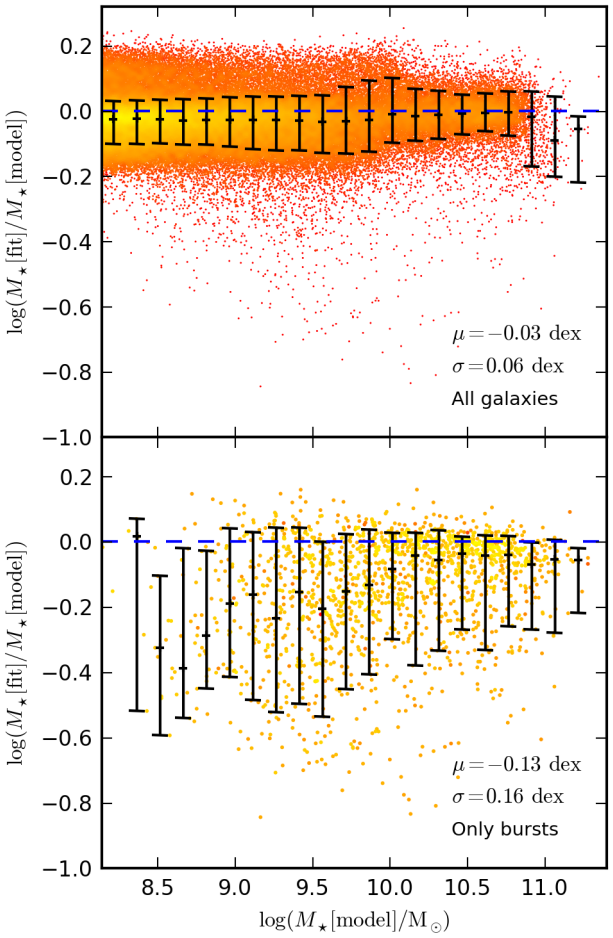


Figure 3.4: The log of the ratio of the stellar mass estimated using SED fitting to the true stellar mass in the Lagos12 model at $z = 2$, plotted as a function of the true stellar mass. As in Fig. 3.2a, both GALFORM and the SED fitting procedure have been modified such that all dust and metallicity effects are removed and the IMF, SPS model and treatment of recycling are consistent between the two calculations. The top panel shows the distribution for all galaxies. The bottom panel shows the distribution for bursting galaxies, selected as model galaxies with a higher SFR in a burst component relative to the quiescent SFR in the galaxy disk. Formatting of points and symbols is the same as in Fig. 3.1.

nitude. In Fig. 3.4, we demonstrate that if a subset of the overall galaxy population is considered, the assumption of an exponentially declining SFH can lead to larger errors in the stellar mass estimation. In this case we compare the average offset and scatter of the entire galaxy population from the Lagos12 model at $z = 2$ with galaxies selected as being dominated by bursts of star-formation. We define bursts as galaxies with higher SFRs in a burst component relative to the SFR associated with quiescent star-formation in galaxy disks. We choose this subset because these galaxies are likely to have SFHs that differ significantly in many cases from an exponentially declining SFH. Our definition of a burst is a straightforward physical definition that can be made in a theoretical model, and should not be confused with the typical observational definition of a starburst as an object with an elevated SFR compared to the mean of the population. Comparison of the distributions shown in Fig. 3.4 for all galaxies (top panel) and for bursts (bottom panel) shows that the stellar masses of bursting galaxies is underestimated on average by $\Delta\mu = -0.1\,\mathrm{dex}$ compared to the average over the total galaxy population. In addition there is significantly increased scatter in $M_\star[\mathrm{fit}]/M_\star[\mathrm{model}]$ when only bursts are considered.

Fig. 3.2b shows a similar scenario to Fig. 3.2a but where the SPS model, IMF and treatment of recycling are changed back to be consistent with the default Lagos12 model and default SED fitting procedure. Specifically, the Lagos12 model uses BC99 SPS models, instantaneous recycling and a Kennicutt IMF in this panel. The SED fitting procedure instead uses BC03 SPS models, non-instantaneous recycling and a Salpeter IMF. Comparison of Fig. 3.2a and 3.2b shows that the different choices of SPS model and IMF, as well as the treatment of recycling, that can be made within SED fitting and GALFORM can cause constant offsets in $M_\star[\mathrm{fit}]/M_\star[\mathrm{model}]$ but do not create additional scatter in the distribution. It is interesting to explore the relative contribution from these different factors to these offsets. The remainder of Table 3.2 shows $\mu$ and $\sigma$ over a set of redshifts for different combinations of choices regarding recycling, the SPS model and the IMF. In all cases, dust and metallicity effects are removed from both GALFORM and the SED fitting procedure.

By default, the SED fitting procedure uses non-instantaneous recycling whereas

GALFORM uses instantaneous recycling with a constant recycled fraction. This constant recycled fraction is fixed, for a given IMF, to the recycled fraction of a SSP with solar metallicity and age $10\,\mathrm{Gyr}$. There are two factors that could lead to systematic errors in stellar mass estimation caused by differences between instantaneous and non-instantaneous recycling. Firstly, the adopted relationship between initial and remnant mass for stars may be different in GALFORM and the BC03 SPS model used in the SED fitting procedure. [1] We check this by comparing the recycled fraction at $10\,\mathrm{Gyr}$ for a solar metallicity BC03 SSP with Salpeter IMF with the corresponding recycled fraction used by GALFORM for a Salpeter IMF. The two recycled fractions at $10\,\mathrm{Gyr}$ are $R = 0.31$ for the BC03 SSP and $R = 0.30$ for GALFORM which are almost consistent. We therefore do not expect this factor to significantly affect the stellar mass estimation. Secondly, for non-instantaneous recycling, the recycled fraction is a function of galaxy SFHs, whereas for instantaneous recycling the recycled fraction is independent of galaxy SFHs. Therefore, as the overall age distribution of the model galaxy population evolves, it is to be expected that part of any systematic error in stellar mass estimation caused by differences between instantaneous and non-instantaneous recycling will be redshift dependent. This is verified by comparing the values of $\mu$ shown in the top and second sections of Table 3.2. Changing from instantaneous recycling (top) to non-instantaneous recycling (second) in the SED fitting procedure has negligible impact at $z = 0$ but results in a $15\%$ offset in stellar mass by $z = 4$. This is a small effect compared to some of the other potential sources of error (e.g. the choice of IMF) but should still be accounted for if an attempt is made to make a precise comparison between stellar masses derived from observations and theoretical models that use instantaneous recycling, particularly at high redshift.

It is beyond the scope of this study to attempt to provide a comprehensive investigation into how stellar mass estimation is affected by uncertainties associated with SPS modelling and the IMF. Comparing the third and bottom sections of Ta-

[1] In GALFORM, we use the relations between initial and remnant masses from Marigo et al. (1996) and Portinari et al. (1998). See Cole et al. (2000) for details.

ble 3.2 shows that the difference between using a Salpeter and Kennicutt IMF is given by $\Delta\mu \approx 0.25-0.29\,\mathrm{dex}$ for $z \in 0, 4$. This simply demonstrates the well known result that changing from Salpeter to an IMF such as Kennicutt, that features a low-mass cutoff, results in $M/L$ ratios that are offset by nearly a constant factor, reflecting the fact that stars at the low-mass end contribute a negligible amount to the integrated light of a SSP. Comparing the second and third sections of Table 3.2 shows that there is also a small, $\approx 7\%$ increase in the scatter of the distribution at $z = 0$ when the transition is made from using BC03 SPS in GALFORM (second) back to the BC99 SPS model (third) used in the default version of the Lagos12 model. We show this for reasons of completeness only because the BC99 and BC03 SPS models both belong to the same overall model family and are thought to be very similar. It should be noted that the difference between these two models almost certainly underestimates the true impact on stellar mass estimation associated with uncertainties in SPS modelling.

### 3.4.3 Wavelength coverage

In the top section of Table 3.2, we show the mean offset $\mu$ and mean spread $\sigma$ for a selection of redshifts in the idealized case where the Lagos12 model and the SED fitting routine are stripped back to the point where only the SFH is different between the SED calculations. For this idealized case, there is no systematic redshift dependence in the mean offset $\mu$. However, there is a gradual increase in the scatter from $\sigma \approx 2\%$ at $z = 0$ up to $\sigma \approx 15\%$ at $z = 2$. The scatter does not continue to increase beyond $z = 2$. The increase in scatter over the redshift range $z \in 0, 1$ could be attributed to two separate effects. Firstly, any changes in the overall distribution of model galaxy SFHs with redshift could affect the accuracy of SED fitting. Over this redshift interval, there is a substantial fall with time in the overall SF activity, which may correspondingly reflect a change in the underlying distribution of SFHs. Secondly, the rest-frame wavelength coverage of the filter set changes with redshift such that the longer wavelengths in the rest-frame galaxy SED are no longer available in the SED fitting process at high redshift. To separate these two

| z | 0 | 0.5 | 1 | 2 | 3 | 4 |
|---|---|---|---|---|---|---|
| All filters - Observer Frame | | | | | | |
| $\mu/\mathrm{dex}$ | -0.01 | -0.01 | -0.03 | -0.02 | -0.01 | -0.01 |
| $\sigma/\mathrm{dex}$ | 0.01 | 0.03 | 0.04 | 0.06 | 0.05 | 0.05 |
| All filters - Rest Frame | | | | | | |
| $\mu/\mathrm{dex}$ | -0.01 | -0.01 | -0.01 | -0.01 | 0.01 | 0.0 |
| $\sigma/\mathrm{dex}$ | 0.01 | 0.02 | 0.03 | 0.02 | 0.02 | 0.03 |
| No IRAC filters - Observer Frame | | | | | | |
| $\mu/\mathrm{dex}$ | -0.01 | -0.01 | -0.03 | -0.04 | -0.03 | -0.03 |
| $\sigma/\mathrm{dex}$ | 0.01 | 0.03 | 0.05 | 0.11 | 0.10 | 0.10 |
| No NIR or IRAC filters - Observer Frame | | | | | | |
| $\mu/\mathrm{dex}$ | -0.01 | -0.02 | -0.04 | -0.05 | -0.07 | -0.07 |
| $\sigma/\mathrm{dex}$ | 0.02 | 0.04 | 0.09 | 0.19 | 0.29 | 0.23 |

Table 3.3: The mean median offset $\mu$ and half the mean $68\%$ range $\sigma$ of distributions in $M_\star[\mathrm{fit}]/M_\star[\mathrm{model}]$ against $M_\star[\mathrm{model}]$. As in Fig. 3.2a, all values listed are for the Lagos12 model in the idealized case where dust and metallicity effects are removed and the choice of SPS model, IMF and treatment of recycling is consistent between GALFORM and the SED fitting procedure. Each column corresponds to a different redshift. Each pair of rows corresponds to a different configuration of filters used to perform the SED fitting. The top pair of rows corresponds to the default case where the 12 broad-band, observer-frame filters listed in Table 3.1 are used, spanning from $B_{435}$ to the $8.0\mu\mathrm{m}$ Spitzer IRAC band. The second pair of rows corresponds to the same filter set with the modification that the filters are fixed in the galaxy rest-frame. The third pair of rows corresponds to a reduced set of observer-frame filters where the Spitzer IRAC filters are removed. The final pair of rows extends this by removing the $J$, $H$ and $K$ bands along with the IRAC filters.

effects, we consider a modification of both the SED fitting procedure and GALFORM to use a filter set that is fixed in the galaxy rest-frame, independent of redshift. The top and second sections of Table 3.3 show values of $\mu$ and mean spread $\sigma$ for the observer frame and rest-frame filter sets respectively. Using the rest-frame filter set removes most of the dependence of $\sigma$ on redshift, revealing that averaged over the entire galaxy population, any change in galaxy SFHs with redshift has a negligible impact on the accuracy of SED fitting when estimating stellar masses, at least when dust and chemical enrichment effects are not present.

For the sake of completeness, it is also interesting to explore how important the NIR filters are for accurately estimating stellar mass in this idealized case where dust, metallicity, SPS model and IMF related effects have all been removed. The bottom four rows of Table 3.3 show $\mu$ and $\sigma$ in the case where either the IRAC filters or all of the NIR filters are removed from the SED fitting process. Comparison to the full observer-frame filter set shown in the top part of Table 3.3 shows that having (perfect) photometry for the IRAC bands reduces the scatter in the stellar mass estimates by $\Delta\sigma \approx 0.05\,\mathrm{dex}$ for $z \geq 2$. In the scenario where only the optical filters are available, the accuracy of SED fitting degrades dramatically above $z = 1$, even for the idealized scenario presented here. There is also an apparent trend whereby stellar masses are increasingly underestimated with increasing redshift. The degradation at higher redshifts demonstrates that it is necessary to sample the rest-frame optical-NIR part of the intrinsic galaxy SED in order to properly account for the contribution from older stars which typically dominate the stellar masses of galaxies.

### 3.4.4 Metallicity

Fig. 3.2c reintroduces metallicity variation back into GALFORM and the SED fitting procedure. For this panel, metallicity is a free parameter in the SED fitting procedure and the full chemical enrichment histories of model galaxies are used to calculate their SEDs in GALFORM. Fig. 3.2c demonstrates that the bimodal features seen in Fig. 3.1 are caused by some aspect of the SED fitting calculation associated with

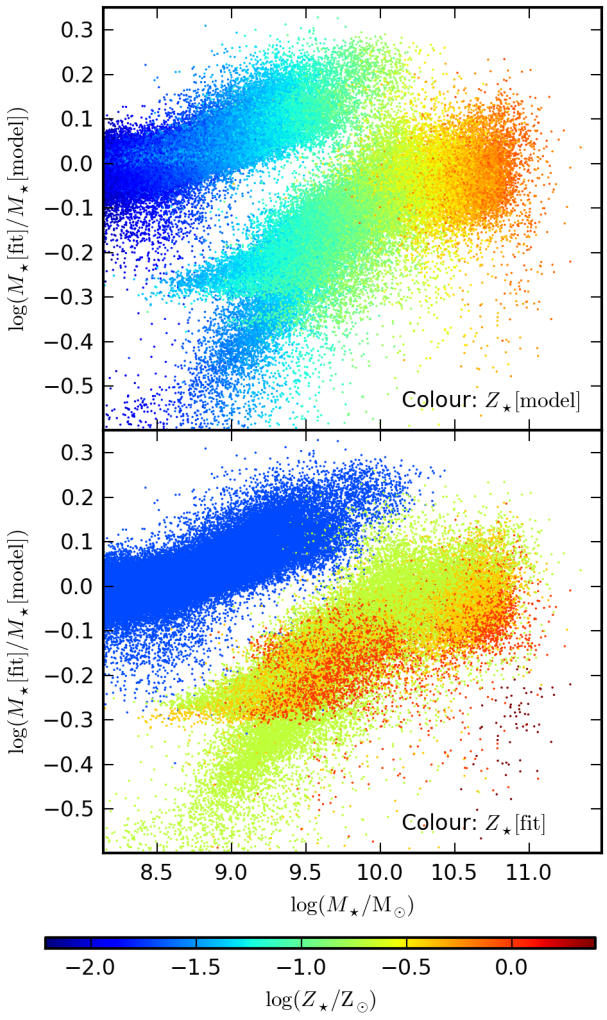


Figure 3.5: The log of the ratio of the stellar mass estimated using SED fitting to the true stellar mass in the Lagos12 model at $z = 2$, plotted as a function of the true stellar mass. As in Fig. 3.2c, both GALFORM and the SED fitting procedure have been modified such that all dust effects are removed, and the IMF, SPS model and treatment of recycling are consistent between the two calculations. *Top:* Each point represents an individual galaxy from the Lagos12 model and is coloured according the mean stellar mass-weighted metallicity calculated by GALFORM for that galaxy. *Bottom:* Each point represents an individual galaxy from the Lagos12 model and is coloured according to the best-fitting metallicity solution calculated in the SED fitting procedure. The parameter grid in $Z_\star$ available to the SED fitting procedure is shown in Table 3.1.

metallicity. To better understand this behaviour, we show in the top and bottom panels of Fig. 3.5 the same distribution with galaxies colour coded by their mean mass-weighted metallicity in GALFORM or by the best-fitting metallicity calculated in the SED fitting procedure. This reveals that while the metallicity of galaxies in GALFORM is continuous across the bimodal feature, the metallicity returned by the SED fitting procedure clearly traces the bimodality seen in Fig. 3.2c. This suggests that the SED fitting procedure could be incorrectly associating a metallicity with a model galaxy because of degeneracies with other parameters such as age (e.g. Bell & de Jong, 2001). Underestimating the metallicity can lead to a corresponding overestimate of the age and hence the $M/L$ ratio. Additionally, it is possible that the parameter grid of metallicities used in SED fitting has insufficient resolution to reproduce the SEDs of model galaxies with mass-weighted metallicities that lie in between the values on the parameter grid.

In order to understand what is causing the bimodal behaviour and to see if it can be removed, we have explored a number of different choices regarding how metallicity is treated in the SED fitting procedure. In Fig. 3.6, we show how these choices affect the distribution of estimated to true stellar mass against stellar mass for the Lagos12 model at $z = 2$, for the case where dust, recycling, SPS model and IMF related effects have been removed. The first and most simple option we explore is simply to fix the metallicity of all galaxies to a constant value in the SED fitting procedure. This choice is often made in observational studies presented in the literature (e.g. Rodighiero et al., 2010; Marchesini et al., 2009). The distribution for this case is shown in Fig. 3.6b. Although fixing the metallicity removes the bimodal behaviour, it also introduces a mass dependent bias into $M_{\star}[\mathrm{fit}]/M_{\star}[\mathrm{model}]$, whereby the stellar masses of less massive galaxies is underestimated. This behaviour is clearly undesirable, although the problem might be alleviated somewhat if a restricted range in stellar mass is considered, as is often the case for high redshift galaxy samples.

In Fig. 3.6c, we force the SED fitting procedure to choose the closest metallicity on the parameter grid to the true mass-weighted metallicity of each model galaxy.

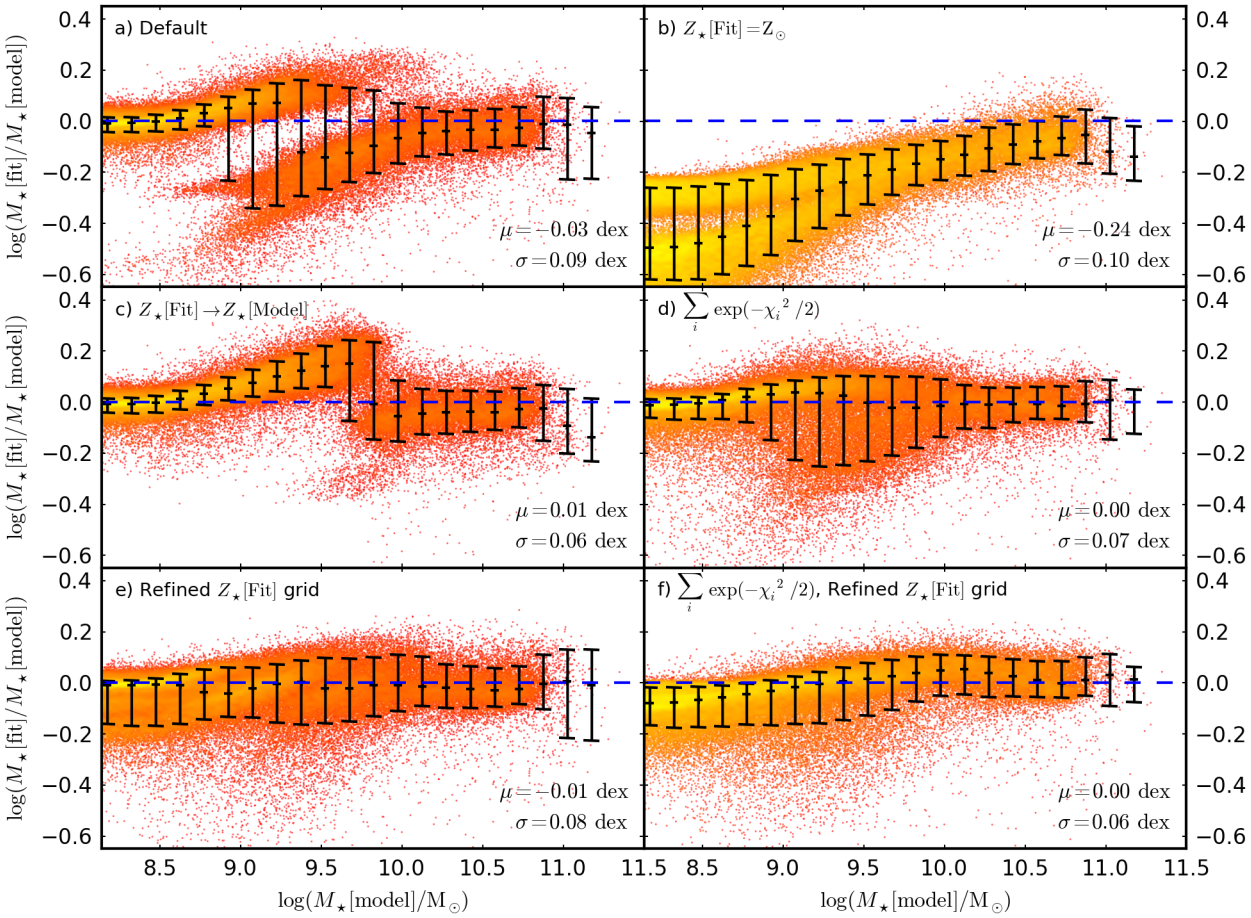


Figure 3.6: The log of the ratio of the stellar mass mass estimated using SED fitting to the true stellar mass in the Lagos12 model at $z = 2$, plotted as a function of the true stellar mass. As in Fig. 3.2c, both GALFORM and the SED fitting procedure have been modified such that all dust effects are removed and the IMF, SPS model and treatment of recycling are consistent between the two calculations. Formatting of points and symbols is the same as in Fig. 3.1. Each panel corresponds to a different configuration of the SED fitting procedure. Caption is continued on the following page.

Figure 3.6: *a)* The default case as shown in Fig. 3.5 where metallicity is a free parameter in the fit and the mode (best-fitting template) of the likelihood distribution is used to estimate the $M/L$ ratio of each model galaxy. *b)* Metallicity is constrained to $Z_\star = Z_\odot$ in the fit. *c)* Metallicity is forced in the fit to use the closest possible value to the true mass-weighted metallicity of each model galaxy. *d)* Metallicity is a free parameter in the fit and the mean over the likelihood distribution is used to estimate the $M/L$ ratio of each model galaxy. The mean is calculated using a likelihood-weighted summation $\sum_i \exp(-{\chi_i}^2/2)M$ over the parameter space. *e)* Metallicity is a free parameter in the fit and additional template SEDs are added to the template grid by interpolating in metallicity. *f)* Metallicity is a free parameter in the fit, additional template SEDs are added to the template grid by interpolating in metallicity and the mean over the likelihood distribution is used to estimate the $M/L$ ratio of each model galaxy.

For each individual model galaxy, this is achieved by calculating the closest metallicity point on the template grid to the true mass-weighted metallicity and then excluding the other metallicity grid points as allowed solutions for that galaxy. This choice could only be replicated in an observational study if external constraints were available on the stellar metallicity for each galaxy in the sample. Comparison of the distribution shown in Fig. 3.6c to the default case shown in Fig. 3.6a shows that constraining the metallicity in this way restricts the bimodal behaviour to a narrow range in $M_\star[\mathrm{model}]$. This in turn indicates that there is a degeneracy between two possible metallicities which is broken when an external constraint is introduced. However, there is still a strong bimodality in the distribution at $M_\star[\mathrm{model}] \approx 4 \times 10^9 \mathrm{M}_\odot$.

Another choice that can be made in SED fitting is to change the statistical method used to obtain the best estimate stellar mass. Instead of picking the point in the parameter space with the smallest $\chi^2$ (which corresponds to the mode of the likelihood distribution), it is also possible to estimate the stellar mass of each galaxy by calculating the mean over the likelihood distribution. This is achieved by performing a likelihood-weighted summation $\sum_i \exp(-{\chi_i}^2/2)$ over the parameter space. Taylor et al. (2011) describe the implementation and advantages of this weighted-

average method in more detail. In principle, taking the mean rather than the mode should result in estimated stellar masses that are more robust against discreteness in the parameter space and could therefore help to remove some of the bimodal behaviour seen in Fig. 3.6a and Fig. 3.6c. We show the distribution when this modified approach is used in Fig. 3.6d. Comparison to Fig. 3.6a reveals that the weighted-average approach does blur the bimodal feature, although the mass estimation is clearly still not perfect.

As a final step, it is also possible to simply interpolate template SEDs between the metallicity points on the SPS metallicity grid. This will help especially in situations where the likelihood distribution associated with a single metallicity grid point is significantly offset in $M/L$ ratio from the others. In this case, neither the mean nor mode of the distribution will return a robust estimate of the true stellar mass if the outlying metallicity grid point dominates the overall distribution. We have confirmed that this is indeed the case for individual galaxies that fall on either side of the bimodal feature seen in Fig. 3.6a. We add points to the parameter space at $Z_\star = 0.5, 0.3, 0.1, 0.05$ and $0.04\,\mathrm{Z}_\odot$ using linear interpolation of the template SEDs in $\log(Z_\star)$. We show the effect of including this extended parameter grid in isolation in Fig. 3.6e and combined with the weighted-average method in Fig. 3.6f. Adding the extra metallicity points in isolation breaks up the main bimodal feature into several smaller, less obvious features, improving the accuracy in the estimated stellar mass. Combining the interpolated metallicity grid with the weighted-average method almost completely removes any artificial bimodality in the distribution of the ratio of estimated to true stellar mass against stellar mass. The overall scatter is also slightly reduced in the process. Comparison with the scatter in Fig. 3.2a shows that when metallicity is treated in this way, including metallicity in GALFORM and the fitting process does not adversely affect the stellar mass estimation. This approach could easily be adopted in observational SED fitting. We discuss this further in Section 3.6.2.

As an aside, it should be noted that the improved stellar mass recovery seen in Fig. 3.6f does not directly imply that metallicity is also successfully recovered

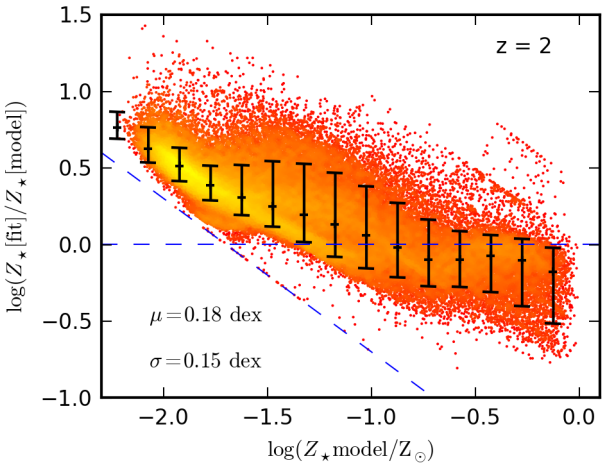


Figure 3.7: The log of the ratio of the stellar metallicity estimated using SED fitting to the true mass-weighted stellar metallicity for model galaxies in the Lagos12 model at $z = 2$, plotted as a function of the true mass-weighted stellar metallicity. No dust effects are included in GALFORM and $E(B-V) = 0$ is applied as a constraint in the fitting. The Lagos12 model is modified to use BC03 SPS models with a Salpeter IMF and the SED fitting procedure is modified to use instantaneous recycling. The SED fitting procedure has also been modified such that the best fit template is formed by a linear summation over all of the templates, weighted by the likelihood of each template. Also, additional templates are added through interpolation in $Z_\star$. The diagonal dashed line marks the lowest metallicity point on the SPS metallicity grid used in the SED fitting. Below this line, the SED fitting is not able to fit a metallicity that matches the metallicity in GALFORM.

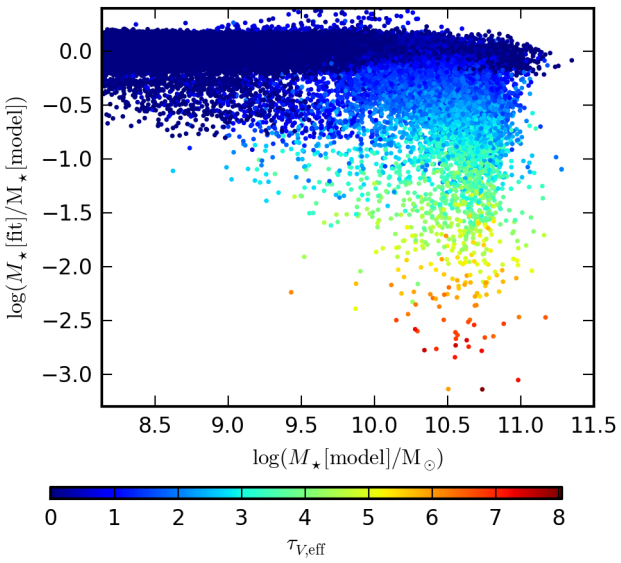


Figure 3.8: The log of the ratio of the stellar mass estimated using SED fitting to the true stellar mass in the Lagos12 model at $z = 2$, plotted as a function of the true stellar mass. As in Fig. 3.2d, both GALFORM and the SED fitting procedure have been modified such that all metallicity effects are removed and the IMF, SPS model and treatment of recycling are consistent between the two calculations. Each point represents an individual galaxy and is coloured by the rest-frame $V$-band effective optical depth, $\tau_{V,\mathrm{eff}}$, as calculated in the Lagos12 model. The colour scaling is indicated by the key.

with this modified fitting approach. In Fig. 3.7, we show the metallicity recovery corresponding to the distribution presented in Fig. 3.6f. Comparing the two distributions shows that SED fitting is more successful at recovering stellar mass than metallicity ($\sigma = 0.15\,\mathrm{dex}$ for metallicity and $\sigma = 0.06\,\mathrm{dex}$ for stellar mass).

### 3.4.5 Dust attenuation

In Fig. 3.2d, we reintroduce dust attenuation back into GALFORM and the SED fitting procedure. Fig. 3.2d shows that some aspect related to how dust attenuation changes galaxy SEDs results in a population of galaxies which are intrinsically massive but have stellar masses which are significantly underestimated by SED fitting. For less massive galaxies, reintroducing dust effects has a negligible impact on the

stellar mass estimation because these galaxies have small dust extinctions in the model. Furthermore, we find that, averaged over the galaxy population, either including or excluding reddening in the fit (whilst retaining the dust extinction calculated by GALFORM) actually has no impact on the recovered stellar mass.

Fig. 3.8 shows the same distribution shown in Fig. 3.2d but with individual galaxies plotted as points coloured by their rest-frame effective optical depth in the $V$-band $\tau_{\rm V,eff}$, as calculated in the Lagos12 model. This shows a clear trend whereby the SED fitting procedure systematically underestimates the stellar masses of the model galaxies with the most dust extinction. Variations between the $M/L$ ratio of template SEDs with sensible combinations of parameters are typically much smaller than the offset in $M_{\star}[\rm fit]/M_{\star}[\rm model]$ seen for these highly extincted galaxies. This indicates that rather than the problem being caused by parameter degeneracies between e.g. dust and age, it seems that the SED fitting is simply not correctly recovering the overall normalization of the intrinsic model galaxy SED. This implies in turn that the Calzetti law must be a poor match to the net attenuation curves calculated for dusty galaxies in GALFORM. We confirm that this is indeed the case in Fig. 3.9 and Fig. 3.10. Fig. 3.9 shows the intrinsic and observed SEDs for 9 individual galaxies which are selected to show a range of offsets in $M_{\star}[\rm fit]/M_{\star}[\rm model]$. It is immediately apparent that the SED fitting procedure underestimates the overall normalization of the intrinsic model galaxy SEDs for the dustiest galaxies. It is also particularly noticeable that the radiative transfer calculation used in the Lagos12 model is applying a significant dust extinction to the entire SED, including up to the NIR for these galaxies. This behaviour cannot be reproduced by the Calzetti law.

This can be seen more clearly in Fig. 3.10, which shows the attenuation curves for the 6 model galaxies shown in the middle and bottom rows of Fig. 3.9. Also plotted is the Calzetti law for a wide range of values of $E(B-V)$. The red dashed line corresponds to the Calzetti law with $E(B-V)=1$, the maximum value we include in the parameter space used in the SED fitting procedure. Fig. 3.10 demonstrates that although the Calzetti law can match the amount of attenuation applied

to the dustiest galaxies by the GALFORM radiative transfer model in the UV, it cannot reproduce the levels of attenuation at optical to NIR wavelengths. Furthermore, even if a different dust attenuation law was used in SED fitting that had the freedom to represent the types of attenuation curve of the model galaxies seen in Fig. 3.10, there would still be a very obvious degeneracy between the presence of a grey dust extinction component and simply having fewer stars producing light in a given galaxy. If such attenuation curves exist in reality, it would be very challenging to accurately constrain the stellar masses of dusty galaxies without performing detailed radiative transfer calculations using the entire UV - FIR SED.

In order to help understand why some of the dusty galaxies in the Lagos12 model have such extreme attenuation curves, it is also useful to consider the physical properties of the model galaxies shown in Fig. 3.9. As discussed in Section 3.3, galaxies are divided in GALFORM between a disk and bulge component. In normal situations, dust is assumed only to be present in the disk but this changes during starbursts, triggered by mergers and disk instabilities. Starbursts are assumed to take place inside the bulges of galaxies and therefore a bulge dust component is required to account for diffuse dust in these systems. We find that the dusty galaxies where the SED fitting procedure fails are typically compact and have high star formation rates. The most extreme examples shown in the bottom row of Fig. 3.9 are compact starbursts. The intermediate cases shown in the middle row of Fig. 3.9 are compact, star-forming disks. It is beyond the scope of this Chapter to provide a detailed analysis of the relationship between the physical properties of model galaxies from GALFORM and their dust attenuation curves. However, it is straightforward to see from Equation 3.4 that compact, gas rich galaxies will have the largest dust attenuations. In Section 3.6.3, we discuss the origin of the shape of the attenuation curves shown in Fig. 3.10. We also discuss whether observed galaxies with high dust content could have similar dust attenuation curves.

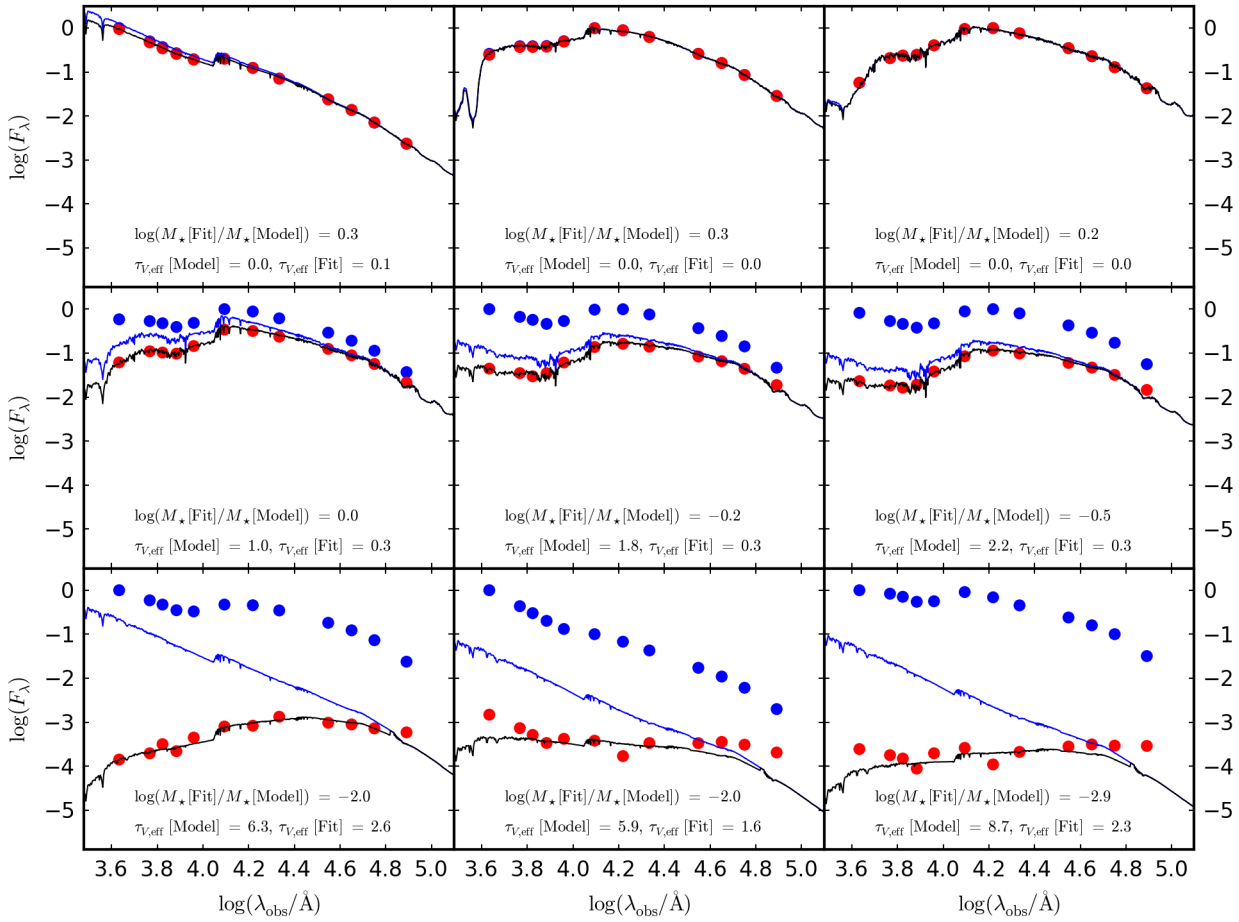


Figure 3.9: SEDs plotted as a function of wavelength in the observer frame for 9 model galaxies generated by the Lagos12 model at $z = 2$. The black and blue solid lines show the dust attenuated and intrinsic SEDs respectively for the best-fitting SED templates calculated by the SED fitting procedure. The blue and red filled points show the intrinsic and attenuated flux respectively for model galaxies in each of the 12 photometric bands used in the fitting process. For plotting purposes, the SEDs are normalized such that the maximum flux of each model galaxy, as calculated by GALFORM, is unity. The three galaxy SEDs shown in the top row are selected quasi-randomly as examples where the SED fitting succeeds in recovering the intrinsic stellar mass. The three galaxy SEDs shown in the bottom row are selected as those with the biggest mass offsets in $M_\star[\mathrm{Fit}]/M_\star[\mathrm{Model}]$. The remaining three galaxy SEDs shown in the middle row are intermediate cases between these two extremes. $\log M_\star[\mathrm{Fit}]/M_\star[\mathrm{Model}]$ is the log of the ratio of the estimated to true stellar mass. $\tau_{V,\mathrm{eff}}[\mathrm{model}]$ is the effective optical depth in the rest-frame $V$ band, as calculated in the Lagos12 model. $\tau_{V,\mathrm{eff}}[\mathrm{fit}]$ is the effective optical depth in the rest-frame $V$ band, as estimated by the SED fitting procedure.

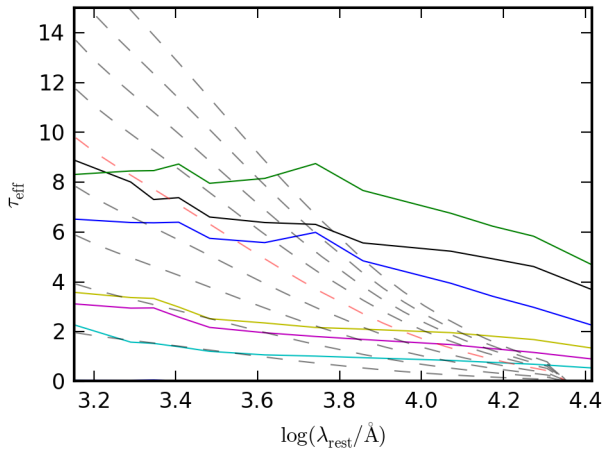


Figure 3.10: Effective optical depth $\tau_{\rm eff}$, plotted as a function of rest-frame wavelength at $z = 2$. Solid coloured lines show the attenuation of the Lagos12 model for the 6 galaxies shown in the middle and bottom rows of Fig. 3.9. The dashed grey lines show the attenuation curve from the Calzetti law for a range of values of $E(B-V)$. The red dashed line corresponds to the specific case where $E(B-V) = 1.0$, which is the maximum reddening considered in the SED fitting procedure.

### 3.4.6 Alternative galaxy formation models

We explained in Section 3.1 that the focus for this study is not to attempt to provide an exhaustive, quantitative guide on the accuracy of stellar mass estimates derived from broad-band SED fitting. Part of the problem with using a SAM for this purpose is that results of this type will depend to some extent on the specific choices and assumptions made as part of that SAM. Instead, we focus on a specific test case and try to understand and explain the origin of different systematics that appear in the distributions shown in Fig. 3.1. As an extension of this analysis, we also explore whether the behaviour seen in Fig. 3.1 is unique to the Lagos12 model. In Fig. 3.11, we compare the distribution in estimated to true stellar mass against stellar mass from the Lagos12 model at $z = 2$ with that in the Lacey13 model introduced in Section 3.3. We use the same SED fitting procedure used to fit model galaxies from the Lagos12 model shown in Fig. 3.1. The two distributions shown in the top and bottom panels of Fig. 3.11 are quite similar in some respects but notably different in others. The general trend whereby the stellar masses of progressively more massive galaxies is increasingly underestimated is seen for both models. However,

unlike for the results for Lagos12 model, the trend traced by the medians of the distribution continues monotonically all the way to the highest mass bins in the Lacey13 model, implying that, on average, even the very most massive galaxies in the Lacey13 model are very dusty. This implies in turn that they are forming stars at an elevated rate. This is an example of how our results can depend on the underlying physics that, in this case, controls the relative fraction of star-forming to passive galaxies.

The $\sigma$ values calculated for the two distributions show that there is a slightly smaller level of random errors when estimating the stellar masses of galaxies from the Lagos12 model, as compared to the Lacey13 model. Visually inspecting percentiles reveals that this difference can be attributed to the smaller scatter in the distribution in the low mass bins shown for the Lagos12 model. The $\Delta\mu \approx 0.3\,\mathrm{dex}$ offset between the two distributions can be understood as a product of two separate effects. Firstly, the recycled fraction associated with the Kennicutt IMF used in the Lagos12 model is set to $R = 0.39$. The corresponding recycled fraction used for stars forming in disks in the Lacey13 model is $R = 0.44$. This can account for $\Delta\mu \approx 0.04\,\mathrm{dex}$ of the total systematic offset. Secondly, the Lacey13 model uses the Maraston (2005) (MA05) SPS model to compute galaxy SEDs whereas both the Lagos12 model and the SED fitting procedure use versions of the Bruzual & Charlot SPS model family. As discussed in Section 3.3, it is established that changing from using MA05 to BC03 SPS models in SED fitting of observed galaxies can change the estimated stellar masses by $\approx 50 - 60\%$ (Maraston et al., 2006; Michałowski et al., 2012). If the TP-AGB contribution is really as uncertain as the discrepancy between the BC03 and MA05 SPS models, the $\Delta\mu \approx 0.3\,\mathrm{dex}$ offset between the two distributions has to be considered as a lower limit on the systematic uncertainty on stellar masses contributed by uncertainties from SPS modelling.

Combined with the uncertainty in the IMF, these differences actually result in a total offset of $\mu = 0.52$ for the Lacey13 model, relative to the SED fitting using a Salpeter IMF. As discussed in Section 3.3, the Lacey13 model uses a top-heavy IMF of slope $x = 1$ in starbursts. We have checked whether this is important for stellar

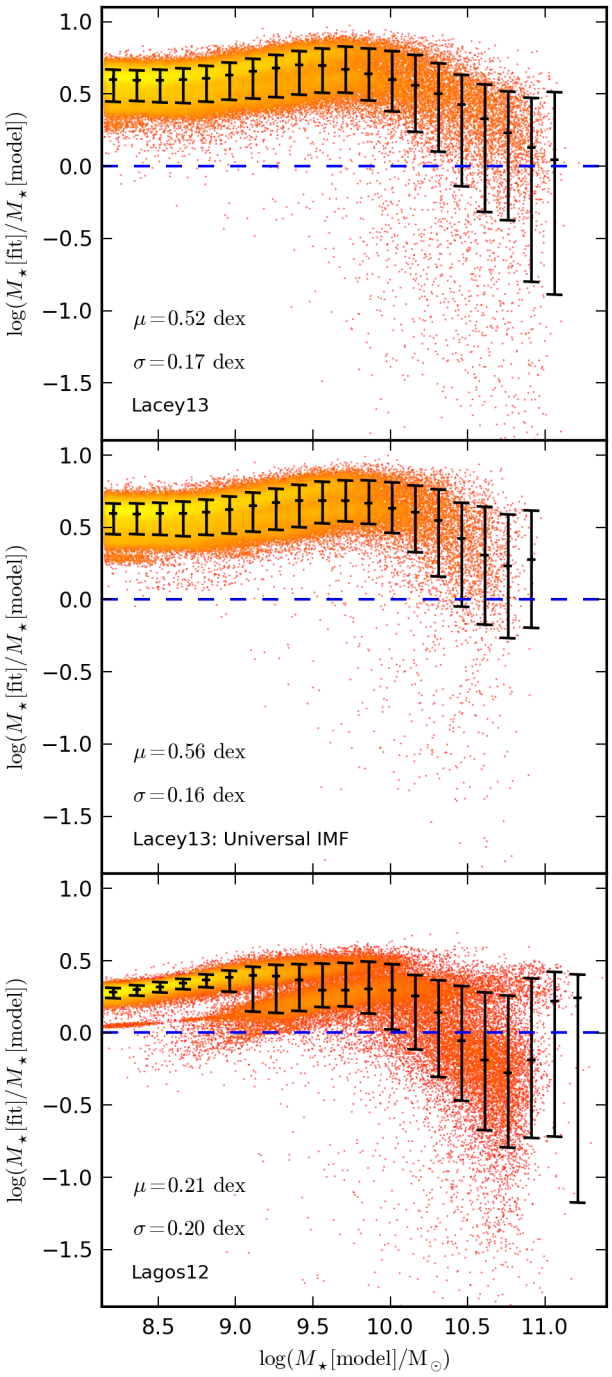


Figure 3.11: Caption continued on the following page.

Figure 3.11: The log of the ratio of the stellar mass estimated using SED fitting to the true stellar mass for different GALFORM models at $z = 2$, plotted as a function of the true stellar mass. The top panel shows the distribution for model galaxies from the default Lacey13 model. The middle panel shows the distribution for model galaxies from a version of the Lacey13 model modified to use a universal Kennicutt IMF. As a reference, the bottom panel shows the distribution for model galaxies from the Lagos12 model, as shown in Fig. 3.1. Formatting of points and symbols is the same as in Fig. 3.1. In all cases, the SED fitting uses a Salpeter IMF.

mass estimation by performing SED fitting on a modified version of the Lacey13 model that uses a universal Kennicutt IMF. The distribution for this scenario is shown in the middle panel of Fig. 3.11. We find that, averaged over the entire galaxy population, the distributions with and without the top-heavy IMF are very similar, at least at $z = 2$. This is not unexpected because the optical-NIR SEDs (which to first order set the estimated stellar mass) of typical galaxies are unlikely, on average, to be dominated by light directly emitted by starbursting populations. However, this will not necessarily be true for UV/FIR selected galaxy samples, particularly at higher redshifts. There is a small $\Delta\mu \approx 0.04\,\mathrm{dex}$ mean offset between the two distributions, whereby the estimated stellar mass is slightly higher, on average, for the universal IMF version of the Lacey13 model. Visual inspection of the percentiles of the two distributions shows that the systematic associated with dust, seen at the high mass end in Fig. 3.2d, is slightly less prominent for this modified version of the Lacey13 model. The offset could therefore be caused by the higher rates of metal injection into the ISM that results from a top-heavy IMF in bursts. This in turn increases the dust content of the ISM in bursting systems, consequently increasing the impact of the systematics associated with dust.

Finally, the bimodal behaviour seen in $M_\star[\mathrm{fit}]/M_\star[\mathrm{model}]$ for the lower to intermediate mass bins in the Lagos12 model is not apparent for the Lacey13 model. We have investigated this further by performing SED fitting on the Lacey13 model in the case where dust effects are ignored. In this case, we find that galaxies which are fitted with different metallicities are, on average, systematically separated in

recovered stellar mass. This is in agreement with the results seen in Fig. 3.5 for the Lagos12 model. However, this effect is not visible in Fig. 3.11 because any underlying bimodality in the distribution is blurred out by the larger overall scatter at low masses seen for the Lacey13 model. We have also explored how this situation changes at lower redshifts. At $z = 0.5$ the large offset caused by TP-AGB stars largely disappears. However, at this redshift, a similarly severe bias appears as a result of metallicity discreteness effects. We find that metallicity grid effects at low redshifts and TP-AGB effects at higher redshifts mean that stellar masses are consistently overestimated by fitting model galaxies from the Lacey13 model for almost the entire redshift range considered in this study.

## 3.5 The stellar mass function

In Section 3.4, we show that there are various systematics that can prevent the SED fitting procedure, described in Section 3.2, from accurately estimating the stellar masses of individual model galaxies calculated by different GALFORM models. We now turn our attention to addressing the question of how these systematics affect the global statistics of the galaxy population. We explore this issue by comparing the intrinsic stellar mass functions predicted by different GALFORM models to the corresponding mass functions recovered from the same models using SED fitting. Measurements of the stellar mass function are often used to constrain hierarchical galaxy formation models (e.g. Guo et al., 2011; Henriques et al., 2013). It is therefore useful to also make a comparison with different observational estimates of the stellar mass function. This also helps to put the systematic effects explored in Section 3.4 into context.

We present stellar mass functions for a selection of redshifts from the Lagos12 model in Fig. 3.12 and from the Lacey13 model in Fig. 3.13. We also present stellar mass functions for the GALFORM model described in Baugh et al. (2005) in Appendix A. We modify our standard SED fitting configuration (outlined in Table 3.1) at this point by assuming a Chabrier IMF instead of a Salpeter IMF. This choice is

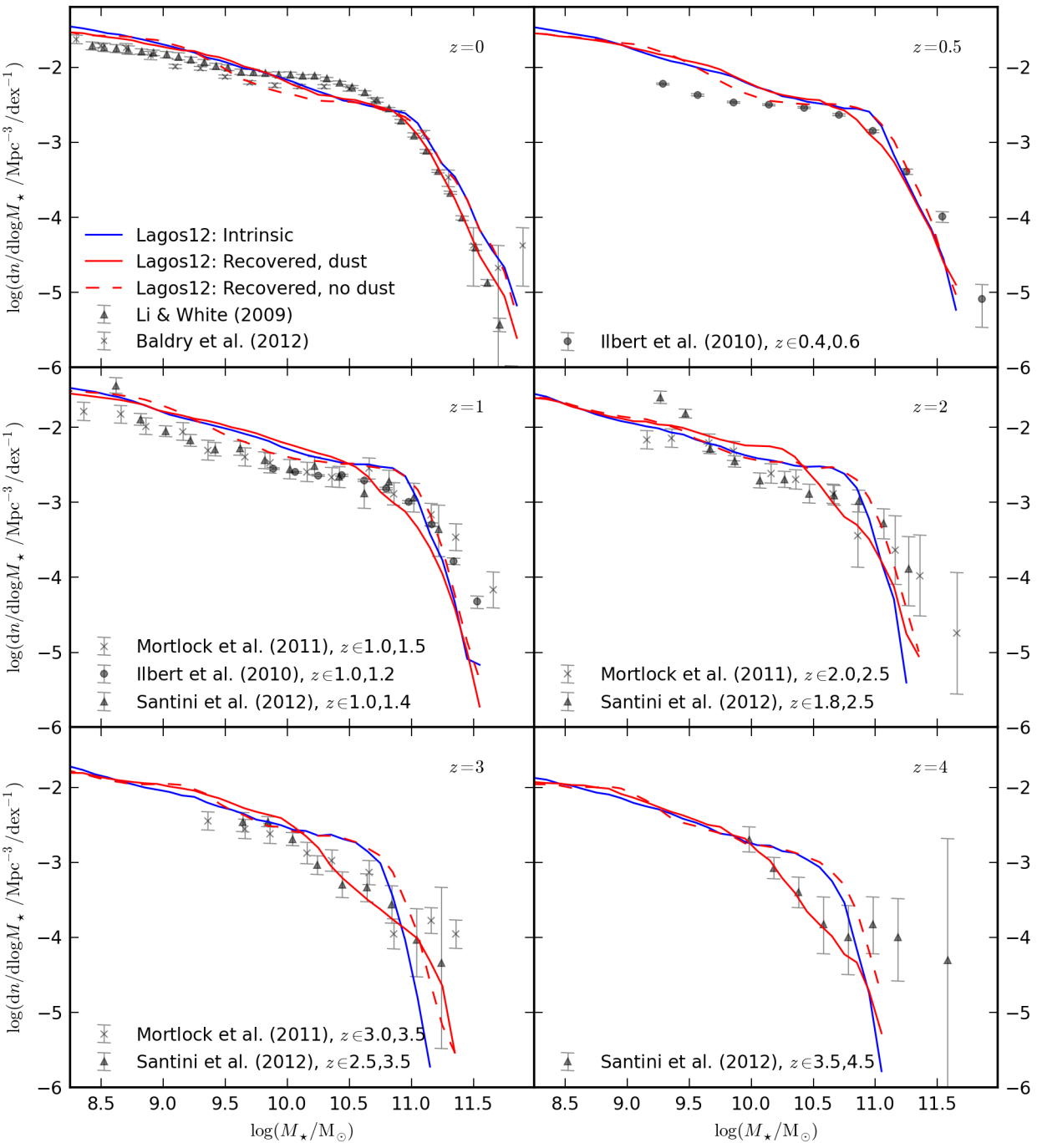


Figure 3.12: Caption continued on the following page.

Figure 3.12: Stellar mass functions predicted by the Lagos12 model for a selection of redshifts, as labelled in each panel. The solid blue line shows the intrinsic stellar mass function produced by the Lagos12 model. The solid red line shows the stellar mass function recovered using SED fitting when dust effects are included and a Chabrier IMF is assumed in the fitting procedure. As a reference, the dashed red line shows the corresponding stellar mass function where no dust extinction is applied to the model galaxy SEDs and $E(B-V)=0$ is used as a constraint in the fitting procedure. The grey points and error bars show observational estimates of the stellar mass function from Li & White (2009), Baldry et al. (2012), Ilbert et al. (2010), Santini et al. (2012) and Mortlock et al. (2011). Where necessary we convert these observational results from a Salpeter to a Chabrier IMF using a $-0.24\,\mathrm{dex}$ correction, calculated by comparing the recovered stellar mass using Salpeter and Chabrier IMFs with BC03 SPS models.

made in order to be consistent with the bulk of the observational studies shown in Fig. 3.12 and Fig. 3.13. For simplicity, we do not choose to change our SED fitting procedure between each redshift panel. It should be noted, however, that the different observational studies all use slightly different variations of SED fitting parameters and filter sets. In addition, the low redshift observational studies (Li & White, 2009; Baldry et al., 2012) use alternative SED fitting methods compared to the standard procedure described in Section 3.2. Baldry et al. (2012) use the likelihood-weighted summation technique, as explored briefly in Section 3.4.4 and described in detail in Taylor et al. (2011). Li & White (2009) use stellar masses calculated with the non-negative matrix factorization technique described in Blanton & Roweis (2007). For consistency with the results shown at other redshifts, we do not use these alternative methods for the mass functions recovered from the model.

Comparison of the intrinsic model mass function (solid-blue line) with the mass function recovered using SED fitting (solid-red line) in Fig. 3.12 shows that the systematics seen in Fig. 3.1 can have an appreciable impact on the inferred global statistical properties of the galaxy population. The intrinsic and recovered model mass functions agree best at the low mass end but disagree at the knee of the mass function and at the high mass end. This becomes increasingly evident in the higher redshift panels. The dominant factor responsible for this disagreement is dust, as

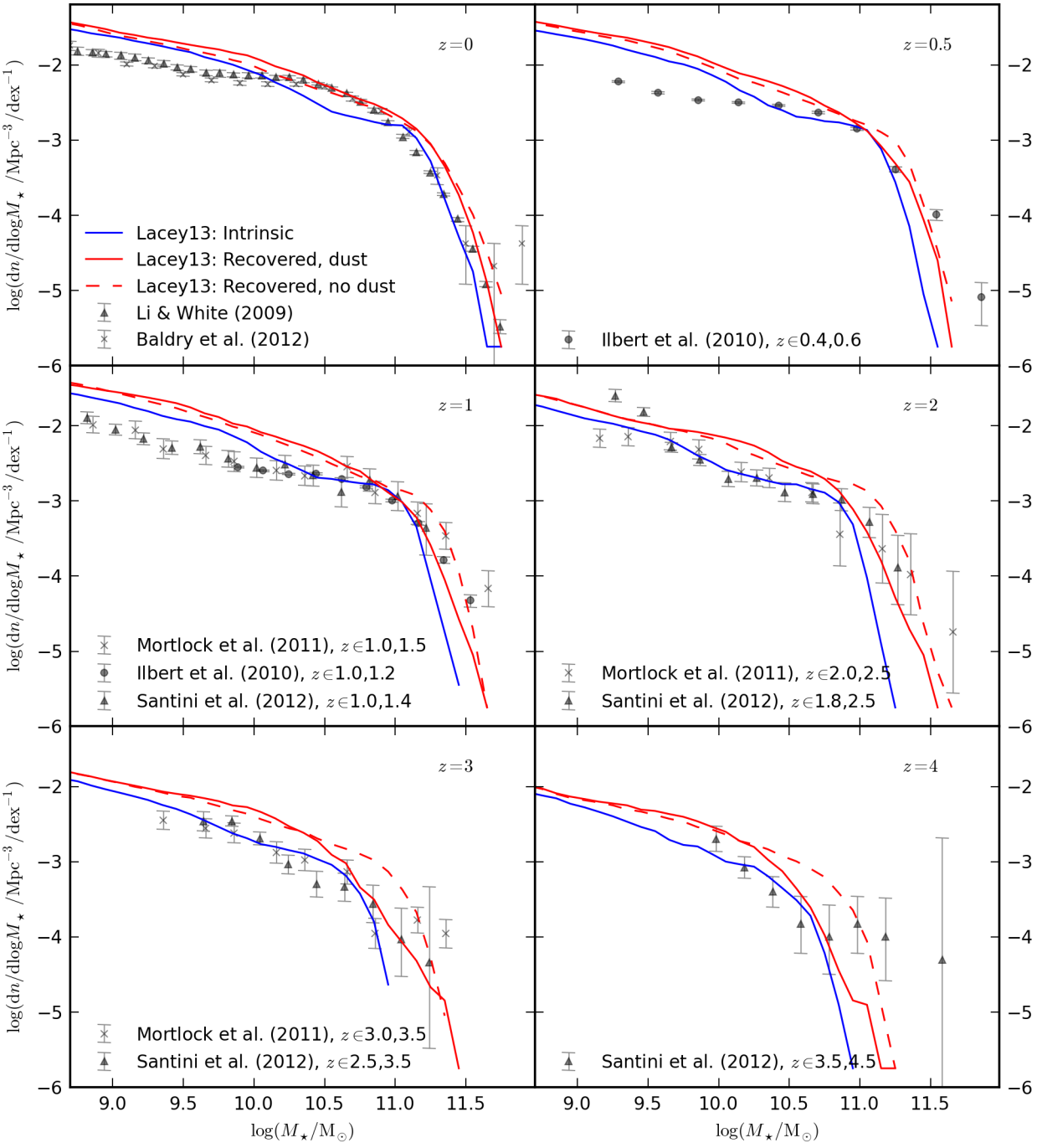


Figure 3.13: Stellar mass functions predicted by the Lacey13 model for a selection of redshifts, as labelled in each panel. The definition and formatting of the lines and points is the same as in Fig. 3.12.

discussed in Section 3.4.5. This is demonstrated by comparing the recovered stellar mass functions when dust effects are (solid red line) and are not (dashed red line) included in the Lagos12 model and the SED fitting process. The recovered stellar mass function that includes dust extinction effectively cuts away the knee of the intrinsic model mass function for $z > 0$. This is not seen when dust effects are not included, which can be understood by comparing Fig. 3.2a with Fig. 3.2d. A common feature of the recovered mass functions, both including and not including dust, is that in the highest redshift panels, the abundance of the most massive galaxies is increased with respect to the intrinsic stellar mass function predicted by the model. This simply reflects the Eddington bias where the exponential decline of the mass function at the massive end means that any scatter in the stellar mass estimation shifts more galaxies into higher mass bins than vice versa. This effect competes with the impact of dust attenuation to give the resultant shape of the solid red line in Fig. 3.12. Comparison to the observational data shows that, in some cases, the relative differences between the intrinsic and recovered model stellar mass functions are much smaller than the disagreement with the observational estimates of the stellar mass function, particularly at the low-mass end and at low redshift. In such cases, the model clearly does not accurately reproduce the observational data and the stellar mass function can be used as a meaningful constraint. However, in the higher redshift panels the uncertainties on the observational data are larger and the differences between the intrinsic and recovered model stellar mass functions also become larger. Taking the difference between the recovered and intrinsic model mass functions as a measure of the level of uncertainty regarding what model curve should actually be compared to the data, it is then apparent that it becomes difficult to place any meaningful constraints on the model using the observed stellar mass function at high redshift.

Fig. 3.13 shows the same information as Fig. 3.12 but for the Lacey13 model instead of the Lagos12 model. The relationship between the intrinsic and recovered stellar mass function is similar to what is seen in Fig. 3.12 but there are also a number of differences. The most obvious difference is that the overall density

normalization of the recovered stellar mass function is higher than for the intrinsic stellar mass function. This occurs predominantly because of differences between the MA05 SPS model used in the Lacey13 model compared to the BC03 SPS model used in the SED fitting procedure. As discussed in Section 3.4.6, this means that the stellar masses of individual model galaxies are systematically overestimated for the Lacey13 model by SED fitting, shifting the overall stellar mass function to the right. Comparison of the two recovered model stellar mass functions when dust effects are (solid red line) and are not (dashed red line) included shows behaviour similar to what is seen in Fig. 3.12, whereby the perceived abundance of massive galaxies at and above the knee of the mass function is suppressed, with the level of suppression increasing towards higher redshifts. It is particularly striking that the entire shape of the mass function can change dramatically, even in the lower to intermediate redshift panels. At these redshifts, the intrinsic stellar mass function predicted by the Lacey13 model does not resemble a single Schechter function as there is an apparent change in the power-law slope before the break. This feature is washed out in the recovered stellar mass function, which instead resembles a single Schechter function when dust effects are included. Finally, as an aside, it is interesting to note that there is a fairly strong level of disagreement between the shape of all of the model stellar mass functions and the shape of the observed mass function at $z = 0$. A disagreement in the overall shape cannot be explained by any systematic uncertainty such as the $M/L$ associated with the IMF, and is interesting given that the model is tuned to reproduce the $z = 0$ $K$-band luminosity function. This suggests that the stellar mass function can, at least at low redshift, provide useful constraints for galaxy-formation models that are complementary to those provided by luminosity function data.

### 3.5.1 Lyman-break galaxies

Up until this point we have focused on the relationship between the recovered and intrinsic stellar mass predicted for galaxies at low to intermediate redshift. At these redshifts, typically the photometric errors are small and colour selections do

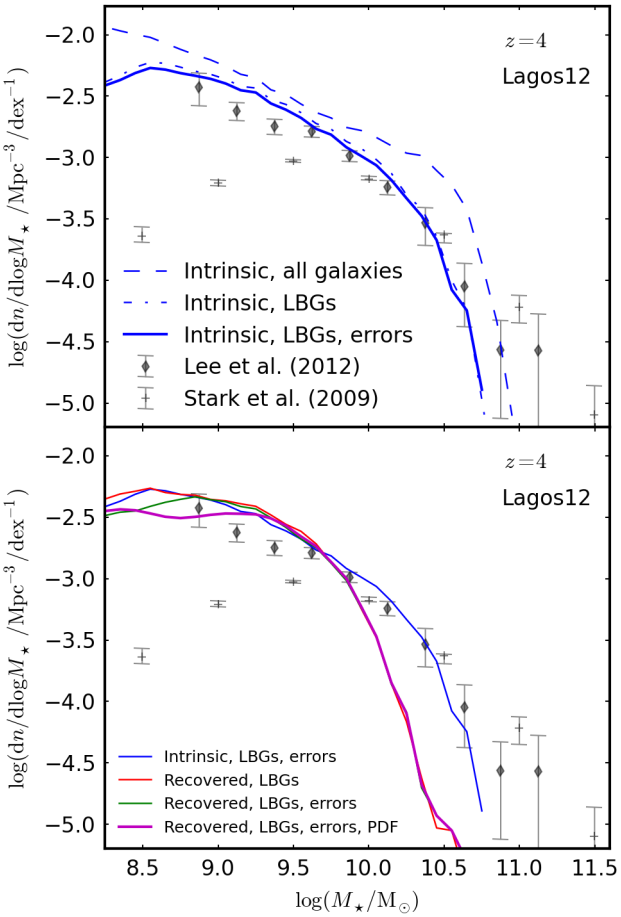


Figure 3.14: Stellar mass functions predicted by the Lagos12 model at $z = 4$. The top panel demonstrates how the intrinsic stellar mass function predicted by the model is reshaped as a result of LBG selection criteria. The dashed blue line shows the intrinsic stellar mass function of all galaxies predicted by the Lagos12 model. The dash-dotted blue line shows the intrinsic stellar mass function of galaxies selected using the $B$-dropout criterion from Stark et al. (2009) if no flux errors are included. The solid blue lines, present in both panels, show the corresponding intrinsic stellar mass functions of LBGs when the selection includes the effects of artificial flux errors. The model galaxy fluxes are artificially perturbed to mimic the $S/N$ for each band quoted in Table 1 of Lee et al. (2012). Caption continued on following page.

Figure 3.14: The bottom panel demonstrates how the stellar mass function of LBGs, as recovered using SED fitting, is reshaped as a result of errors on the photometry and the statistical method used to construct the mass function. The red line shows the stellar mass function of LBGs recovered by SED fitting. The green line shows the corresponding recovered mass function when the model galaxy fluxes are artificially perturbed. This line lies underneath the red and magenta lines at all but low masses. The magenta line shows the corresponding recovered mass function when the model galaxy fluxes are artificially perturbed and the full stellar mass PDF of each individual galaxy is used to construct the mass function. The points and corresponding error bars show the observationally inferred stellar mass functions from Stark et al. (2009) and Lee et al. (2012).

not need to be used in order to obtain well defined galaxy samples. Given that we find that the systematics in the distribution of $\log(M_{\star}[\mathrm{fit}]/M_{\star}[\mathrm{model}])$ can have an appreciable impact on the recovered stellar mass function at these redshifts, it is interesting to explore how these effects translate to high redshift Lyman break galaxy (LBG) samples, where the photometric and redshift errors can become large, colour selections exclude parts of the galaxy population and the available optical to NIR wavelength coverage in the rest frame is reduced.

We modify our SED fitting set-up at this point in order to more closely resemble the choices made by Stark et al. (2009) and Lee et al. (2012), who estimate the stellar mass function of LBGs. This alternative parameter grid is outlined in the bottom half of Table 3.1 and is described in Section 3.2. We also consider a number of effects relevant for LBG samples that were not considered previously. Firstly, we explore the effect of artificially perturbing the fluxes of model galaxies, following a Gaussian distribution consistent with the $5\sigma$ limiting depths listed in Table 1 of Lee et al. (2012). These limiting depths are also used to calculate $\sigma_n$ in Eq. 3.1 when performing SED fitting. When the flux of a model galaxy falls below the $1\sigma$ limiting depth in a given band, we use the method of dealing with non-detections described in Section 3.1 of Lee et al. (2012). Secondly, we explore the effect of LBG selection, taking the dropout criteria from Stark et al. (2009) (both $S/N$ and colour selection criteria), which extends in redshift beyond Lee et al. (2012) to include $z \approx 6$ $i_{775}$

dropouts. When exploring how the SED fitting performs without including the effects of dust attenuation, we still use attenuated fluxes for the purposes of deciding which galaxies pass the LBG selection criteria and to decide which bands are counted as detections for individual galaxies. This ensures that the galaxy samples are consistent when comparing different recovered mass functions. Finally, Lee et al. (2012) construct their observed stellar mass functions by summing together the stellar mass probability distribution functions (PDFs) calculated by their SED fitting procedure for each individual galaxy, hereafter referred to as the PDF method. This is distinct from standard practice in SED fitting where a single stellar mass value is assigned to each galaxy by considering only the best-fitting template to a given galaxy. This difference could potentially become significant at the low mass end of the mass function where galaxies are sufficiently faint that they are only detected in filters sampling the rest-frame UV. UV photometry does not provide strong constraints on the stellar mass associated with older stars in galaxies and this uncertainty will be accounted for on an object-by-object basis when using the PDF method to construct the stellar mass function. To provide a fair comparison to the mass functions from Lee et al. (2012), we also explore the effect of using the PDF method on our recovered mass functions.

In Fig. 3.14, we demonstrate how these various choices and optional modifications affect the stellar mass function predicted by the Lagos12 model at $z = 4$. The top panel shows how the intrinsic mass function predicted by the Lagos12 model is reshaped by LBG selection and artificial flux errors. LBG selection criteria are designed to isolate UV-bright, star-forming galaxies over a given redshift range. For the Lagos12 model, this has the effect of reducing the normalization of the mass function in a fairly uniform manner over the range of masses considered here. The impact of including artificial flux errors has minimal impact on LBG selection. The bottom panel shows how the stellar mass function of LBGs, as recovered by SED fitting, is affected by artificial flux errors and the PDF method. All of the recovered mass functions shown are virtually identical apart from at the low mass end. This simply reflects the fact that more massive galaxies are typically brighter and are

therefore detected with higher overall $S/N$ and at optical-NIR wavelengths where the photometry is not as deep.

In Fig. 3.15, we present recovered and intrinsic model stellar mass functions from the Lagos12 and Lacey13 models for a selection of redshifts. All of the model mass functions shown are constructed using LBG selection criteria and artificially perturbed model galaxy fluxes. The PDF method is used to construct the recovered mass functions, consistent with Lee et al. (2012). We also show measurements of the mass functions of LBG-selected samples from Stark et al. (2009) and Lee et al. (2012). It should be noted that Stark et al. (2009) apply an absolute magnitude cut at $M_{1500} = -20$, the effect of which can be clearly seen as the abundance of galaxies starts to fall below $M_{\star} \approx 2 \times 10^{9} \mathrm{M}_{\odot}$. Stark et al. (2009) also give their results for a Salpeter IMF which we correct by $-0.24\,\mathrm{dex}$. This correction was estimated by comparing the recovered stellar mass using Salpeter and Chabrier IMFs with BC03 SPS models. When comparing the model mass functions with observational data, it should be noted that we do not attempt to mimic errors associated with photometric redshifts for our model galaxies. Including redshift errors is likely to increase the abundance of galaxies at the high-mass end, in line with observational samples that do not attempt to account for the Eddington bias associated with redshift errors.

On first examination, Fig. 3.15 shows a similar picture to that seen in Fig. 3.12 and Fig. 3.13. The inclusion of dust effects in the SED fitting procedure reshapes the recovered stellar mass function at the intermediate to high mass end (as seen by comparing the solid and dashed red lines). It is interesting to see that while the intrinsic model stellar mass functions (blue lines) are quite a good match to the observed stellar mass functions in many cases, the model mass functions recovered using SED fitting are in very poor agreement when dust effects are included. This emphasizes the danger of directly comparing intrinsic mass functions predicted by theoretical models to observational data at high redshift, without accounting for the relevant uncertainties. It is also notable that the significant differences between recovered mass functions that include (solid red lines) and do not include dust

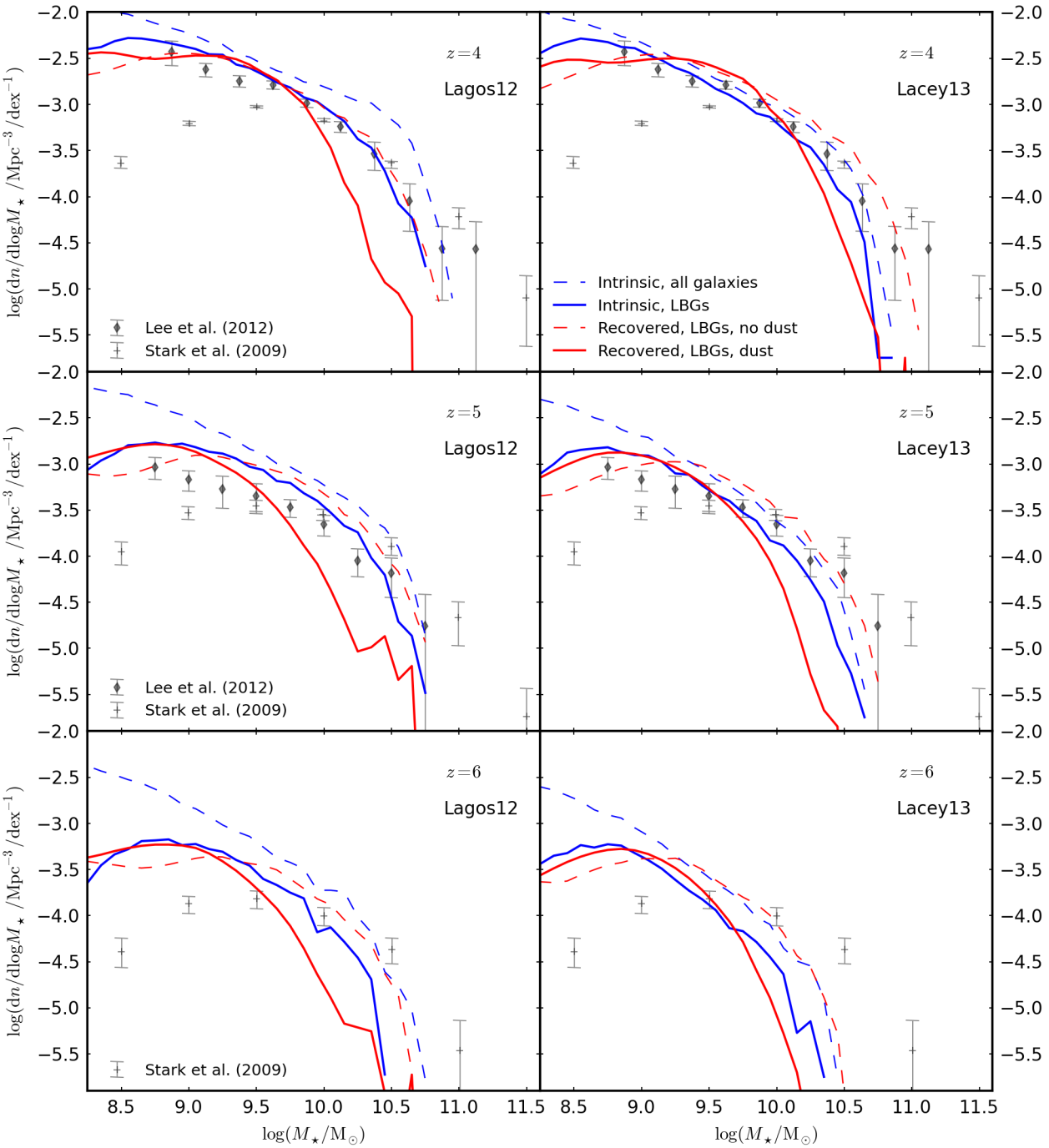


Figure 3.15: Caption continued on the following page.

Figure 3.15: Stellar mass functions predicted by the Lagos12 (left side) and Lacey13 (right side) models for a selection of redshifts, as labelled in each panel. The dashed blue lines show the intrinsic mass functions predicted by the models without imposing any selection criteria. In all of the other cases, model galaxy samples are constructed using the LBG selection criteria from Stark et al. (2009). The flux of each galaxy is artificially perturbed to mimic the $S/N$ for each band quoted in Table 1 of Lee et al. (2012). The solid blue lines show the intrinsic stellar mass functions of LBG-selected galaxies predicted by GALFORM. The solid red lines show the recovered model stellar mass functions of LBG-selected galaxies when dust effects are included in the SED fitting procedure. The dashed red lines show the corresponding recovered model stellar mass functions when dust effects are removed after selection criteria have been applied. All of the recovered mass functions are constructed using the full stellar mass PDF of each individual galaxy. The points and corresponding error bars show the stellar mass functions from Stark et al. (2009) and Lee et al. (2012).

effects (dashed red lines) are present in all of the panels shown. This demonstrates that for the models considered in our analysis, dust continues to play a role in reshaping the entire UV-NIR SEDs of massive galaxies all the way out to $z = 6$. Overall, similar to the situation seen in Fig. 3.12 and Fig. 3.13, it is striking that the relationship between the recovered and intrinsic model stellar mass functions shown in Fig. 3.15 can vary dramatically, dependent on the different SED fitting choices which are made and the redshift considered.

## 3.6 Discussion

### 3.6.1 The role of the SFH in estimating accurate stellar masses

Estimating the physical properties of galaxies from SED fitting requires the adoption of a prior distribution of galaxy SFHs. Large variations exist in the prior distributions used in different observational studies, reflecting the overall uncertainty in the optimal choice of SFH distribution. As a consequence, considerable effort has gone into establishing how these choices can affect the different galaxy properties that can be estimated from SED fitting (e.g. Lee et al., 2009; Maraston et al.,

2010; Pforr et al., 2012; Michałowski et al., 2012; Banerji et al., 2013; Schaerer et al., 2013). Lee et al. (2009) and Schaerer et al. (2013) arrive at similar conclusions in that they both find that the stellar masses of LBGs are not particularly sensitive to the choice of SFH prior. At face value, this seems to conflict with the conclusions from other studies which find that the estimated stellar masses of specific galaxy classes at high redshift are strongly sensitive to the assumed SFH distribution (e.g. Maraston et al., 2010; Michałowski et al., 2012; Banerji et al., 2013). It should be noted, however, that Michałowski et al. (2012) and Banerji et al. (2013) allow for the possibility of multi-component SFHs. This choice gives the SED fitting procedure more freedom to fit a very young, UV-bright stellar population at the same time as including a significant population of older stars that contribute to the total SED primarily at longer wavelengths. This approach is shown to yield systematically higher stellar masses relative to assuming a smooth exponentially declining SFH or an instantaneous starburst.

We have demonstrated in the top section of Table 3.2 that, averaged over the entire galaxy population at a given redshift, the assumption of an exponentially declining SFH does not lead to a mean systematic offset in stellar mass. This result can be understood qualitatively by considering the shape of the average SFHs shown in Fig. 3.3. In addition, we have shown that the scatter associated with fitting the SFH of model galaxies is negligible relative to the random and systematic errors caused by other factors in the SED modelling. We note that Lee et al. (2009) also find that, averaged over a population of model LBGs, stellar masses are well constrained using an exponentially declining SFH. It should be noted that this result only applies strictly to the case of fitting the SFHs of model galaxies in isolation, independent of dust and chemical enrichment effects. In practice, assuming a given prior SFH distribution may play a larger role in creating errors in stellar mass estimates because of the degeneracies that exist between the effects of age, metallicity and dust. Comparison of Fig. 3.6f and Fig. 3.2a shows that when dust effects are ignored and the treatment of metallicity in the fitting is improved, the result that assuming exponentially declining SFHs does not adversely affect stellar

mass estimation still holds even when metallicity effects are reintroduced. On the other hand, as an example of the problems caused by degeneracies associated with dust, Pforr et al. (2012) show that in some cases it can be necessary to ignore dust entirely when applying SED fitting to galaxies with SEDs dominated by older stellar populations. This prevents the SED fitting procedure from incorrectly fitting young and highly reddened galaxy templates to these galaxies.

We have also demonstrated in Fig. 3.4 that if galaxies are selected as being burst dominated, the errors on the estimated stellar masses associated with assuming an exponentially declining SFH are greatly increased relative to the average error for the total galaxy population. This is not a particularly surprising result; we have simply selected galaxies for which a single component, exponentially declining SFH is least likely to be appropriate. However, it does serve to reconcile our results with the findings of Michałowski et al. (2012) in the sense that fitting smoothly varying SFHs to galaxies that are expected to have undergone recent bursts of star-formation (e.g. submillimeter galaxies) can lead to systematically underestimating the stellar masses of these objects.

### 3.6.2 How should metallicity be included in SED fitting?

It is standard practice to either fix the metallicity or to use a small number of discretely spaced metallicities when performing broad-band SED fitting to estimate the physical properties of galaxies. Typically, interpolation between the metallicities is not used. This situation can be attributed to a combination of the inability of broad-band SED fitting to constrain metallicity (e.g. Pforr et al., 2012), the small number of SSP metallicities made available for popular SPS models and for reasons of numerical efficiency. Our analysis has shown that using a discrete and sparsely sampled metallicity grid causes undesirable bimodal features in the distribution of $\log(M_{\star}[\mathrm{fit}]/M_{\star}[\mathrm{model}])$, as seen over a specific range in stellar mass in Fig. 3.5. We have also shown in Fig. 3.6b that the decision to instead fix the metallicity of all galaxies to $Z_{\star} = \mathrm{Z}_{\odot}$ leads to an equally undesirable mass-dependent bias in $\log(M_{\star}[\mathrm{fit}]/M_{\star}[\mathrm{model}])$. This behaviour is straightforward to remove. Fig. 3.6f

demonstrates that using interpolation to add more metallicities to the parameter grid as well as taking the mean rather than the mode of the probability distribution to estimate stellar mass can resolve any biases in stellar mass estimation associated with metallicity. This works primarily because interpolation acts to fill the gaps between metallicity grid points that are significantly offset in $M/L$ ratio for a given age but also because taking the mean helps to blur out discreteness in the distribution of $M/L$ ratios for a given parameter grid (as discussed in Taylor et al., 2011). These steps could easily be incorporated into the standard SED fitting procedures used in observational studies.

The success of the revised fitting procedure shown in Fig. 3.6f suggests that the standard assumption of a single stellar metallicity for all of the stars in a galaxy is acceptable, provided that interpolation and the method of performing a likelihood-weighted average over all templates is used. This is perhaps surprising given that model galaxies in GALFORM can have complex chemical enrichment histories. In particular, the metallicity of the individual stellar populations that make up model galaxies is strongly correlated with age. Conroy et al. (2009) find that there is no significant difference between the optical and NIR colours of a single metallicity SSP and those of a multi metallicity SSP of the same average metallicity. This would imply that SED fitting should correctly infer the $M/L$ ratios of galaxies, provided that the procedure selects the correct average metallicity for a given galaxy. This is entirely consistent with our results. However, Conroy et al. (2009) note that they do not account for a correlation between metallicity and age in their analysis which could feasibly create a significant difference in the colours of single and multi-metallicity stellar populations. Given that such correlations exist for model galaxies in GALFORM, it is therefore reassuring that Fig. 3.6f shows that this effect does not have a significant impact on the estimated stellar masses of galaxies. Gallazzi & Bell (2009) do find that fitting single or double colours of mock galaxies with chemical enrichment histories that contain an age-metallicity correlation has an impact on inferred $M/L$ ratios. However, they find that this effect is small, consistent with our results. It should be noted that there is still a small level of mass-dependent

bias evident in Fig. 3.6f. Given the results of Gallazzi & Bell (2009), this could potentially be explained as a result of fitting model galaxies' multi-metallicity stellar populations with single metallicity templates.

Stellar mass and stellar metallicity are extremely strongly correlated in the Lagos12 model, as can be seen in Fig. 3.5. This is potentially significant in the context of our analysis because the strength of this correlation may serve to exaggerate the strength of the bimodal features seen in Fig. 3.5. In addition, if the stellar metallicity of real galaxies at a fixed stellar mass differs from that of model galaxies predicted by the Lagos12 model, then the mass scale where any bimodal behaviour appears will change, compared to the feature seen in Fig. 3.5. We also note that it is specifically the lowest sub-solar metallicities which are responsible for the offsets seen in Fig. 3.5. If the stellar metallicities of real galaxies, at a given stellar mass, are higher than predicted by the Lagos12 model, then it is possible that these sub-solar metallicities will not be relevant for the galaxies probed in most observational samples. In this case, the size of the discreteness effects seen in Fig. 3.5 will be significantly reduced.

### 3.6.3 Can galaxies have significant dust attenuation at optical to NIR wavelengths?

The most significant source of error we encounter in estimating the stellar masses of model galaxies is found when SED fitting is applied to very dusty model galaxies. In Fig. 3.10, we have shown that these galaxies have much larger amounts of attenuation at longer wavelengths than is possible from the Calzetti law. This causes the stellar masses of dusty model galaxies to be significantly underestimated. In extreme cases, this underestimate can be by factors as large as several hundred. From Fig. 3.1, it can be seen that this error affects the majority of model galaxies above $10^{10}\,\mathrm{M}_{\odot}$ at $z > 2$. Consequently, for these redshifts, the errors associated with dust can completely reshape the recovered stellar mass functions shown in Fig. 3.12. Accordingly, the intrinsic rest-frame optical and NIR luminosity functions predicted

by GALFORM will also be reshaped by dust. This will have a significant impact on any attempt to compare this particular model with observational data at higher redshifts.

In order to understand this overall result, it is useful to consider how there can be significant dust attenuation at optical to NIR wavelengths for model galaxies in GALFORM. Firstly, it is important to note that for the assumption of a star-dust geometry corresponding to a uniform foreground dust screen, and for a specific dust grain model, the ratio of absolute extinction $A_{\rm V}$ relative to the reddening $E(B-V)$ must be constant. Calzetti et al. (2000) assumed this star-dust geometry and applied energy balance arguments to UV and FIR observations of 4 local starbursts to fix $R_{\rm V} = A_{\rm V}/E(B-V) = 4.05$. Once $R_{\rm V}$ has been fixed in this way, the attenuation curve from Calzetti et al. (1994) can no longer reproduce the attenuation curves shown in Fig. 3.10.

In reality, the assumption of a uniform dust screen is a very poor approximation to a realistic star-dust geometry. In GALFORM, disk stars are embedded in a diffuse dust component with the same spatial distribution as the stars. In this case, the path length through the diffuse dust to the observer will be different for each star. Therefore, the light from each star will experience a different amount of attenuation, yielding a net attenuation curve for the entire galaxy which can be significantly different from the input extinction curve of the dust grains (Gonzalez-Perez et al., 2013). A simple example that demonstrates this behaviour is to consider a star-dust geometry corresponding to an infinite uniform slab containing stars and dust mixed together with the same uniform spatial distribution. The effective optical depth, $\tau_{\rm eff}$, for this geometrical configuration is given by

$$\tau_{{\rm eff},\lambda} = -\ln\left(\frac{1-\exp\left(-\tau_{0,\lambda}\sec i\right)}{\tau_{0,\lambda}\sec i}\right), \tag{3.5}$$

where $i$ is the inclination angle of the slab relative to the observer and $\tau_{0,\lambda}$ is the face-on extinction optical depth for a single sightline through the slab. In the limit that $\tau_{0,\lambda}$ becomes large, so that the slab is optically thick, this simplifies to $\tau_{{\rm eff},\lambda} \simeq \ln(\tau_{0,\lambda}\sec i)$. In this scenario, nearly all of the light emitted by stellar populations

from within the slab is absorbed and only light from a layer of stars at the surface can reach the observer. The light that escapes the slab only passes through a small amount of diffuse dust and as a consequence, is only reddened by a small amount. Therefore, for the optically thick case, this configuration will yield net attenuation curves which, compared to the Calzetti law, are considerably greyer. This explains how the attenuation curves of very dusty galaxies in GALFORM can have significant amounts of attenuation at long wavelengths.

In reality, dust in galaxies is not thought to exactly trace the spatial distribution of stars in galaxy disks. By comparing the reddening of nebula emission (i.e. through the $H_\alpha$ to $H_\beta$ line luminosity ratio) with the reddening observed in the total UV continuum of galaxies, it is apparent that dust in the ISM must be concentrated around star-forming regions (e.g. Calzetti et al., 1994). This observation has motivated the use of two-component dust models (e.g. Silva et al., 1998) that contain a compact, birth-cloud dust component that attenuates the light emitted by very young stellar populations. This scheme is applied in GALFORM and as such, the net attenuation curves of model galaxies shown in this Chapter take this effect into account. However, the diffuse dust in galaxies is also not thought to exactly trace the spatial distribution of stars. Specifically, the scale height of diffuse dust is known to be smaller than the overall scale height of stars in galaxy disks, particularly when considering older stellar populations (e.g. Wild et al., 2011).

Additionally, the presence of a clumpy ISM means that there are likely to be some sightlines through galaxy disks which are relatively free of dust. This effect was considered by Conroy et al. (2010b) who explored the effect of a clumpy ISM with a lognormal column density distribution of dust combined with the empirical dust model from Charlot & Fall (2000). Although they show that the clumpiness of the ISM (characterized by the width of the lognormal column density distribution) can have a large impact upon NUV and optical colours, they state that there is negligible impact from dust on the $K$-band luminosity function. It should be noted that this conclusion depends strongly on how they calculate the total amount of dust in the diffuse ISM. If there is a sufficiently large mass in diffuse dust, a clumpy ISM

will produce similar emergent behaviour in terms of the shape of the total attenuation curves to that of the slab geometry considered earlier. That is, the total SED of a dusty galaxy with a clumpy ISM will be dominated by light emitted by stars that lie along relatively unobscured sightlines (which experience only minimal reddening) while light emitted from behind or within optically thick regions will be completely absorbed in comparison. However, the effect of having a clumpy ISM will, for an equal mass in diffuse dust, result in a lower normalization of the total attenuation curve as compared to an optically thick, uniform slab. This is simply because a higher fraction of the stars will be unobscured for the case of a clumpy ISM. At present, the dust modelling in GALFORM does not account for any clumpiness of diffuse dust in the ISM. This may result in a higher normalization for the attenuation curves of very dusty model galaxies, compared to real dusty galaxies. Although the inclusion of a birth-cloud dust component does account in part for clumpiness in the ISM, the impact from birth clouds will be of secondary importance if the diffuse dust component contains enough mass to absorb all of the light not emitted from close to the surface of the galaxy disk.

The problem of choosing an appropriate star-dust geometry becomes even more complex in the case of a galaxy merger. It is well established from numerical simulations that pressure forces experienced by gas in the ISM can decouple the spatial distributions of gas relative to stars, such that gas is funnelled into a compact region in the centre of the system, producing a nuclear burst of star-formation. Wuyts et al. (2009) show that by applying SED fitting to a suite of idealized hydrodynamical simulations of galaxy mergers, the stellar masses of simulated galaxies can be systematically underestimated. This occurs because as the diffuse dust is concentrated into the central region, any light emitted from within or behind that region will be almost entirely cut out of the observed galaxy SED. In addition, the overall stellar distribution will be much more spatially extended than the gas during this phase and consequently will suffer minimal reddening. This is exactly analogous to the behaviour discussed previously for an embedded star-dust geometry or a clumpy ISM. However, as noted by Wuyts et al. (2009), the situation is complicated

in this case by the fact that the stellar populations which are heavily obscured are younger, on average, compared to the total stellar population. A strong correlation between stellar population age and the dust column density will serve to dilute the greying effect discussed for the slab and clumpy ISM examples (see Section 4.3.2 in Wuyts et al., 2009). At present, GALFORM fails to account for these effects in specific situations; in the event of a major merger or disk instability, stars of all ages are mixed evenly with diffuse dust and gas in the galaxy bulge. This geometry is unlikely to be representative of real merging systems (although the situation is far less clear at high redshift) and as such, the attenuation curves of systems in GALFORM that are undergoing major mergers or disk instabilities may be unrealistic. In this case, the impact of dust on stellar mass estimation could be exaggerated to some extent for these systems. Changing the radial scale length of the burst compared to the stellar bulge would represent only a small change to the current implementation in GALFORM and we plan to investigate the impact of this change in future work.

Aside from uncertainties associated with the star-dust geometry, it is important to appreciate the uncertainties associated with calculating the mass and density of dust in the ISM of galaxies, particularly at high redshift. Generally speaking, theoretical galaxy formation models that attempt to model dust use local relations that give the ratio of dust to metals in the ISM (Cole et al., 2000). These local relations are then applied universally, which is a large extrapolation in the case of actively star-forming galaxies at high redshift where the physical conditions in the ISM can be very different. In addition, other aspects of a given theoretical galaxy formation model will have a strong impact on the final effect of dust on model galaxy SEDs. For example, in the case of our analysis, if the calculations of metallicities or galaxy sizes are incorrect in GALFORM, then the size of the errors associated with dust on stellar mass estimation will also be incorrect.

In summary, the assumption of a uniform foreground dust screen must be incorrect in most cases for real galaxies, but the details of the star-dust geometry in real galaxies may also be more complex than what is assumed in GALFORM. In

addition, both the mass and density of dust calculated by GALFORM is dependent on both the overall accuracy of the model and being able to extrapolate the local dust to metal ratio up to high redshift. We plan to explore how these factors could affect our results for stellar mass estimation in future work.

Having explained why dusty galaxies in GALFORM can have significant amounts of attenuation at longer wavelengths relative to the Calzetti law, it is useful to consider if there is any evidence for this behaviour from other observational or theoretical studies. Pforr et al. (2012) and Lee et al. (2009) do not find any evidence that dust can cause the stellar masses of galaxies to be significantly underestimated when they fit model galaxies from other SAMs. However, we emphasize that the SAMs considered in these studies do not attempt to model dust attenuation in a physically motivated way. Instead, they adopt the same Calzetti attenuation curve in the SAM as in the SED fitting. It is therefore of no surprise that these authors do not recover the same results shown by our analysis.

Lo Faro et al. (2013) fit the full UV-FIR SEDs (albeit with limited photometry) of an observed sample of 31 luminous and ultraluminous infrared galaxies at $z = 1$ and $z = 2$. From their Figures 2, 5 and 7 it can be seen that their fitting method estimates significant attenuation of the stellar continuum across the entire UV-NIR SED for a number of objects in their sample. They also apply a standard UV-NIR SED fitting procedure to the same galaxy sample and find that, for the most dust obscured galaxies, the stellar mass obtained in this case is underestimated relative to what is estimated from the full UV-FIR fitting procedure. In the top-left panel of their Figure 6, they show a clear trend whereby stellar mass is increasingly underestimated by UV-NIR SED fitting for increasingly dust obscured systems. This is in qualitative agreement with our results. It should be noted that they use the radiative transfer code GRASIL (Silva et al., 1998) to generate UV-FIR templates. GRASIL assumes the same star-dust geometry as is assumed in GALFORM. On the one hand, this assumed geometry is physically motivated and is clearly superior to the crude assumption of a uniform foreground dust screen. However, the various uncertainties discussed earlier associated with choosing this particular star-dust

geometry are also relevant for their analysis.

Michałowski et al. (2010) also used GRASIL to fit the full UV-FIR SEDs of a sample of 76 spectroscopically confirmed submillimeter galaxies, estimating stellar masses for these objects. Michałowski et al. (2012) then revisited the same sample but instead applied a standard UV-NIR SED fitting procedure to estimate stellar masses. As discussed in Section 3.6.1, the intention behind their analysis was to investigate how priors on the SFH distribution of submillimeter galaxies can affect stellar mass estimation for this class of objects. However, in the context of this discussion, it is interesting to consider the top-right panel of Figure 2 in Michałowski et al. (2012), where the stellar masses estimated using standard UV-NIR SED fitting are compared to the stellar masses calculated using GRASIL modelling of the full UV-NIR SED from Michałowski et al. (2010). Submillimeter galaxies correspond to the objects in our analysis where the stellar mass would be most affected by optical-NIR attenuation. Therefore, it is striking that in contrast to the results from Lo Faro et al. (2013), there does not appear to be a significant systematic difference between the stellar masses estimated using the standard UV-NIR and GRASIL-based UV-FIR methods of fitting submillimeter galaxy SEDs, at least compared to the uncertainties associated with choosing an appropriate SFH.

It is important to note that the SED fitting method applied in Michałowski et al. (2010) differs from Lo Faro et al. (2013) in that they use set of template SEDs from Iglesias-Páramo et al. (2007). These templates were constructed for a limited range of the possible parameter space in GRASIL, chosen to reproduce the SEDs of star-forming galaxies in the local Universe. In contrast, Lo Faro et al. (2013) do not impose any strong priors on the various free parameters in GRASIL, exploring a large parameter space. This difference in approach could potentially explain how stellar mass estimation from standard UV-NIR SED fitting is only found to be strongly affected by Lo Faro et al. (2013). Clearly, for the complex UV-FIR SED fitting procedures applied by Michałowski et al. (2010) and Lo Faro et al. (2013), the resultant stellar masses will depend strongly on the priors and assumptions that are adopted.

da Cunha et al. (2010) fit the UV-FIR SEDs of 16 local ultraluminous infrared galaxies using an alternative procedure to GRASIL. Although they do not attempt to compare the stellar masses of these objects estimated using their UV-FIR SED fitting method with what would be estimated from standard UV-NIR SED fitting, it can be clearly seen that their fitting procedure favours a significant level of dust attenuation at optical-NIR wavelengths for all of the objects in their sample. This is consistent with the behaviour revealed by our analysis and with Lo Faro et al. (2013).

In the local Universe, the problems associated with assuming a specific star-dust geometry can be lessened for resolved, low inclination galaxies. Zibetti et al. (2009) show that when optical-NIR SED fitting is applied locally to derive the stellar mass density at each pixel in the images of resolved galaxies with prominent dust lanes, the total stellar mass calculated can be higher by up to $40\,\%$ relative to the stellar mass obtained by fitting integrated photometry. This result is consistent with the trends shown in our analysis and can be understood as the result of the light emitted by stars that reside either within or behind optically thick dust lanes being subdominant in the total galaxy SED, compared to the light emitted by stars on unobscured sightlines. Unfortunately, this method cannot be readily extended to high redshift where very dusty galaxies are more common.

### 3.6.4 How should theoretical galaxy formation models be compared to observational data?

Our analysis is intended to demonstrate that aside from the well documented uncertainties on stellar mass estimation associated with SPS modelling and the form of the IMF (e.g. Conroy et al., 2009), stellar mass estimation can also be significantly affected by the combined effects of dust, metallicity and recycling. However, viewed from another perspective our method of applying SED fitting to model galaxy SEDs offers, in principle, a new way to compare predictions that involve stellar mass to the results from observational studies. This approach is attractive

because it allows models to be self-consistently compared with different observational data sets without the need to change various parameters in the model (SPS model, IMF) in each instance to make a fair comparison. In addition, the scatter between intrinsic and estimated stellar mass is self-consistently accounted for using this method. This alleviates the need to invoke an arbitrary level of scatter in order to create agreement between model predictions and observations (e.g. Guo et al., 2011; Bower et al., 2012). In the case where predictions from a theoretical model are compared simultaneously to both observables and inferred quantities such as stellar mass, it is clear that our methodology should be followed to make the comparisons self-consistent with each other. Otherwise, the process of transforming from observables to intrinsic galaxy properties will become confused. For example, assumptions made in theoretical models to predict luminosity functions are likely to be in conflict with the assumptions made in SED fitting to estimate stellar mass functions. Unless our methodology is followed, using both of these diagnostics at the same time could therefore adversely affect any attempt to constrain the underlying physics of galaxy formation.

It is important to realise that our methodology does not avoid the problem of converting intrinsic galaxy properties into observables. Instead, the burden of accounting for these uncertainties is simply shifted from the observational SED fitting procedure back to the theoretical modelling process. The natural alternative is to only consider intrinsic galaxy properties and leave all of the uncertainties in the observational process of estimating these quantities. This approach is widely used in both the semi-analytic modelling and hydrodynamical simulation communities (e.g. Bower et al., 2006; Neistein & Weinmann, 2010; Davé et al., 2011; Guo et al., 2011; Khochfar & Silk, 2011; Lagos et al., 2011b; Lamastra et al., 2013; Ciambur et al., 2013). Conroy et al. (2010b) advocate using this latter approach with the caveat that derived quantities such as stellar mass should only be calculated with the inclusion of a full marginalisation over all of the relevant uncertainties in SPS and dust modelling. Such a process would require that these uncertainties can be fully characterized by a discrete set of parameters and that robust prior distribu-

tions for the plausible ranges of these parameters can be found. Our study serves to emphasize that choosing an appropriate distribution of priors would be extremely difficult. For example, the extinction optical depth of diffuse dust, assumed to be small in Conroy et al. (2010b), turns out to play a very important role in stellar mass estimation for our analysis when the optical depth becomes large.

Finally, Fig. 3.12 and Fig. 3.13 show that the systematics and biases that affect stellar mass estimation in our analysis cannot fully account for the level of disagreement between the stellar mass functions predicted by GALFORM models and the mass functions estimated from observational data. Given that these models were tuned to reproduce luminosity function data, this demonstrates that stellar mass functions contain complementary information to luminosity functions, independent of the uncertainties associated with converting intrinsic galaxy properties into observables. This is encouraging and suggests that provided the comparison between theoretical models and observations is made self-consistently, existing estimates of the stellar mass function can provide significant constraining power for galaxy formation models.

## 3.7 Summary

Motivated by the desire to understand whether stellar mass is an appropriate tool for constraining hierarchical galaxy formation models, we have used the observational technique of SED fitting to estimate the stellar masses of model galaxies from the semi-analytic model GALFORM. Following the standard SED fitting procedure for fitting broad-band photometry, we find that effects associated with metallicity, recycling and dust can bias stellar mass estimates. In some specific cases, these effects can create systematic errors in stellar mass that are comparable to or greater than the potential systematic errors associated with the uncertain form of the IMF. Furthermore, we have shown that these error sources are often stellar mass dependent, such that the stellar mass function of model galaxies recovered using SED fitting can differ substantially in shape as well as in normalization from the intrin-

sic mass function predicted by a given model.

The cause and nature of the individual systematic error sources uncovered by our analysis are as follows:

- The exponentially declining star-formation histories that are typically assumed in SED fitting do not, averaged over the entire galaxy population, create any significant systematic errors in stellar mass. In addition, when averaged over the entire galaxy population, the random errors in stellar mass caused by fitting with exponentially declining SFHs are small. This is demonstrated in Fig. 3.2a and Table 3.2. These results are selection dependent. If model galaxies are deliberately selected to be undergoing bursts of star formation, the assumption of an exponentially declining SFH leads to both systematic underestimates and a significantly larger scatter in the estimated stellar masses of these systems.

- Differing assumptions regarding recycling of mass from stars back into the ISM can lead to small, redshift dependent systematics in stellar mass. These are outlined in Table 3.2. Theoretical galaxy formation models typically apply the instantaneous recycling approximation, whereas standard SED fitting procedures use the best-fitting template SFH to estimate the recycled mass. Neither approach will give the correct answer in detail. Furthermore, the systematic differences between the two approaches should be accounted for when the stellar masses predicted by theoretical models that assume instantaneous recycling are compared to observational data.

- Metallicity has the effect of introducing undesirable bimodal features into the distribution of recovered stellar mass that can be seen in Fig 3.2c. This behaviour arises because the standard SED fitting procedure uses discrete, poorly sampled metallicity grids and a statistical method of choosing only a single best-fitting template (the mode of the probability distribution). Alternatively, if the equally common choice of fixing metallicity in SED fitting is implemented, the resultant estimated stellar mass suffers a strong mass-

dependent bias. These problems can be solved in a straightforward manner by following two simple steps. Firstly, interpolation can be used to fill in the gaps of the original metallicity grid provided for publicly available SPS models. Secondly, the statistical technique advocated by Taylor et al. (2011) can be implemented where the mean over the probability distribution, calculated from a likelihood-weighted average over all templates, is used to calculate a best estimate for the stellar mass of a given galaxy.

- Dust attenuation in massive, dusty galaxies causes standard SED fitting procedures that assume a Calzetti law to systematically underestimate stellar mass. This occurs because the radiative transfer calculations performed in GALFORM predict significant dust attenuation at optical-NIR wavelengths in some cases. Thus, the light emitted by obscured stellar populations in these galaxies is not properly accounted for when estimating stellar mass. We also find that either including or excluding dust attenuation in the SED fitting process using the Calzetti prescription has only a negligible impact on the estimated stellar mass. This suggests that, for the purposes of stellar mass estimation, it is unimportant whether dust attenuation is included in the fitting process, if a Calzetti law is being assumed.

We find that the shape of the stellar mass function at $z = 0$ is robust against these error sources. However, at higher redshifts the systematic errors associated with dust significantly reshape the recovered mass functions such that a clear break in the intrinsic model mass function at these redshifts can be blurred out. Furthermore, the effects of dust can reduce the normalization at the high mass end by up to $0.6\,\mathrm{dex}$ in some cases. We are forced to conclude that any attempt to constrain theoretical galaxy formation models using stellar mass functions from high redshift galaxy samples should only be performed with great care, given the potential for large mass-dependent systematics in stellar mass estimation from SED fitting.

# Chapter 4

# *The evolution of the star forming sequence*

## 4.1 Introduction

Understanding the star formation history of the Universe represents an important goal of contemporary astronomy, both in theoretical modelling and from observations of the galaxy population. Traditionally, the main diagnostic used to characterise the cosmic star formation history is the volume averaged star formation rate (SFR) density (e.g. Lilly et al., 1996; Madau et al., 1996; Hopkins & Beacom, 2006). This quantity encompasses the combined effect of all the physical processes that are implemented in a given theoretical model of galaxy formation. The lack of a complete theory of how these processes operate within galaxies means that these models are typically designed to be flexible, utilising simple parametrisations with adjustable model parameters. The cosmic star formation rate density, along with other global diagnostics used to assess the plausibility of a given model, is sensitive to all of these model parameters. Hence, while simply selecting a set of parameters to define a viable model is already challenging, the problem is compounded by the possibility of degeneracies between different model parameters. This has prompted the use of statistical algorithms as tools to explore and identify the allowed parameter space of contemporary galaxy formation models (Bower et al., 2010; Henriques et al., 2013; Lu et al., 2013a; Mutch et al., 2013; Ruiz et al., 2013).

An alternative to attempting to "solve" the entire galaxy formation problem from the top down is to try to find observational diagnostics that are sensitive to some specific physical processes but not to others. A promising area in this regard revolves around the discovery of a correlation between the star formation rate

(SFR) and the stellar mass of star forming galaxies, forming a sequence of star forming galaxies (e.g. Brinchmann et al., 2004; Noeske et al., 2007a; Daddi et al., 2007; Elbaz et al., 2007). This is most convincingly demonstrated in the Sloan Digital Sky Survey (SDSS; York et al., 2000) which exhibits a clear star forming sequence with relatively small scatter and a power-law slope which is slightly below unity (e.g. Brinchmann et al., 2004; Salim et al., 2007; Peng et al., 2010; Huang et al., 2012).

The discovery of the star forming sequence in the local Universe has motivated a series of studies which try to establish whether the sequence is in place at higher redshifts (e.g. Noeske et al., 2007b). This task is challenging because of the difficulties in reliably measuring the star formation rates of galaxies. Beyond the local Universe, star formation tracers that do not require the application of uncertain dust corrections are typically available for only the most actively star forming galaxies. This makes it difficult to prove whether or not there is a clear bimodality between star forming and passive galaxies in the SFR-stellar mass plane. On the other hand, it has been demonstrated that star forming and passive galaxies can be separated on the basis of their colours over a wide range of redshifts (e.g. Daddi et al., 2004; Wuyts et al., 2007; Williams et al., 2009; Ilbert et al., 2010; Whitaker et al., 2011; Muzzin et al., 2013a). This technique can then be combined with stacking in order to measure the average SFR of star forming galaxies as a function of both stellar mass and redshift. However, the extent to which these convenient colour selection techniques can truly separate galaxies that reside on a tight star forming sequence from the remainder of the population remains uncertain.

The significance of the star forming sequence as a constraint on how galaxies grow in stellar mass has been discussed in a number of studies (e.g. Noeske et al., 2007b; Renzini, 2009; Firmani et al., 2010; Peng et al., 2010; Leitner, 2012; Heinis et al., 2014). The small scatter of the sequence implies that the star formation histories of star forming galaxies must, on average, be fairly smooth. This has been taken as evidence against a dominant contribution to the star formation history of the Universe from star formation triggered by galaxy mergers (e.g. Feulner et al., 2005; Noeske et al., 2007b; Drory & Alvarez, 2008). This viewpoint is supported

by studies that demonstrate that the contribution from heavily star forming objects that reside above the star forming sequence represents a negligible contribution to the number density and only a modest contribution to the star formation density of star forming galaxies (e.g. Rodighiero et al., 2011; Sargent et al., 2012).

Various studies have shown that a star forming sequence is naturally predicted both by theoretical galaxy formation models (e.g. Somerville et al., 2008; Dutton et al., 2010; Lagos et al., 2011b; Stringer et al., 2011; Ciambur et al., 2013; Lamastra et al., 2013; Lu et al., 2013b) and by hydrodynamical simulations of a cosmologically representative volume (e.g Davé, 2008; Kannan et al., 2014; Torrey et al., 2014). These models have reported a slope and scatter that is generally fairly consistent with observational estimates. However, there have been a number of reported cases where it appears that the evolution in the normalisation of the sequence predicted by galaxy formation models is inconsistent with observational estimates (e.g. Daddi et al., 2007; Davé, 2008; Damen et al., 2009; Santini et al., 2009; Dutton et al., 2010; Lin et al., 2012; Lamastra et al., 2013; Genel et al., 2014; González et al., 2014; Kannan et al., 2014; Torrey et al., 2014). This disagreement is often quantified by comparing model predictions with observational estimates of the specific star formation rates of galaxies of a given stellar mass as a function of redshift. This comparison can also be made for suites of hydrodynamical zoom simulations which exchange higher resolution for a loss in statistical information for the predicted galaxy formation population (Aumer et al., 2013; Hirschmann et al., 2013; Hopkins et al., 2013b; Obreja et al., 2014). These studies find that it is possible to roughly reproduce the observed specific star formation rate evolution, greatly improving over earlier simulations. However, upon closer inspection, it appears that in detail, they may suffer from a similar problem to larger simulations and semi-analytical models with reproducing the observed evolution of the star forming sequence, as noted by Aumer et al. (2013), Hopkins et al. (2013b) and Obreja et al. (2014).

It is important to be aware that below $z \approx 2$, comparisons of specific star formation rates can yield different constraints on theoretical models depending on

whether or not star forming galaxies are separated from passive galaxies. In principle, if star forming galaxies are successfully separated, any disagreement in the evolution of their average specific star formation rates between models and observational data should be independent of "quenching" caused by environmental processes or AGN feedback. Hence, testing the model using the evolution in the normalisation of the star forming sequence potentially offers a significant advantage, as compared to more commonly used diagnostics such as the cosmic star formation rate density, luminosity functions and stellar mass functions. In particular, the reduced number of relevant physical processes makes the problem more tractable and offers a way to improve our understanding of galaxy formation without having to resort to exhaustive parameter space searches, where arriving at an intuitive interpretation of any results can be challenging. This is particularly pertinent if the simple parametrisations used in theoretical galaxy formation models for processes such as feedback are not suitable to capture the behaviour seen in the observed galaxy population.

Here, we use the GALFORM semi-analytic galaxy formation model along with an extensive literature compilation of observations of the star forming sequence to explore the shape of the star formation histories of galaxies within the context of a full hierarchical galaxy formation model. Our aim is to understand the origin of any discrepancies between the predicted and observed evolution in the normalisation of the star forming sequence and to demonstrate potential improvements that could be made in the modelling of the interplay between star formation, stellar feedback and the reincorporation of ejected gas.

The layout of the Chapter is as follows. In Section 4.2, we describe the relevant features of the GALFORM galaxy formation model used for this study. In Section 4.3, we present model predictions for the star forming sequence of galaxies and provide a comparison with a compilation of observational data extracted from the literature. In Section 4.4, we compare the predicted stellar mass assembly histories of star forming galaxies with the average stellar mass assembly histories inferred by integrating observations of the star forming sequence. We also explore

the connection between stellar and halo mass assembly, highlighting the role of different physical processes included in the model. In Section 4.5, we explore modifications that can bring the model into better agreement with the data. We discuss our results and present our conclusions in Section 4.6 and Section 4.7 respectively. Appendix B provides a detailed introduction and exploration of how the stellar mass assembly histories of star forming galaxies can be inferred from observations of the star forming sequence. Appendix C discusses the impact of changing various parameters in the GALFORM model. Appendix D presents a short analysis of how well the various models presented in this Chapter can reproduce the evolution in the stellar mass function inferred from observations.

## 4.2 The GALFORM galaxy formation model

In this section we describe the GALFORM semi-analytic galaxy formation model, which we use to simulate the assembly of the galaxy population within the ΛCDM model of structure formation. The GALFORM model belongs to a class of galaxy formation models which connect the hierarchical assembly of dark matter haloes to galaxies by coupling merger trees generated by cosmological N-body simulations of structure formation to a series of continuity equations which control the flow of baryonic mass and metals between hot halo gas, cold disk gas and stellar components. These continuity equations are designed to encapsulate the effects of physical processes such as the inflow of gas onto galaxy disks by cooling from shock heated hydrostatic haloes. Other processes include quiescent star formation in galaxy disks, chemical enrichment of the ISM, the ejection of cold gas and metals by supernovae, the suppression of gas cooling by AGN and photoionization feedback, galaxy merging and disk instabilities which in turn can trigger both spheroid formation and bursts of star formation. A detailed introduction to the model and the associated underlying physics can be found in Cole et al. (2000), Baugh (2006) and Benson (2010).

Rather than attempting to solve the equations of hydrodynamics to self con-

sistently predict the full spatial distributions of stars, gas and dark matter within haloes, the equations within GALFORM can instead be solved by assuming idealised density profiles for the various components of a galaxy-halo system. For example, the hot gas and dark matter density profiles are assumed to be spherically symmetric and galaxy disks are assumed to follow an exponential surface density profile. Despite these simplifications, the lack of a complete theory of star formation and feedback processes means that the continuity equations can only be formulated and solved using a phenomenological approach.

Several variants of the GALFORM model have appeared in the literature which feature different parametrisations of the physics of galaxy formation. For this study we adopt a slightly modified version of the model presented in Lagos et al. (2012) as our fiducial model. The model used in Lagos et al. (2012) is descended from that originally presented in Bower et al. (2006) (see also Lagos et al., 2011b,a). For the fiducial model used in this study, we make a change from an older gas cooling model used in Lagos et al. (2012), which evolves according to discrete halo mass doubling events, to the continuous gas cooling model presented in Benson & Bower (2010). In the older cooling model (first presented in Cole et al., 2000), the hot gas profile is reset and the radius within which hot halo gas is allowed to cool onto a disk is reset to zero when haloes double in mass. For this analysis, we found that this simplification could lead to artificial suppression of cooling inside haloes hosting massive star forming galaxies at low redshift. Changing to a continuous cooling model removes this problem but has the side effect of slightly increasing the amount of gas available to form stars in the central galaxies of massive haloes. Therefore, in order to recover approximate agreement with the local stellar mass function of galaxies, we lower the threshold required for radio mode AGN feedback to be effective at suppressing gas cooling in our fiducial model by changing the model parameter $\alpha_{\rm cool}$ from $0.58$ (as in Lagos et al., 2012) to $1.0$. All of the models used in this study use merger trees extracted from the Millennium dark matter N-body simulation (Springel et al., 2005). A description of the merger tree construction can be found in Jiang et al. (2014a) and Merson et al. (2013).

### 4.2.1 Star formation, supernova feedback and gas reincorporation

We now give a more detailed introduction to the treatment of several physical processes included in GALFORM that are particularly relevant to this study. Firstly, our fiducial GALFORM model uses the empirical star formation law presented in Blitz & Rosolowsky (2006), which has the form

$$\Sigma_{\rm SFR} = \nu_{\rm SF} f_{\rm mol} \Sigma_{\rm gas}, \tag{4.1}$$

where $\Sigma_{\rm SFR}$ is the surface density of star formation rate, $\Sigma_{\rm gas}$ is the total surface density of cold gas in the galaxy disk, $f_{\rm mol}$ is the fraction of cold hydrogen gas contained in the molecular phase and $\nu_{\rm SF}$ is the inverse of a characteristic star formation timescale. $\nu_{\rm SF}$ is constrained directly using observations of local galaxies and is set to $0.5\,{\rm Gyr}^{-1}$ for our fiducial model (Lagos et al., 2011b). $f_{\rm mol}$ is calculated using an empirical relationship which depends on the internal hydrostatic pressure of galaxy disks (Blitz & Rosolowsky, 2006; Lagos et al., 2011b).

Secondly, the effects of supernova feedback are modelled by expelling cold gas from galaxy disks over each timestep as stars are formed. The outflow rate is parametrised as a function of the disk circular velocity at the half mass radius, $V_{\rm disk}$, and is given by

$$\dot{M}_{\rm ej} = \psi \left(V_{\rm disk}/V_{\rm hot}\right)^{-\alpha_{\rm hot}}, \tag{4.2}$$

where $V_{\rm hot}$ and $\alpha_{\rm hot}$ are numerical parameters and $\psi$ is the star formation rate. It should be noted that these quantities refer to the outflow and star formation rates integrated over the entire galaxy disk. The outflow rate is, by convention, characterised in turn by the dimensionless mass loading factor, $\beta_{\rm ml} \equiv \dot{M}_{\rm ej}/\psi$. Unlike the parameters included in the prescription for star formation, $\alpha_{\rm hot}$ and $V_{\rm hot}$ are treated as free numerical parameters and are set in order to reproduce the observed local galaxy luminosity functions (Bower et al., 2006). For our fiducial model, $V_{\rm hot}$ is set to $485\,{\rm km\,s}^{-1}$ and $\alpha_{\rm hot}$ is set to $3.2$, as in the Bower et al. (2006) and Lagos et al. (2012) models.

All of the gas that is expelled from the galaxy disk is then added to a reservoir of ejected gas which, in turn, is reincorporated at the virial temperature back into the hot gas halo at a rate given by

$$\dot{M}_{\rm hot} = \alpha_{\rm reheat} M_{\rm res}/t_{\rm dyn}, \tag{4.3}$$

where $\alpha_{\rm reheat}$ is a numerical parameter, $M_{\rm res}$ is the mass of gas in the reservoir and $t_{\rm dyn}$ is the dynamical timescale of the halo. For our fiducial model, $\alpha_{\rm reheat}$ is set to $1.26$. Once gas is reincorporated back into the halo, it is free to cool back onto the galaxy disk. Hence, gas can be recycled many times over the lifetime of a given halo before finally being converted into stars.

### 4.2.2 Quenching processes

This cycle of gas accretion, cooling, star formation, gas expulsion and reincorporation can be disrupted in GALFORM through a number of different physical processes which we briefly outline here. The focus in this study is on actively star forming galaxies which are unaffected by these processes. Quenching mechanisms are therefore not the primary focus of our analysis as, to first order, they change which galaxies populate the star forming sequence, not the position of the sequence in the star formation rate versus stellar mass plane. Nonetheless, it is still important to recognise the conditions under which a given model galaxy will drop out of the samples of star forming galaxies which form the basis of this study.

Firstly, galaxies that form inside dark matter haloes which are accreted onto larger haloes become satellite galaxies. Satellites are assumed to lose their hot gas reservoirs to the hot gas halo of the host dark matter halo as a result of ram pressure stripping. Consequently, once a satellite uses up its cold disk gas to form stars, it will become permanently quenched. We note that the instantaneous removal of the hot gas haloes of satellites is, at best, a crude representation of the environmental processes such as ram pressure stripping. A more detailed stripping model has been explored in GALFORM (Font et al., 2008) but inclusion of this would have only

a minimal impact on the model central star forming galaxy population which will be the focus of this study.

Secondly, as the mean density of the Universe drops towards the present day, radiative cooling timescales for hot gas inside haloes grow longer. In the past, this mechanism was the key for theoretical galaxy formation models to match the observed break at the bright end of the galaxy luminosity function. However, after improved cosmological constraints favoured a higher universal baryon fraction, it was demonstrated that this mechanism could no longer fully explain the break (e.g. Benson et al., 2003). Instead, feedback associated with active galactic nuclei (AGN) is invoked as the primary mechanism responsible for quenching massive central galaxies in the current generation of galaxy formation models (e.g. De Lucia et al., 2004; Bower et al., 2006; Croton et al., 2006; Somerville et al., 2008). AGN feedback in GALFORM is implemented by assuming that cooling from the hot gas halo is completely suppressed if *a)* the halo is in a quasi-hydrostatic cooling regime and *b)* the radiative cooling luminosity of the halo is smaller than the AGN luminosity multiplied by an efficiency factor. For more details see Bower et al. (2006).

## 4.3 The star forming sequence of galaxies

In this section we first present the relationship between specific star formation rate and stellar mass predicted by our fiducial GALFORM model over a range of redshifts. We then explain how we separate star forming and passive model galaxies at different redshifts. We also present a compilation of observational data that describe how the average specific star formation rate of star forming galaxies depends on redshift and stellar mass. Finally, we compare our model predictions with the observational data.

### 4.3.1 The star forming sequence in GALFORM

Fig. 4.1 shows the distribution of specific star formation rate against stellar mass in our fiducial GALFORM model for a selection of redshifts. We choose to show indi-

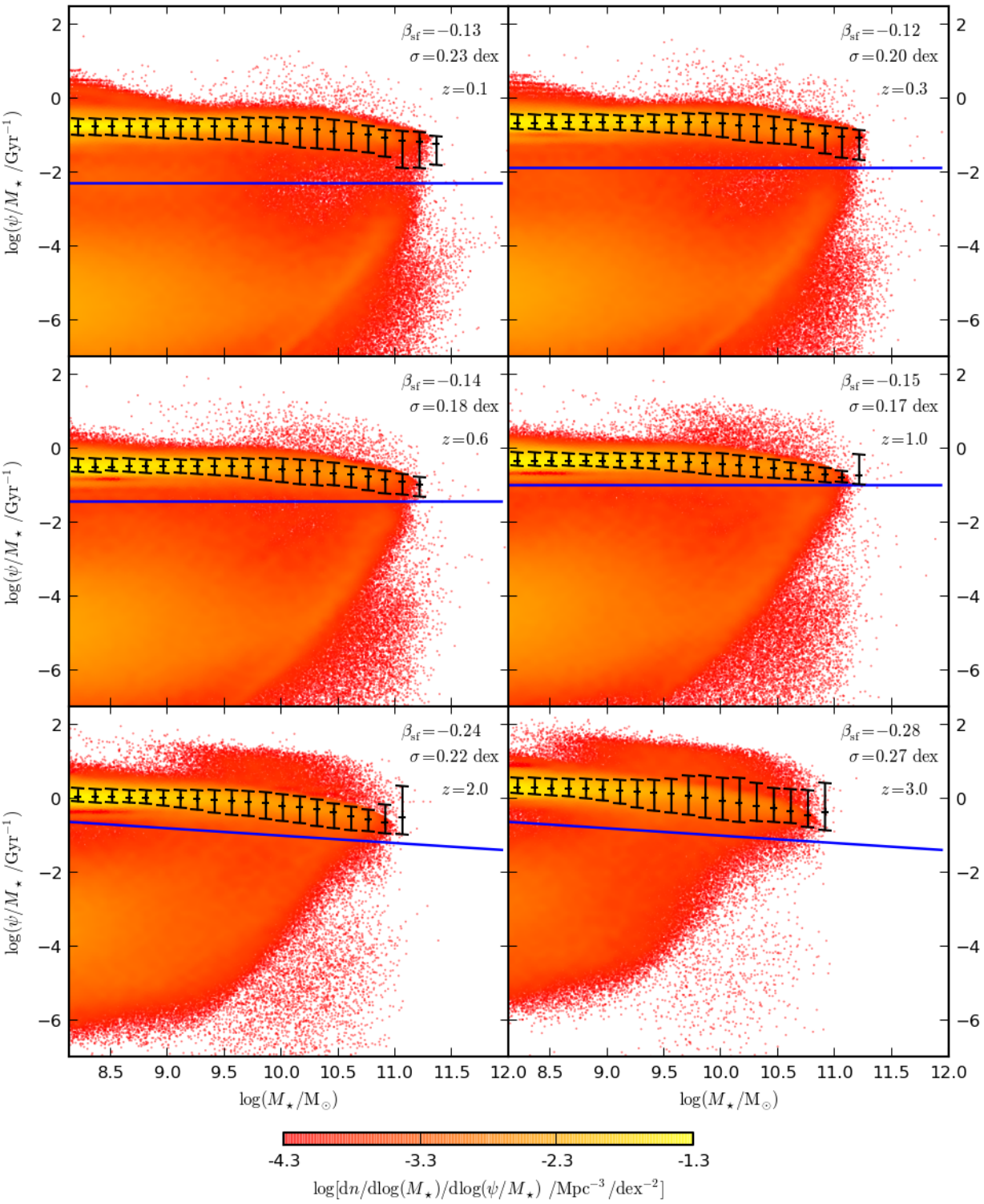


Figure 4.1: Caption continued on the following page.

Figure 4.1: Specific star formation rate plotted as a function of stellar mass for all galaxies from our fiducial GALFORM model. Each panel corresponds to a different redshift as labelled. The coloured points represent individual model galaxies and the point colours are scaled logarithmically with the local number density of galaxies in each panel, from red at low density to yellow at high density. The corresponding number densities are indicated by the colour bar at the bottom of the figure. The blue lines show our cut between star forming and passive galaxies for each redshift. The black points and corresponding error bars show the median, $10^{\rm th}$ and $90^{\rm th}$ percentiles of the distribution in the specific star formation rates of star forming galaxies, binned as a function of stellar mass. $\beta_{\rm sf}$ is the slope of a power-law fit to the medians of the distribution for star forming galaxies. $\sigma$ quantifies the average scatter and is defined as half of the mean central $68\%$ range of the distribution for star forming galaxies.

vidual galaxies as points, coloured by the logarithmic density of points at a given position in the plane. For reference, the number of galaxies shown in each redshift panel is of order $10^6$. The most obvious feature that can be seen in Fig. 4.1 is a strong sequence of star forming galaxies that extends over several decades in stellar mass. Outliers that reside above this sequence do exist but are rare, becoming slightly more prevalent towards higher redshifts. Passive galaxies reside below the sequence, with a broad distribution of specific star formation rates at a given stellar mass.

For the remainder of this study, we choose to focus on the star forming galaxies that reside either on or above the star forming sequence. We separate passive galaxies by applying a power-law cut that evolves with redshift. The division is shown as solid blue lines in Fig. 4.1. The exact position and slope of the power-law cuts are fixed by hand in order to best separate the star forming sequence from the locus of passive galaxies that can be seen stretching diagonally across the plane for the most massive passive galaxies at lower redshifts. Although this is a subjective process, we find that our results are, in general, insensitive to the precise location of the cut because of the strong bimodality in the distribution. This is demonstrated by the fact that the $10^{\rm th}$ percentiles of the distribution of star forming galaxies do

not reside close to our dividing line between star forming and passive galaxies in most cases. The exception to this is seen at $z = 1$ where the locus of massive passive galaxies joins onto the star forming sequence, making it difficult to objectively separate star forming from passive galaxies at $M_\star \approx 10^{11}\mathrm{M}_\odot$.

To characterise the slope and normalisation of the star forming sequence seen in Fig. 4.1, we adopt the convention from Karim et al. (2011) who use a power-law fit of the following functional form,

$$\psi/M_\star = c \left( \frac{M_\star}{10^{11}\mathrm{M}_\odot} \right)^{\beta_{\mathrm{sf}}}, \tag{4.4}$$

where $\beta_{\mathrm{sf}}$ is the slope of the sequence and $c$ sets the normalisation. We also define the scatter in the star forming sequence, $\sigma$, as half of the mean value over stellar mass bins of the central $68\%$ range in the distribution of $\log_{10}(\psi/M_\star/\mathrm{Gyr}^{-1})$, calculated for each bin in stellar mass. The scatter, $\sigma$, and best fitting power-law slope, $\beta_{\mathrm{sf}}$, to the star forming sequence are labelled for each panel shown in Fig. 4.1. We find that the slope steepens from $\beta_{\mathrm{sf}} \approx -0.13$ at $z \leq 1$ up to $\beta_{\mathrm{sf}} = -0.28$ at $z = 3$. This range of slopes lies comfortably within the range of slopes that are reported by observational studies (see Appendix B). The mean scatter, $\sigma$, does not vary strongly with redshift below $z = 3$ and is typically $\approx 0.2\,\mathrm{dex}$. The increase to $0.27\,\mathrm{dex}$ at $z = 3$ can be attributed to an increased abundance of outlying galaxies that reside above the star forming sequence at this redshift. Finally, we note that the normalisation of the star forming sequence can be seen to increase by roughly an order of magnitude over $0 < z < 3$. We explore this in greater depth in Section 4.3.3.

Compared to the results reported for the model from Dutton et al. (2010), the star forming sequence predicted by our fiducial model has a larger intrinsic scatter by $\Delta\sigma \approx 0.1\,\mathrm{dex}$. Dutton et al. (2010) explain that they expect their model to underpredict the scatter because their model features a simplified treatment of the mass assembly histories of dark matter haloes, neglecting various aspects of the hierarchical galaxy formation process that are included in GALFORM. On the other hand, we note that the hydrodynamical simulations presented in Torrey et al. (2014) and Obreja et al. (2014) predict a larger scatter of $\approx 0.3\,\mathrm{dex}$. This could reflect a failing of

the simplified treatment of physical processes used in GALFORM when compared to a full hydrodynamical simulation. The larger scatter reported by Torrey et al. (2014) is consistent with the upper limit on the intrinsic scatter typically reported from observational studies (e.g Noeske et al., 2007b; Whitaker et al., 2012) but it is difficult to accurately assess the true uncertainty on the star formation tracers used in these studies. For the purposes of this study, the scatter in our model is small enough to be consistent with the observational upper limit and from here on, we focus instead on the slope and normalisation of the star forming sequence.

Compared to our fiducial model, the slope of the star forming sequence decreases more slowly with redshift in the Dutton et al. (2010) model, varying from $\beta_{\rm sf} = -0.04$ at $z = 0$ to $-0.1$ at $z = 3$. This slope is slightly shallower than predicted by our fiducial model. This could potentially be explained by the lack of any quenching or starburst processes in the Dutton et al. (2010) model. The slope of $-0.2 < \beta_{\rm sf} < -0.1$ predicted by the model presented in Lamastra et al. (2013) is consistent with our fiducial model although this somewhat unsurprising given the many similarities between the two models. On the other hand, the hydrodynamical simulations presented in Torrey et al. (2014) report a slope of $-0.05 < \beta_{\rm sf} < 0.0$ which is more similar to Dutton et al. (2010). Obreja et al. (2014) also find a slope consistent with $\beta_{\rm sf} = 0$.

### 4.3.2 The star forming sequence inferred from observations

For this study, we have compiled a set of observational data on the star forming sequence for the purposes of providing a comparison with model predictions. Specifically, we have compiled the average specific star formation rate of star forming galaxies for bins of stellar mass and redshift. Both mean and median star formation rates have been used to quantify the average in the literature and we include both quantities in the compilation. The list of sources used in the compilation is presented in Table 4.1. We include information on the redshift range covered, the initial selection technique, the technique to separate star forming galaxies and the star formation rate tracer used. We only include observational data sets that have

| Source | Redshift | Selection | SF cut | Tracer |
|---|---|---|---|---|
| Noeske et al. (2007a) | 0.2-1.1 | K | blue colour/$24\mu$m detection | $24\mu$m+UV/Em Lines |
| SDSS DR7 | 0.08 | r | sSFR-$M_\star$ distribution | $H_\alpha$ |
| Pannella et al. (2009) | 1.5-2.5 | BzK | sBzK | Radio |
| Oliver et al. (2010) | 0-2 | Optical | template fitting | $70/160\mu$m |
| Magdis et al. (2010) | 3 | LBG | blue colour | UV (corrected) |
| Peng et al. (2010) | 0-1 | Optical | blue colour | SED fitting |
| Rodighiero et al. (2010) | 0-2.5 | $4.5\mu$m | blue colour/$24\mu$m detection | FIR |
| Karim et al. (2011) | 0.2-3 | $3.6\mu$m | blue colour | Radio |
| Huang et al. (2012) | 0 | HI / r | HI detection/blue colour | SED fitting |
| Lin et al. (2012) | 1.8-2.2 | BzK | sBzK | UV (corrected) |
| Reddy et al. (2012) | 1.4-3.7 | LBG | blue colour | $24\mu$m+UV |
| Whitaker et al. (2012) | 0-2.5 | K | (U-V/V-J) cut | $24\mu$m+UV |
| Bauer et al. (2013) | 0.05-0.32 | r | $H_\alpha$ flux/$EW$ | $H_\alpha$ |
| Stark et al. (2013) | 4-7 | LBG | blue colour | UV (corrected) |
| Wang et al. (2013) | 0.2-2 | K | SFR-$M_\star$ distribution | SED fitting / FIR |
| González et al. (2014) | 4-6 | LBG | blue colour | SED fitting |

Table 4.1: List of the sources of the observed average specific star formation rates of star forming galaxies, $\langle\psi/M_\star\rangle(M_\star, z)$, which we extract from the literature. We list the source, redshift range or median redshift, galaxy selection technique, the subsequent star forming galaxy selection technique, and the tracer used to estimate the instantaneous star formation rate. For LBG-selected samples, it should be noted that the initial galaxy selection technique is strongly biased towards blue star forming galaxies, so typically no additional cut to separate star forming galaxies is performed. SDSS DR7 data corresponds to an update of the Brinchmann et al. (2004) analysis. For Karim et al. (2011), we use both the star forming galaxy sample presented in their Table 3 as well as the "active population" which is shown in their Figure 13 (which uses a bluer colour cut).

either made an attempt to separate star forming galaxies from passive galaxies or have a selection function which intrinsically selects only actively star forming objects. Where necessary, we convert stellar masses quoted that assume a Salpeter IMF by $\Delta \log(M_\star/\mathrm{M}_\odot) = -0.24\,\mathrm{dex}$ in order to be consistent with a Chabrier IMF (Ilbert et al., 2010), which in turn is very similar to the Kennicutt IMF that is assumed in our model. We do not attempt to correct specific star formation rates for IMF variations as we expect both the stellar mass and star formation rate corrections to approximately cancel in most cases.

It is very important to be aware that the average star formation rate, particularly for large stellar masses at low redshift, will depend strongly on the method used to separate star forming from passive galaxies. In general, it is not possible in practice to simply make the separation based on identifying the star forming sequence in the star formation rate versus stellar mass plane. This is only really possible in the local Universe with surveys such as the SDSS. Instead, star forming galaxies are often separated using colour selection criteria (e.g. Daddi et al., 2004; Ilbert et al., 2010). These issues are particularly pertinent for studies that employ stacking techniques, where it is impossible to ascertain whether a star forming sequence is really present in the data (Oliver et al., 2010; Rodighiero et al., 2010; Elbaz et al., 2011; Karim et al., 2011).

### 4.3.3 Comparing the star forming sequence from GALFORM with observational data

Fig. 4.2 shows the average specific star formation rates of star forming galaxies as a function of stellar mass for a selection of redshifts. Observational data from the compilation presented in Table 4.1 are shown in grey and can be compared to the mean and median relations predicted by the our fiducial model. It should be noted that the error bars on the observational data points show only a lower limit on the statistical uncertainty on each data point. These error bars are only shown for the studies where an estimate of this lower limit could be obtained. The error

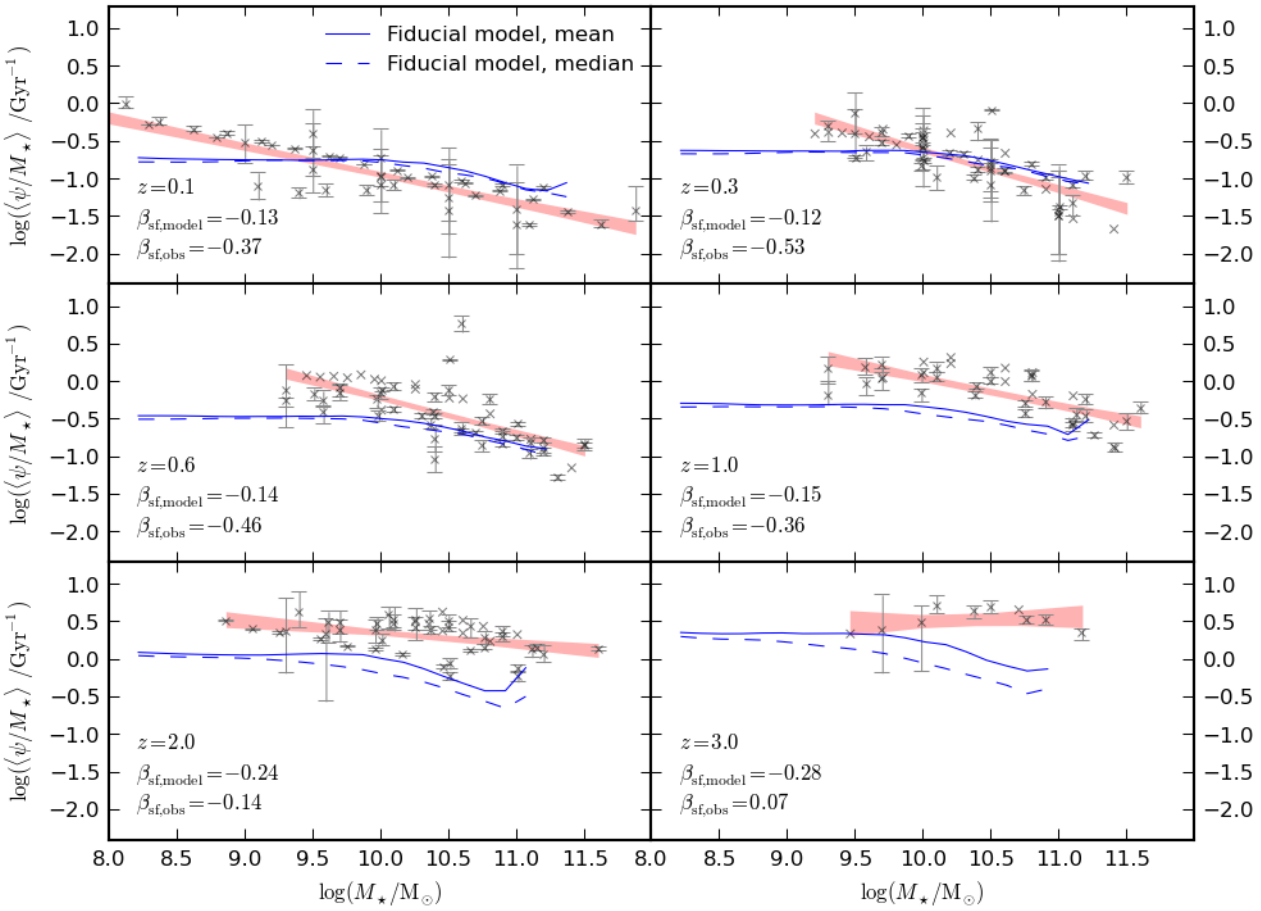


Figure 4.2: The average specific star formation rate of star forming galaxies plotted as a function of stellar mass. Each panel corresponds to a different redshift as labelled. Blue solid and dashed lines show predictions from our fiducial GALFORM model for the mean and median specific star formation rates respectively. Grey points show observational estimates of either the mean or median average specific star formation rate of star forming galaxies. A list of the sources of these observational data points is presented in Table 4.1. When shown, the corresponding error bars show a lower limit on the statistical uncertainty on the average for each data point. The shaded region shows the $1\sigma$ range of power-law fits to the observational data, using a fixed error on the data points of $0.20\,\mathrm{dex}$. $\beta_{\rm sf,model}$ is the best fitting power-law slope to the medians of the distribution predicted by our fiducial model. $\beta_{\rm sf,obs}$ is the best fitting power-law slope to the observational data presented in each panel.

bars do not represent the dispersion in the underlying distribution. We attempt to estimate a more realistic uncertainty on the average specific star formation rate by measuring the average central $68\%$ range for measurements in all stellar mass bins containing more than two data points. We find that the uncertainty on the specific star formation rate estimated in this way is $0.20\,\mathrm{dex}$. The pink shaded regions shown in Fig. 4.2 then enclose the set of best fitting power laws to the data within a $1\sigma$ range, assuming $0.2\,\mathrm{dex}$ errors in each mass bin.

Given the large systematic uncertainties that are thought to affect stellar mass and SFR estimates and that each data set uses a different method to select star forming galaxies, it is reassuring that the observational data are fairly self consistent in normalisation within each respective redshift panel. There are some outlying data sets however. In general, the observations seem consistent with a star forming sequence where the average specific star formation rate is modestly anti-correlated with stellar mass. We note however that there are significant variations in the slope seen between different redshift panels. The best fitting power-law slopes at each redshift vary from $\beta_{\mathrm{sf}} \approx -0.4$ at $z = 0$ to $\beta_{\mathrm{sf}} \approx 0.1$ at $z = 3$. Whether or not this variation is driven by an intrinsic shift in the slope of a star forming sequence of galaxies is extremely unclear. We explore this issue in more detail in Appendix B.

Comparison of the observed slope with predictions from our fiducial model indicate that the model has a slope which is too shallow at low redshift and too steep at high redshift. In addition, compared to the data, the slope variation with redshift acts in the opposite direction in the model, such that the high redshift slope is steeper than the local relation. However, it is difficult to be confident whether this truly reflects a flaw in the model or can be explained as a result of selection effects. To answer this question satisfactorily would require a self-consistent comparison between the model and the data in terms of selection. However, this task is made challenging because of the difficulty in predicting accurate colour distributions for galaxies from hierarchical galaxy formation models. Historically, various GALFORM models have struggled to reproduce the observed colour distributions of galaxies, making it difficult to reproduce observational colour cuts in detail (e.g.

Guo et al., 2013a).

Although it is difficult to draw strong conclusions from comparing the slopes of the observed and predicted distributions, it is apparent that the normalisation of the star forming sequence evolves more rapidly in the observational data than in the model. This problem is best viewed by plotting the evolution of the average specific star formation rate of star forming galaxies as a function of lookback time for selected stellar mass bins, which we show in Fig. 4.3. In general, we find that the observational data are consistent with exponential evolution in $\langle \psi / M_{\star} \rangle$ with lookback time. The best fit to the observational data in each panel gives $\langle \psi / M_{\star} \rangle \propto e^{a\, t_{\rm lb}}$ where $a$ is found to vary between $0.29$ and $0.43$. The variation in $a$ is such that the average specific star formation rate drops more rapidly with time in the highest mass bins shown. Although there is some scatter at a given redshift, the data within each mass bin appear to be mostly self consistent in normalisation at a given redshift. Repeating the same process as for Fig. 4.2, we estimate the uncertainty on the average specific star formation rates and again find that the uncertainty is approximately $0.20\,{\rm dex}$.

In contrast to the trend that emerges from the observational compilation, our fiducial model (blue lines) predicts slower evolution than the data (until higher redshifts, where the evolution in the model becomes steeper than an extrapolation of the trend seen in the data). This behaviour has been seen for various published models in the literature (e.g. Davé, 2008; Damen et al., 2009; Dutton et al., 2010; González et al., 2014; Torrey et al., 2014) and the origin of the discrepancy is the subject of the remainder of this Chapter. Finally, at this stage we note that the evolution in the fiducial GALFORM model scales very closely with the inverse of the age of the universe at a given time, $t_{\rm age}$. We return to this point in Section 4.4.2.

## 4.4 The stellar mass assembly of star forming galaxies

It is clear from Fig. 4.3 that the specific star formation rates of galaxies at a fixed stellar mass evolve more slowly with redshift in our fiducial GALFORM model than

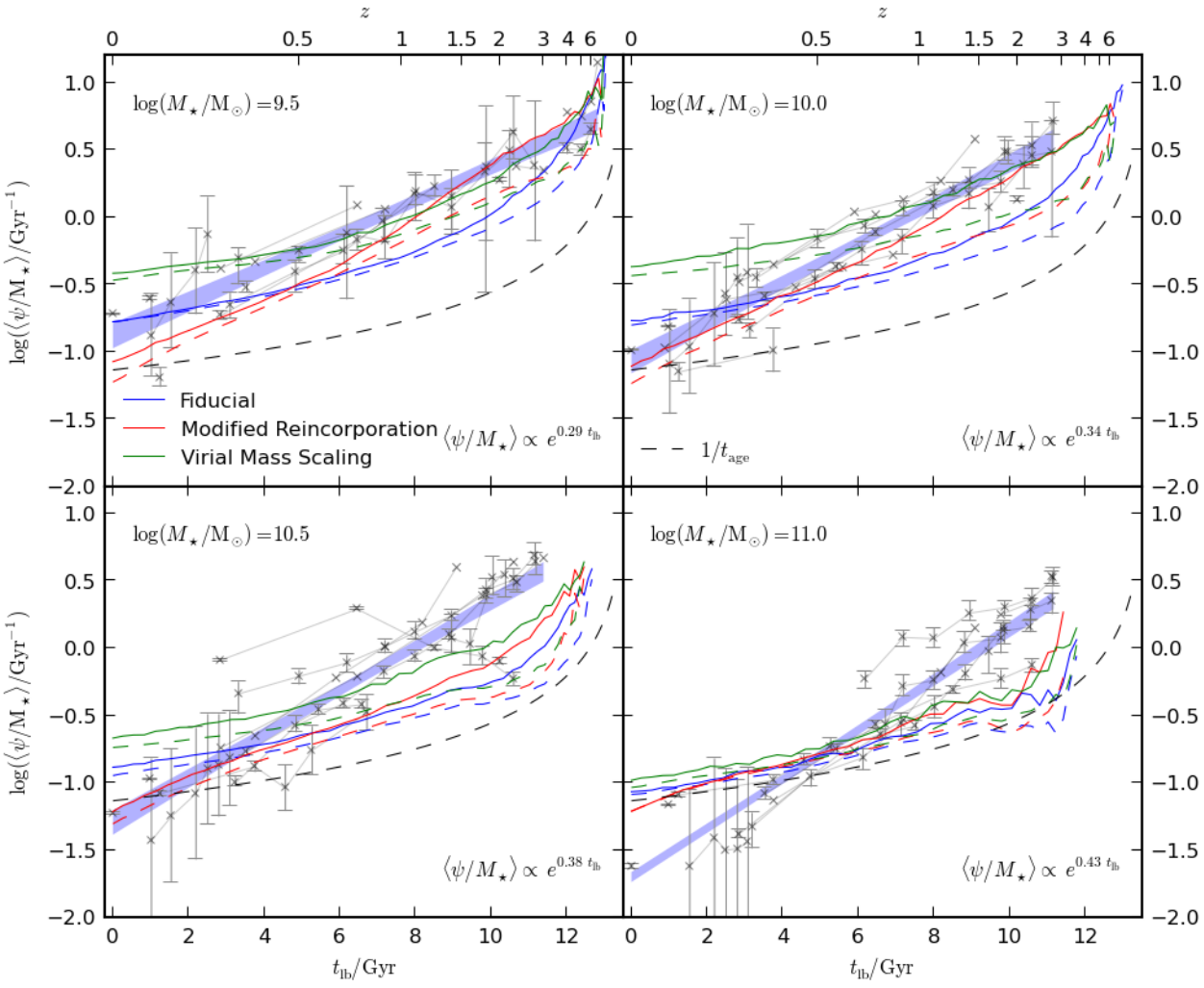


Figure 4.3: The average specific star formation rate of star forming galaxies plotted as a function of lookback time. Each panel corresponds to a different stellar mass bin as labelled. Blue solid and dashed lines show predictions from our fiducial GALFORM model for the mean and median specific star formation rates respectively. Red lines show the same information but for the modified reincorporation model. Green lines show the same information but for a model using the virial mass scaling for the reincorporation timescale proposed by Henriques et al. (2013). Dashed black lines show the inverse of the age of the universe as a function of lookback time. Caption continued on the following page.

Figure 4.3: Grey points show observational estimates of either the mean or median average specific star formation rate of star forming galaxies. A list of the sources of these observational data points is presented in Table 4.1. When shown, the corresponding error bars show a lower limit on the statistical uncertainty on the average for each data point. Grey points taken from a single observational study are connected by grey lines. The blue shaded region shows the $1\sigma$ range of exponential fits to the observational data, assuming a fixed error on the data points of $0.20\,\mathrm{dex}$. This shaded region is consistent with, but not identical to, the pink shaded region shown in Fig. 4.2. The best fit to the evolution in the observational data is given in each panel.

is implied by the observational data. However, it should be noted that the galaxy population which is probed at each redshift for a given stellar mass bin will not be the same; star forming galaxies grow in stellar mass before becoming quenched and consequently dropping out of the star forming samples which we consider. This complicates the interpretation of Fig. 4.3 with regard to understanding the physical origin of any flaws in the model.

It is therefore worthwhile to search for a another way to characterise the evolution of star forming galaxies which traces only a single population across cosmic time. One way to achieve this is to try to infer the stellar mass assembly histories of star forming galaxies by tracing how they grow in stellar mass as they evolve along a star forming sequence. This technique has already appeared in various guises in the literature (e.g. Drory & Alvarez, 2008; Renzini, 2009; Leitner & Kravtsov, 2011; Leitner, 2012; Heinis et al., 2014). From here on in, we adopt the terminology of Leitner (2012) and refer to this technique as Main Sequence Integration (MSI).

In this section, we explore the origin of the discrepancy between the predicted and observed evolution in the specific star formation rates of star forming galaxies shown in Fig. 4.3 We start by making use of the MSI technique to compare the predicted and observationally inferred stellar mass assembly histories of galaxies that are still star forming at $z = 0$. We then go on to discuss why the predicted stellar mass assembly histories have a particular form, connecting the halo assembly process with the way stellar feedback is implemented in our model.

An introduction to the MSI technique is presented in Appendix B.1. An exploration of how well MSI can recover the predicted stellar mass assembly histories calculated in our model can be found in Appendix B.2. Details of the observational compilation of measurements of the star forming sequence which we use for this study can be found in Appendix B.3.

### 4.4.1 Comparing the inferred stellar mass assembly histories of star forming galaxies with model predictions

In Fig. 4.4, we compare the predicted average stellar mass assembly histories of central galaxies that are still star forming at $z = 0$ from our fiducial GALFORM model with the results of applying MSI to the observational compilation presented in Appendix B.3. To facilitate a comparison with the average stellar mass assembly histories obtained using the MSI technique for a given starting mass, model galaxies are binned by their stellar mass at $z = 0$. By default in this study, stellar mass assembly histories are obtained by tracing back the main stellar progenitor of each $z = 0$ central star forming galaxy. We define the main stellar progenitor as the most massive stellar progenitor traced between each consecutive pair of output times. The impact of this choice (as compared to summing over all possible progenitors) is discussed in Appendix B.2. We have chosen to plot $\langle \dot{M}_\star / M_\star(t_0) \rangle$ in order to eliminate dispersion associated with the finite width of the stellar mass bins which we use ($\Delta \log(M_\star / \mathrm{M}_\odot) = 0.5\,\mathrm{dex}$). The remaining dispersion therefore reflects the intrinsic scatter in our model in the shape of stellar mass assembly histories of galaxies that are central and star forming at $z = 0$. The choice to include only galaxies that are central at $z = 0$ is made in order to minimise the impact of any environmental effects. When comparing to mass assembly histories inferred from observations (which include a combination of satellite and central galaxies), the exclusion of satellite galaxies is justified by observational results that indicate that the form of the star forming sequence is independent of environment (e.g. Peng et al., 2010).

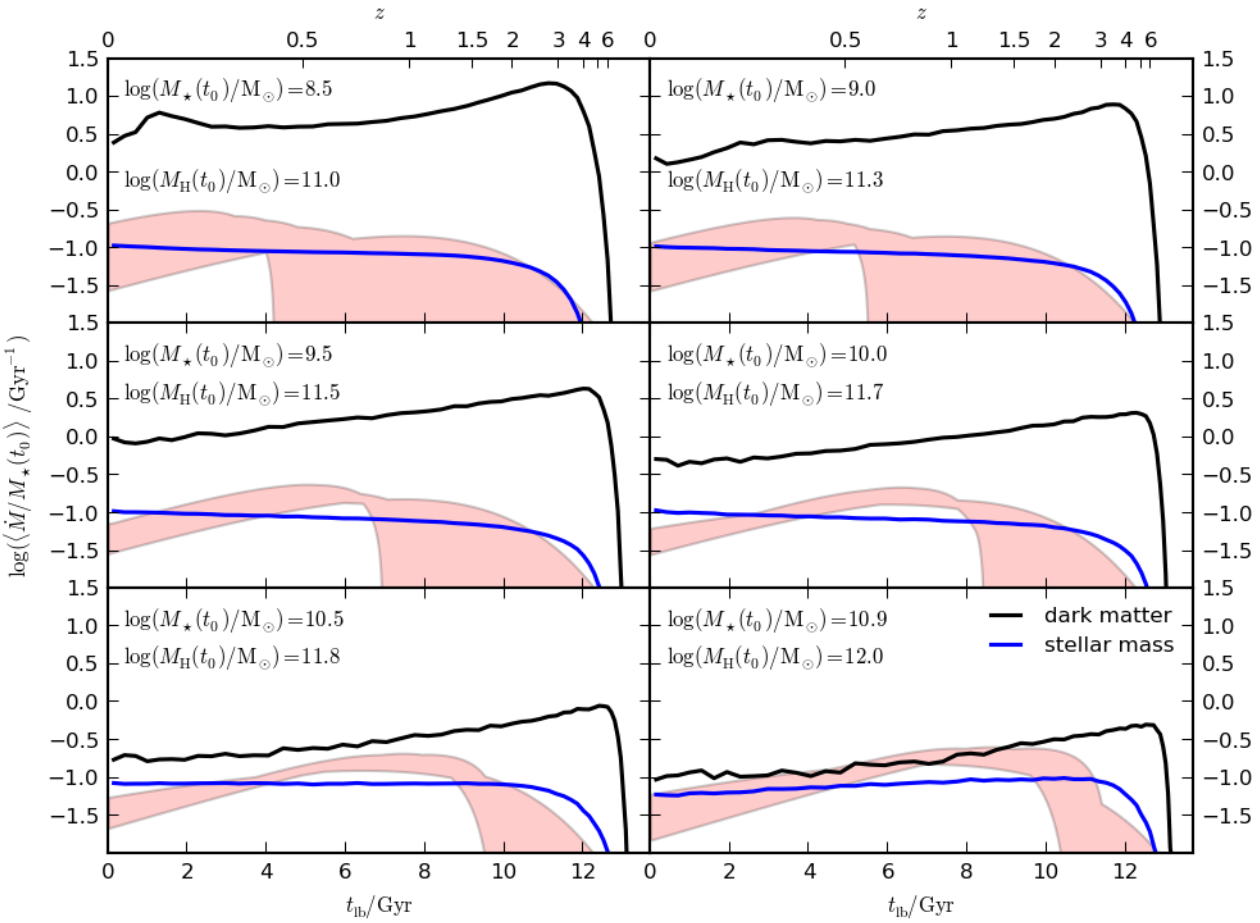


Figure 4.4: The mean mass assembly histories of galaxies that are central and star forming at $z = 0$, plotted as a function of lookback time. Blue lines show predictions for the mean stellar mass assembly histories for the main stellar progenitors of central galaxies, taken directly from our fiducial GALFORM model. Black lines show the corresponding dark matter halo mass assembly histories of the progenitor haloes that host the main stellar progenitors of central galaxies at $z = 0$. These curves are rescaled by $f_{\rm b} \equiv \Omega_{\rm b}/\Omega_{\rm M}$ to show the baryonic accretion rate onto these haloes. Model galaxies are binned by their stellar mass at $z = 0$, with each panel corresponding to a different mass bin. The median $z = 0$ stellar mass in each bin is labelled in each panel. The corresponding median $z = 0$ dark matter halo mass in each stellar mass bin is also labelled. The filled pink region shows the range of stellar mass assembly histories that are inferred by applying the MSI technique to observational data from the literature.

Quantitatively, the model predicts stellar mass assembly rates that are broadly consistent to within factors of 2 compared to the data. However, despite the weak constraints provided by MSI in some cases, there is a clear qualitative disagreement between the model and the data regarding the shape of the stellar mass assembly histories predicted by GALFORM. In the model, the rate of star formation rises rapidly at early times before slowing down to a gradual rise or to a constant level of activity at later times. The observational data instead favours a scenario where star formation activity builds towards a peak at an intermediate time before dropping significantly towards $z = 0$. This disagreement is consistent with the trend seen in Fig. 4.3 where the specific star formation rates of galaxies in the model are too low compared to the data at intermediate times before rapidly rising towards high redshift.

At this stage, it should be noted that our fiducial model is only one specific realisation of GALFORM with regard to the various model parameters that can be changed. While these parameters are constrained by requiring that the model matches local global diagnostics of the galaxy population, it is important to understand whether the disagreement between predictions and data seen in Fig. 4.3 and Fig. 4.4 is specific to the combination of parameters used in our fiducial model. An analysis of this issue is presented in Appendix C. To summarise, we find that for a given stellar mass at $z = 0$, the shapes of the average stellar mass assembly histories of central star forming galaxies in GALFORM are almost entirely invariant when changing model parameters relating to star formation, feedback and gas reincorporation. As a consequence, the disagreements seen in Fig. 4.3 and Fig. 4.4 do indeed seem to be generic for any model that uses the same parametrisations to represent these physical processes. This also helps to explain why similar models find a similar disagreement in other studies.

As well as stellar mass assembly histories, we also show in Fig. 4.4 the corresponding average dark matter halo mass assembly histories of central galaxies from our fiducial GALFORM model that are star forming at $z = 0$. We choose to define the dark matter halo mass assembly rate, $\dot{M}_{\rm H}$, by tracing backwards the host

halo of the main stellar progenitor (see Appendix B.2). This definition is useful for making comparisons with the stellar mass assembly process. However, it should be noted that in some cases this definition could deviate from the standard definition of halo mass assembly histories where instead the main halo progenitor is traced backwards (e.g Fakhouri et al., 2010). To quantify the average halo mass assembly rate, we take the mean of the distribution at each lookback time. This choice is made because the individual halo assembly histories are very stochastic with respect to our temporal resolution (which is determined by the number of available outputs from the Millenium simulation). As a consequence, we find that only the mean halo mass assembly history integrates to the correct average halo mass at $z = 0$ while the median does not. Incidentally, this stochasticity is why even the average halo mass assembly histories shown in Fig. 4.4 get visibly noisy towards late times due to a drop in the average rate of significant accretion events.

From Fig. 4.4, we can begin to understand why there is a disagreement in the stellar mass assembly process between our fiducial GALFORM model and the trends implied by the data. In the model, despite the enormous variation in the efficiency of star formation relative to gas accretion between haloes of different mass at $z = 0$, stellar mass assembly broadly tracks the halo assembly process. Stars start to form as soon as their host haloes accrete an appreciable fraction of their final mass and this continues all the way to the present day. Differences between the stellar and halo assembly histories do exist however. For example, the stellar mass assembly histories do not show the peak at $t_{\rm lb} \approx 12\,{\rm Gyr}$ which is fairly prominent for the haloes. Also, the halo accretion rates fall slowly towards late times after this peak, whereas most star forming galaxies form stellar mass at either a constant or slightly increasing rate over their lifetimes. However, the decline in the halo mass accretion rates is generally not as steep as the rate of decline in star formation rates inferred from the observational data. This can be seen more clearly in Fig. 4.5 where we show the ratio of the rates of mean stellar mass assembly to halo mass assembly.

In order to broadly reproduce the observed $z = 0$ stellar mass or luminosity functions, it is necessary that a given galaxy population model, on average, places

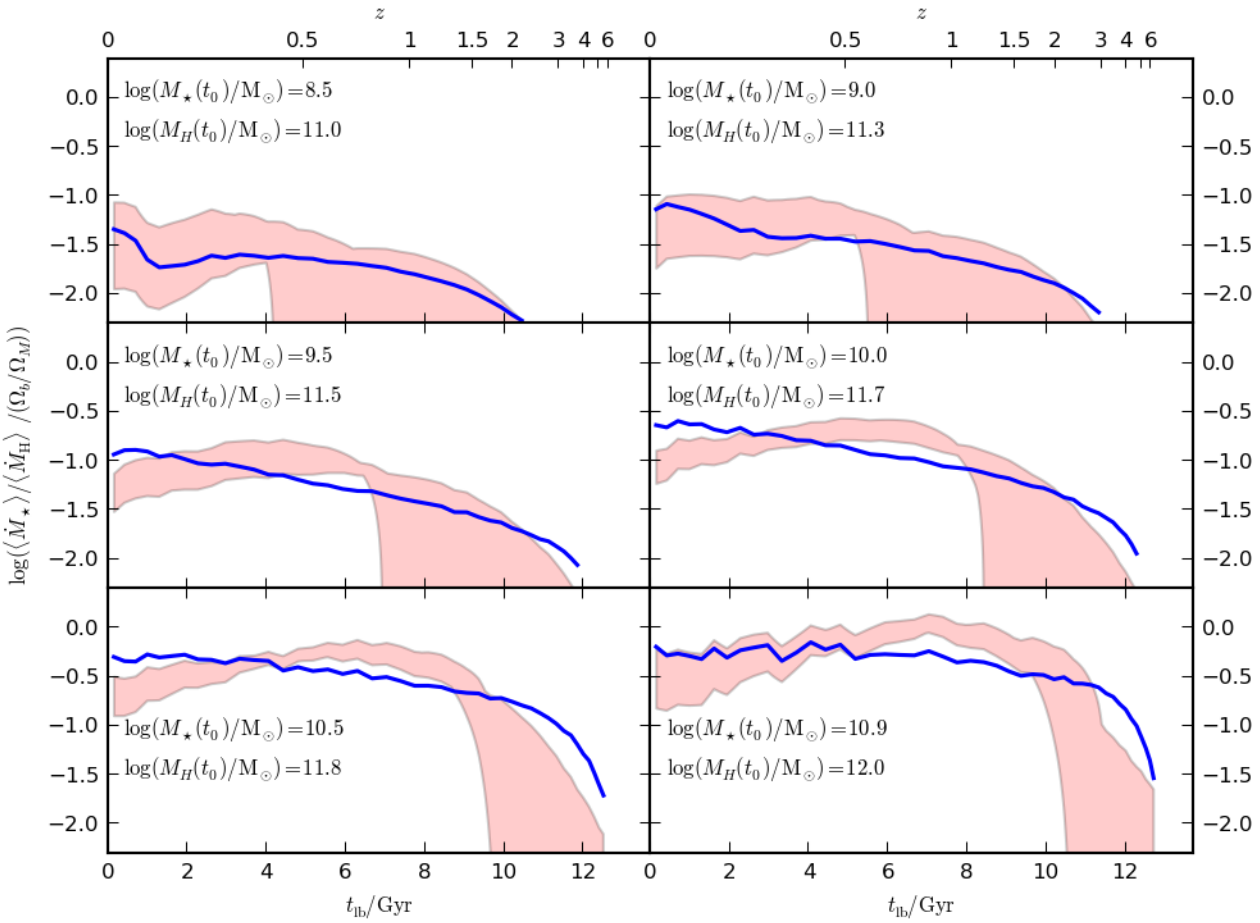


Figure 4.5: The ratio of mean stellar mass assembly rate to mean baryonic halo mass assembly rate for galaxies that are star forming at $z = 0$, plotted as a function of lookback time. Blue lines show predictions from our fiducial GALFORM model for this ratio for galaxies that are central at $z = 0$. Model galaxies are binned according to their $z = 0$ stellar mass with each panel corresponding to a different mass bin. The median $z = 0$ stellar mass in each bin is labelled in each panel. The corresponding median $z = 0$ dark matter halo mass of each stellar mass bin is also labelled. The filled pink regions show the range in the ratio of galaxy to halo mass assembly rates inferred from observational data. This is obtained using a combination of stellar mass assembly histories inferred from observational data using the MSI technique and average halo mass assembly histories from GALFORM. This assumes that the true ratio between stellar mass and halo mass at $z = 0$ is the same as in our fiducial GALFORM model.

galaxies of a given stellar mass inside haloes of the mass corresponding approximately to the correct abundance. Given that our fiducial GALFORM model roughly reproduces the local stellar mass function, the halo assembly histories shown in Fig. 4.4 should therefore correspond roughly to the true halo formation histories of real galaxies, for the case of a $\Lambda$CDM universe. Adopting this as a working assumption, we also show in Fig. 4.5 the efficiency of star formation inferred from observations using MSI if we use the relationship between stellar mass and halo mass at $z = 0$ for star forming galaxies in our model. This extra step allows us to infer how efficiently haloes that host star forming galaxies at $z = 0$ convert accreted baryons into stars. It can be seen that in the model, the efficiency of star formation relative to halo gas accretion rises monotonically from early times to the present day, whereas the data, in general, favours a scenario where this efficiency peaks at some intermediate time for the higher stellar mass bins.

In Appendix B.3, we discuss how, depending on the slope of the observed star forming sequence, $\beta_{\rm sf}$, the inferred stellar mass assembly of galaxies that are still star forming at $z = 0$ can show a downsizing trend, such that the lower mass star forming galaxies start forming stars later with respect to massive star forming galaxies. Fig. 4.4 shows that any possible downsizing trend suggested by the data is, at best, only weakly reproduced by the model. The different stellar mass assembly histories that we infer from the observational data agree best with our model for the $\beta_{\rm sf} = 0.0$ or $-0.1$ cases shown in Fig. B.5. The assembly histories derived from these bins show the weakest downsizing trend (no downsizing for $\beta_{\rm sf} = 0.0$) and form a greater fraction of stars at early times. It should be noted that the better agreement with the model for these curves is not surprising given that the slope of the star forming sequence in the fiducial GALFORM model is $\beta_{\rm sf} \approx -0.15$. For the opposite extreme case in the data where $\beta_{\rm sf} \approx -0.5$, the model predictions are in dramatic disagreement with the trends implied by the data for low mass galaxies.

Another consequence of a strong downsizing trend is that the stellar mass assembly process is significantly delayed relative to the halo assembly process for low mass systems. Fig. 4.4 shows that the shape of the mean halo mass assem-

bly histories is only a very weak function of the final halo mass. Therefore, any possible downsizing trend that exists purely in the star forming population would have to be caused by a physical process which is separate from the growth of the hosting dark matter haloes. For the case where $\beta_{\rm sf} \approx -0.4$, such a process would result in the existence of a population of dark haloes that have not formed any appreciable amount of stars at intermediate redshifts of $1 < z < 2$. We note that the star formation histories presented in Leitner (2012), derived by applying MSI to data from Karim et al. (2011) with $\beta_{\rm sf} = -0.35$ and from Oliver et al. (2010), would also have this consequence. Reproducing this behaviour in models or simulations would require much stronger feedback (or the inclusion of another physical mechanism with the same effect) at early times than is typically assumed for galaxies that reside within the progenitors of haloes of mass $11 < \log(M_{\rm H}(t_0)/{\rm M}_{\odot}) < 12$.

### 4.4.2 Explaining the form of stellar mass assembly histories in GALFORM

In Section 4.4.1, we show that the stellar mass assembly process in our fiducial GALFORM model broadly traces the halo mass assembly process. The closeness in this predicted co-evolution appears to be in qualitative disagreement with trends inferred from the star formation rates of galaxies inferred from observational data. This leads to the slower evolution in the predicted average specific star formation rates of star forming galaxies compared to the observational data seen in Fig. 4.3. Fig. 4.3 also demonstrates that this evolution in the model closely traces the inverse of the age of the universe, $t_{\rm age}$, such that $\psi/M_{\star} \propto 1/t_{\rm age}$. We now consider why the model behaves in this way.

*i) Cooling timescale:* For the star forming galaxy population which we consider in this study, we expect the radiative cooling timescales for shock heated halo gas to cool onto galaxy disks to be short compared to the age of the Universe at a given epoch. In the top panel of Fig. 4.6, we see that this is indeed the case if we trace backwards the main stellar progenitors of galaxies that are central and star forming

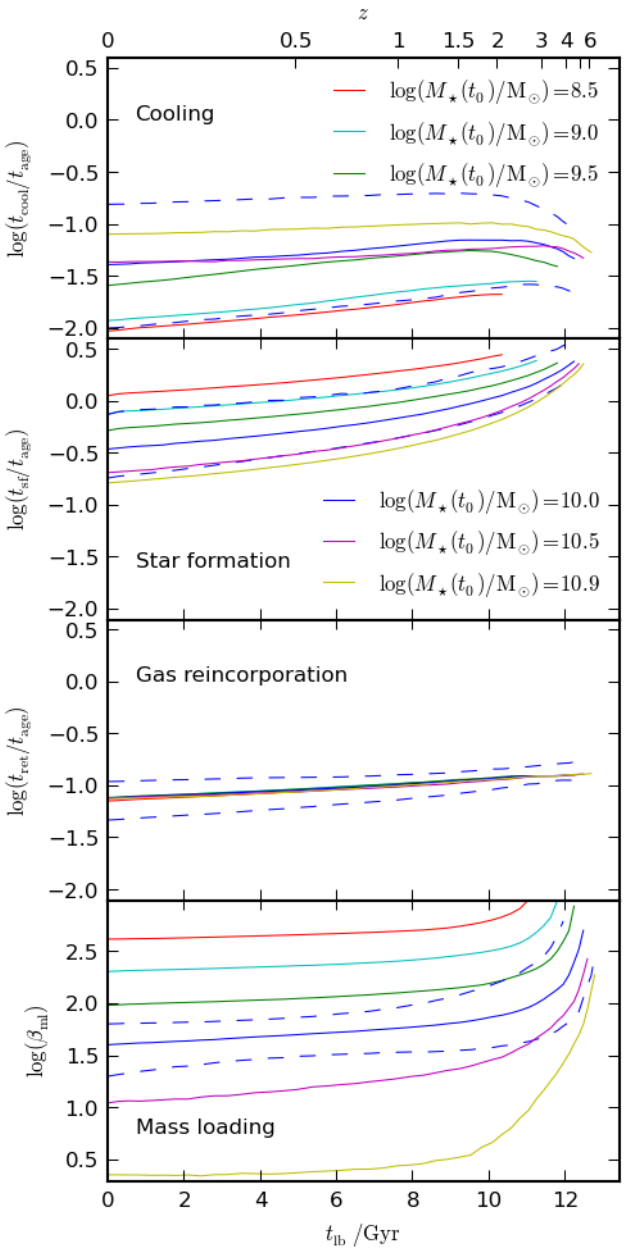


Figure 4.6: The ratio of average characteristic timescales of model galaxies which are central and star forming at $z = 0$ to the age of the universe, $t_{\rm age}$, plotted as a function of lookback time. Model galaxies are binned according to their $z = 0$ stellar mass with each solid coloured line showing the median of the distribution for a different bin. The blue dashed lines show the $10^{\rm th}$ and $90^{\rm th}$ percentiles for the $\log(M_\star(t_0)/{\rm M}_\odot) = 10$ bin. Caption continued on the following page.

Figure 4.6: The top three panels each correspond to a different timescale. The bottom panel instead shows the efficiency with which gas is ejected from galaxy disks. *Top:* The characteristic gas cooling timescale, $t_{\rm cool}$, for hot halo gas to cool onto a galaxy disk. *Second:* The characteristic star formation timescale, $t_{\rm sf}$, for disk gas to be converted to stars in the absence of feedback. *Third:* The characteristic gas reincorporation timescale, $t_{\rm ret}$, for gas ejected by feedback to be reincorporated back into the hot gas halo. *Bottom:* The mass loading factor of outflows, $\beta_{\rm ml}$.

at $z = 0$, following the methodology introduced in Section 4.4.1. We define the characteristic cooling timescale, $t_{\rm cool}$, as the time for gas with the mean density within the virial radius to cool. Given that this timescale is short, the only three remaining physical processes in the model which are relevant for the star forming galaxy population considered here are star formation, outflows triggered by SNe feedback and the subsequent reincorporation of ejected gas back into the hot halo gas component.

*ii) Star formation timescale:* The efficiency of star formation can be characterised by the timescale required to consume cold disk gas in the absence of feedback. This is given by $t_{\rm sf} \equiv M_{\rm cold}(t)/\psi(t)$. We show the average evolution in this quantity for the star forming population in the second panel of Fig. 4.6, relative to the age of the universe at a given epoch. It can be seen that this timescale is typically comparable to the age of the universe, although there is an order of magnitude variation depending on the time and final stellar mass of the galaxies being considered. The consequence of the balance between the star formation timescale and the age of the Universe is that cooling gas can be effectively converted into stars in a quasi-steady state. In practice, the true gas depletion timescale will be significantly shorter than $t_{\rm sf}$ in the model when the mass loading factor of outflows, $\beta_{\rm ml}$, rises above unity, which is typically the case for the galaxies considered here.

*iii) Mass loading factor:* In our model, the efficiency of SNe feedback in ejecting cold gas from galaxies is characterised by the mass loading factor, $\beta_{\rm ml}$. The average evolution in $\beta_{\rm ml}$ is shown in the bottom panel of Fig. 4.6. As described in Section 4.2.1, $\beta_{\rm ml}$ in our fiducial GALFORM model scales $\propto V_{\rm disk}^{-3.2}$, where $V_{\rm disk}$ is the

circular velocity of the galaxy disk at the half mass radius. The evolution in this quantity over the lifetime of the star forming galaxies which we consider here is very modest. In general, $V_{\rm disk}$ rises at early times before becoming almost constant at intermediate to late times. This lack of evolution in $V_{\rm disk}$ is primarily driven by the corresponding lack of evolution in the circular velocity of the host haloes at the virial radius, $V_{\rm vir}$. The strong scaling of $\beta_{\rm ml}$ with $V_{\rm disk}$ means that there is a stronger evolution in the efficiency of feedback with lookback time, particularly for massive galaxies at early times where $\beta_{\rm ml}$ grows significantly above unity. The increased feedback efficiency at early times explains why the galaxy stellar mass assembly histories do not share the peak at $t_{\rm lb} \approx 12\,{\rm Gyr}$ seen for the halo mass assembly histories shown in Fig. 4.4. At late times, $\beta_{\rm ml}$ becomes approximately constant in time for all galaxies, which will result in a fixed modulation of the efficiency in converting accreted gas into stars.

*iv) Reincorporation timescale:* It is also important to consider how efficiently gas that is ejected by feedback is able to return back into the hot gas halo. As described in Section 4.2.1, ejected gas is placed into a reservoir of mass $M_{\rm res}$. This gas then returns to the halo on a characteristic timescale given by $t_{\rm ret}(t) \equiv M_{\rm res}/\dot{M}_{\rm ret}$ (Bower et al., 2006). In GALFORM, this quantity scales $\propto t_{\rm dyn}^{-1}$ where $t_{\rm dyn}$ is the halo dynamical time (see Eqn. 4.3). We characterise the efficiency of gas reincorporation by $t_{\rm ret}/t_{\rm age}$. The average evolution in this reincorporation timescale for model galaxies that are central and star forming at $z = 0$ is shown in the third panel of Fig. 4.6. This shows that the timescale for reincorporation is close to an order of magnitude shorter than the age of the universe at all times. The timescale is also almost completely independent of the final stellar or halo mass. This is because the halo dynamical time, to first order, depends only on the current mean density of the universe. As the mean density of the universe falls with time, so does the timescale for reincorporation.

By combining the picture that is presented in Fig. 4.6 with simple arguments, we now proceed to demonstrate analytically the origin of the behaviour seen in Fig. 4.3 for the predicted evolution of the specific star formation rates of star form-

ing galaxies. Firstly, we can relate the mean density of a halo, $\bar{\rho}_{\rm H}$ to the circular velocity at the virial radius, $V_{\rm vir}$, and the virial radius, $R_{\rm vir}$, through

$$\bar{\rho}_{\rm H} = \frac{3}{4\pi}\frac{M_{\rm H}}{R_{\rm vir}^3} = \frac{3}{4\pi G^3}\frac{V_{\rm vir}^6}{M_{\rm H}^2}. \tag{4.5}$$

This can be rearranged into

$$M_{\rm H} \propto \bar{\rho}_{\rm H}^{-0.5} V_{\rm vir}^3. \tag{4.6}$$

The average density of a halo can be related to the mean density of the universe, $\bar{\rho}$, by

$$\bar{\rho}_{\rm H} = \Delta_{\rm v}\bar{\rho}, \tag{4.7}$$

where $\Delta_{\rm v}$ is the mean overdensity given by the spherical collapse model (Gunn & Gott, 1972). For the simplified case of an $\Omega_{\rm M} = 1$ universe, $\Delta_{\rm v} = 18\pi^2$ and $\bar{\rho} \propto 1/t_{\rm age}^2$. In this case, we can write

$$M_{\rm H} \propto t_{\rm age}\, V_{\rm vir}^3. \tag{4.8}$$

As discussed earlier, evolution in $V_{\rm vir}$ over the lifetime of a given galaxy is weak, particularly at intermediate to late times. We can therefore make the approximation that $V_{\rm vir}$ is constant with time, yielding

$$\dot{M}_{\rm H} \propto V_{\rm vir}^3. \tag{4.9}$$

If we temporarily ignore gas reincorporation and assume that the star formation, freefall and cooling timescales of a halo are all short, then balancing the rate of accretion of gas to star formation and gas ejection gives

$$f_{\rm b}\dot{M}_{\rm H} = \dot{M}_\star + \dot{M}_{\rm ej}, \tag{4.10}$$

where $\dot{M}_{\rm ej}$ is the rate of ejection of gas mass by feedback and $f_{\rm b}$ is the baryon fraction relative to dark matter. Eqn. 4.10 can be rewritten in terms of the dimensionless mass loading factor, $\beta_{\rm ml} = \dot{M}_{\rm ej}/\psi$, yielding

$$f_{\rm b}\dot{M}_{\rm H} = \dot{M}_{\star}\,(1+\beta_{\rm ml}/(1-R)), \tag{4.11}$$

where $R$ is the fraction of gas recycled back into the ISM as a result of stellar evolution, which is assumed to be a constant so that $\dot{M}_{\star} = (1-R)\psi$. At this stage we note that supernova feedback in our fiducial GALFORM model is parametrised as $\beta_{\rm ml} \propto V_{\rm disk}^{-3.2}$ (see eqn. 4.2). Therefore, in the regime under consideration where $V_{\rm disk}$ does not evolve with time, $\beta_{\rm ml}$ is constant. In this regime, Eqn. 4.11 can be integrated to give

$$f_{\rm b}M_{\rm H} = M_{\star}\,(1+\beta_{\rm ml}/(1-R)). \tag{4.12}$$

If we then substitute the scalings from eqns 4.8 and 4.9 into 4.12 and 4.11 and then divide 4.11 by 4.12, we find that the specific stellar mass assembly rate is given by

$$\frac{\dot{M}_{\star}}{M_{\star}} = \frac{\dot{M}_{\rm H}}{M_{\rm H}} = \frac{1}{t_{\rm age}}. \tag{4.13}$$

We note that Stringer et al. (2011) obtain the same result, where they argue that this behaviour is generic in the regime where the halo mass assembly process is approximately self-similar.

In Fig. 4.3, it can be seen that the evolution of the average specific star formation rates in our fiducial GALFORM model closely tracks the inverse of the age of the universe at a given epoch. By following the derivation of Eqn. 4.13, it can be seen that this behaviour will naturally emerge if $V_{\rm vir}$ and $\beta_{\rm ml}$ remain approximately constant with lookback time. We note that although this is true for the majority of the lifetimes of star forming galaxies in our fiducial model, Fig. 4.6 shows that the situation changes for $\beta_{\rm ml}$ at early times. This explains why the efficiency of converting accreted gas into stars, as shown in Fig. 4.5, rises rapidly at early times.

The derivation of Eqn. 4.13 ignores the reincorporation of gas after ejection by feedback. This is actually a very poor approximation given that Fig. 4.6 shows that $\beta_{\rm ml}$ is always $\gg 1$ over the lifetime of the galaxies which we consider. In addition, the bottom panel of Fig. 4.6 shows that the reincorporation timescale is typically

between a factor of $6$ and $20$ shorter than the age of the universe. Combined, these two features of the model mean that gas reincorporation will be highly significant in shaping the predicted star formation histories of star forming galaxies. Therefore, it is clear that Eqn. 4.10 needs to be modified in order to account for the fact that the gas will typically have been recycled between the galaxy disk and the halo many times before forming into stars. To incorporate this effect, Eqn. 4.10 can be rewritten as

$$f_{\rm b}\dot{M}_{\rm H} + \dot{M}_{\rm ret} = \dot{M}_{\star} + \dot{M}_{\rm ej} = \dot{M}_{\star}\,(1 + \beta_{\rm ml}/(1-R)), \tag{4.14}$$

where the rate of return of gas from a reservoir of ejected gas of mass $M_{\rm res}$ is given by $\dot{M}_{\rm ret} = M_{\rm res}/t_{\rm ret}$. For the case where $\beta_{\rm ml} \gg 1$, Eqn. 4.14 simplifies to

$$f_{\rm b}\dot{M}_{\rm H} + \dot{M}_{\rm ret} \approx \dot{M}_{\star}\frac{\beta_{\rm ml}}{1-R} = \dot{M}_{\rm ej}. \tag{4.15}$$

The gas mass in the reservoir is given by

$$M_{\rm res} = \int_0^{t_{\rm age}} \left(\dot{M}_{\rm ej} - \dot{M}_{\rm ret}\right)\,{\rm d}t. \tag{4.16}$$

For the case where the halo mass accretion rate is approximately constant over a time scale, $t_{\rm age}$, substituting Eqn. 4.15 into 4.16 yields

$$M_{\rm res} \approx \int_0^{t_{\rm age}} f_{\rm b}\dot{M}_{\rm H}\,{\rm d}t \approx f_{\rm b}\dot{M}_{\rm H}\,t_{\rm age}. \tag{4.17}$$

Therefore, in this idealised case $\dot{M}_{\rm ret}$ can be written as

$$\dot{M}_{\rm ret} = M_{\rm res}/t_{\rm ret} \approx f_{\rm b}\dot{M}_{\rm H}\,\frac{t_{\rm age}}{t_{\rm ret}}. \tag{4.18}$$

Combining Eqns 4.18 and 4.15, we find that

$$f_{\rm b}\dot{M}_{\rm H}\left(1 + \frac{t_{\rm age}}{t_{\rm ret}}\right) \approx \dot{M}_{\star}\frac{\beta_{\rm ml}}{1-R}. \tag{4.19}$$

In GALFORM, the return timescale is parametrised as

$$t_{\rm ret} = \frac{t_{\rm dyn}}{\alpha_{\rm reheat}} = \frac{1}{\alpha_{\rm reheat}}\sqrt{\frac{3}{4\pi G\bar{\rho}_{\rm H}}}, \tag{4.20}$$

where $t_{\rm dyn} = R_{\rm vir}/V_{\rm vir}$ is the dynamical timescale of the halo and $\alpha_{\rm reheat}$ is a dimensionless model parameter set to $1.26$ for our fiducial model. As before, we can use Eqn. 4.7 and adopt the case of an $\Omega_{\rm M} = 1$ universe, yielding

$$t_{\rm ret} = \frac{t_{\rm age}}{2\pi\alpha_{\rm reheat}}. \tag{4.21}$$

Examination of the bottom panel of Fig. 4.6 shows that this is a reasonable approximation. Finally, combining eqns 4.21 and 4.19 yields

$$f_{\rm b}\dot{M}_{\rm H}(1 + 2\pi\alpha_{\rm reheat}) \approx \dot{M}_{\star}\frac{\beta_{\rm ml}}{1-R}. \tag{4.22}$$

Therefore, for the idealised case where $\beta_{\rm ml} \gg 1$, $t_{\rm cool} < t_{\rm ret}$, and $\dot{M}_{\rm H}$ remaining approximately constant over a time scale, $t_{\rm age}$, then the effect of including gas recycling is to increase the amount of gas available for star formation roughly by a factor of $1 + 2\pi\alpha_{\rm reheat}$. For our fiducial GALFORM model with $\alpha_{\rm reheat} = 1.26$, this factor is $\sim 9$. We note that this modulation factor is completely independent of galaxy stellar mass, provided $\beta_{\rm ml} \gg 1$. Finally, as Equation 4.22 is equivalent to Equation 4.11 multiplied by a constant factor, repeating the exercise of integrating Equation 4.22 will give the same result that the specific stellar mass assembly rate is simply given by $\dot{M}_{\star}/M_{\star} = 1/t_{\rm age}$, provided that $V_{\rm vir}$ remains constant with time.

## 4.5 Towards reproducing the inferred stellar mass assembly histories of star-forming galaxies

In Section 4.4 and Appendix C, we have demonstrated that for the standard parametrisations of supernova feedback, star formation and gas reincorporation used in GALFORM, it is not possible to reproduce the stellar mass assembly histories of star forming galaxies inferred from observations. The next logical step is to consider how these parametrisations would need to be changed in order to better reproduce the inferred observational trends. Clearly, the ideal scenario is to change the parametrisations such that they are more physically motivated and/or satisfy

direct empirical constraints. The opposite and less desirable extreme is to use increasingly flexible parametrisations which have to be constrained statistically to reproduce global diagnostics of the galaxy population. Currently, the implementation of star formation in GALFORM can be argued to fall into the former case while the default implementations of feedback and reincorporation fall into the latter. We therefore choose to focus on how the implementation of feedback and gas reincorporation could be modified to change the model predictions relevant to our analysis.

### 4.5.1 Modifying the mass loading factor for supernova feedback

From the comparison between the predicted and inferred efficiency of stellar mass assembly shown in Fig. 4.5, it is clear that the degree of coevolution between stellar mass and halo mass assembly rates needs to be reduced in GALFORM in order to reproduce the trends we infer according to the observations. This requirement appears to be particularly pertinent from intermediate through to late times (roughly in the redshift range, $0 < z < 1$), where the efficiency of converting accreted gas into stars is inferred from the observations to drop after a peak at intermediate redshift. In Section 4.4.2, we demonstrated that the efficiency of feedback in our fiducial model, characterised by the mass loading factor, $\beta_{\rm ml}$, does not vary significantly over this redshift range. This is because the disk circular velocity does not evolve strongly over the lifetime of a typical star forming galaxy in GALFORM. A different parametrisation for $\beta_{\rm ml}$ that does not depend only on circular velocity could potentially change this behaviour.

Lagos et al. (2013) have recently introduced an alternative parametrisation for the ejection of gas from galaxy disks and bulges as a result of feedback from supernovae (see also Creasey et al., 2013). This offers a natural starting point for our investigation because their work is motivated on physical grounds. Briefly, their methodology is to track the evolution of bubbles driven by supernovae as they expand into the ambient ISM. They calculate the rate at which mass entrained in these bubbles escapes vertically out of the disk and find that $\beta_{\rm ml}$ cannot be natu-

rally parametrised as a function of the disk circular velocity. Instead, they find that $\beta_{\rm ml}$ is better described as a function of the gas fraction in the disk, $f_{\rm g}$, and either the total gas surface density, $\Sigma_{\rm g}$, of the disk at the half mass radius, $r_{50}$, or the gas scale-height, $h_{\rm g}$, of the disk at the half mass radius. From this point onwards we refer to the former as the surface density parametrisation and the latter as the scaleheight parametrisation. The surface density parametrisation is given by

$$\beta_{\rm ml} = \left[\frac{\Sigma_{\rm g}(r_{50})}{1600{\rm M}_{\odot}{\rm pc}^{-2}}\right]^{-0.6} \left[\frac{f_{\rm gas}}{0.12}\right]^{0.8}, \tag{4.23}$$

and the scaleheight parametrisation is given by

$$\beta_{\rm ml} = \left[\frac{h_{\rm g}(r_{50})}{15{\rm pc}}\right]^{1.1} \left[\frac{f_{\rm gas}}{0.02}\right]^{0.4}. \tag{4.24}$$

We have used both of these parametrisations as separate modifications to our fiducial model and find that neither significantly changes the shapes of the stellar mass assembly histories of star forming galaxies to the extent that the model predictions are brought into better agreement with the data. The reason for this failure is illustrated in Fig 4.7, where we compare the average evolution in $\beta_{\rm ml}$ for galaxies that are star forming and central at $z = 0$ between the different models. It can be seen that although the modifications change the overall normalisation of $\beta_{\rm ml}$ and the dependence on $M_{\star}(t_0)$, the modified models actually result in even less evolution of $\beta_{\rm ml}$ over the lifetime of a typical star forming galaxy. Further investigation shows that this outcome arises because the effect on $\beta_{\rm ml}$ caused by the decline in the surface densities of star forming galaxies as they evolve is cancelled out by a corresponding drop in the gas fractions.

### 4.5.2 Modifying the gas reincorporation timescale

In addition to the mass loading factor, $\beta_{\rm ml}$, the way that ejected gas is reincorporated back into haloes is also modelled in a phenomenological manner in GALFORM. Therefore, an alternative to modifying the mass loading factor supernova feedback in our model is to alter the timescale for gas reincorporation for gas that

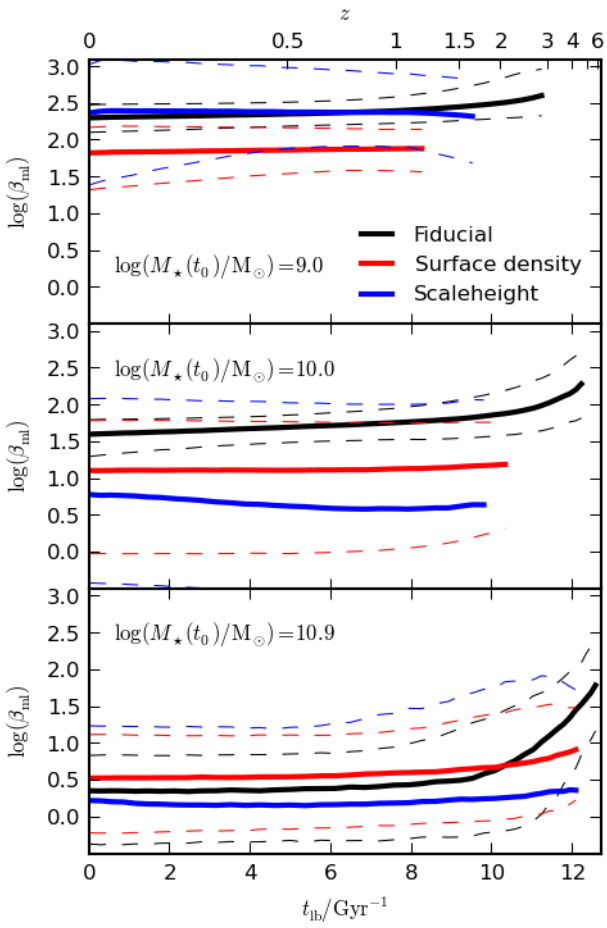


Figure 4.7: The average evolution in the mass loading factor of outflows, $\beta_{\rm ml}$, for model galaxies which are central and star forming at $z = 0$. Model galaxies are binned according to their $z = 0$ stellar mass, with each panel corresponding to a different mass bin. The median $z = 0$ stellar mass in each bin is labelled in each panel. Solid black lines show the mean mass loading factor from our fiducial GALFORM model. Dashed black lines show the corresponding median, $10^{\rm th}$ and $90^{\rm th}$ percentiles. Red lines show the same information but for a version of our fiducial model modified to use the surface density mass loading parametrisation, given by Eqn. 4.23 (Lagos et al., 2013). Blue lines show the same information but for a version of our fiducial model modified to use the scaleheight mass loading parametrisation, given by Eqn. 4.24.

has been ejected, $t_{\rm ret}$. At this stage, we choose to revert to the default parametrisation of $\beta_{\rm ml}$ (which depends on circular velocity) at this stage because using the modified models from Lagos et al. (2013) would require substantial retuning of various model parameters to recover an agreement with the observed local luminosity and stellar mass functions.

In the third panel of Fig. 4.6, we show the ratio of the characteristic gas reincorporation timescale relative to the age of the universe as a function of lookback time for our fiducial model. As discussed in Section 4.4.2, this ratio of timescales evolves very little over the lifetime of a typical star forming galaxy, partly explaining the close levels of coevolution between stellar and halo mass assembly seen in Fig. 4.5 for our fiducial model. The most desirable step as this stage would be to formulate a physically motivated model for gas reincorporation timescales in the hope that a more realistic model could change this behaviour. Such an undertaking is beyond the scope of this study, but as an intermediate step, we instead introduce an *ad hoc* modification to the parametrisation of gas reincorporation timescales used in GALFORM. We note that this step essentially amounts to an empirical fit to the trends which we infer from the data and is of little scientific value in itself. However, the resulting evolution in the reincorporation timescale for star forming galaxies can serve as a guide for the development of a physically motivated model in future work.

To match the shape of the stellar mass assembly histories inferred from the data shown in Fig. 4.4, we consider a model where $t_{\rm age}/t_{\rm ret}$ rises from early times to a peak at $z = 2$, before falling to $z = 0$. A natural way to achieve an early time rise is to make $t_{\rm age}/t_{\rm ret}$ correlate positively with halo mass. This is the same scaling that Henriques et al. (2013) adopt in order to allow their model to reproduce the observed evolution in the stellar mass function. However, a natural scaling that results in a drop in $t_{\rm age}/t_{\rm ret}$ at late times is less obvious and we instead choose to simply introduce an arbitrary function of redshift to achieve this. After a process of experimentation and iteration, we arrive at the following modified parametrisation for gas reincorporation,

$$\dot{M}_{\rm hot} = \frac{\alpha_{\rm reheat}}{t_{\rm dyn}} \left( \frac{M_{\rm H}}{10^{11.9}{\rm M}_{\odot}} \right) f(z), \tag{4.25}$$

where $f(z)$ is given by

$$\log[f(z)] = 6 \, \exp \left[ -\frac{(1+z)}{3} \right] \log[1+z]. \tag{4.26}$$

At this stage we note that in Appendix C, we show that the shapes of the stellar mass assembly histories predicted by GALFORM are almost invariant under changes in the model parameters which control the relationship between stellar and halo mass. In other words, this means that until now, our results for the shape of the stellar mass assembly histories of star forming galaxies have been independent of whether or not the model provides a good match to the $z = 0$ stellar mass function. However, once we change the parametrisation of the gas reincorporation in GALFORM, this feature of the model may not be preserved. Consequently, we now have to consider whether our modified GALFORM models can also reproduce the $z = 0$ stellar mass function, particularly because we have introduced a dependence on halo mass into Eqn. 4.25. We find that we can recover reasonable agreement with the local stellar mass function simply by fine tuning the various model parameters that appear in Eqn. 4.25. We also reduce the threshold for AGN feedback to be effective at suppressing gas cooling in haloes by changing the model parameter $\alpha_{\rm cool}$ from $1.0$ to $1.3$ (see Bower et al., 2006). From this point onwards, we refer to this modified model simply as the modified reincorporation model.

A comparison between our fiducial model and the modified reincorporation model for the evolution in $t_{\rm ret}/t_{\rm age}$ for star forming galaxies is presented in Fig. 4.8. In addition, Fig. 4.8 also shows the corresponding timescale proposed by Henriques et al. (2013) which scales only with the virial mass. By construction, $t_{\rm ret}/t_{\rm age}$ evolves much more strongly in our modified reincorporation model than in our fiducial model. Additionally, the dispersion in $t_{\rm ret}/t_{\rm age}$ can be slightly larger in the modified model for some lookback times. Given that Eqn. 4.25 introduces a dependence on halo mass, the change is presumably caused by scatter in the relationship between the stellar mass and halo mass of central star forming galaxies. This is

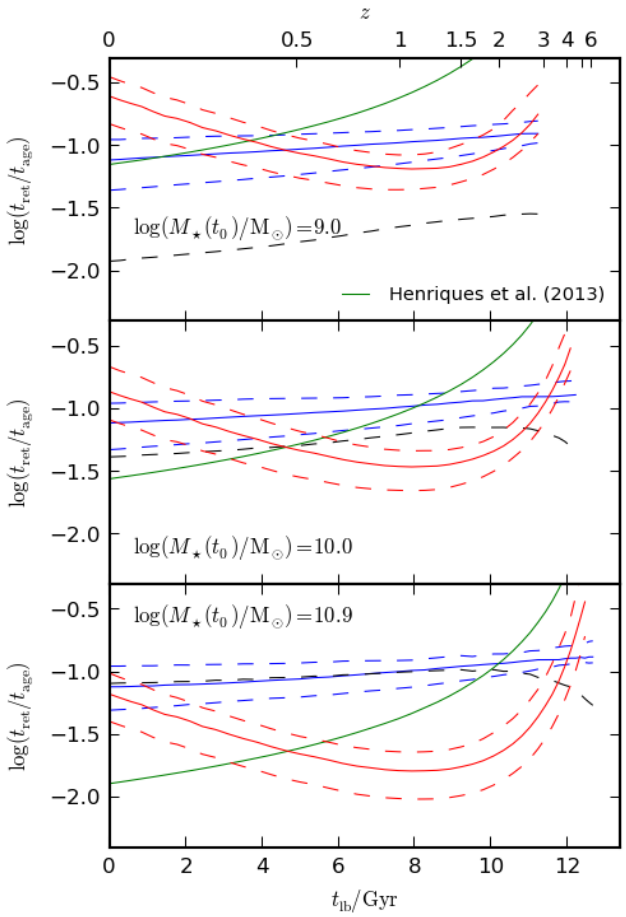


Figure 4.8: The ratio of the average reincorporation timescale to the age of the universe for model galaxies which are central and star forming at $z = 0$, plotted as a function of lookback time. Model galaxies are binned according to their $z = 0$ stellar mass and each panel shows a different stellar mass bin. The median $z = 0$ stellar mass in each bin is labelled in each panel. Solid blue lines show the medians of the distribution from our fiducial GALFORM model. Dashed blue lines show the corresponding $10^{\rm th}$ and $90^{\rm th}$ percentiles. Red lines show the same information but for the modified reincorporation model. Green solid lines show the median of the distribution for galaxies from our fiducial model which would be obtained if we were to use the reincorporation timescale from eqn. 8 in Henriques et al. (2013). For reference, black dashed lines show the ratio of the median cooling timescale, $t_{\rm cool}$, to the age of the universe for model galaxies from our fiducial model.

noteworthy because any change in the scatter in $t_{\rm ret}/t_{\rm age}$ could have an effect on the scatter of the star forming sequence predicted by our modified reincorporation model.

The evolution in the cooling timescale is also shown in Fig. 4.8. It can be seen that for our modified reincorporation model, the cooling timescale can become significantly longer than the reincorporation timescale for the most star forming galaxies. In this regime, gas that is rapidly reincorporated back into the halo will be delayed from returning to the galaxy disk until the gas is able to cool. This is important because further shortening the reincorporation timescale in this regime will cease to have a significant impact on the rate at which gas is made available for star formation.

A comparison between our fiducial model and the modified reincorporation model for the predicted stellar mass assembly histories of star forming galaxies is presented in Fig. 4.9. Again, by construction we have tuned the modified reincorporation model in order to ensure qualitative agreement with the pink shaded region inferred from the observations using MSI. Comparison with the stellar mass assembly histories inferred from observational data shown in Fig. B.5 shows that this agreement holds with MSI applied to observational data where the slope of the star forming sequence, $\beta_{\rm sf} \approx 0$. As discussed in Section 4.4.1, a lower value of $\beta_{\rm sf}$ introduces a strong downsizing trend into the stellar mass assembly histories of star forming galaxies which is difficult to reconcile with the approximately self-similar shape of the halo mass assembly histories predicted by the $\Lambda$CDM cosmological model. In principle, we could adjust Eqn. 4.25 even further to try to reproduce this downsizing trend. However, we have already introduced a very strong redshift scaling into the reincorporation timescale. Therefore, we choose to present a modified model which is closest to our fiducial model while still showing consistency with the pink shaded region in Fig. 4.9.

Finally, we show the comparison between our fiducial model and the modified reincorporation model for the evolution in the specific star formation rates of star forming galaxies in Fig. 4.3. Our modification to the reincorporation timescale has

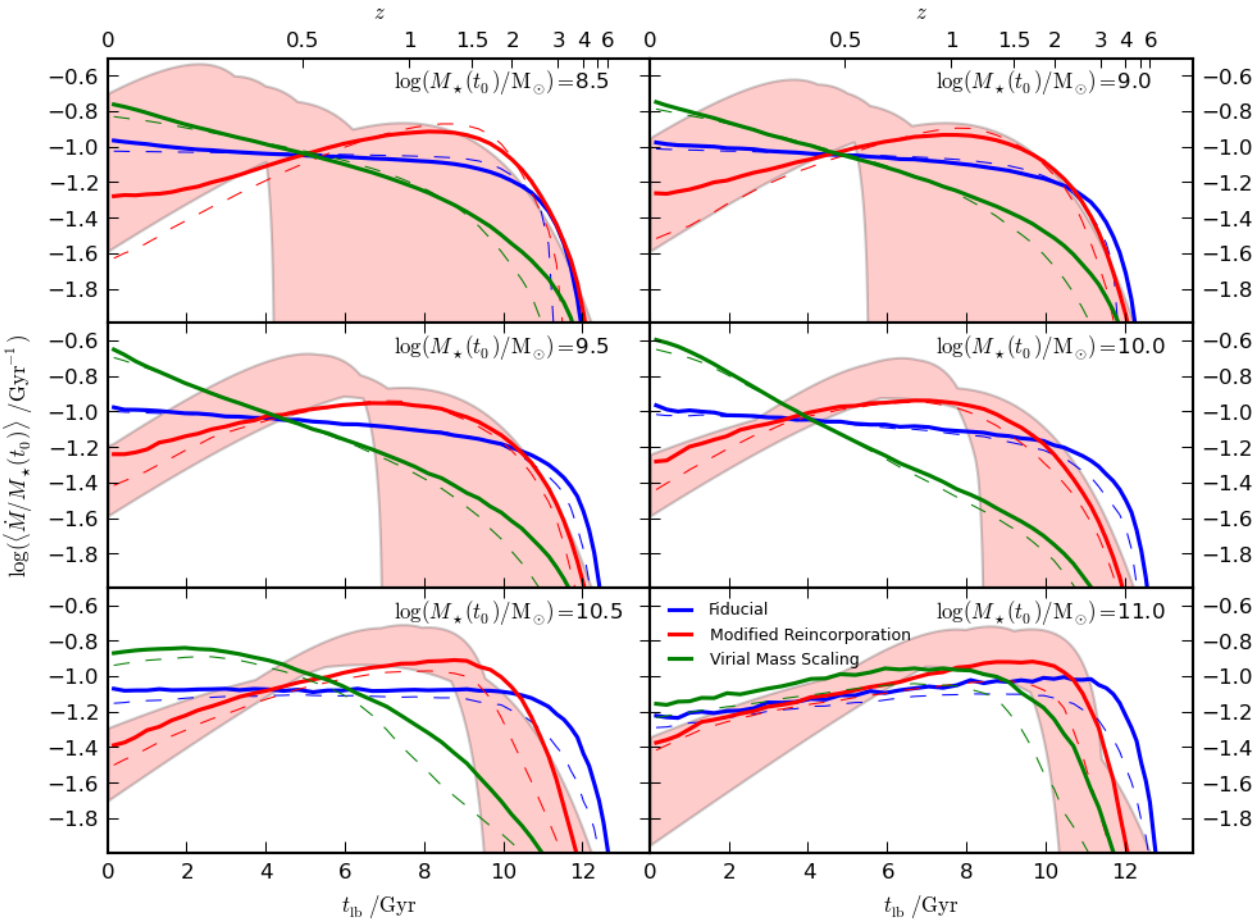


Figure 4.9: The average stellar mass assembly histories of galaxies that are star forming at $z = 0$, plotted as a function of lookback time. Blue solid lines show predictions from our fiducial GALFORM model for the mean mass assembly histories of the main stellar progenitors of central galaxies. Dashed blue lines show the corresponding medians of the distribution. Red lines show the same information but for the modified reincorporation model. Green lines show the same information but for a model using the virial mass scaling for the reincorporation timescale proposed by Henriques et al. (2013). Model galaxies are binned according to their $z = 0$ stellar mass with each panel corresponding to a different mass bin. The median $z = 0$ stellar mass in each bin is labelled in each panel. The filled pink region shows the range of stellar mass assembly histories that are inferred by applying the MSI technique to observational data from the literature.

mixed success. For the top two panels, corresponding to the $\log(M_\star/\mathrm{M}_\odot) = 9.5, 10$ bins, the modified model shows a significantly improved agreement with the observational trend. Unlike for the fiducial model, the evolution in the mean specific star formation rates in the modified model does not trace the inverse of the age of the Universe as a function of lookback time. Instead, specific star formation rates are elevated at early times before dropping below the fiducial model at $z < 0.5$. For the $\log(M_\star/\mathrm{M}_\odot) = 10.5$ bin, the modified reincorporation model has a steeper drop below $z \approx 0.5$ compared to the fiducial model but the two models are very similar at higher redshifts, in disagreement with the data. The two models are very similar for all lookback times in the $\log(M_\star/\mathrm{M}_\odot) = 11$ bin and are both in disagreement with the data.

At first glance it is puzzling that modified reincorporation model fails to reconcile the model predictions with the observational data for massive star forming galaxies while it does qualitatively reproduce the inferred stellar mass assembly histories shown in Fig. 4.9. However, it must be kept in mind that our modification to the reincorporation timescale was constructed only to reproduce the shape of the stellar mass assembly histories of galaxies that are still star forming at $z = 0$. Galaxies observed at $z > 0$ in the most massive stellar mass bins shown in Fig. 4.3 will, typically, have dropped below the star forming sequence by $z = 0$. Therefore, the specific star formation rates of the most massive galaxies at high redshift will not have been constrained by our analysis of stellar mass assembly histories of galaxies that are still star forming at $z = 0$. Furthermore, galaxies that are quenched above $z \approx 1 - 2$ will be less affected by the rapid evolution in the reincorporation timescale which we impose in Eqn. 4.26 below $z = 2$. This highlights the need for a physical model of gas reincorporation rather than the artificial redshift scaling which we use here. In addition, for the most massive star forming galaxies, we show in Fig. 4.8 that the cooling timescales become long relative to the modified reincorporation timescales. As discussed earlier, this will reduce the impact of any modification towards shorter reincorporation timescales. Finally, the mass loading factor, $\beta_{\mathrm{ml}}$, for the most massive galaxies is smaller than for lower mass galaxies.

Therefore, a larger fraction of gas accreted onto the haloes of these systems for the first time will be able to form stars without being affected by the reincorporation timescale.

Fig. 4.9 and Fig. 4.3 also show the stellar mass assembly histories and specific star formation rate evolution predicted by an alternative GALFORM model that uses the virial mass scaling for the reincorporation timescale proposed by Henriques et al. (2013). Details of this model and a discussion of the differences with our modified reincorporation model are presented in Appendix D. To summarise, we find that this alternative model with the virial mass scaling is considerably more successful than either our fiducial model or our modified reincorporation model in reproducing the observed evolution in the stellar mass function. However, Fig. 4.9 and Fig. 4.3 show that this alternative model fails to reproduce the stellar mass assembly and star formation rate evolution inferred from observations. We strongly emphasise that this result will not necessarily hold for the Henriques et al. (2013) model where the treatment of gas that is ejected from galaxy disks differs from the GALFORM model.

## 4.6 Discussion

The focus of this study has been on using the observed evolution of the star forming sequence as a constraint on galaxy formation models. The disagreement in this evolution between models and observational data is undoubtedly related to the problems with reproducing the correct evolution in the low mass end of the stellar mass function which has recently received considerable attention in the literature (e.g. Avila-Reese et al., 2011; Weinmann et al., 2012; Henriques et al., 2013; Lu et al., 2013a,b). Specifically, there is a general finding that models and simulations overpredict the ages of low mass galaxies and consequently underpredict evolution in the low mass end of the stellar mass function at low redshift. Weinmann et al. (2012) interpret this problem as an indication that the level of coevolution between halo and stellar mass assembly needs to be reduced, broadly in agreement with our

results. However, part of the reason why they arrive at this conclusion is because they identify the prediction of a positive correlation between specific star formation rate and stellar mass as a key problem with respect to the data. We note that in contrast, GALFORM naturally predicts a slightly negative correlation for star forming galaxies and that this is also true for many other models and simulations presented in the literature (e.g. Santini et al., 2009; Dutton et al., 2010; Lamastra et al., 2013; Torrey et al., 2014).

Henriques et al. (2013) show that there is no combination of parameters for their standard galaxy formation model that can reconcile the model with the observed evolution in the stellar mass and luminosity functions. This is consistent with the findings of Lu et al. (2013a), who use a similar methodology but for a different model. Lu et al. (2013b) compare three different models of galaxy formation and find that they all predict very similar stellar mass assembly histories and suffer from predicting too much star formation at high redshift in low mass haloes. We note that the models presented in Lu et al. (2013b) are all very similar to GALFORM in many respects and that therefore the similarity of the predictions from their three models makes sense in the context of the discussion we present in Appendix C.

Henriques et al. (2013) go one step further to suggest an empirical modification to the reincorporation timescale within their model that reduces the rate of star formation at early times in low mass haloes. In this respect, their equation 8 uses the same scaling between reincorporation timescale and halo mass which we introduce in Eqn. 4.25 for the same reason. However, our modification diverges from their suggestion in that we also require an additional redshift dependence that lengthens the reincorporation timescale towards low redshift. The modification suggested by Henriques et al. (2013) can be compared to our modification in Fig. 4.8. The difference between the two suggested modifications stems from the way that our analysis indicates that it is not simply that stars form too early in the model. Instead, we find that it is the precise shape of the stellar mass assembly history which is inconsistent with the currently available data which favours a peak of activity at intermediate times. This highlights how the differences in method-

ology between different studies can lead to different conclusions. Our analysis is designed to reduce the number of relevant physical processes by focusing only on the normalisation of the star forming sequence. In principle, this approach can provide a more direct insight into how the implementation of different physical processes within galaxy formation models needs to be changed, provided that the uncertainty in the relevant observations can be correctly accounted for. On the other hand, as discussed in Appendix D, our modified reincorporation model does not reproduce the evolution in the stellar mass function inferred from recent observations. We again emphasise that the focus of this study is on the evolution of the normalisation of the star forming sequence and that the stellar mass function can be affected by the quenching processes which we have not considered in our analysis. Nonetheless, it may well be the case that our methodology is limited by the lack of a consensus on the slope of the star forming sequence in observations. Alternatively, there could be some inconsistency between observations of the star forming sequence and observations of the evolution in the stellar mass function. We note that the latter possibility is disfavoured by recent abundance matching results (e.g. Behroozi et al., 2013b; Moster et al., 2013).

### 4.6.1 Do the stellar mass assembly histories of star forming galaxies rise and then fall?

Our suggestion that the reincorporation timescale needs to be increased at low redshift stems from our inference from observations that the stellar mass assembly histories of star forming galaxies rise to a peak before falling towards the present day. As discussed in Appendix B.3, this inference is consistent with the findings of Leitner (2012) who use a similar methodology, albeit with the caveat that we find that evidence of a strong downsizing trend in the purely star forming population is not conclusive. Instead, we find that the considerable uncertainty that remains in the power-law slope of the star forming sequence means that overall, the observational data are also consistent with no downsizing, such that the shapes of the

stellar mass assembly histories of star forming galaxies are independent of the final stellar mass. Clearly, any improvements in measuring the form of the star forming sequence as a function of lookback time would greatly increase the constraining power of the MSI technique with respect to galaxy formation models. If the slope of the sequence, $\beta_{\rm sf}$, can be conclusively shown to be significantly below zero as advocated, for example by Karim et al. (2011), then even larger modifications than those considered here towards separating stellar and halo mass assembly would be required.

Another methodology that can be used to infer the shape of the stellar mass assembly histories of galaxies is to employ abundance matching to make an empirical link between the dark matter halo population predicted by theory and the observed galaxy population (e.g. Behroozi et al., 2013b; Moster et al., 2013; Yang et al., 2013). Comparison with stellar mass assembly histories of the star forming galaxies that are discussed in this study is complicated by the fact that abundance matching has only been used so far to predict the average star formation histories of all galaxies (including passive galaxies) and as a function of halo mass. On average, the haloes hosting the galaxies which we consider in this study have median masses of $\log(M_{\rm H}/{\rm M}_{\odot}) < 12$, where the fraction of passive central galaxies relative to star forming centrals is predicted to be negligible. However, because there is substantial scatter between stellar mass and halo mass for central galaxies, the fraction of passive galaxies at a given stellar mass is not negligible for most of the stellar mass bins which we consider in this study. For example, the fraction of central galaxies with $\log(M_{\star}/{\rm M}_{\odot}) = 10$ that are passive is predicted to be $25\%$ at $z = 0$ in our fiducial GALFORM model. Furthermore, the star forming galaxies considered in this study and in Leitner (2012) are hosted by haloes that reside within a fairly narrow range of halo mass. If we ignore these issues, then qualitatively speaking, it is apparent that the shape of stellar mass assembly histories inferred by Behroozi et al. (2013b) and Yang et al. (2013) are broadly consistent with what we and Leitner (2012) infer from the data, in that there is a rise with time towards a peak at some intermediate redshift before a fall towards the present day. Moster et al. (2013)

show qualitative agreement with this picture for $\log(M_{\rm H}/{\rm M}_{\odot}) = 12$ haloes, but find a constant rise from early to late times in the stellar mass assembly rates of galaxies that reside within haloes with $\log(M_{\rm H}/{\rm M}_{\odot}) = 11$.

Finally, we also note that Pacifici et al. (2013) find that the spectral energy distributions of massive star forming galaxies are well described by models that feature initially rising then declining star formation histories. However, for lower mass galaxies they find that the SEDs are best reproduced using star formation histories that monotonically rise towards the present day, in qualitative agreement with the results from Moster et al. (2013). However, their galaxy sample does not include any galaxies observed below $z = 0.2$, corresponding to a lookback time of $t_{\rm lb} \approx 3\,{\rm Gyr}$. It is therefore unclear whether their analysis disfavours a drop in the star formation rates of lower mass galaxies at late times.

### 4.6.2 Modifications to galaxy formation models

The parametrisations for star formation and feedback that are implemented in most galaxy formation models can reproduce the shape of the local luminosity and stellar mass functions. However, as observational data that characterises the evolution of the galaxy population has improved, it has now been demonstrated that either one or more of these parametrisations is inadequate or alternatively that another important physical process has been neglected in the models entirely. The assumption that the reincorporation timescale for ejected gas scales with the dynamical timescale of the host halo is common to various semi-analytic galaxy formation models (e.g. Bower et al., 2006; Croton et al., 2006; Somerville et al., 2008; Lu et al., 2011). If the reincorporation timescale is set to exactly the dynamical timescale, the associated physical assumption is that ejected gas simply behaves in a ballistic manner, ignoring any possible hydrodynamical interaction between the ejected gas and the larger scale environment. In practice, these models (including ours) typically introduce a model parameter such that the reincorporation timescale is not exactly equal to the dynamical timescale, reflecting the considerable uncertainty on predicting this timescale. Nonetheless, the assumption that this uncertainty can

be represented by a single parameter and that there is no additional scaling with other galaxy or halo properties is clearly naive. Comparison with hydrodynamical simulations will clearly be useful in this respect, provided that the reincorporation rates can be clearly defined and measured from the simulations and that the effect of the assumptions made in sub-grid feedback models can be understood.

While we and Henriques et al. (2013) show that a modification to the reincorporation timescale for gas ejected by feedback can be one solution, we could equally change the parametrisation for the mass loading factor, $\beta_{\rm ml}$, or the star formation law introduced in Lagos et al. (2011b). In this analysis, we found that the physically motivated parametrisation for the mass loading factor of SNe driven winds presented in Lagos et al. (2013) fails to reconcile the model with the data. However, it should be noted that unlike the fiducial model we consider for this study, the supernova feedback model presented in Lagos et al. (2013) relies heavily upon correctly predicting the evolution in the sizes of galaxies. In principle, if the predicted sizes evolved differently in our model, it is possible that using the Lagos et al. (2013) supernova feedback model could help to reconcile model predictions for the stellar mass assembly histories of galaxies with the observational data. As for modifying the star formation law, the implementation used in GALFORM is derived from direct empirical constraints. Furthermore, changing the star formation law will have little impact on the stellar mass assembly histories of star forming galaxies as long as the characteristic halo accretion timescale is longer than the disk depletion timescale. Of course, an alternative to the physically motivated Lagos et al. (2013) model is simply to implement an ad hoc modification to the mass loading, similar to that given by Eqn. 4.25 for the reincorporation timescale. We note that by doing this, we find it is possible to produce a model that almost exactly matches the predictions made by the modified reincorporation model presented in this Chapter. It therefore suffers from the same problems as the modified reincorporation model in reproducing the observed evolution of the stellar mass function and the decline in the specific star formation rates of the most massive star forming galaxies at a given redshift.

Many other suggestions for changing the stellar mass assembly histories predicted by models and simulations have been made recently in the literature, typically focusing on reducing the fraction of stars that form at high redshift. For example, Krumholz & Dekel (2012) argue that early star formation is reduced once the dependence of star formation on metallicity is properly implemented in hydrodynamical simulations. Gabor & Bournaud (2014) suggest that if galaxies at high redshift accrete directly from cold streams of gas, the accreted gas injects turbulent energy into galaxy disks, increasing the vertical scaleheight and consequently lowering the star formation efficiency in these systems by factors of up to 3. Lu et al. (2014a) demonstrate that if the circum-halo medium can be preheated at early times up to a certain entropy level, the accretion of baryons onto haloes can be delayed, reducing the amount of early star formation. Various authors (e.g Aumer et al., 2013; Stinson et al., 2013; Trujillo-Gomez et al., 2013) find that implementing a coupling between the radiation emitted by young stars and the surrounding gas into their simulations can significantly reduce the levels of star formation in high redshift galaxies. Hopkins et al. (2013a) and Hopkins et al. (2013b) echo these findings and emphasise the highly non-linear nature of the problem once sufficient resolution is obtained to start resolving giant molecular cloud structures. They argue that radiative feedback is essential to disrupt dense star forming gas before SNe feedback comes into effect to heat and inject momentum into lower density gas, avoiding the overcooling problem as a result. It remains to be seen at this stage whether the emergent behaviour from such simulations, once averaged over an entire galaxy disk or bulge, can be captured in the parametrisations that are used in semi-analytic galaxy formation models.

## 4.7 Summary

We have performed a detailed comparison between predictions from the GALFORM semi-analytic model of galaxy formation with observational data that describe the average star formation rates of star forming galaxies as a function of stellar mass

and lookback time. To better understand the origin of discrepancies between the model and the data, we also use the observational data to infer the shape of the stellar mass assembly histories of galaxies that are still central and star forming at the present day. This is achieved by integrating the inferred relationship between star formation rate and stellar mass for star forming galaxies back in time from the present day. Crucially, we account for the considerable uncertainty that remains in the literature regarding the slope of the power-law dependence of star formation rate on stellar mass. We then attempt to explain our results by analysing the timescales of the various physical processes in the model which are important for shaping the stellar mass assembly histories of star forming galaxies.

Our main results are summarised as follows:

- For our fiducial model, there are qualitative differences with the observational data in the way that the average specific star formation rates of star forming galaxies evolve with time at a given stellar mass. The model predicts average specific star formation rates that evolve too slowly with lookback time, tracing the inverse of the age of the universe at a given epoch. In contrast the observational data implies that the average specific star formation rates of star forming galaxies grow exponentially as a function of lookback time. Quantitatively, this leads to discrepancies in the predicted average specific star formation rates of up to $0.5\,\mathrm{dex}$ compared to the data.

- We show that the main sequence integration technique, as advocated by Leitner (2012), can qualitatively recover the shape of the stellar mass assembly histories of galaxies that are still star forming at the present day when it is applied to our fiducial model.

- After applying this technique to a compilation of observational data, we show that there is a qualitative difference between the inferred shape of the stellar mass assembly histories of star forming galaxies and the predictions from our fiducial model. Specifically, the model predicts stellar mass assembly histories that are almost flat over most of the lifetime of star forming galaxies. In

contrast, the trend we infer from the data is that stellar mass assembly histories rise from early times, peak at an intermediate redshift and subsequently fall towards the present day.

- The exact position of the peak in these inferred stellar mass assembly histories depends sensitively on the slope of the star forming sequence of galaxies. We show that no clear consensus on this slope has emerged yet from observations presented in the literature. For the case where the specific star formation rate is independent of stellar mass, the resulting shape of the stellar mass assembly histories of galaxies that are still star forming at the present day is also independent of stellar mass. For the case where there is a strong anti-correlation between specific star formation rate and stellar mass, there is also a strong downsizing trend that emerges for this population of galaxies. In this case, less massive galaxies start forming stars at a later time with respect to more massive star forming galaxies. We emphasise that this should be completely independent of processes that quench star formation in galaxies. Such a downsizing trend in the purely star forming population is difficult to reconcile with the approximately self-similar halo mass assembly histories predicted by simulations of structure formation.

- The shapes of the stellar mass assembly histories predicted by our fiducial model are unaffected by changes to the various input parameters to the GALFORM model. This is despite the fact that for the same changes to these model parameters, it is possible to significantly affect the present day relationship between stellar mass and halo mass.

- The roughly flat stellar mass assembly histories predicted by our fiducial model arise because of the standard parametrisations for supernova feedback that are implemented in semi-analytic galaxy formation models. The efficiency with which cold gas is ejected from galaxy disks evolves very little over the majority of the lifetimes of star forming galaxies. This comes as a result of the standard scheme used in semi-analytic models where the mass

loading factor is a parametrised as a function of circular velocity which, in turn, is almost constant over the lifetime of an individual star forming galaxy. Similarly, the timescale, relative to the age of the Universe, over which gas ejected by feedback is reincorporated into galaxy haloes also varies very little for individual star forming galaxies. In this case, the typical assumption that the reincorporation timescale scales with the halo dynamical time results in this behaviour. We also show using simple arguments that when the efficiency of feedback does not vary with time for a given galaxy, the specific star formation rates of star forming galaxies will naturally trace the inverse of the age of the Universe at a given stellar mass.

We demonstrate that a modification to the reincorporation timescale, such that this timescale is lengthened at early and late times, can produce peaked stellar mass assembly histories for galaxies that are still star forming at the present day. This modification significantly improves the agreement with the data for the evolution in the average specific star formation rates of star forming galaxies with $9.5 < \log(M_{\star}/\mathrm{M}_{\odot}) < 10.0$. However, the modification is less effective for more massive star forming galaxies where radiative cooling timescales become comparable to or longer than the corresponding reincorporation timescales. We also show that the modification fails to reproduce the rapid evolution in the low mass end of the stellar mass function inferred from observations below $z = 2$.

We conclude that modifications to the standard implementations of supernova feedback used in galaxy formation models and cosmological hydrodynamical simulations are probably required. Rather than altering the efficiency of feedback or star formation in a global sense over the lifetime of a given galaxy, it appears to be necessary to introduce a dependency that changes the efficiency of one or both of these processes with time.

# Chapter 5

# *The evolution of the relationship between stellar mass and halo mass*

## 5.1 Introduction

Over the last decade, interest has steadily grown in using statistical inference to construct empirical models that describe how galaxies are distributed within a population of dark matter haloes (e.g. Peacock & Smith, 2000; Berlind & Weinberg, 2002; Yang et al., 2003; Behroozi et al., 2010; Moster et al., 2010; Wake et al., 2011; Yang et al., 2012; Wang et al., 2013; Durkalec et al., 2014; Lu et al., 2014b; Shankar et al., 2014; McCracken et al., 2014). By combining observed abundances and clustering of galaxies with theoretical predictions for the abundance and clustering of dark matter haloes, earlier work in this area used galaxy abundances and/or clustering as a function of luminosity to constrain parameters in such models (e.g. Berlind & Weinberg, 2002; Yang et al., 2003). As multi-wavelength galaxy surveys have become increasingly prevalent, it has become commonplace to replace galaxy luminosity with stellar mass (which can be estimated from broad-band photometry) as the dependent variable in this type of analysis (e.g. Behroozi et al., 2010; Moster et al., 2010).

It has been demonstrated that it is possible to provide an acceptable statistical fit to stellar mass functions inferred from observations by assuming the following.

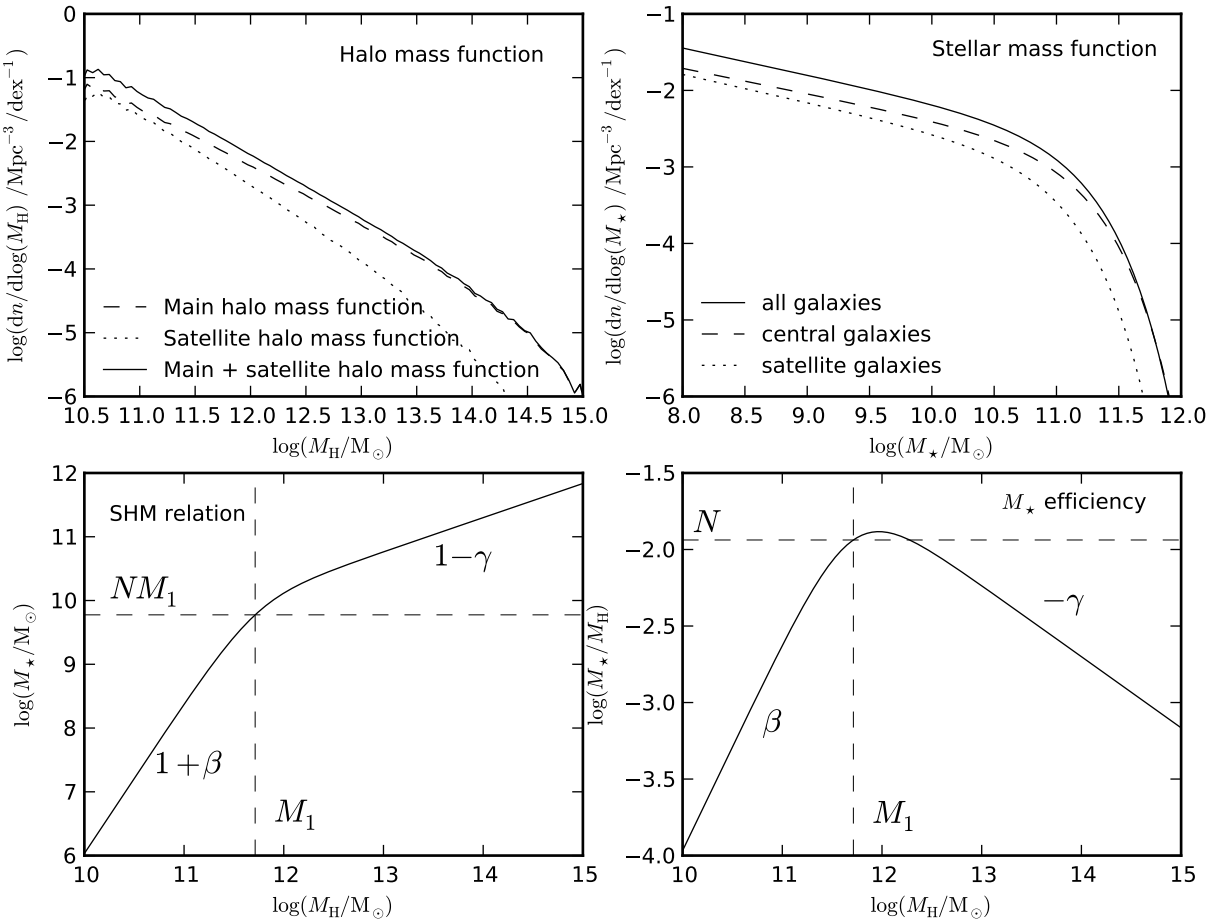


Figure 5.1: Schematic to demonstrate the relationship at $z = 0$ between the halo mass function, the stellar mass function and the median SHM relation. The meanings of the parameters from Eqn 5.1 are also illustrated. *Upper left:* Main halo mass function (dashed), satellite halo mass function (dotted) and combined main plus satellite halo mass function (solid). The satellite halo mass plotted is the mass of the host subhalo at infall. *Upper right:* Stellar mass function of all galaxies (solid), central galaxies (dashed) and satellite galaxies (dotted). *Lower left:* Stellar mass versus halo mass (SHM) relation. *Lower right:* Median stellar mass assembly efficiency, $M_\star/M_\mathrm{H}$, plotted as a function of halo mass.

First, that the distribution of stellar mass at fixed halo mass is lognormal with constant width. Second, that the median stellar mass versus halo mass (SHM) relation can be parametrised by two power laws that connect at a stellar mass corresponding roughly to the knee of the stellar mass function (e.g. Moster et al., 2010; Yang et al., 2012). Although more complex parametrisations have been advocated (e.g. Behroozi et al., 2010, 2013b), the basic picture is that there are two regimes (the two power laws) that describe how the efficiency of stellar mass assembly[1], $M_{\star}/M_{\rm H}$, drops away from a peak halo mass (which corresponds roughly to the knee of the stellar mass function). An illustration of the relationship between the halo mass function, the stellar mass function and the median SHM relation is shown in Fig. 5.1.

A weaker level of consensus has been achieved regarding the amount of evolution in the median SHM relation that is implied by observational data. For example, Behroozi et al. (2013b) report that the SHM relation is marginally consistent with no evolution over the range $0 < z < 6$, although their analysis prefers a solution where the characteristic halo mass at which stellar mass assembly is maximally efficient evolves, peaking at $z = 2$. In contrast, the analysis of Moster et al. (2013) finds significant evidence for monotonic evolution in the SHM relation. Disagreements between different studies are not surprising, given that errors on stellar mass estimates can strongly affect the inferred stellar mass function for large stellar masses beyond the knee of the stellar mass function (e.g. Marchesini et al., 2009; Behroozi et al., 2010). As such, fairly strong priors on the size and form of error parametrisations have to be adopted when constraining SHM parameters (e.g. Behroozi et al., 2013b; Moster et al., 2013). In addition, different studies use different observational datasets as inputs. For the case of stellar mass functions, limited depth in rest frame optical bands, as well as complicated selection functions, can make measurements of the stellar mass function at low stellar mass below the knee very challenging at $z = 2$ and beyond, although an encouraging level of consensus

[1]We use the convention that stellar mass assembly refers to both star formation and galaxy mergers.

has been achieved in recent years (Ilbert et al., 2013; Muzzin et al., 2013b; Tomczak et al., 2014).

Another way to connect the predicted halo population to the observed stellar population is to build a physical model that couples dark matter halo merger trees with a simple set of ordinary differential equations that govern the exchange of mass, metals and angular momentum between different discrete galaxy and halo components. These models are typically referred to as semi-analytic galaxy formation models (e.g. Cole et al., 2000; Bower et al., 2006; Somerville et al., 2008; Guo et al., 2011). Alternatively, modern computers make it possible to perform hydrodynamical simulations at a resolution capable of resolving galaxies on kpc scales within a volume that samples the halo population up to medium size clusters (Vogelsberger et al., 2014; Schaye et al., 2015). Using either of these two modelling techniques, the stellar mass function hosted by a given halo population is predicted and can then be compared against observational estimates of the stellar mass function without having to assume any parametric form for the SHM relation. In general, these modelling techniques have provided support for the parametric forms assumed in empirical studies (e.g. Zehavi et al., 2012; Henriques et al., 2013).

In this Chapter, we analyse the predictions made by the semi-analytic model GALFORM in the context of the SHM relation. Unlike other recent work using similar models, we do not attempt to find a best-fitting model that has maximal likelihood with respect to some combination of observational data. Instead, we attempt to address the questions of what type of evolution is predicted for the SHM relation, how much variation in this evolution results from adjusting model parameters, and what this evolution tells us about the underlying galaxy formation physics.

The layout of the Chapter is as follows. In Section 5.2, we give a brief overview of our reference model. In Section 5.3, we present model predictions for the evolution in the SHM relation. In Section 5.4, we attempt to explain these predictions in simple terms. In Section 5.5, we assess the impact of changing individual model parameters. In Section 5.6, we consider the range in SHM evolution that is dis-

played by a number of models that have been roughly tuned to match the local stellar mass function. We discuss and summarise our results in Sections 5.7 and 5.8 respectively.

## 5.2 The GALFORM galaxy formation model

For this Chapter, we use the published model of González et al. (2014) as our reference model. This version of GALFORM represents an update of the Lagos et al. (2012) GALFORM model, which in turn represents an evolution of the model published in Bower et al. (2006). The parameters of the González et al. (2014) model were tuned to reproduce the observed $b_{\rm J}$ and $K$-band luminosity functions at $z = 0$, while also giving reasonable evolution compared to the observed rest-frame UV and $K$-band luminosity functions. With respect to Bower et al. (2006), the model presented in González et al. (2014) features the empirical SF law presented in Lagos et al. (2011b) and is updated to the WMAP-7 cosmological parameters (Komatsu et al., 2011). The model uses merger trees extracted from the MILLENIUM WMAP-7 simulation (Guo et al., 2013b), an updated version of the MILLENIUM simulation (Springel et al., 2005) that uses the WMAP-7 cosmological parameters. As such, we assume the following cosmological parameters for most of the analysis presented in this Chapter: $\Omega_{\rm m} = 0.28$, $\Omega_{\Lambda} = 0.728$, $\Omega_{\rm b} = 0.045$, $\sigma_8 = 0.81$ and $h = 0.704$.

For all results presented in this Chapter, we use DHalo masses to represent the masses of dark matter haloes and subhaloes (Jiang et al., 2014b)[2]. For central galaxies, the halo mass quoted is the corresponding DHalo mass for that galaxy. For satellite galaxies, the halo mass quoted is the DHalo mass of the subhalo associated with that satellite galaxy at the last snapshot where the subhalo was identified before it became a satellite (i.e., before infall). DHalo masses are defined as the sum of the masses of subhaloes associated by the DHalo algorithm with that halo. In-

[2]We note that that the DHalo masses shown here are taken directly from GALFORM output. As such, they are distinct from the DHalo masses that are input into GALFORM because we impose mass conservation to ensure that all haloes most grow monotonically in mass.

dividual subhaloes are identified and masses assigned by the SUBFIND algorithm (Springel et al., 2001). SUBFIND first identifies overdense regions that are enclosed by an isodensity contour that traverses a saddle point. A gravitational unbinding procedure is then performed on the particles within these regions to define subhaloes (and therefore subhalo masses) as collections of gravitationally self-bound particles. This halo mass definition is not equivalent to the conventions followed by the abundance matching studies which we include for comparative purposes later in this Chapter (Behroozi et al., 2013b; Moster et al., 2013). We present a partial analysis of this effect, along with other differences in subhalo statistics between GALFORM and these abundance matching studies in Appendix E.

## 5.3 The predicted evolution in the SHM relation

In Fig. 5.2, we show the evolution in the SHM distribution from our reference model. To quantify the evolution in this distribution, we adopt the parametrisation of Moster et al. (2013), which relates median stellar mass at a given halo mass to halo mass by

$$\frac{M_\star}{M_\mathrm{H}} = 2N \left[ \left( \frac{M_\mathrm{H}}{M_1} \right)^{-\beta} + \left( \frac{M_\mathrm{H}}{M_1} \right)^{\gamma} \right]^{-1}, \tag{5.1}$$

where $N$ is a parameter controlling the normalisation, $M_1$ controls the position of the break, $\beta$ sets the power law slope below the break and $\gamma$ sets the slope above it. The role of each parameter can be seen intuitively in Fig. 5.1. The evolution in these parameters is shown in Fig. 5.3, along with results obtained using abundance matching from Moster et al. (2013) for comparison. Specifically, we show the evolution in SHM parameters using the best-fitting parametric evolution from Table 1 in Moster et al. (2013). These best-fitting SHM parameters were inferred from observational stellar mass function data from Pérez-González et al. (2008), Li & White (2009) and Santini et al. (2012). Compared to the results from Moster et al. (2013), our reference model predicts very modest evolution in most of the SHM parameters. Specifically, the $1\,\sigma$ posterior distributions for $\beta$, $M_1$ and $N$ are consistent

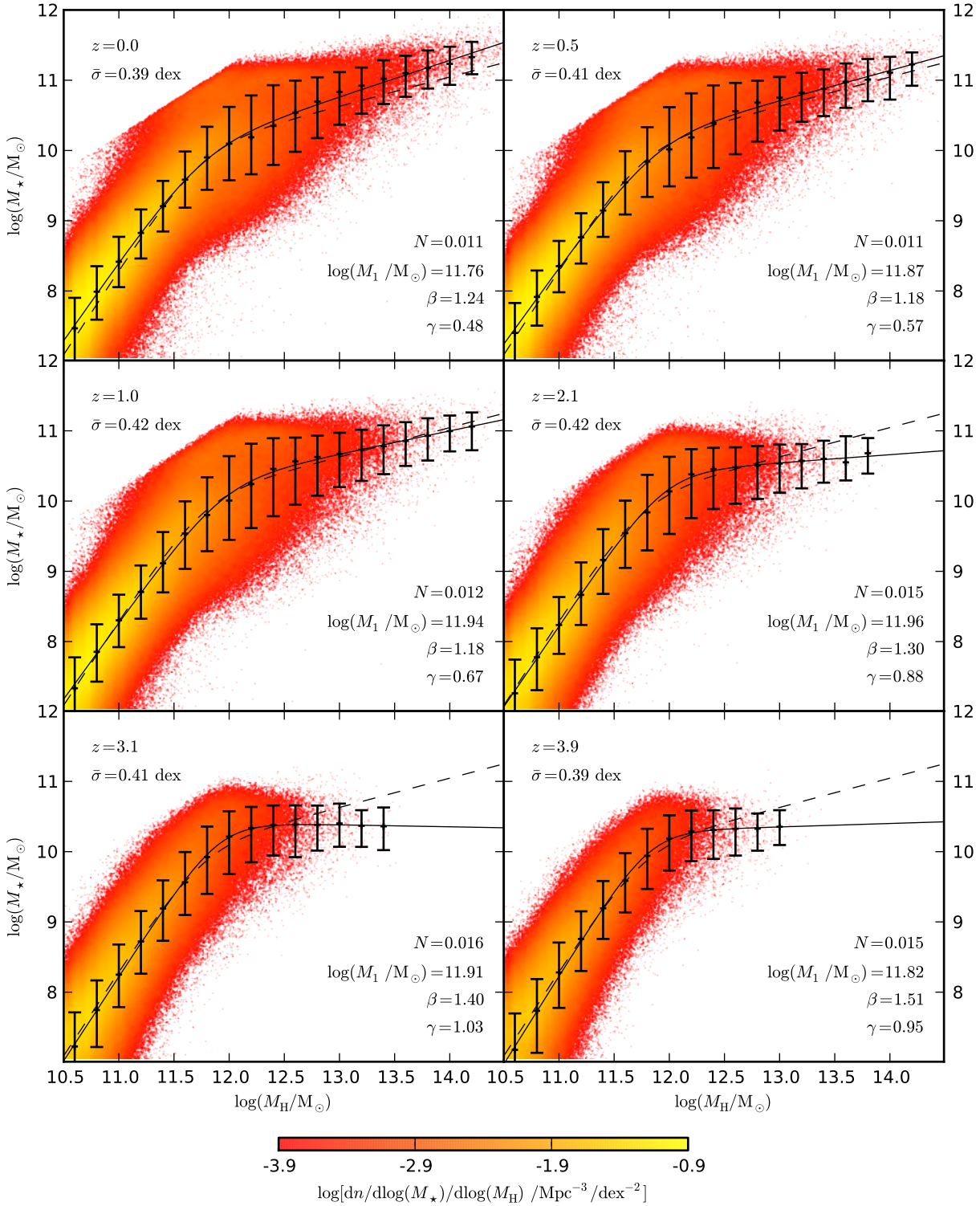


Figure 5.2: Caption continued on the following page.

Figure 5.2: Stellar mass plotted as a function of halo mass for our reference model. Each panel corresponds to a different redshift, as labelled. The coloured points represent individual model galaxies and the point colours are scaled with the logarithm of the local point density. The corresponding number densities are indicated by the colour bar at the bottom of the figure. The black points and corresponding error bars show the median, $16^{\rm th}$ and $84^{\rm th}$ percentiles of the distribution. $\bar{\sigma}$ quantifies the mean scatter in stellar mass within bins of halo mass above $\log(M_{\rm H}/M_{\odot}) = 10.5$. The scatter in each bin is defined as half of the central $68\%$ range in stellar mass. Black solid lines show the parametrisation given in Eqn 5.1, fit to the medians of the distribution. $N, M_1, \beta$ and $\gamma$ show the best-fitting parameters from this parametrisation. Black dashed lines show a corresponding fit but with the constraint that the fitting parameters do not evolve with redshift.

with there being no evolution in these parameters for $z < 4$. This is in contrast to the observational abundance matching results, which find comparatively strong evolution in $\beta$ and $M_1$ over the same redshift range.

To try and understand the reasons for the modest amount of evolution in the SHM relation predicted by our reference model, we split the overall population into subsamples of star forming, central passive and satellite galaxies. To split star forming and passive galaxies, we use the same cut in specific star formation rate against stellar mass as was used in Chapter 4. The evolution in the SHM relations for these subsamples are shown in Fig. 5.4, Fig. 5.5 and Fig. 5.6. Starting with star forming galaxies, in Fig. 5.4 we show how a sample of model galaxies that are central and star forming at $z = 0$ have evolved since $z = 2$. This shows directly that these model galaxies essentially evolve along an invariant power law in the $M_{\star}$ verses $M_{\rm H}$ plane. This power law is consistent with the overall SHM relation below the break mass ($M_1$), explaining why the overall SHM relation does not evolve significantly in this halo mass range.

In Fig. 5.5, we show a sample of central model galaxies that are star forming before $z = 2$ before becoming passive at $z < 2$. Specifically, we select galaxies that are star forming for $> 90\%$ of the simulation output times for $z > 2$ and are passive for $> 90\%$ of the simulation output times for $z < 2$. These galaxies are displaced

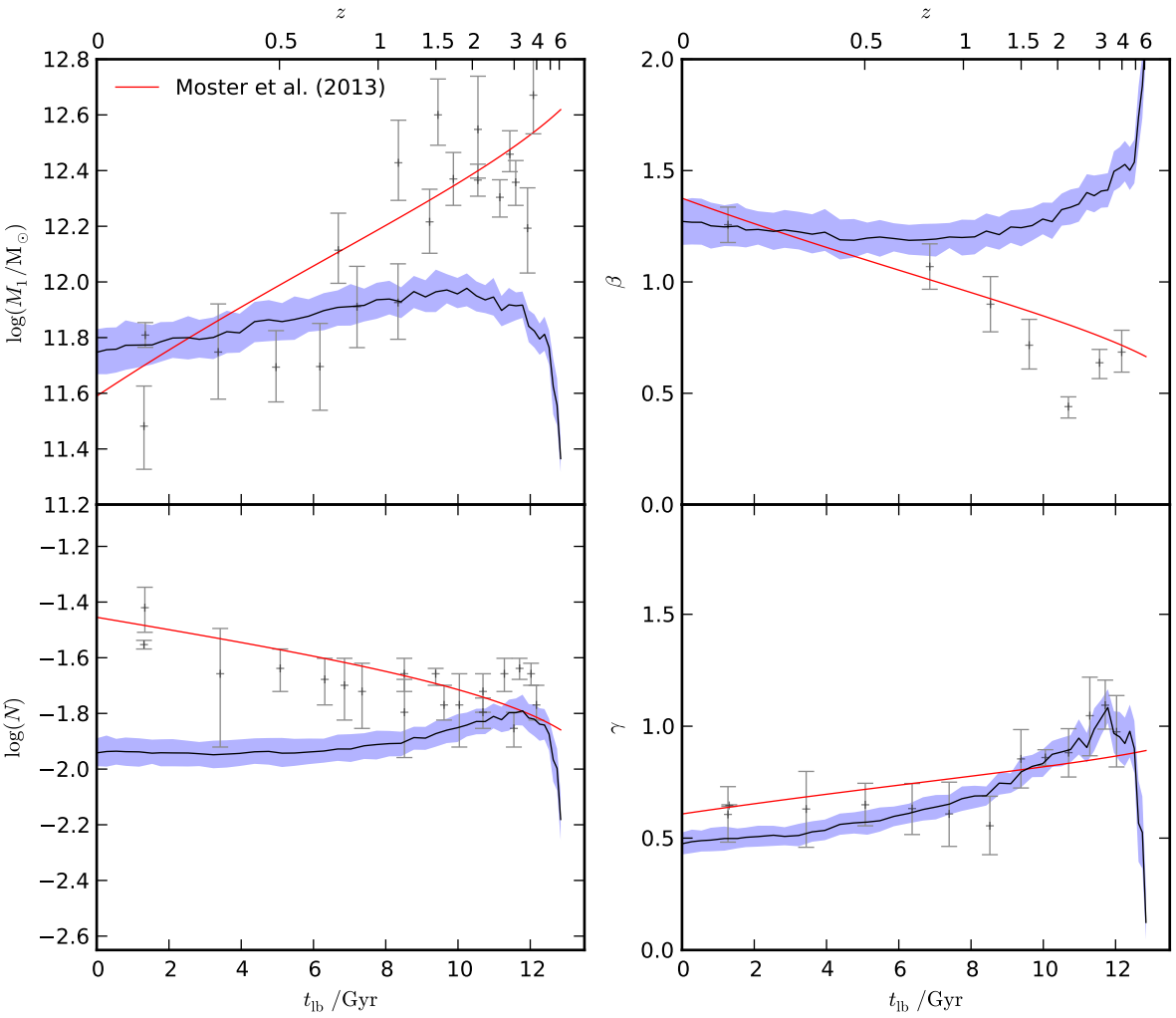


Figure 5.3: Evolution in fitting parameters for the median relationship between stellar mass and halo mass from our reference model. Black solid lines show the median of the projected posterior distribution for each parameter. Blue shaded regions show the $16^{\rm th}$ to $84^{\rm th}$ percentile range of the posterior distributions. Red solid lines show the best-fitting parametric evolution from Moster et al. (2013). Grey points show the associated best-fitting SHM parameters and $1\sigma$ errorbars determined by Moster et al. (2013) using single epoch abundance matching applied to individual stellar mass functions from the literature.

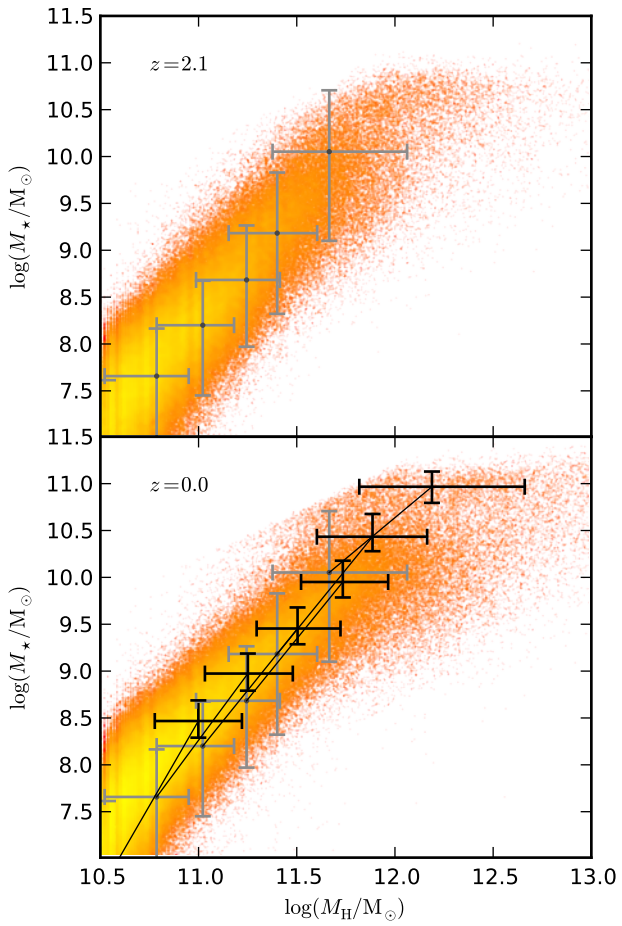


Figure 5.4: Evolution of star forming central galaxies in the stellar mass versus halo mass plane in our reference model. In both panels, the coloured points show the distribution from the entire galaxy population. *Top*: The distribution at $z = 2$. Grey points and corresponding error bars show medians and percentiles for a sample of model galaxies that are both central and star forming at $z = 0$. The sample is split into stellar mass bins (according to galaxy stellar mass at $z = 2$) and each point corresponds to a bin. The error bars show the $10^{\rm th}$ and $90^{\rm th}$ percentiles of each bin. *Bottom*: The distribution at $z = 0$. Grey points and error bars are the same as the grey points and error bars in the top panel. Black points and error bars show how the stellar mass bins from the top panel have evolved from $z = 2$ to $z = 0$.

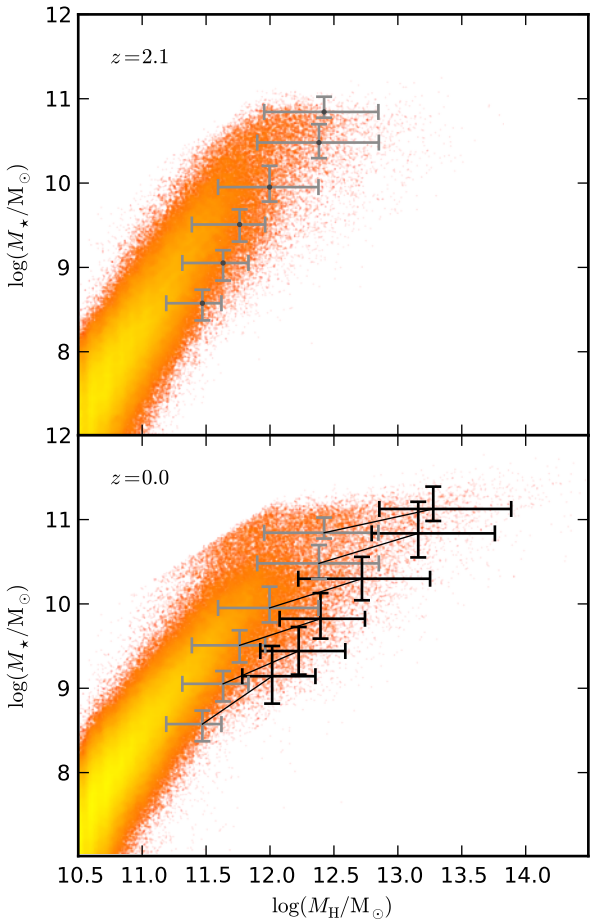


Figure 5.5: Evolution of passive central galaxies in the stellar mass versus halo mass plane in our reference model. In both panels, the coloured points show the distribution from the entire galaxy population. *Top*: The distribution at $z = 2$. Grey points and corresponding error bars show medians and percentiles for a sample of model galaxies that are star forming before $z = 2$ but are then passive after $z = 2$ and are central passive galaxies at $z = 0$. The sample is split into stellar mass bins (according to galaxy stellar mass at $z = 2$) and each point corresponds to a bin. The error bars show the $10^{\rm th}$ and $90^{\rm th}$ percentiles of each bin. *Bottom*: The distribution at $z = 0$. Grey points and error bars are the same as the grey points and error bars in the top panel. Black points and error bars show how the stellar mass bins from the top panel have evolved from $z = 2$ to $z = 0$.

from the median of the overall SHM distribution, preferentially residing in more massive haloes at a given stellar mass. It is apparent that these passive galaxies do not follow the same evolutionary path as the star forming galaxies shown in Fig. 5.4. Instead, the growth in their host dark matter haloes outpaces any stellar mass assembly through galaxy mergers. This behaviour creates the break in the SHM relation above $M_{\rm H} = M_1$, where passive central galaxies dominate the overall population.

Finally, for completeness, in Fig. 5.6 we show a sample of model galaxies that are central before $z = 2$ before becoming satellites after $z = 2$. Specifically, we select galaxies that are central for $> 90\%$ of the simulation output times before $z = 2$ and are satellites for $> 90\%$ of the simulation output times for $z < 2$. Fig. 5.6 shows the expected result that satellite galaxies are predicted by the model to not grow significantly in stellar mass after infall. This results in this version of GALFORM because of the implementation of hot gas stripping and SNe feedback [3]. By definition, the satellite halo masses are set as the mass of the associated subhalo at infall. Without any significant star formation activity after infall, satellites therefore simply remain frozen in place within the SHM plane. As the SHM relation below the break does not evolve significantly in our reference model, satellites do not become significantly displaced from the total SHM distribution after infall.

## 5.4 Physical reasons for the lack of evolution in the predicted SHM relation

### 5.4.1 Star forming galaxies

The extremely modest evolution in the median SHM relationship below $M_1$ found for our reference model is interesting given that the value of the low mass SHM slope, $1 + \beta$, is $\approx 2.3$ for $z < 4$. For clarity, we introduce here variables $\beta' \equiv 1 + \beta$

[3] hot gas is instantaneously stripped and strong SNe feedback typically ejects the majority of the cold gas

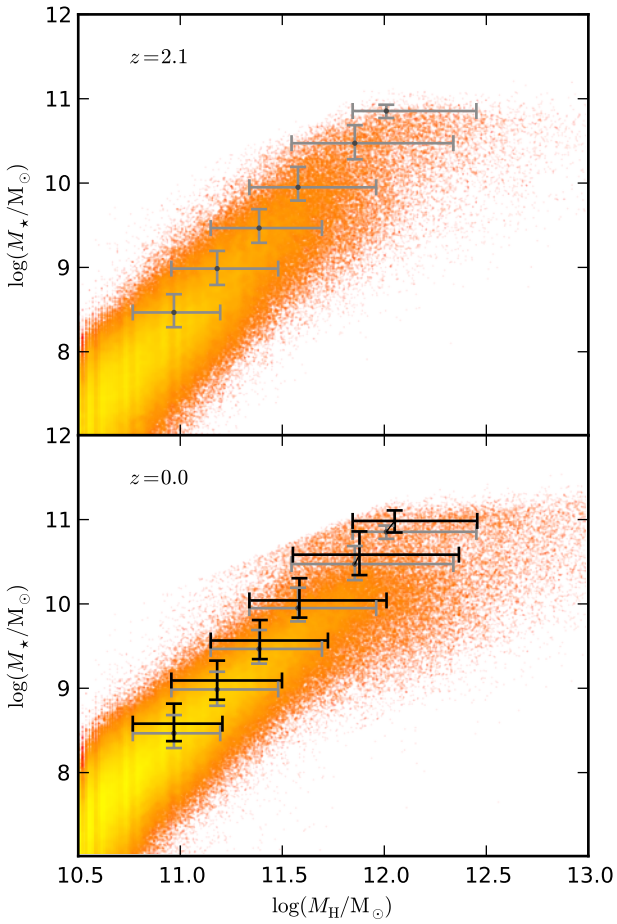


Figure 5.6: Evolution of satellite galaxies in the stellar mass versus halo mass plane in our reference model. In both panels, the coloured points show the distribution from the entire galaxy population. *Top*: The distribution at $z = 2$. Grey points and corresponding error bars show medians and percentiles for a sample of model galaxies that are central before $z \sim 2$ that then become satellites after $z \sim 2$. The sample is split into stellar mass bins (according to galaxy stellar mass at $z = 2$) and each point corresponds to a bin. The error bars show the $10^{\rm th}$ and $90^{\rm th}$ percentiles of each bin. *Bottom*: The distribution at $z = 0$. Grey points and error bars are the same as the grey points and error bars in the top panel. Black points and error bars show how the stellar mass bins from the top panel have evolved from $z = 2$ to $z = 0$.

and $\gamma' \equiv 1 - \gamma$ such that $M_\star \propto M_{\rm H}^{\beta'}$ for $M_{\rm H} << M_1$ and $M_\star \propto M_{\rm H}^{\gamma'}$ for $M_{\rm H} >> M_1$.

For star forming galaxies, it might be expected in the simplest case that the star formation rate, $\dot{M}_\star$, would simply track the accretion rate onto haloes, $\dot{M}_{\rm H}$. However, in this case individual galaxies would evolve along a power law in the SHM plane with slope, $\beta' = 1$. To evolve along a power law where $\beta' \approx 2.3$ requires instead that

$$\dot{M}_\star \propto M_{\rm H}^{1.3} \dot{M}_{\rm H}, \tag{5.2}$$

implying that stellar mass assembly increases in efficiency as the hosting haloes grow in mass. It should be noted that this also requires that at fixed halo mass, the instantaneous star formation efficiency,

$$\eta_{\rm SF} \equiv \dot{M}_\star / (f_{\rm B} \dot{M}_{\rm H}), \tag{5.3}$$

is constant across cosmic time (here, $f_{\rm B}$ is the cosmic baryon fraction). In Chapter 4, we showed that $\eta_{\rm SF}$ does evolve for populations of star forming galaxies in GALFORM as their haloes grow in mass. This occurs predominantly because of evolution in the mass loading factor for SNe feedback, $\beta_{\rm ml}$ (see Eqn 2.22 in Chapter 2.3.3), although a small amount of evolution in the gas reincorporation efficiency also contributes.

In GALFORM, $\beta_{\rm ml} \propto V_{\rm D}^{-\alpha_{\rm hot}}$, where $V_{\rm D}$ is the disk circular velocity. Roughly speaking, the disk circular velocity scales with the halo circular velocity, $V_{\rm H}$, in smaller haloes where self gravity effects are not important. These are the haloes that typically host star forming galaxies and also the haloes where SNe feedback plays the largest role in regulating star formation rates. Again, roughly speaking[4], it is expected that the instantaneous star formation efficiency, $\eta_{\rm SF}$, will scale with $(1 + \beta_{\rm ml})^{-1} \approx \beta_{\rm ml}^{-1}$ (see Chapter 4.4.2). Therefore, it is to be expected that in low mass haloes that host star forming galaxies,

[4]This is not a precise statement because finite gas reincorporation and freefall/radiative cooling timescales will cause the full effects of any instantaneous changes in $\beta_{\rm ml}$ to take time to propagate through the system of equations.

$$\eta_{\rm SF} \propto \beta_{\rm ml}^{-1} \propto V_{\rm D}^{\alpha_{\rm hot}} \propto V_{\rm H}^{\alpha_{\rm hot}} \propto M_{\rm H}^{\alpha_{\rm hot}/3} \left[\bar{\rho}_{\rm H}\right]^{\alpha_{\rm hot}/6}, \tag{5.4}$$

where $\bar{\rho}_{\rm H}$ is the mean halo density, which is related to $V_{\rm H}$ through

$$\bar{\rho}_{\rm H} = \frac{3M_{\rm H}}{4\pi R_{\rm H}^3}, \quad V_{\rm H}^2 = \frac{GM_{\rm H}}{R_{\rm H}}. \tag{5.5}$$

$\bar{\rho}_{\rm H}$ is independent of halo mass, but does instead depend on expansion factor through

$$\bar{\rho}_{\rm H} = \Delta_{\rm vir}(a)\bar{\rho}(a), \tag{5.6}$$

where $\Delta_{\rm vir}(a)$ is the overdensity of collapsed haloes and $\bar{\rho}(a)$ is the mean density of the Universe.

If we make the approximation that $\bar{\rho}_{\rm H}$ is constant across cosmic time, then straightforward integration of Eqn 5.4 yields

$$M_\star \propto M_{\rm H}^{1+\alpha_{\rm hot}/3}, \tag{5.7}$$

which, for the value of $\alpha_{\rm hot} = 3.2$ used by our reference model, yields $M_\star \propto M_{\rm H}^{2.07}$. This would imply $\beta' = 2.07$, close to the value, $\beta' = 2.3$ predicted by our reference model. Therefore, we see that the slope of the SHM relation primarily reflects the slope of the exponent in the SNe feedback relation, $\alpha_{\rm hot}$.

We note that the mean halo density, $\bar{\rho}_{\rm H}$, is not constant across cosmic time. However, in Appendix F we explain why this is not a bad approximation when integrating Eqn 5.4. We show that for $z > 1$, halo mass accretion rates greatly outpace the rate of change in $\bar{\rho}_{\rm H}$. Another very important effect is that, on average, halo densities evolve more slowly for haloes in GALFORM than would be given by the spherical collapse model. This is because halo circular velocities (and hence mean halo densities at fixed halo mass) are only updated to match the spherical collapse model in our reference model when haloes double in mass (see Chapter 2.8.2). This effect is particularly important for $z < 1$ when halo mass doubling events are rare.

### 5.4.2 AGN feedback

We now consider the modest evolution in the SHM break mass, $M_1$, predicted by our reference model. For the AGN feedback model implemented in GALFORM, gas cooling is suppressed in haloes where

$$t_{\rm cool}(r_{\rm cool}) > \alpha_{\rm cool}^{-1}\, t_{\rm ff}(r_{\rm cool}), \tag{5.8}$$

where $t_{\rm cool}$ is the radiative cooling timescale evaluated at a radius $r_{\rm cool}$, $\alpha_{\rm cool}$ is a model parameter and $t_{\rm ff}$ is the gravitational freefall timescale in a NFW halo. A simple scaling for how this AGN feedback threshold depends on halo mass can be obtained by evaluating $t_{\rm cool}$ at the mean gas density within the halo, $\bar{\rho}_{\rm g}$, such that

$$t_{\rm cool}(\rho_{\rm g} = \bar{\rho}_{\rm g}) = \frac{3}{2}\frac{k_{\rm B}T}{\mu m_{\rm p}}\frac{1}{\bar{\rho}_{\rm g}\Lambda(Z_{\rm g},T)}, \tag{5.9}$$

where $\Lambda(Z_{\rm g},T)$ is the cooling function and $T$ is the gas temperature at the mean density (e.g. Cole et al., 2000). Assuming the gas temperature is equal to the virial temperature of the halo, $T_{\rm vir}$, given by

$$T_{\rm vir} = \frac{1}{2}\frac{\mu m_{\rm p}}{k_{\rm B}}V_{\rm H}^2, \tag{5.10}$$

we obtain the scaling that

$$t_{\rm cool} \propto \frac{V_{\rm H}^2}{\bar{\rho}_{\rm g}\Lambda(T,Z)} \propto \frac{V_{\rm H}^2}{\bar{\rho}_{\rm H}\Lambda(T,Z)} \propto \frac{M_{\rm H}^{2/3}}{\bar{\rho}_{\rm H}^{2/3}}\frac{1}{\Lambda(T,Z)}. \tag{5.11}$$

For a fixed NFW halo concentration, the freefall timescale scales with the halo dynamical timescale, $t_{\rm dyn} = GM_{\rm H}/V_{\rm H}^3$, such that

$$t_{\rm ff} \propto t_{\rm dyn} \propto \frac{M_{\rm H}}{V_{\rm H}^3} \propto \bar{\rho}_{\rm H}^{-1/2}. \tag{5.12}$$

We can then evaluate Eqn 5.8 for $t_{\rm cool} = t_{\rm ff}$, yielding

$$\frac{M_{\rm H}^{2/3}}{\bar{\rho}_{\rm H}^{2/3}}\frac{1}{\Lambda(T,Z)} \propto \bar{\rho}_{\rm H}^{-1/2}, \tag{5.13}$$

which simplifies to

$$M_{\rm H} \propto \Lambda(T,Z)^{3/2}\bar{\rho}_{\rm H}^{-1/4} \propto \Lambda(T,Z)^{3/2}\left[\Delta_{\rm c}(a)\bar{\rho}(a)\right]^{1/4}. \tag{5.14}$$

In other words, we expect AGN feedback to suppress cooling (and therefore star formation) at a characteristic halo mass which is only weakly dependent on redshift ($M_{\rm H} \propto [\Delta_{\rm c}(a)\bar{\rho}(a)]^{1/4}$). This simple expectation is consistent with the modest evolution in the SHM break mass predicted by our reference model. We note that the temperature dependence of the cooling function will introduce an additional redshift dependence. However, the cooling function is approximately constant at low metallicity for temperatures $\approx 10^6\,{\rm K}$, which corresponds to virial temperature of haloes with masses close to the AGN feedback threshold mass ($M_{\rm H} \approx 10^{12}\,{\rm M}_\odot$).

### 5.4.3 Mergers

Finally, we give brief consideration to the evolution from $\gamma' \approx 0$ at $z = 4$ to $\gamma' \approx 0.5$ at $z = 0$ that is predicted by our reference model. In this halo mass regime above the SHM break, stellar mass assembly is dominated by galaxy mergers rather than star formation. Without galaxy mergers, stellar mass assembly essentially stops entirely, resulting in passive galaxies evolving along a power law consistent with $\gamma' = 0$ as their host haloes continue to grow in mass. In the opposite extreme where passive galaxies instantly merge after halo mergers, the expectation is instead that stellar mass assembly will simple trace the hierarchical halo assembly process. In this case, passive central galaxies evolve along a power law consistent with $\gamma' = 1$. Finite dynamical friction timescales for subhaloes mean that the first passive central galaxies will evolve along a $\gamma' = 0$ relationship at high redshift, delayed galaxy mergers will push $\gamma'$ to higher values with cosmic time.

## 5.5 Dependence on individual model parameters

Fig. 5.4 shows that in our reference model, the lack of evolution in the predicted median SHM relation is driven primarily by a characteristic evolutionary path that

star forming galaxies follow across the SHM plane. For star forming galaxies to evolve in this way requires a fairly specific evolution in the instantaneous star formation efficiency, $\eta_{\rm SF}$. This raises the question of whether this characteristic evolutionary path is a general prediction made by GALFORM, or just a feature specific to the combination of model parameters used in our reference model.

To answer this question, we now explore the evolution of the SHM relation predicted by models with alternative sets of model parameters. Changing individual model parameters in isolation will typically result in models that give a poor match to the local galaxy luminosity function. Nonetheless, this exercise is still useful for giving an idea as to the effect that each parameter has on the evolution of the median SHM relationship. A list of the model parameters which we consider for this exercise is presented in Table 5.1.

The results for the range in evolution of the SHM relation predicted by this model suite are shown in Fig. 5.7 and Fig. 5.8. In Fig. 5.7, we show the evolution in the fitting parameters for the parametric SHM relation given by Eqn 5.1. Comparing each variant model in turn with the reference model, it is clear that the modest evolution in the SHM relation predicted by the reference model is not a general prediction of GALFORM. Instead, the reference model appears to occupy a fairly unique position in the overall parameter space.

Fig. 5.8 shows an alternative view of this range in evolution, this time considering the evolution in fixed halo mass bins. Here, it becomes apparent that our reference model is most distinct from the variant models presented in Table 5.1 in the $\log(M_{\rm H}) = 11.6,\ 12.6$ mass range. We note that these are the bins that approximately bracket the SHM break mass, $M_1$. For the other two bins at the lowest and highest halo masses considered ($\log(M_{\rm H}) = 10.6,\ 13.6$), our reference model is more typical of the variant models we consider here for the predicted evolution.

| | |
|---|---|
| $V_{\rm hot}$ | Normalisation of SNe feedback. Set to $425\,{\rm km\,s^{-1}}$ in the reference model. Change such that the mass loading factor, $\beta_{\rm ml}$, changes up or down by a factor of three. |
| $\alpha_{\rm hot}$ | Dependence of SNe feedback on galaxy circular velocity. Set to $3.2$ in the reference model. Change up or down by $\pm 50\%$. Also change $V_{\rm hot}$ such that $\beta_{\rm ml}$ does is fixed for a circular velocity, $V_{\rm D} = 200\,{\rm km\,s^{-1}}$. |
| $\alpha_{\rm reheat}$ | Ejected gas reincorporation rate. Set to $1.26$ in the reference model. Change such that $1 + 2\pi\alpha_{\rm reheat}$ changes up or down by a factor of three. This factor corresponds to the approximate reincorporation efficiency, given by Eqn 4.22 in Chapter 4. |
| $\nu_{\rm sf}$ | Disk SF law normalisation. Set to $0.5\,{\rm Gyr^{-1}}$ in the reference model. Change up or down by a factor of three. |
| $\alpha_{\rm cool}$ | AGN feedback cooling suppression threshold. Set to $0.6$ in the reference model. Change up or down by a factor of three. |
| $\eta_{\rm disk}$ | Disk instability threshold. Set to $0.8$ in the reference model. Change up or down by a factor of three. |
| $f_{\rm dyn}$ | Burst duration factor. Set to $10$ in the reference model. Change up or down by a factor of three. |
| $f_{\rm df}$ | Rescaling factor for the dynamical friction timescale. Set to 1.5 in the reference model. Change up or down by a factor of three. |

Table 5.1: Description of the model parameters that are varied in Section 5.5 to produce the set of models shown in Fig. 5.7.

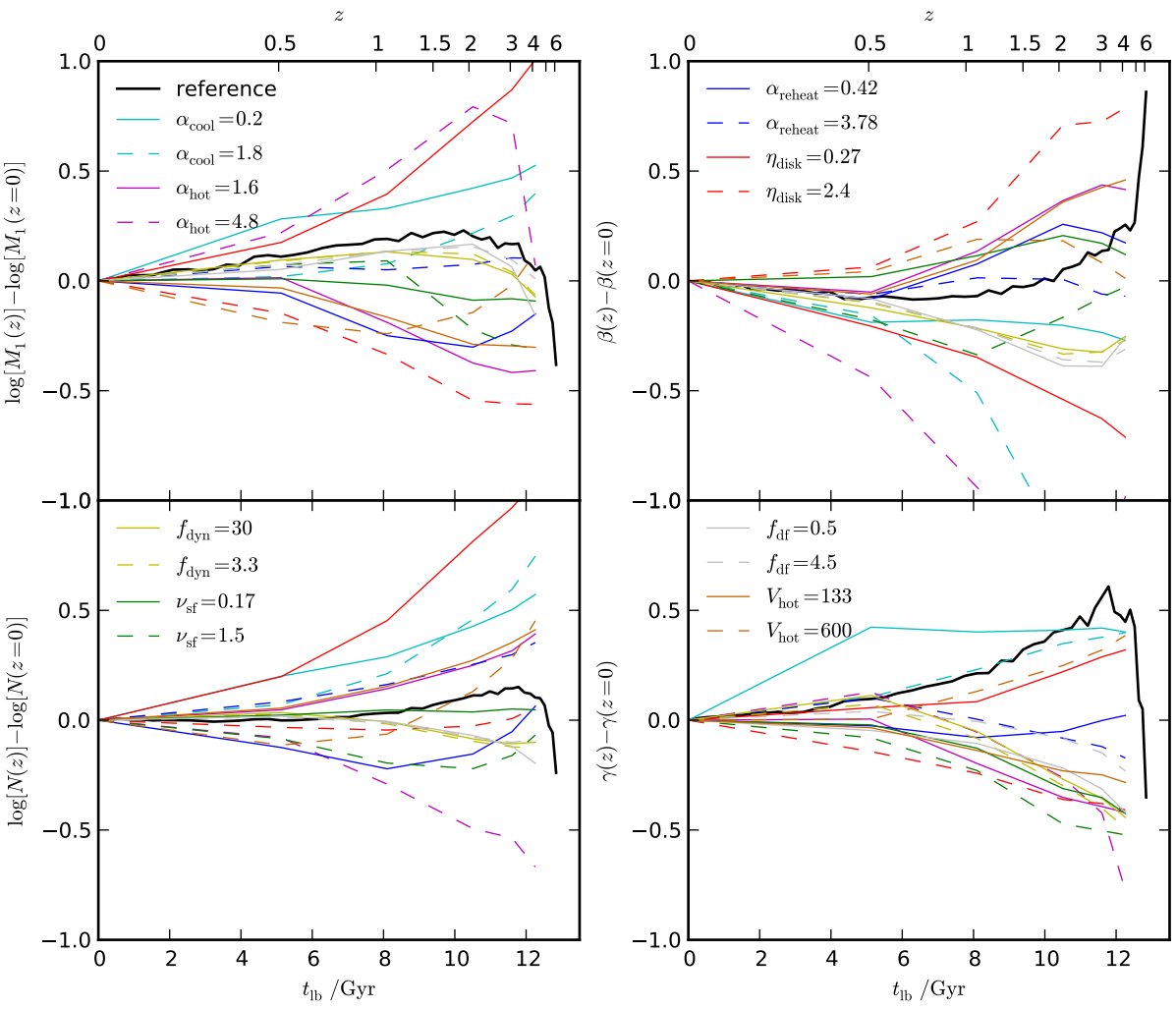


Figure 5.7: Evolution with respect to $z = 0$ of fitting parameters for the median SHM relation (see Eqn 5.1). Each line shows the median of the projected posterior distribution for a given parameter and model, as labelled. Each model has a single parameter varied with respect to the reference model, as described in Table 5.1.

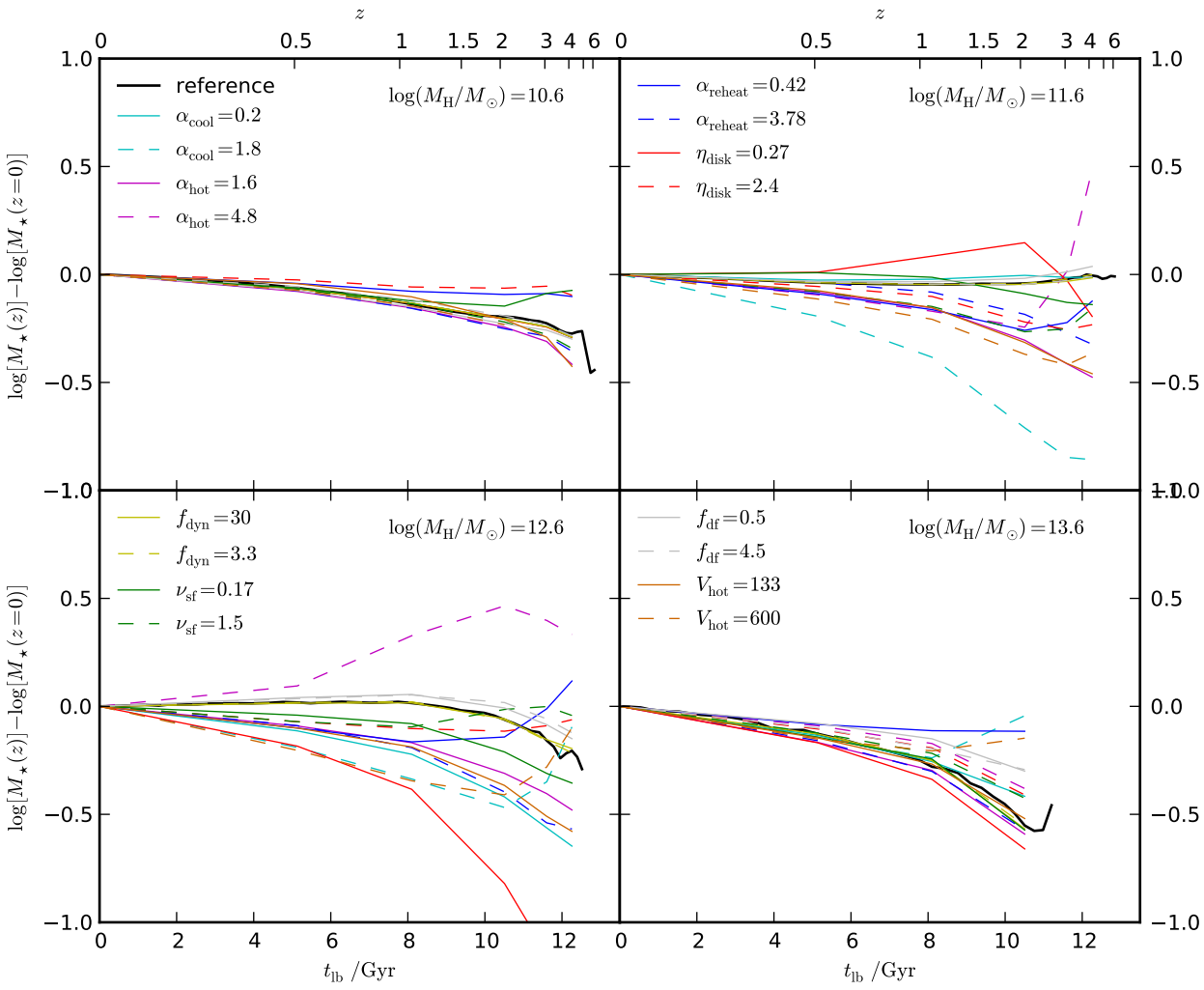


Figure 5.8: Evolution with respect to $z = 0$ in the median stellar mass within a given halo mass bin. Each panel corresponds to a different halo mass bin, as labelled. Each line shows the evolution in the median stellar mass for a given model, relative to the median stellar mass at $z = 0$. Each model has a single parameter varied with respect to the reference model, as described in Table 5.1.

## 5.6 Alternative models

Fig. 5.7 and Fig. 5.8 show that the small amount of evolution in the SHM relation seen for our reference model is not a general prediction of all GALFORM models. However, the set of models considered in Section 5.5 do not, in general, produce an acceptable match to the local stellar mass function. This then raises the question of how much variation in the evolution of the SHM relation can be predicted by a family of models that do provide an adequate fit to the local stellar mass function inferred from observations. Another way to phrase this is to ask the following. To what extent does the form of the local stellar mass function inferred from observations constrain galaxy formation models to predict a specific type of evolution in the SHM relation?

To answer this question properly would require constructing a full posterior distribution from the model parameter space to find all acceptable models, using the local stellar mass function as a constraint. Here, we take an intermediate step by instead considering only a limited number of different models which have been tuned to roughly match the local stellar mass function. These models encapsulate some of the variations which, through intuition, we expect to be interesting within the context of exploring why our reference model predicts very little evolution in the SHM relation.

Specifically, we consider five additional models, with model parameters which we outline in Table 5.2. Two of these models represent variations of the reference model from this Chapter. They use the same physics parametrisations as the reference model. These two variant models are chosen to highlight that there is a degeneracy between the reincorporation rate coefficient, $\alpha_{\rm reheat}$, and the normalisation of the mass loading factor, $V_{\rm hot}$. By either raising or lowering both of these parameters together, it is possible to preserve roughly the same stellar mass function as the reference model. This process also requires a slight adjustment to the AGN feedback threshold parameter, $\alpha_{\rm cool}$ to keep the break of the stellar mass function at the correct stellar mass. We refer to these two variant models as the strong feedback

| Model Parameter | Reference | SFB | WFB | M14 | SFH | VM |
|---|---|---|---|---|---|---|
| $\alpha_{\rm hot}$ | 3.2 | 3.2 | 3.2 | 3.2 | 3.2 | 3.2 |
| $V_{\rm hot}$ /km s$^{-1}$ | 425 | 700 | 300 | 485 | 485 | 485 |
| $\alpha_{\rm reheat}$ | 1.26 | 8.0 | 0.3 | 1.26 | 0.023 | 0.24 |
| $\alpha_{\rm cool}$ | 0.6 | 0.65 | 0.4 | 1.0 | 1.3 | 1.0 |

Table 5.2: Model parameters used in the five variant models explored in Section 5.6. $\alpha_{\rm hot}$ sets the mass loading dependence on circular velocity, $V_{\rm hot}$ sets the mass loading normalisation, $\alpha_{\rm reheat}$ sets the reincorporation rate and $\alpha_{\rm cool}$ controls the AGN feedback threshold. The variant models considered here include the strong and weak feedback models (SFB and WFB), which feature stronger/weaker feedback but with shorter/longer reincorporation timescales to compensate. M14 is the reference model from Chapter 4. The star formation history (SFH) and virial mass (VM) models feature different modifications to the reincorporation timescale, as described in the text.

(SFB, high mass loading, fast reincorporation) and the weak feedback (WFB, low mass loading, slow reincorporation) models.

The other three models which we consider here are the three models presented in Chapter 4. For this Chapter, we are primarily interested in the two models from Chapter 4 that featured modified parametrisations for the reincorporation timescale. However, the models presented in Chapter 4 were run on merger trees extracted from the original Millenium simulation, which assumed a WMAP-1 cosmology (Springel et al., 2005). Therefore, to act as a point of comparison for these two modified reincorporation models, we also include the reference model from Chapter 4. In this Chapter, we refer to the reference model from Chapter 4 as the M14 model. In addition to the changes in merger trees and cosmological parameters, the three models taken from Chapter 4 also use the updated cooling scheme from Benson & Bower (2010). For reference, the default GALFORM reincorporation timescale parametrisation (as used in the M14, reference, SFB and WFB models) is given by

$$\dot{M}_{\rm ret} = \frac{\alpha_{\rm reheat}}{t_{\rm dyn}} M_{\rm res}, \tag{5.15}$$

where $\dot{M}_{\rm ret}$ is the gas reincorporation rate, $\alpha_{\rm reheat}$ is a dimensionless model parameter, $t_{\rm dyn}$ is the halo dynamical timescale and $M_{\rm res}$ is the mass in a reservoir of gas ejected from the galaxy by SNe feedback.

The first of the two modified reincorporation models from Chapter 4 which we consider here, referred to here as the star formation history (SFH) model, was designed to try to reproduce the shapes of star formation histories for star forming galaxies inferred from observations. For all but the most massive star forming galaxies, this model reproduces the trend implied by observational data that the specific star formation rate at fixed stellar mass has declined exponentially from high redshifts to today. With respect to our reference model, the SFH model uses a different parametrisation for the reincorporation rate, $\dot{M}_{\rm ret}$, given by

$$\dot{M}_{\rm ret} = \frac{\alpha_{\rm reheat}}{t_{\rm dyn}} \left( \frac{M_{\rm H}}{10^{10} {\rm M}_{\odot} h^{-1}} \right) F(z) M_{\rm res}, \tag{5.16}$$

where $t_{\rm dyn}$ is the halo dynamical time and $F(z)$ is a function given by

$$\log[F(z)] = 6 \, \exp \left[ \frac{-(1+z)}{3} \right] \log_{10}[1+z]. \tag{5.17}$$

This parametrisation has no physical motivation and essentially just represents an empirical fit to the peaked star formation histories inferred for star forming galaxies in Chapter 4. This is achieved by making reincorporation rates very slow at early times when haloes have yet to accrete most of their mass. The exponential function then dramatically lengthens the reincorporation timescale at late times to achieve the exponential drop in star formation rates implied by observational data.

The final model from Chapter 4, referred to here as the virial mass (VM) model, uses the reincorporation parametrisation advocated by Henriques et al. (2013) and Henriques et al. (2014). This parametrisation is given by

$$\dot{M}_{\rm ret} = \frac{\alpha_{\rm reheat}}{1 \, {\rm Gyr}} \left( \frac{M_{\rm H}}{10^{10} {\rm M}_{\odot} h^{-1}} \right) M_{\rm res}. \tag{5.18}$$

In Appendix D, we show that this model produces a good fit to the evolution inferred from observations in the stellar mass function below the break.

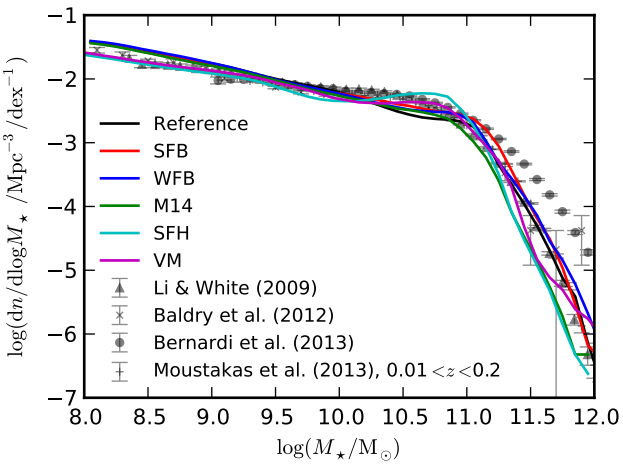


Figure 5.9: Stellar mass function at $z = 0$ for the models described in Table 5.2. Each line corresponds to a different model, as labelled. Points and associated errorbars show observational estimates of the local stellar mass function from Li & White (2009), Baldry et al. (2012), Bernardi et al. (2013) and Moustakas et al. (2013).

Before proceeding to analyse the predicted evolution in the SHM relation from the six models presented in Table 5.2, we first show in Fig. 5.9 the stellar mass function at $z = 0$ for this family of models. None of the models precisely match the shape of the stellar mass function inferred from observations. Specifically, all models underpredict the abundance of galaxies just below the knee. Furthermore, all but the VM and SFH models predict an overabundance of galaxies at the low mass end. For this analysis however, we simply require that each model give a similar level of agreement as the reference model to the observational estimates of the local stellar mass function. As such, we consider the consistency between the models and data shown in Fig. 5.9 to be acceptable for our purposes.

Fig. 5.10 shows the median SHM relation from the family of models presented in Table 5.2 for a range of redshifts. Before proceeding to analyse the results, we first note that when comparing evolution predicted by different models, we expect the most prominent (and interesting) differences between the models will be displayed for halo masses both around and below the break in the SHM relation ($\log(M_{\rm H}/M_{\odot}) < 12.5$). The reason for this expectation is that this is the halo mass

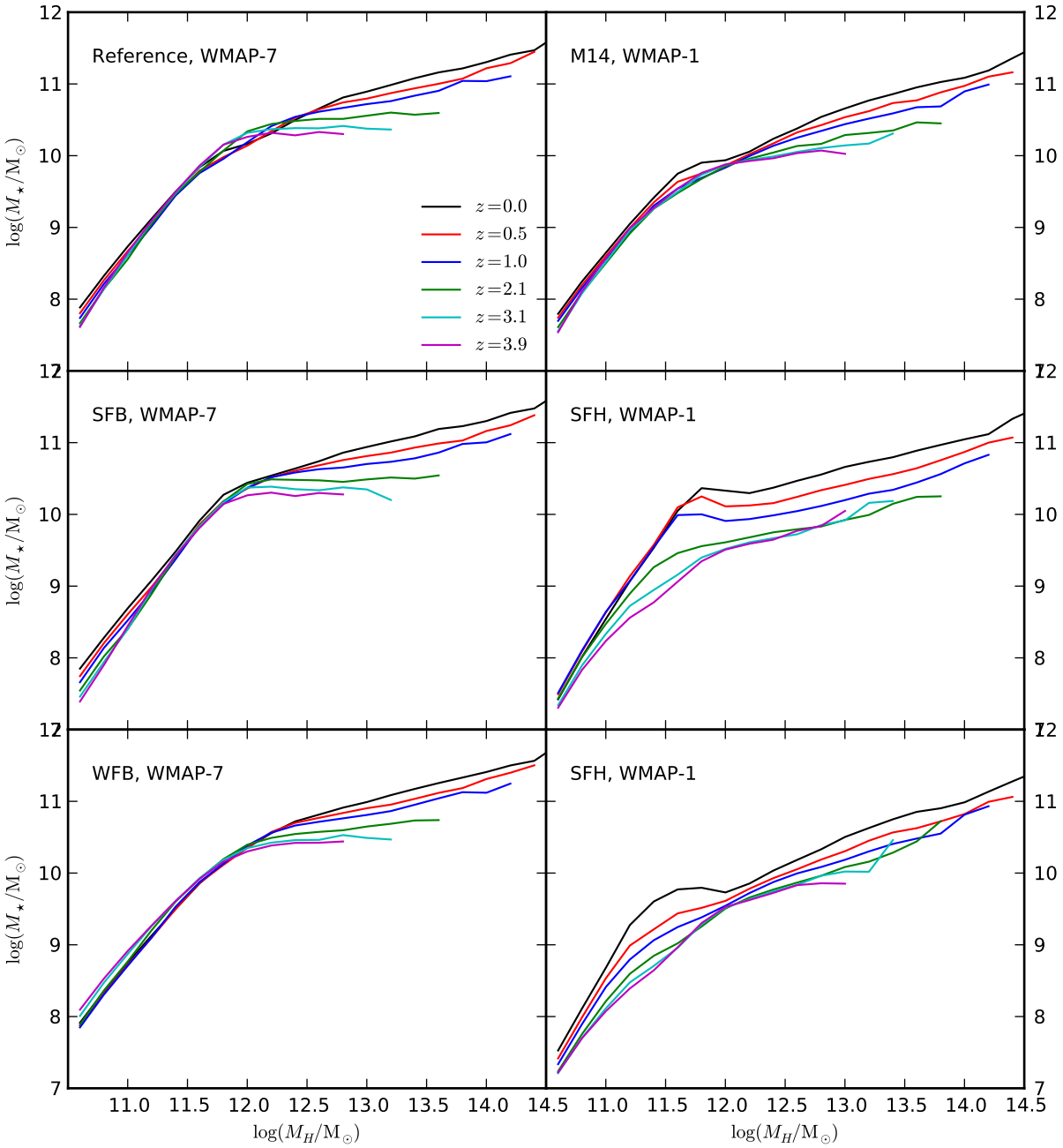


Figure 5.10: Median stellar mass as a function of halo mass for the models described in Table 5.2. Each panel corresponds to a different model, as labelled. The cosmological parameter set used for each model is also labelled.

range which contains star forming galaxies. In more massive haloes, stellar mass assembly takes place primarily through mergers, and the details of the SHM relation will be primarily determined by AGN feedback and the merging parametrisations, which we do not vary outside of adjusting the AGN feedback threshold, $\alpha_{\rm cool}$ [5]. The variant models here are instead primarily distinct from each other in the parametrisations and parameters adopted for feedback and gas reincorporation. These are processes that affect the actively star forming galaxy population.

By examining Fig. 5.10, it is apparent that for halo masses above the SHM break, all the models display similar evolution (although not identical) in the SHM relation. This presumably reflects the fact that we do not change the AGN feedback model (beyond the threshold) or the galaxy-galaxy merging timescale between the different models. At and below the break ($\log(M_{\rm H}/M_{\odot}) < 12.5$), larger variations between some of the models become apparent. Specifically, it can be seen that the trend for the SHM relation below the break to remain approximately constant with redshift is displayed for all the models (Reference, WFB, SFB, M14) using the standard reincorporation timescale. This is not an exact statement and the dynamic range displayed in Fig. 5.10 is large [6]. Comparatively, the SFH and VM models display much more significant evolution at and below the SHM break. For the SFH model in this halo mass range, the SHM relation evolves significantly for $z \geq 2$ before becoming fixed in place for $z \leq 1$. This can be understood given that the model was designed implicitly to force star formation rates at fixed stellar mass to drop exponentially with cosmic time. The VM model also displays significant evolution in the SHM relation but in this case the evolution also occurs for $z \leq 1$. This behaviour can be understood because the VM model is designed implicitly to increase star formation rates at late times relative to the standard reincorporation parametrisation used in the Reference, WFB, SFB and M14 models.

Another view of the evolution of the SHM relation is shown in Fig. 5.11, which

[5] To first order, $\alpha_{\rm cool}$ can be considered a parameter which only controls the break mass in the SHM relation.

[6] The more subtle variations between the Reference, WFB, SFB and M14 models are better viewed with lower dynamic range, which we address with subsequent figures.

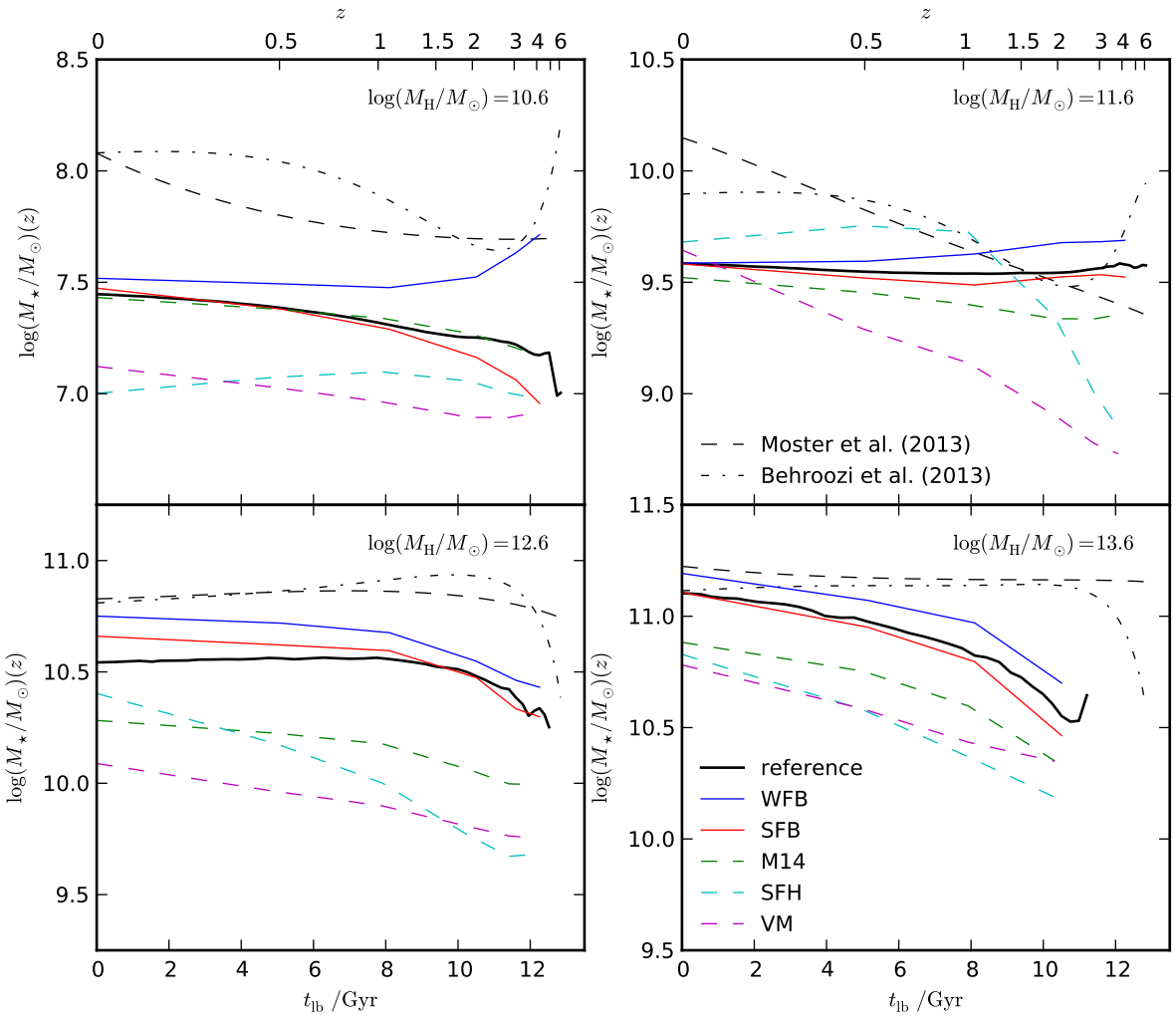


Figure 5.11: Evolution in the median stellar mass within a given halo mass bin. Each panel corresponds to a different halo mass bin, as labelled. Each solid line shows the median stellar mass for models that use a WMAP-7 cosmology. Coloured dashed lines show the median stellar mass for models that use a WMAP-1 cosmology. Black dashed and dash-dotted lines show the best-fit parametric SHM relations from Moster et al. (2013) and Behroozi et al. (2013b) respectively.

shows the evolution in median stellar mass at fixed halo mass. Here, for comparison, we also show the SHM evolution inferred using abundance matching from Moster et al. (2013) and Behroozi et al. (2013b). As in Fig. 5.10, the VM and SFH models are clearly distinct in that they predict significant evolution in the $\log(M_{\rm H}/M_{\odot}) = 11.6$ bin. This is also the bin where the abundance matching results display the most significant evolution. Again, it is apparent that all of the models predict very similar evolutionary trends for the most massive haloes ($\log(M_{\rm H}/M_{\odot}) = 13.6$ bin). It is interesting to note that this is contrary to abundance matching results which imply minimal evolution in this mass range.

Fig. 5.11 also shows more subtle differences between the models. For example, in the $\log(M_{\rm H}/M_{\odot}) = 10.6$ bin, the WFB and SFB models both clearly start to diverge in opposite directions from the reference model for $z \geq 1$. This demonstrates how the degeneracy between $\alpha_{\rm reheat}$ and $V_{\rm hot}$ in the SHM relation at $z = 0$ in this halo mass range is broken by considering the evolution.

An alternative view of the evolutionary behaviour in the SHM relation is presented in Fig. 5.12, which shows the evolution in the fitting parameters from Eqn 5.1. In this case, it is only possible to make the comparison with the results from Moster et al. (2013), which share the same parametrisation for the SHM relation. We note that when considering results using the Moster et al. (2013) SHM parametrisation, it should be kept in mind that this parametrisation does not provide a good fit to the SHM relations for the SFH and VM models at lower redshifts (see Fig. 5.10).

Starting with the break mass in the SHM relation, $M_1$, Fig. 5.12 shows that the models we consider predict very little evolution. The exception is the VM model, which predicts that the break mass drops by $\sim 0.7\,{\rm dex}$ between $z = 0$ and $4$. This is in contrast to the trend inferred from Moster et al. (2013), who favour an increase in the break mass towards high redshift. For the normalisation of the SHM relation at the break, $N$, most of the models we consider predict minimal evolution, consistent with Moster et al. (2013). The exceptions are the VM and SFH models, where $N$ starts to increase after $z = 0.5$ and $z = 1$ respectively.

For the low mass SHM slope, $\beta$, the differences between the different models

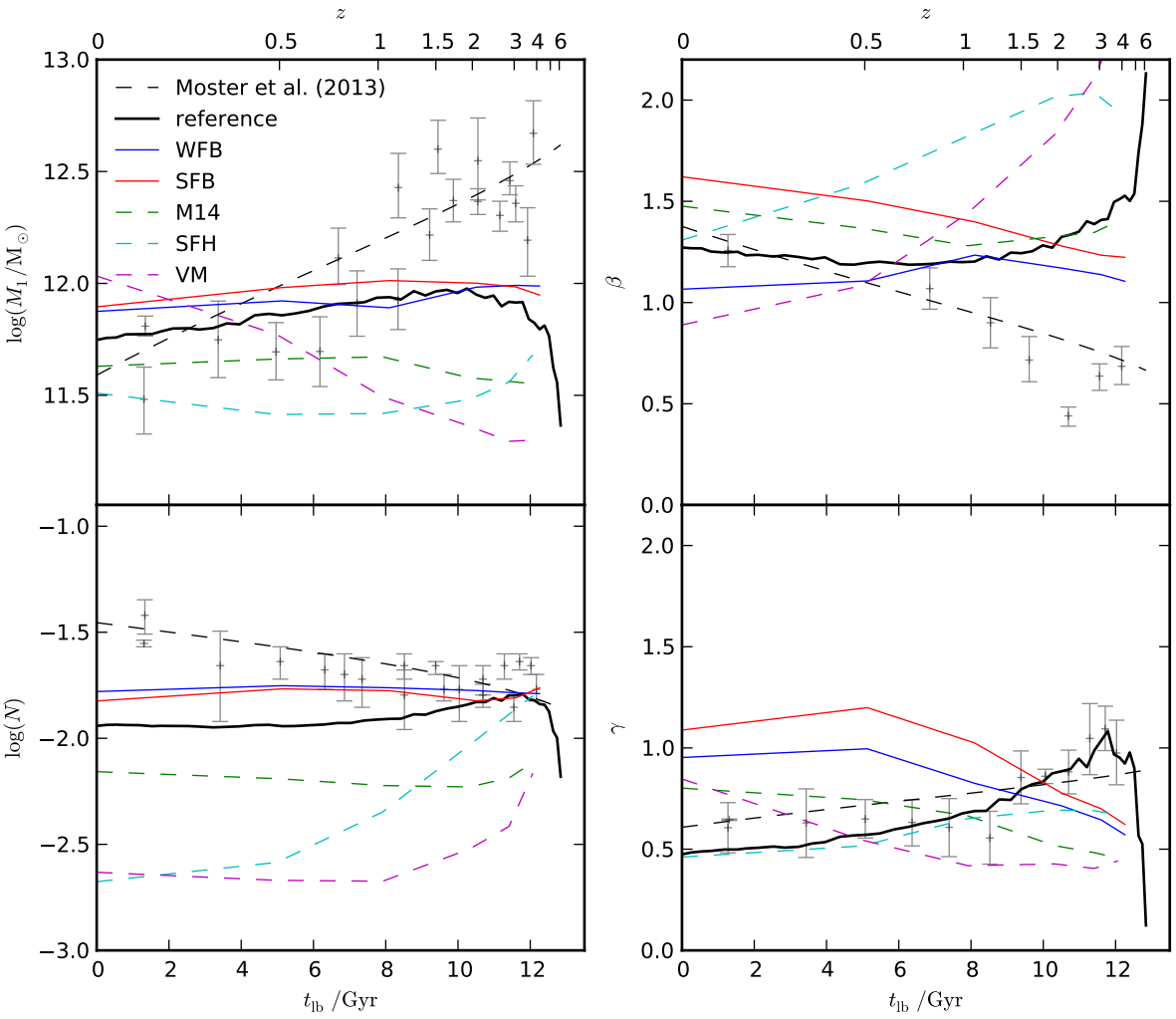


Figure 5.12: Evolution in fitting parameters for the median SHM relation. Solid lines show the median of the projected posterior distribution for models that use a WMAP-7 cosmology. Coloured dashed lines show the median of the projected posterior distribution for models that use a WMAP-1 cosmology. The black dashed lines show the best-fit parametric evolution in the SHM relation from Moster et al. (2013). Datapoints show the SHM parameters from Moster et al. (2013), derived from applying abundance matching to stellar mass functions in single redshift bins.

become more apparent. The WFB and SFB models again bracket the evolution predicted by the reference model. The VM and SFH models predict that $\beta$ increases substantially with lookback time, in contrast to the M14 model and Moster et al. (2013), demonstrating the importance of the reincorporation timescale parametrisation in galaxy formation models. For the high mass SHM slope, $\gamma$, the models we consider all predict fairly modest evolution, consistent with Moster et al. (2013).

## 5.7 Discussion

In Chapter 4 we found that it was necessary to modify the parametrisation of one of the physical processes in our model that is relevant for star forming galaxies. As one of the most uncertain aspects of our modelling approach, we chose to modify the reincorporation timescale to illustrate this point. However, we then found that two contradictory modifications to the reincorporation timescale were required to explain the evolution of the stellar mass function versus the evolution of star formation rates in star forming galaxies. Specifically, we introduced the SFH model to reproduce the star formation rate evolution inferred from observations and the VM to reproduce the evolution of the stellar mass function.

Given that these modifications to the reincorporation timescale have a significant impact on predicted stellar mass functions and star formation rates, one naturally expects differences to also appear in the predicted evolution of the SHM relation. We find that this is indeed the case close to the break in the SHM relation. However, neither of our modified models predict evolution that closely resembles results from abundance matching studies of Moster et al. (2013) and Behroozi et al. (2013b), despite claims from those studies that they reproduce both the star formation rates and the stellar mass assembly inferred from observations. This is puzzling, particularly given that reproducing the evolution in star formation rates and/or stellar mass functions inferred from observations is a problem that appears to be common for a wide range of contemporary models and simulations (e.g. Lamastra et al., 2013; Furlong et al., 2014; Cousin et al., 2015; Sparre et al.,

2015), although see also Henriques et al. (2014).

While this could reflect a failing of our modelling approach, there are various factors that need to also be taken into consideration. As discussed in Appendix E, we have good reason to suspect that the absolute SHM callibration will be different between GALFORM and these abundance matching studies as a result of differences in halo mass definitions and satellite halo abundances. Another important uncertainty is the fact that abundance matching approach does not, at present, distinguish between star forming and passive galaxy populations at a given halo mass (although see Hearin & Watson, 2013; Watson et al., 2015). This is likely to be problematic close to the SHM break mass, where the dominant central galaxy population gradually transitions between star forming and passive galaxies. We note that this is precisely the most interesting halo mass range for distinguishing between the different models considered in our analysis.

Another important consideration is that the recent estimates of the stellar mass function from deep Ultra-VISTA and ZFOURGE data display significant differences with respect to older observational estimates, particularly above $z = 2$ (Ilbert et al., 2013; Muzzin et al., 2013a; Tomczak et al., 2014). These more recent datasets are important for distinguishing between different GALFORM models, identifying the VM model as the preferred model if the inferred stellar mass functions are free from significant systematics (see Appendix D). It will be interesting to see if estimates of the SHM from abundance matching change significantly once these more recent datasets are included as constraints.

## 5.8 Summary

We have explored the evolution of the median SHM relation predicted by different versions of the semi-analytic galaxy formation model, GALFORM. For our reference model, where the return timescale for gas ejected from galaxies by SNe feedback scales with the halo dynamical timescale, we find that the median SHM evolves only very modestly between $z = 0$ and $z = 4$. This implies that the efficiency of

stellar mass assembly (star formation plus galaxy mergers) within haloes at fixed halo mass is approximately independent of cosmic time (see Behroozi et al., 2013a, for a discussion of this point). In our model, this behaviour is primarily driven by the evolution of the efficiency of SNe feedback in regulating star formation rates of actively star forming galaxies. This efficiency drops as haloes grow in mass, resulting in star forming galaxies evolving along a power law given by $M_\star \propto M_{\rm H}^{2.3}$. Another factor in the predicted lack of evolution in the SHM relation is the AGN feedback model implemented within GALFORM. Specifically, the threshold for AGN feedback to become effective at suppressing gas cooling in haloes in the model corresponds to a halo mass which is only weakly dependent on cosmic time. This causes the break mass in the SHM relation predicted by GALFORM to evolve only very modestly.

To reproduce the shape of the local stellar mass function inferred from observations requires a particular form for the median SHM relation at $z = 0$. We show that with this single constraint in place, standard [7] semi-analytic galaxy formation models tend not to predict significant evolution in the SHM relation. This behaviour is broken close to the SHM break mass (closely connected the knee of the stellar mass function) for the models introduced in Chapter 4 that feature modified gas reincorporation timescales. At present, abundance matching studies (Behroozi et al., 2013b; Moster et al., 2013) do not strongly support either of these modified GALFORM models. It is unclear to what extent this simply reflects failings of all the GALFORM models considered in this analysis. Alternatively, we find that disagreements could also simply reflect the differences in the observational constraints, halo mass definitions and satellite abundances used in GALFORM compared to these abundance matching studies.

[7] By this we mean models where the efficiency of gas reincorporation after ejection by feedback evolves only weakly across cosmic time.

# Chapter 6 | *Conclusions*

## 6.1 Summary

Semi-analytic galaxy formation models are now an established tool for understanding galaxy formation and evolution within the context of the hierarchical structure formation paradigm. For the semi-analytic model, GALFORM, there are several established variants of the model which have undergone only fairly minor revisions over almost a decade (Baugh et al., 2005; Bower et al., 2006). During this time, observational data from multi-wavelength surveys have dramatically improved our knowledge of how the galaxy population has evolved over cosmic time. In this thesis, we have explored how these established GALFORM models hold up when faced with some of these observational results.

In Chapter 3, we test how well standard observational SED fitting techniques perform at estimating stellar masses from the photometry of simulated model galaxies. From this analysis, we arrived at the following conclusions:

- We find that assumption, commonly adopted in SED fitting, of exponentially declining star formation histories does not bias stellar mass recovery when considering the galaxy population as a whole. On the other hand, we find this parametric form for star formation histories is inappropriate when applied to model galaxies undergoing bursts of star formation, leading to systematic stellar mass underestimation with significant scatter.

- We find that the assumption, commonly adopted in SED fitting, of a coarse grid of metallicities can have an adverse effect on stellar mass estimation. This problem can be alleviated simply by interpolating between a coarse metallicity grid.

- We find that the assumption, commonly adopted in SED fitting, of a dust law which physically corresponds to a uniform foreground dust screen can cause significant underestimation of stellar masses in optically thick model galaxies. The impact of this systematic could be exaggerated in importance when applied to GALFORM because of the small galaxy sizes for dusty star forming galaxies predicted by the model.

Chapter 3 also serves as a proof of concept for a methodology where SED fitting is applied to model galaxies to constrain the role of systematics when comparing model predictions with intrinsic galaxy properties inferred from observations. As an example, we use the stellar mass function to illustrate this process.

In Chapter 4, we analyse the implications of the result inferred from a large number of observational studies which indicate that, at a given stellar mass, the average star formation rate of the actively star forming galaxy population has dropped exponentially across cosmic time. We show that this implies that the star formation histories of galaxies that are still star forming today peaked at $z \approx 2$.

In contrast, semi-analytic galaxy formation models such as GALFORM tend to predict corresponding star formation histories which are flat or slowly rising. We explain how this behaviour predicted by the model is determined by a combination of halo accretion rates and the implementation of SNe feedback and associated gas reincorporation rates. We demonstrate, as an example, that a modification to the gas reincorporation timescale can be designed to empirically fit the shape of the star formation histories implied by observational data. With this modification, gas reincorporation rates are artificially suppressed at both early and late times, resulting in peaked star formation histories. Finally, we show that this modification does not produce a good match the evolution of the stellar mass function inferred from observations. Another model, with a different modification to the gas reincorporation timescale, can reproduce the stellar mass function evolution but is in very poor agreement with the star formation histories inferred from observational data.

In Chapter 5, we analyse the evolution predicted by GALFORM for the me-

dian SHM (stellar mass versus halo mass) relationship. This analysis is performed within the context of the large amount of attention from the community in recent years in inferring this evolution by using statistical inference to construct empirical models. We show that within GALFORM, the SHM relation does not evolve significantly over cosmic time in all but the most massive haloes. This occurs in the model because star forming galaxies evolve along a power law that is aligned with the median SHM relation, and because satellite galaxies do not evolve significantly in stellar mass after infall. Central passive galaxies do evolve off the power law path traced by star forming galaxies because they grow more strongly in halo mass compared to stellar mass. This means that the predicted SHM relation steepens with cosmic time in the most massive haloes.

We show that the predicted evolutionary path traced by star forming galaxies in GALFORM is caused primarily by the evolving efficiency of SNe feedback, which decreases as haloes grow in mass. We also show why the break mass in the SHM relation (caused by the transition between radiative cooling and freefall regimes for gas infall) evolves weakly with cosmic time because of the implementation of AGN feedback in the model. We investigate how the predicted evolution in the SHM relation is sensitive to different models parameters, finding that standard GALFORM models do occupy a somewhat unique position within the overall model parameter space. However, we then go on to show that with the local stellar mass function inferred from observations applied as a constraint, the lack of evolution in the predicted SHM relation does appear to emerge as a general property of different GALFORM models. However, this result does not hold for the models with modified reincorporation timescales from Chapter 4, for which the predicted SHM relation does evolve significantly over cosmic time. We find that current abundance matching studies do not appear to strongly distinguish between any of these competing models.

## 6.2 Future Work

A recurring issue with the work presented in this thesis is the question of whether GALFORM predicts realistic galaxy sizes for star forming galaxies. Preliminary work which does not appear in this thesis suggests that there are significant differences between observed and predicted galaxy sizes as a function of both stellar mass and redshift. This is highly significant for the results from this thesis because of how galaxy sizes determine the strength of SNe feedback and dust attenuation corrections in GALFORM. We plan to expand on our preliminary work on comparing model predictions with observational data from HST CANDELS data (van der Wel et al., 2014).

As a related project, we plan to expand upon work from Lagos et al. (2011b) and Lagos et al. (2013) who introduced a split between molecular and atomic gas as well as the new parametrisations for SNe feedback discussed in Chapter 4. Rather than parametrise the mass loading factor, $\beta_{\rm ml}$, as a global average a galaxy, we plan to integrate the $\beta_{\rm ml}$ evaluated locally in annuli. This has the significant advantage in that it allows a corresponding angular momentum loading factor to be calculated following an angular momentum weighted integral. Combined with changing the model to self-consistently track angular momentum as well as the mass that is cycled by SNe feedback, we will assess whether observed galaxy sizes are more successfully reproduced.

As well as galaxy sizes, another observational constraint which received very little attention in this thesis is chemical enrichment. Preliminary work, not presented in this thesis, shows that standard GALFORM models do not predict the relationship between stellar mass and metallicity inferred from observations. This is problematic because, within these models, the predicted mass-metallicity relation is essentially determined by the stellar mass function. In other words, it does not appear to be possible to reproduce observed chemical abundances without spoiling the agreement of the model with observed luminosity functions. This problem clearly merits further investigation.

As an extension of Chapter 5, we plan to continue preliminary work exploring the scatter in stellar mass at a given halo mass predicted by GALFORM. We find that the scatter predicted by GALFORM can be significantly different from predictions made by other semi-analytic models and from what is assumed in abundance matching. This is primarily caused by the implicit coupling between galaxy sizes and SNe feedback efficiency that is implemented within GALFORM.

As well as comparison with observational data, we plan to test some of the assumptions adopted within GALFORM against the EAGLE hydrodynamical simulations (Schaye et al., 2015). A preliminary study comparing global properties of the galaxy population has already been completed (Guo et al., in preparation). However, we plan to compare simulated galaxies on a halo by halo basis, focussing on gas cycling from feedback (both mass and angular momentum) and on adiabatic contraction.

To rapidly test possible modifications to the standard implementation of different physics in GALFORM, we plan to continue developing a new semi-analytic galaxy formation code developed within the python programming language. This code is much more easily modified than the existing fortran GALFORM code, making it an ideal test bench for testing new ideas. That said, the new python implementation does not compete with GALFORM in terms of performance.

# Appendix A

# *Stellar mass functions for the Baugh05 model*

Throughout Chapter 3 we consider the Lagos12 model from Lagos et al. (2012) and the Lacey13 model from Lacey et al. (2015, in preparation). In this appendix, we also consider the model described in Baugh et al. (2005) (hereafter Baugh05). The Baugh05 model is distinct from the Lagos12 and Lacey13 models in that it does not include bursts of star formation triggered by disk instabilities or the updated star-formation law described in Lagos et al. (2011b). The Baugh05 model also uses different time-scales for star formation, both in galaxy disks and in bursts, and uses supernova driven superwinds instead of AGN feedback as a mechanism to suppress the bright end of the luminosity function. Finally, as described in Section 3.3.1, the Baugh05 model uses a top-heavy IMF in bursts with a slope of $x = 0$. This is more extreme than the $x = 1$ slope used in the Lacey13 model.

We present stellar mass functions for a selection of redshifts from the Baugh05 model in Fig. A.1. Neither the intrinsic or recovered stellar mass functions agree with the observational estimates of the stellar mass function at $z = 0$. The model overpredicts the abundance of low mass galaxies at $z \leq 1$ and overpredicts the abundance of the most massive galaxies at $z = 0$, suggesting that the feedback schemes implemented in this model could be unrealistic. Similar behaviour regarding the effect of dust on the recovered stellar mass functions is seen with respect to the Lagos12 and Lacey13 models. At $z = 0$, the recovered stellar mass functions (both including and excluding dust attenuation effects) are lower in normalization with respect to the intrinsic model mass function. This could be a result of the SPS models used in the Baugh05 model. Alternatively, the difference could be caused by the top-heavy IMF in bursts.

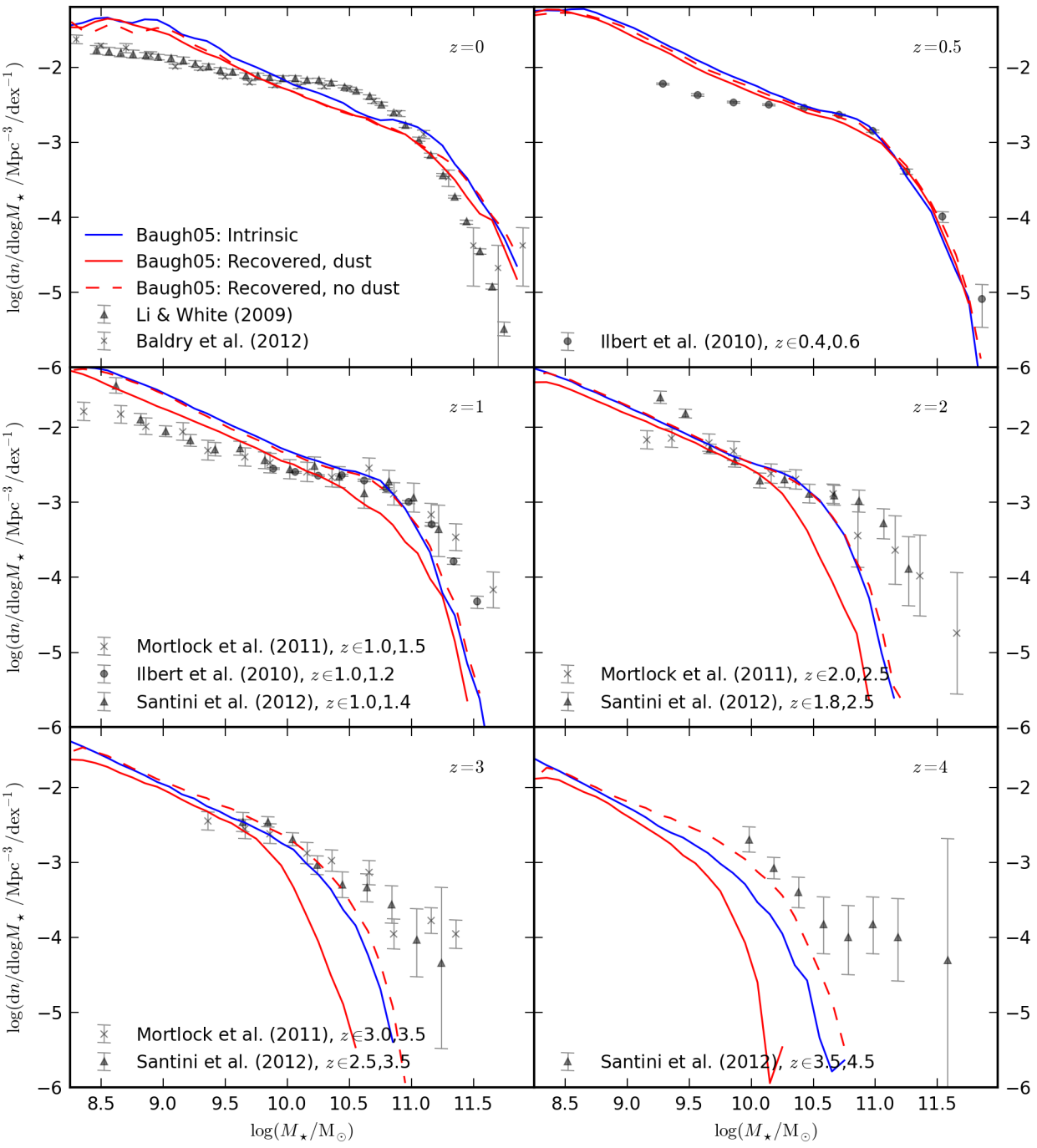


Figure A.1: Caption continued on the following page.

Figure A.1: Stellar mass functions predicted by the Baugh05 model for a selection of redshifts, as labelled in each panel. The solid blue line shows the intrinsic stellar mass function produced by the Baugh05 model. The solid red line shows the stellar mass function recovered using SED fitting when dust effects are included and a Chabrier IMF is assumed in the fitting procedure. As a reference, the dashed red line shows the corresponding stellar mass function where no dust extinction is applied to the model galaxy SEDs and $E(B-V)=0$ is used as a constraint in the fitting procedure. The grey points and error bars show observational estimates of the stellar mass function from Li & White (2009), Baldry et al. (2012), Ilbert et al. (2010), Santini et al. (2012) and Mortlock et al. (2011). Where necessary we convert these observational results from a Salpeter to a Chabrier IMF using a $-0.24\,\mathrm{dex}$ correction, calculated by comparing the recovered stellar mass using Salpeter and Chabrier IMFs with BC03 SPS models.

# Appendix B

# *Inferring star formation histories*

This appendix introduces the main sequence integration (MSI) technique as a method of inferring the average stellar mass assembly histories of star forming galaxies. We then present a discussion of testing the technique by attempting to recover the stellar mass assembly histories predicted by GALFORM. Finally, details of the observational compilation used to infer the stellar mass assembly histories of star forming galaxies and a discussion of the results is provided.

## B.1 Main sequence integration

The underlying idea of MSI is that an "average" galaxy can be tracked across the star formation rate versus stellar mass plane by using measurements of the average star formation rate, at a given stellar mass and lookback time, for galaxies which belong to a star forming sequence. This evolutionary track is then integrated, either forwards or backwards in time, from a specified starting mass, $M_\star(t_0)$, and starting time, $t_0$. For the case of integrating backwards in time, the resulting stellar mass assembly history is given by

$$\begin{aligned} M_\star(t) = M_\star(t_0) &- \int_t^{t_0} \langle \psi(M_\star, t') \rangle \, \mathrm{d}t' \\ &+ \int_0^{t_0} \langle \psi(M_\star, t') \rangle \, R(t_0 - t') \, \mathrm{d}t' \\ &- \int_0^{t} \langle \psi(M_\star, t') \rangle \, R(t - t') \, \mathrm{d}t', \end{aligned} \tag{B.1}$$

where $\langle \psi(M_\star, t) \rangle$ is the average star formation rate of star forming galaxies of stellar mass $M_\star$ at time $t$ and $R(t)$ is the fraction of mass returned to the ISM by SNe and

stellar winds for a simple stellar population of age $t$. For the case of integrating backwards in time, this equation can only be solved numerically using an iterative method in order to account for the returned fraction (see Leitner & Kravtsov (2011)). For this study, we instead choose to be consistent with the approach used in GALFORM by adopting the instantaneous recycling approximation. In this case, $R(t)$ is replaced by a constant (set to $0.39$ to be consistent with our fiducial GALFORM model) and Equation B.1 simplifies to

$$M_\star(t) = M_\star(t_0) - (1 - R) \int_t^{t_0} \langle \psi(M_\star, t') \rangle \, \mathrm{d}t', \tag{B.2}$$

which can be solved numerically using a simple Runge-Kutta integration scheme. The effect of assuming instantaneous recycling can be seen by examining Fig. 9 in Leitner (2012). Relative to the other uncertainties on the inferred stellar mass assembly histories which we discuss later, we expect from their Fig. 9 that the effect of assuming instantaneous recycling is most likely negligible.

In order to calculate $M_\star(t)$ using Equation B.2 at each timestep, the average star formation rate of star forming galaxies, $\langle \psi(M_\star, t) \rangle$, must be specified using measurements of the star forming sequence. Our parametrisation of $\langle \psi(M_\star, t) \rangle$ is described in Appendix B.2 for our application to GALFORM, and in Appendix B.3 for our application to a compilation of observational data. Finally, for a more intuitive link to the dark matter halo mass assembly histories which we consider later, we choose to work in terms of stellar mass assembly histories rather than star formation histories. As we assume instantaneous recycling, both in the model and when analysing the observational data, these are related trivially by linking the stellar mass assembly rate, $\dot{M}_\star$, to the star formation rate using $\dot{M}_\star = (1 - R) \, \psi(M_\star, t)$.

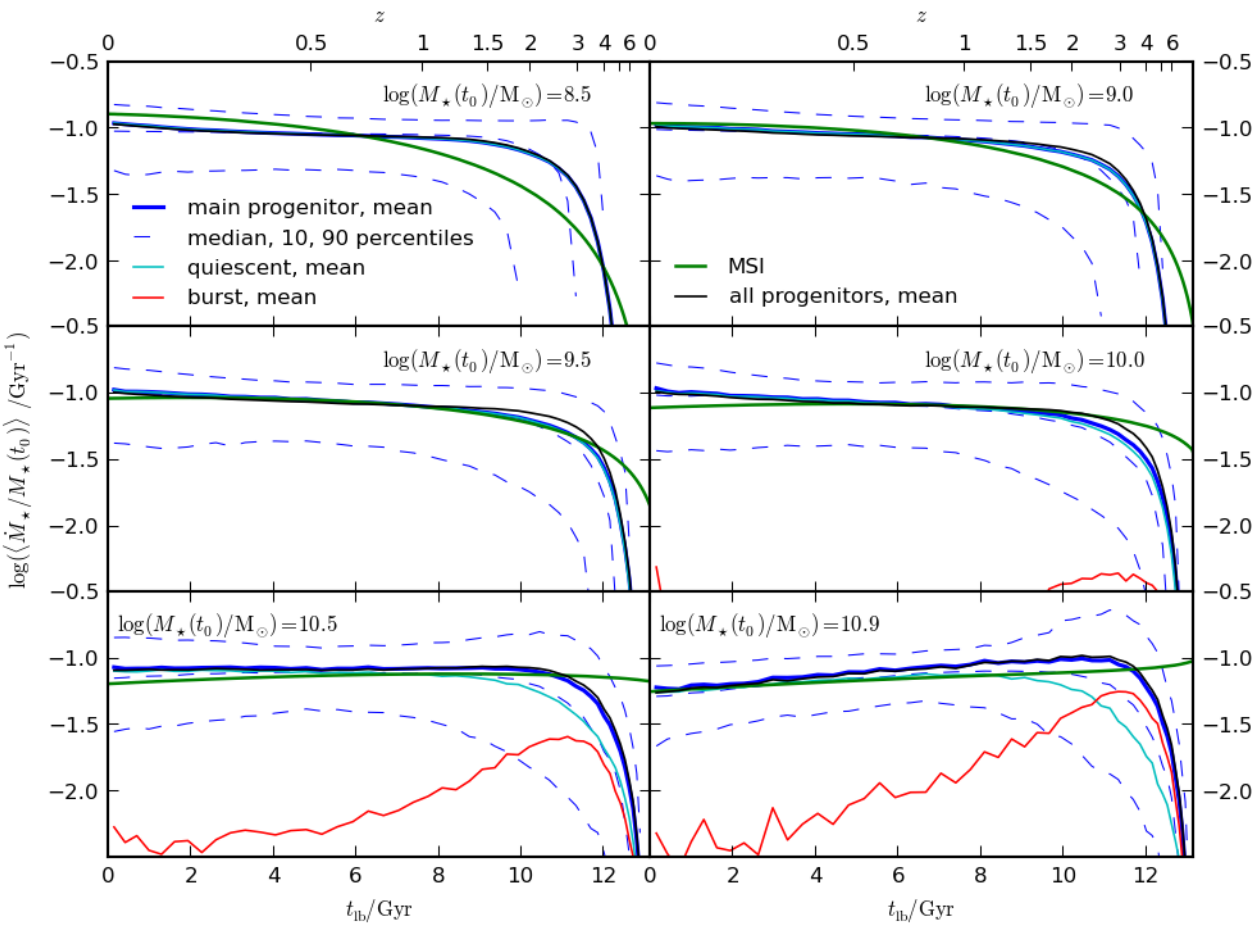


Figure B.1: The average stellar mass assembly histories from our fiducial GALFORM model of central galaxies that are star forming at $z = 0$, plotted as a function of lookback time. Model galaxies are binned by their stellar mass at $z = 0$, with each panel corresponding to a different mass bin. The median $z = 0$ stellar mass in each bin is labelled in each panel. Heavy blue solid lines show the mean stellar mass assembly histories for the main stellar progenitors, as calculated directly from our fiducial model. Dashed blue lines show the corresponding $10^{\mathrm{th}}$, median and $90^{\mathrm{th}}$ percentiles of the distribution. Cyan and red lines show respectively the contribution to the mass assembly histories from quiescent star formation and bursts. Black lines show the mean stellar mass assembly histories but for the case of summing over all of the stellar progenitors of each $z = 0$ galaxy. These are largely coincident with the heavy blue lines. Green lines show the stellar mass assembly histories calculated by applying the MSI technique to the star forming sequence predicted by our fiducial model.

## B.2 Stellar mass assembly histories of GALFORM galaxies and validation of MSI

In Fig. B.1 we show the average stellar mass assembly histories of galaxies from our fiducial GALFORM model that are central and star forming at $z = 0$. The solid blue lines in Fig. B.1 show the mean stellar mass assembly histories taken directly from our fiducial model. It can be seen that, roughly speaking, the overall shape of the mass assembly histories is nearly independent of the final stellar mass. Each stellar mass bin shows a sharp rise at early times before flattening out over the majority of the age of the universe. There is a slight deviation from this behaviour for galaxies with $M_\star(t_0) \approx 10^{11}\,\mathrm{M}_\odot$, which instead display a gradual decline in the stellar mass assembly rate after a peak at $t_{\rm lb} \approx 11\,\mathrm{Gyr}$. The dashed blue lines in Fig. B.1 show the $10^{\rm th}$, median and $90^{\rm th}$ percentiles, indicating the spread in the distribution around the mean.

As well as using the MSI technique to compare these model predictions with any trends inferred from observational data, it is useful to test how well the MSI technique works when applied to the star forming sequence predicted by our fiducial model. To apply MSI to GALFORM, it is necessary to first specify the form of the star forming sequence in the model by parametrising $\langle\psi(M_\star, t)\rangle$. In principle, we could tabulate this for all of the output times used to generate the assembly histories shown in Fig. B.1. However, to serve as a fairer comparison to the case where MSI is applied to observational data, we instead choose a simple parametric form for $\psi(M_\star, t)$ given by

$$\frac{\langle\psi(M_\star, t)\rangle}{\mathrm{M}_\odot\mathrm{Gyr}^{-1}} = 10^{11}\,\left(\frac{c(t)}{\mathrm{Gyr}^{-1}}\right)\left(\frac{M_\star}{10^{11}\,\mathrm{M}_\odot}\right)^{1+\beta_{\rm sf}}, \tag{B.3}$$

where $\beta_{\rm sf}$ is the power-law slope of the star forming sequence which is assumed to be constant with time. $c(t)$ specifies the evolution in the normalisation of the star forming sequence. We find that a reasonable parametrisation for the normalisation is given by fitting a power law of the form

$$c(t) = 0.95\,(1+z)^{1.23}\,\mathrm{Gyr}^{-1}. \tag{B.4}$$

We note that this simple parametrisation of $\langle\psi(M_\star, t)\rangle$ is clearly an oversimplification given that the predicted power-law slope, $\beta_{\rm sf}$, of the sequence shown in Fig. 4.1 and Fig. 4.2 steepens with redshift. However, the slope inferred from the observational data described in Appendix B.3 is not sufficiently well constrained with regard to showing a convincing evolution with redshift. Therefore, for the purposes of making a fair assessment of the MSI technique when applied to observational data, we choose to keep $\beta_{\rm sf}$ as constant in time.

The result of applying MSI to our fiducial GALFORM model can be seen by comparing the blue (intrinsic) and green (inferred from MSI) lines in Fig. B.1. The agreement is not perfect. However, it can be seen that MSI broadly reproduces the flat shape of the stellar mass assembly histories predicted by our fiducial model. The worst agreement is seen for the $\log(M_\star(t_0)/\mathrm{M}_\odot) = 8.5$ bin, where MSI predicts that the mass assembly rate should steadily rise from early times up to $z = 0$. In addition, our application of MSI slightly underpredicts the mass assembly rates of the most massive galaxies, such that the predicted stellar mass assembly histories do not drop correctly at early times.

We now consider several potential shortcomings of the MSI technique that could all contribute to this disagreement. Firstly, MSI assumes that star forming galaxies at a given point in time have always been on the star forming sequence prior to that time. We showed in Fig. 4.1 that there is a tight star forming sequence predicted by our fiducial model. However, in principle it is possible that galaxies could be quenched (for example by a major merger triggered starburst event using up all the cold gas) before accreting enough fresh gas onto a disk to rejoin the star forming sequence. The impact from such a scenario can be tested in a straightforward manner by considering the dispersion in the distribution of mass assembly rates around the mean, as shown in Fig. B.1. We find that the typical dispersion is roughly compatible with the dispersion at a given stellar mass of the star forming sequence shown in Fig. 4.1. This supports, in a statistical sense, the assumption folded into the MSI

technique that galaxies which are star forming at $z = 0$ do not drop below the sequence at some earlier stage in their evolution, at least for a significant period of time.

A second potential shortcoming of the MSI technique is that it ignores the hierarchical assembly of stellar mass through galaxy merging events. It is possible that a significant fraction of the stellar mass of a star forming galaxy at $z = 0$ was formed in multiple progenitors, in which case the MSI method breaks down unless the sum of these progenitors also conspires to reside on the star forming sequence. We check for the contribution from merging by comparing the mean stellar mass assembly histories of the main stellar progenitors (solid blue lines) to the sum of all stellar progenitors (black lines) in Fig. B.1. Over all of the stellar mass bins considered, it can be seen from Fig. B.1 that the stellar mass assembly histories of galaxies that are central and still star forming at $z = 0$ are dominated by the main stellar progenitor, providing support for the validity of the MSI technique. This result is perhaps unsurprising, in that in order for the stellar mass of a secondary progenitor to become significant relative to the stellar mass of the main progenitor, the system must undergo a major merging event which would ultimately quench star formation in the resulting galaxy as gas is used up in a starburst event.

To emphasise the difference between the star forming galaxy population we consider here and passive galaxies, we show in Fig. B.2 the average stellar mass assembly histories of model galaxies that are central and passive at $z = 0$. In contrast to Fig. B.1, the stellar mass assembly histories of the main progenitors of passive centrals (blue lines) are significantly different from the stellar mass assembly histories obtained from summing over all progenitors (black lines). This difference is largest for the most massive galaxies where a significant amount of stellar mass is assembled in secondary progenitors at early times which merge onto the main progenitor galaxy later. The blue lines also include the rate of accretion of stellar mass from secondary progenitors and can therefore exceed the black lines in this case.

Returning to the star forming galaxy sample, Fig. B.1 also shows that quies-

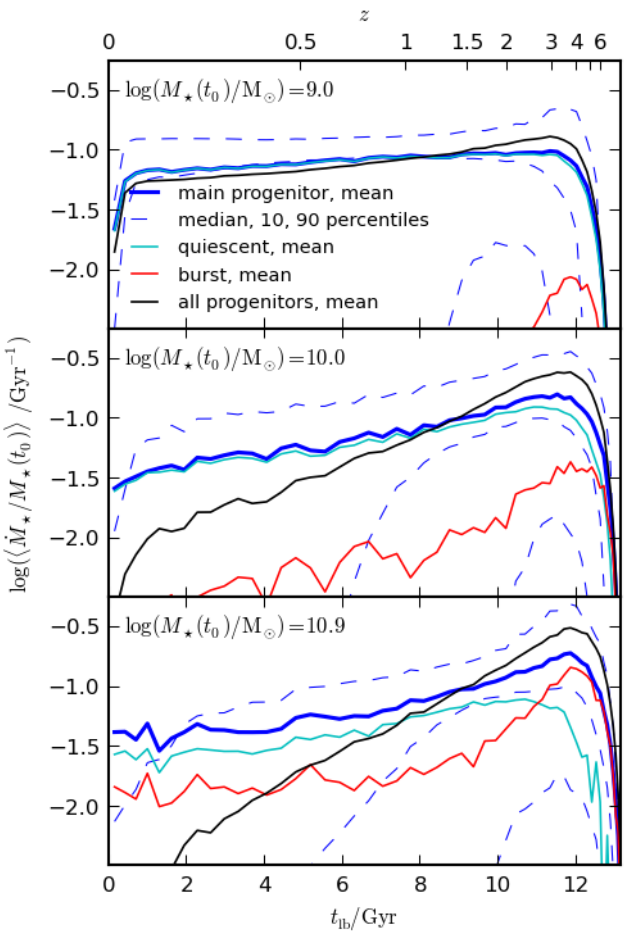


Figure B.2: The average stellar mass assembly histories of central galaxies that are passive at $z = 0$ from our fiducial GALFORM model, plotted as a function of lookback time. Model galaxies are binned by their stellar mass at $z = 0$, with each panel corresponding to a different mass bin. The median $z = 0$ stellar mass in each bin is labelled in each panel. The meaning of the lines is the same as for Fig. B.1.

cent star formation (cyan lines) mostly dominates the stellar mass assembly rates of galaxies which are still star forming at $z = 0$, as compared to star formation in bursts (red lines). The only exception to this is for the progenitors of massive star forming galaxies at $z = 0$, where bursts briefly dominate the stellar mass assembly process at high redshift. Integrated over the lifetime of these galaxies however, the burst star formation mode is still entirely subdominant. This is important for the MSI technique because bursts can perturb galaxies above the star forming sequence. However, as has also been shown by Lamastra et al. (2013), we find that actively bursting galaxies in hierarchical galaxy formation models can also reside on (or in same cases below) the star forming sequence. As an aside, the result that star formation in the galaxies considered in Fig. B.1 is dominated by quiescent star formation in the main stellar progenitor lends support to the methodology employed by galaxy formation models which ignore galaxy merging and disk instabilities, provided that these models are used only to predict the statistical properties of actively star forming central galaxies (e.g. Dutton et al., 2010).

Finally, it should be noted that the MSI technique which we employ for this study includes the assumption that the star forming sequence can be described by a single, unbroken power law over all relevant scales in stellar mass. Fig. 4.2 shows that this is only approximately true for the star forming sequence in our fiducial GALFORM model. If the true star forming sequence cannot be adequately described by a single power law then the resulting stellar mass assembly histories inferred using the MSI technique will be in error. As we start the integration process at $z = 0$, this error would become more severe at early times. In addition, as noted earlier, Fig. 4.2 shows that the power-law slope of the star forming sequence, $\beta_{\rm sf}$, evolves with redshift in our fiducial model. Comparison of the true (solid blue) and inferred (green) average stellar mass assembly histories in Fig. B.1 shows that MSI does not perfectly agree with the direct model prediction, and that the disagreement becomes worse at early times. Given that the other potential sources of error which we have considered until now appear to be insignificant, we attribute the disagreement between MSI and the direct model output seen in

Fig. B.1 to the simple power-law parametrisation of $\langle\psi(M_\star, t)\rangle$ which we use to perform MSI. Given these problems, any comparison between MSI and direct model predictions should only be interpreted taking into account that the MSI technique likely fails to precisely constrain the shape of the stellar mass assembly histories of galaxies, particularly at early times. Nonetheless, the qualitative trend of almost flat stellar mass assembly histories seen in Fig. B.1 is broadly reproduced by the MSI technique for all but the least massive galaxies. We can therefore proceed to perform a qualitative comparison between the shapes of the stellar mass assembly histories predicted by our model and those inferred from observational data using MSI.

## B.3 Applying main sequence integration to observational data

To infer the average stellar mass assembly histories of galaxies from observations using the MSI technique, it is necessary to specify $\langle\psi(M_\star, t)\rangle$ for all possible values of $M_\star$ and $t$. Rather than attempt to interpolate directly between the observational data on the average specific star formation rates presented in Section 4.3.3, we instead choose to first compile a list of power-law fits to the star forming sequence for different redshifts from the literature. Basic information on this compilation is presented in Table B.1. Using Equation B.3, we parametrise these power-law fits with the slope, $\beta_{\rm sf}$ and the normalisation, $c(t)$. We convert the fits taken from studies that assume a Salpeter IMF to a Chabrier IMF by applying a correction of $-0.24\,\mathrm{dex}$ to both $\psi$ and $M_\star$ (Ilbert et al., 2010; Mitchell et al., 2013). This typically makes only a very small difference to the resulting power-law fits.

We show our observational compilation of $\beta_{\rm sf}$ as a function of lookback time in Fig. B.3. This shows that currently there is not a strong consensus on the slope of the star forming sequence in the literature. Given the wide range of selection techniques that are used to separate star forming galaxies, we expect the variation in $\beta_{\rm sf}$ seen in Fig. B.3 to be driven primarily by selection effects. For example, Karim et al.

| Source | Redshift | Selection | SF cut | Tracer | Symbol |
|---|---|---|---|---|---|
| Daddi et al. (2007) | 1.4-2.5 | BzK | sBzK | UV (corrected) | $\times$ |
| Elbaz et al. (2007) | 0.8-1.2 | z | blue colour | $24\mu$m+UV | $\times$ |
| Salim et al. (2007) | 0.05-0.2 | r | BPT diagram | SED fitting | $\times$ |
| Santini et al. (2009) | 0.3-2.5 | $K_{\rm s}$ | SFR-$M_\star$ distribution | $24\mu$m+UV | $\blacklozenge$ |
| Labbé et al. (2010) | 7 | LBG | blue colour | UV (corrected) | $\blacksquare$ |
| Oliver et al. (2010) | 0-2 | Optical | template fitting | $70/160\mu$m | $\blacklozenge$ |
| Peng et al. (2010) | 0-1 | Optical | blue colour | SED fitting | $\times$ |
| Rodighiero et al. (2010) | 0-2.5 | $4.5\mu$m | blue colour/$24\mu$m detection | FIR | $\bigstar$ |
| Elbaz et al. (2011) | 0-3 | $24\mu$m | $24\mu$m detection | FIR | $\blacktriangleright$ |
| Karim et al. (2011) | 0.2-3 | $3.6\mu$m | blue colour | Radio | $\bullet$, $\bullet$ |
| Bouwens et al. (2012) | 4 | LBG | blue colour | UV (corrected) | $+$ |
| Lin et al. (2012) | 1.8-2.2 | BzK | sBzK | UV (corrected) | $\blacktriangle$ |
| Reddy et al. (2012) | 1.4-3.7 | LBG | blue colour | $24\mu$m+UV | $+$ |
| Sawicki (2012) | 2.3 | UV | blue colour | UV (corrected) | $\blacksquare$ |
| Whitaker et al. (2012) | 0-2.5 | K | (U-V/V-J) cut | $24\mu$m+UV | $+$ |
| Koyama et al. (2013) | 0.4,0.8,2.2 | $H_\alpha$ | $H_\alpha$ | $H_\alpha$ (corrected) | $\blacklozenge$ |
| Wang et al. (2013) | 0.2-2 | K | SFR-$M_\star$ distribution | SED fitting / FIR | $\blacksquare$ |

Table B.1: List of the sources of power-law fits to the observed star forming sequence extracted from the literature. We list the source, redshift range or median redshift, galaxy selection technique, the subsequent star forming galaxy selection technique, and the tracer used to estimate the instantaneous star formation rate. The symbols used for each source in Fig. B.3 and Fig. B.4 are also shown. For LBG selected samples, it should be noted that the initial galaxy selection technique is strongly biased towards blue star forming galaxies, so typically no additional cut to separate star forming galaxies is performed. For Karim et al. (2011), we use both the star forming galaxy sample presented in their Table 3 as well as the active population which is shown in their Figure 13 (which uses a bluer colour cut).

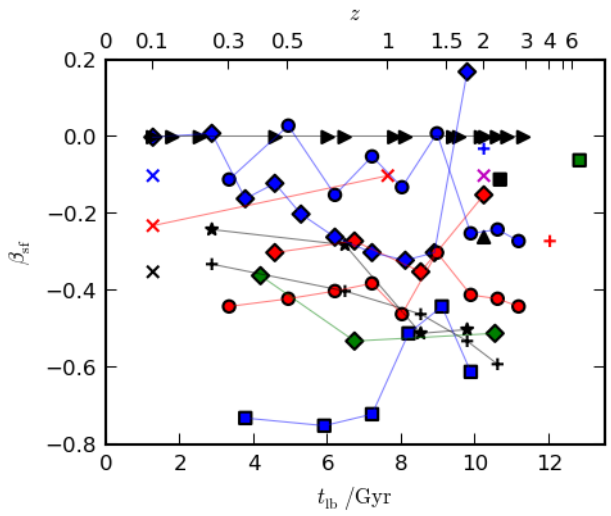


Figure B.3: The slope of power-law fits to the observed star forming sequence from the literature, plotted as a function of lookback time. Each symbol corresponds to data from a different source. The list of sources for the compilation is presented in Table B.1, which also references which source matches a given symbol.

(2011) explore this issue in an appendix and show that increasingly blue rest-frame $(NUV - r)$ colour cuts result in increased values of $\beta_{\rm sf}$. Another issue is whether the star forming sequence can really be described by a single unbroken power law in $M_\star$ (see Huang et al., 2012). For example, if the slope of the sequence changes at the high mass end then the range in stellar mass probed by each individual study will have an effect on the inferred slopes. Inspection of Fig. 4.2 shows evidence that this does indeed occur in our fiducial model.

Given this uncertainty in the true slope of the star forming sequence, we first make the simplest possible assumption, which is that the slope remains constant with lookback time. We then choose to estimate $\langle\psi(M_\star, t)\rangle$ by first binning the power-law fits from Table B.1 in $\beta_{\rm sf}$, before performing a fit to $c(t)$ for each bin as a function of lookback time. For two of the studies included in our compilation (Lin et al., 2012; Reddy et al., 2012), a best fitting slope to the star forming sequence is provided but the corresponding normalisation is not available, and so they do not appear in Fig. B.4 or feature in the following fits. The resulting data and fits to the evolution in the normalisation are shown in Fig. B.4.

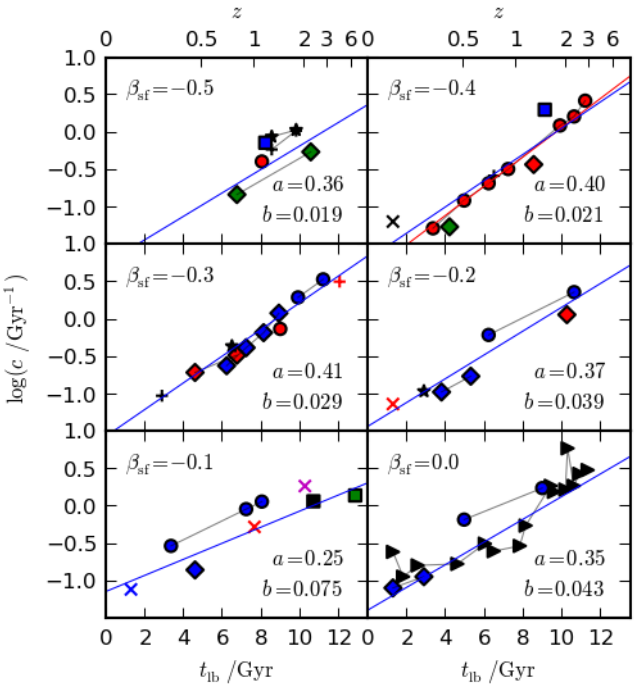


Figure B.4: Normalisation of power-law fits to the star forming sequence from the literature, plotted as a function of lookback time. The list of sources for the compilation is presented in Table B.1, which also references which source matches a given symbol. Each panel shows the normalisation for different bins of the fitted power-law slope to the star forming sequence, $\beta_{\rm sf}$, as labelled. For each panel, the evolution of the normalisation is fitted by $(c/{\rm Gyr}^{-1}) = b\ \exp(a\, t_{\rm lb}/{\rm Gyr})$ and the best fitting $a$ and $b$ are labelled. These fits are shown as blue lines and use all of the observational data, including data from Karim et al. (2011). In addition, we also perform an independent fit (red line) to just the Karim et al. (2011) star forming sample (red circles) in isolation for the $\beta_{\rm sf} = -0.4$ bin.

Unlike the slope, there is actually a reasonable consensus in the literature on the evolution in $c(t)$ for a given $\beta_{\rm sf}$ bin. We find that the evolution in the normalisation seen in Fig. B.4 is best fit as an exponential function of lookback time rather than as a power law in $(1+z)$. We therefore parametrise the evolution in the normalisation using

$$\frac{c(t)}{\mathrm{Gyr}^{-1}} = b\ \exp\left(a\,\frac{t_{\rm lb}}{\mathrm{Gyr}}\right). \tag{B.5}$$

To account for the oversampling in the number of points at $z \approx 2$ in some of the $\beta_{\rm sf}$ bins, we weight all the points shown in Fig. B.4 to give equal weight to each bin in $\Delta t_{\rm lb} = 1\,\mathrm{Gyr}$ within each panel. In order to facilitate a qualitative comparison with the method used by Leitner (2012) to estimate the star formation histories of star forming galaxies, we also perform an independent fit to the star forming galaxy sample from Karim et al. (2011), fixing $\beta_{\rm sf} = -0.4$. This fit to the evolution in the normalisation, $c(t)$, is shown by the red line in Fig. B.4.

Once $\langle\psi(M_\star, t)\rangle$ has been parametrised, we can apply MSI to infer the average stellar mass assembly histories of $z = 0$ star forming galaxies for different values of the stellar mass at $z = 0$, $M_\star(t_0)$. The results of this exercise are shown as coloured lines in Fig. B.5, with each line corresponding to a different bin in $\beta_{\rm sf}$. To compare with the approach used by Leitner (2012), we also apply MSI to only the star forming sample presented in Karim et al. (2011). The results of doing this are shown by the dashed black curves in Fig. B.5.

It is immediately apparent that the uncertainty on the slope of the star forming sequence reported in the literature translates to a considerable uncertainty on the stellar mass assembly histories inferred from the data. The uncertainty is largest for low mass galaxies where, in particular, the formation time at which a given galaxy forms a given fraction of its stars is very poorly constrained. This partly reflects the fact that an increasingly large extrapolation in $\langle\psi(M_\star, t)\rangle$ has to be made for smaller galaxies as the stellar mass of their progenitors typically drops below the completeness limit of the observational surveys used to obtain $\langle\psi(M_\star, t)\rangle$.

Despite the considerable uncertainties, qualitatively the data seems to favour a

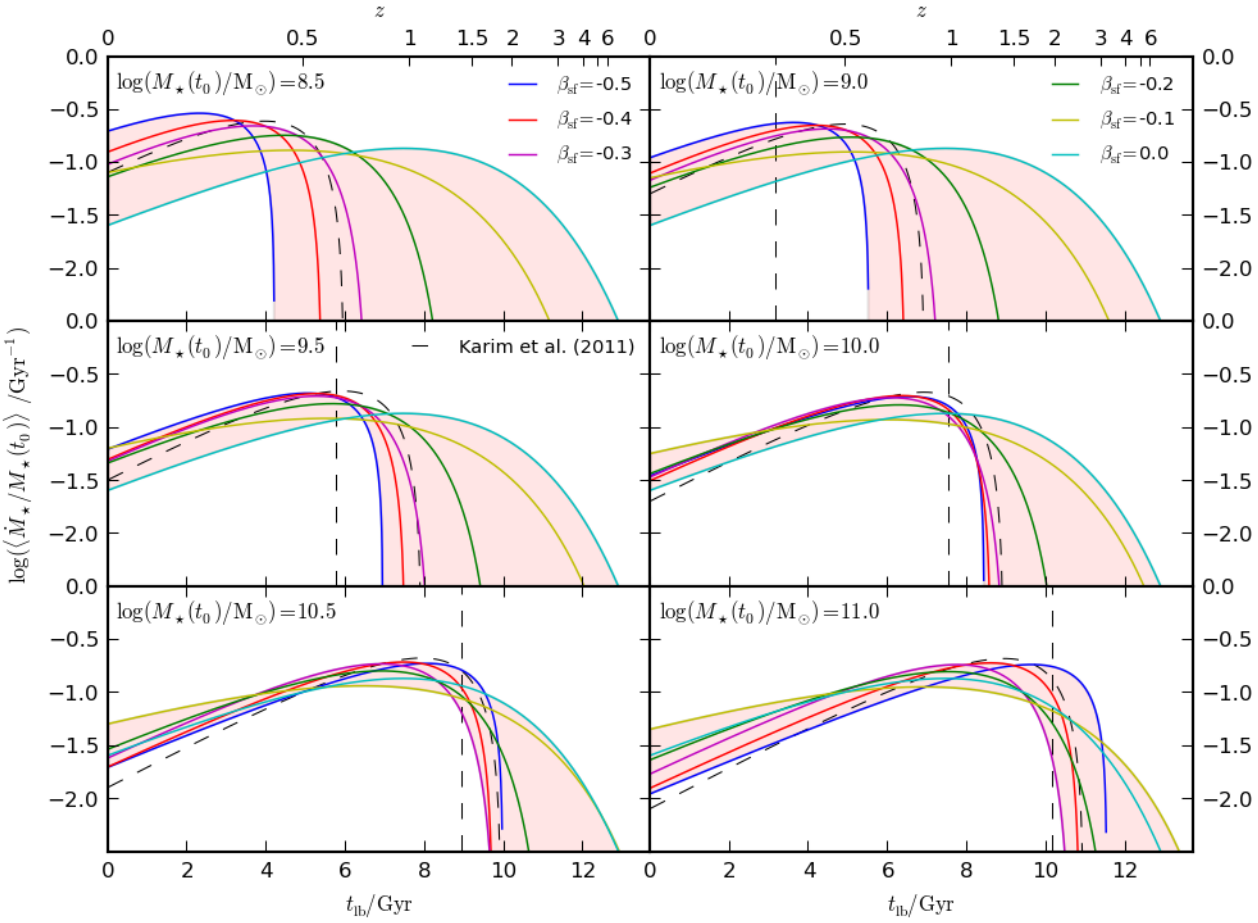


Figure B.5: The stellar mass assembly histories of star forming galaxies inferred by applying MSI to observational data, plotted as a function of lookback time. Each panel corresponds to a different $z = 0$ stellar mass, as labelled. Coloured solid lines show the mass assembly histories inferred by applying MSI to the observational compilation presented in Table B.1. Each solid line in a given panel corresponds to a different bin in the power-law slope of the star forming sequence, $\beta_{\rm sf}$, as taken from the compilation. Dashed black curves show the mass assembly histories inferred by applying MSI to the star forming galaxy sample from Karim et al. (2011). The dashed vertical lines show the lookback time beyond which the MSI technique, applied to the Karim et al. (2011) sample, extrapolates below the stellar mass completeness limits of Karim et al. (2011). For the $\log(M_\star(t_0)/{\rm M}_\odot) = 8.5$ panel, the entire stellar mass assembly history inferred from Karim et al. (2011) involves an extrapolation below this mass completeness limit.

scenario where galaxies that are still star forming at $z = 0$ undergo a peak phase of star formation activity at $z \approx 1$, followed by a drop towards late times. The actual position of the peak and the rate of late time decline are somewhat poorly constrained. Furthermore, for $\beta_{\rm sf} < -0.2$, the position of this peak clearly depends on $M_{\star}(t_0)$, such that a downsizing trend is apparent. Massive star forming galaxies are inferred to form a greater fraction of their stellar mass at early times compared to lower mass galaxies in this case. This is the conclusion presented in Leitner (2012) who use only data from Oliver et al. (2010) and the star forming sample from Karim et al. (2011) as inputs to their application of MSI. Such a downsizing trend, provided that star forming galaxies are successfully separated from passive galaxies, should be completely independent of any physical processes that cause permanent quenching of star formation. On the other hand, if $\beta_{\rm sf}$ is larger, then the shapes of the stellar mass assembly histories of galaxies that are star forming at $z = 0$ are almost completely independent of their final stellar mass.

The stellar mass assembly histories inferred from applying MSI to only the star forming sample presented in Karim et al. (2011) (dashed black lines) are mostly consistent with the curves obtained by fitting to data taken from the entire observational compilation. This implies that the approach used by Leitner (2012), which relies primarily on the Karim et al. (2011) data, should yield results that are consistent with ours. On the other hand, it can be seen from the red line shown in Fig. B.4 that extrapolating the Karim et al. (2011) results down to $z = 0$ favour a steeper late time drop in the normalisation of the star forming sequence than is implied by SDSS data (Salim et al., 2007). This is reflected in the steeper drop in the stellar mass assembly histories inferred from applying MSI to only the Karim et al. (2011) data in Fig. B.5. This emphasises the need to consider results from as much of the literature as possible in order to try to account for the considerable uncertainties on the slope and normalisation of the star forming sequence.

# Appendix C

# *Invariance in the shape of predicted star formation histories*

In Section 4.4.1, we demonstrated that, qualitatively, the stellar mass assembly histories predicted by our fiducial GALFORM model do not agree closely with the trends we infer from observational data. In this appendix, we address the fact that our fiducial model is only one specific realisation of GALFORM with regard to the various model parameters that can be changed. These parameters are constrained by matching global diagnostics of the galaxy population. We now proceed to demonstrate that the disagreement between GALFORM and the observational data holds for a wide range of choices of these model parameters. This result stems from our finding that the shapes of the average stellar mass assembly histories of central star forming galaxies in GALFORM are almost entirely invariant when changing model parameters relating to star formation, feedback and gas reincorporation.

We demonstrate this behaviour in Fig. C.1, which shows the average stellar mass and halo mass assembly histories of model galaxies which are central and star forming at $z = 0$. We show the output of a variety of variants of our fiducial model. These variants are chosen as examples to display the range of mass assembly histories which arise as a result of changing various model parameters in GALFORM which are relevant to star forming galaxies. Included are parameters that control the global efficiency of star formation and SNe feedback, the gas reincorporation timescale and the dependence of the mass loading factor, $\beta$, on the circular velocity of galaxies. Note that it is possible, in principle, that changing

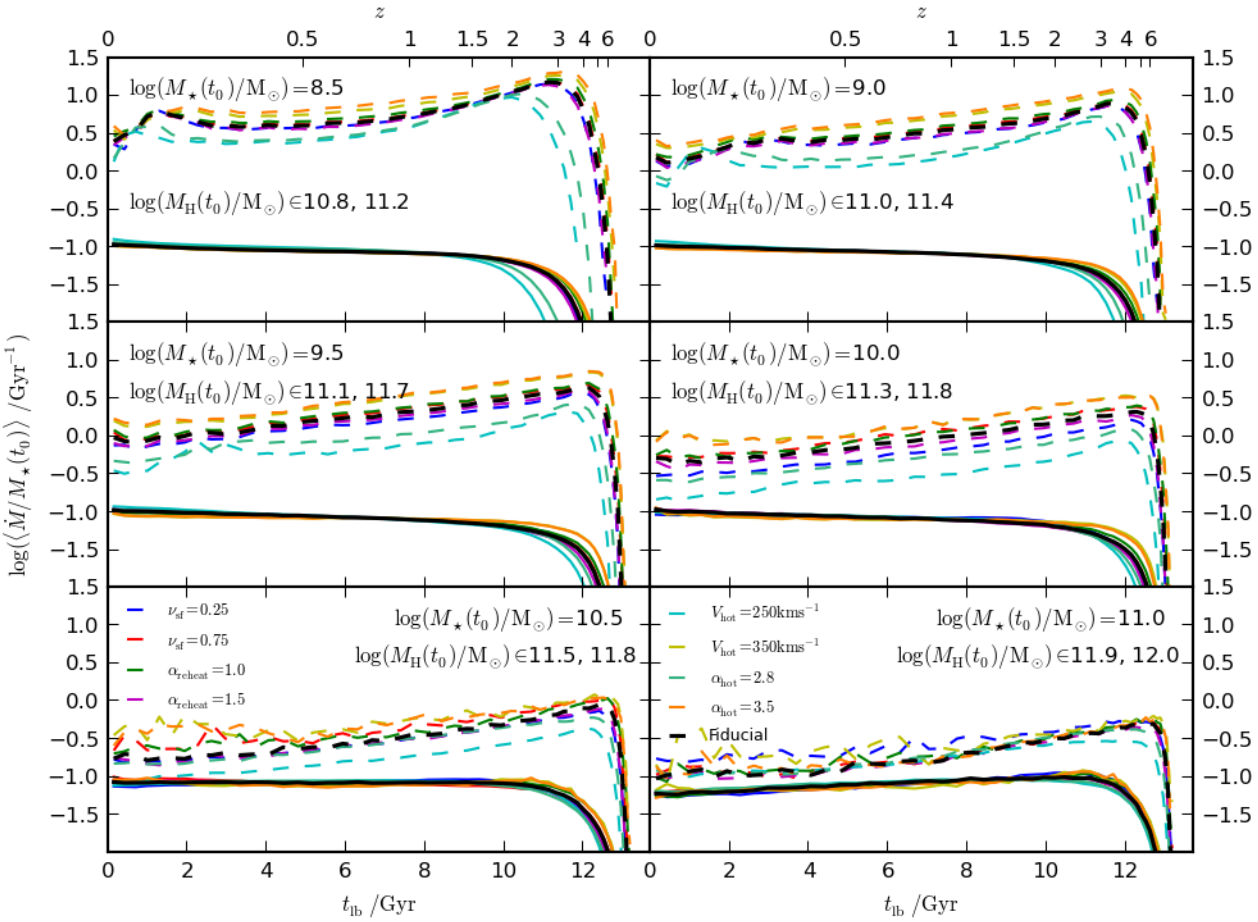


Figure C.1: The mean mass assembly histories of model central galaxies that are star forming at $z = 0$, plotted as a function of lookback time. Solid lines show predictions for the mean stellar mass assembly histories of the main stellar progenitors of galaxies. Black lines correspond to our fiducial GALFORM model. Other colours correspond to variations of our fiducial model, with a single model parameter changed to the labelled value. Definitions of these model parameters can be found in Section 4.2.1. Dashed lines show the corresponding dark matter halo mass assembly histories of the progenitor haloes that host the main stellar progenitors of central star forming galaxies at $z = 0$. The halo mass assembly curves are rescaled by $\Omega_{\rm b}/\Omega_{\rm M}$ to show the baryonic accretion rate onto these haloes. Model galaxies are binned according to their $z = 0$ stellar mass with each panel corresponding to a different mass bin. The median $z = 0$ stellar mass in each bin is labelled in each panel. The range (across all of the GALFORM models shown) in the corresponding median $z = 0$ dark matter halo mass of each stellar mass bin is also labelled.

these model parameters would affect the position of the star forming sequence in GALFORM, invalidating our separation between star forming and passive galaxies. We have verified that this is, in fact, not the case and find that the star forming galaxy cuts shown as blue lines in Fig. 4.1 continue to be effective at isolating the star forming sequence for all the models and redshifts considered here.

To first order, the stellar mass assembly histories for all the models shown in Fig. C.1 are almost identical for a given stellar mass, $M_\star(t_0)$, with significant variations only occurring at early times. In contrast, the normalisation of the halo mass assembly histories shifts significantly between different choices of model parameters. Therefore, while these model parameters in GALFORM are capable of changing the $z = 0$ stellar mass function by changing the relationship between stellar mass and halo mass, they do not significantly affect the stellar mass assembly process of central galaxies of a given stellar mass at $z = 0$.

This result can be understood by first reviewing the way that the stellar mass assembly process takes place in GALFORM. As discussed in, for example, Fakhouri et al. (2010), the specific halo mass assembly rate and consequently the shape of the corresponding dark matter halo mass assembly histories are nearly independent of the final halo mass (see their Equation 2). This can be seen directly in Fig. C.1. Secondly, as shown in Section 4.4.1, stellar mass assembly broadly tracks halo mass assembly in our fiducial GALFORM model. As described in Section 4.4.2, this coevolution arises because the mass loading and reincorporation efficiencies do not evolve significantly over the majority of the lifetimes of typical star forming galaxies. For the parametrisations currently used to model these physical processes in GALFORM, changing the relevant model parameters merely changes their efficiency in a global sense. Therefore, in order to change the shape of the stellar mass assembly histories, an alternative parametrisation of one (or both) of these processes would be required. Such a modification would need to result in significantly stronger evolution in the mass loading factor, $\beta_{\rm ml}$, or the reincorporation timescale, $t_{\rm ret}$, than is seen for our fiducial model in Fig. 4.6.

# Appendix D | *Virial mass scaling model*

In Section 4.5.2, we demonstrate that by modifying the reincorporation timescale in the model to the form given by Eqn 4.25, it is possible to reconcile the predicted and inferred stellar mass assembly histories of galaxies that are still star forming at $z = 0$. In Fig. 4.8 we show that this ad hoc model for the reincorporation timescale is quite different from the modification introduced by Henriques et al. (2013) in order to reproduce the observed evolution of the stellar mass and luminosity functions. We now consider implementing into our model their suggestion that the reincorporation timescale should only scale with the halo virial mass as

$$t_{\rm ret} = \gamma \, \frac{10^{10} \mathrm{M}_{\odot}}{M_{\rm H}}. \tag{D.1}$$

We start by requiring that this virial mass scaling model should provide an adequate match to the $z = 0$ stellar mass function. Starting from our fiducial model, we find that it is possible to do this simply by implementing Eqn D.1 with $\gamma$ changed from $18\,\mathrm{Gyr}$, as in Henriques et al. (2013), to $5.6\,\mathrm{Gyr}$.

Comparisons with the other models considered in Chapter 4 for the evolution in the specific star formation rates and stellar mass assembly histories of star forming galaxies are shown in Fig. 4.3 and Fig. 4.9 respectively. Fig. 4.9 shows that the virial mass scaling model predicts rapidly rising stellar mass assembly histories for all but the most massive star forming galaxies at $z = 0$. For galaxies with $\log(M_{\star}/\mathrm{M}_{\odot}) = 10$ at $z = 0$, this results in dramatic disagreement with the stellar mass assembly histories inferred from observations with too much star formation at late times compared to early times. For low mass galaxies, the observational constraints are very weak, such that any model could be compatible. For the most massive systems, we note that similar to the modified reincorporation model shown in red, the cooling timescale in the virial mass scaling model becomes long compared

the reincorporation timescale for galaxies residing within massive haloes. As discussed in Section 4.5.2, modifying the reincorporation timescale in this regime will have a much smaller impact as the gas cycle becomes limited by cooling. Fig. 4.3 shows that the virial mass scaling model predicts specific star formation rate evolution which is too slow at a fixed stellar mass relative to the rapid evolution inferred from observations. Again, the specific star formation rates of massive star forming galaxies are relatively unaffected by modifications to the reincorporation timescale.

While our modified reincorporation model is more successful than the virial mass scaling model in reproducing the trends inferred from the data in Fig. 4.3 and Fig. 4.9, it is important to also consider the predicted evolution of the stellar mass function, given that this is the main constraint used by Henriques et al. (2013). Stellar mass function predictions for the different models considered in Chapter 4 are compared to a compilation of observational data in Fig. D.1. To first order, the differences between the models can be summarised simply by noting that relative to our fiducial model, the modified reincorporation model suppresses both early and late star formation. The virial mass scaling model also suppresses early star formation but predicts much stronger star formation at late times for all but the most massive galaxies. This results in much stronger evolution in number density short of the break in the mass function below $z = 2$, in good agreement with the most recent observational data. In contrast, our fiducial model predict an overabundance of low mass galaxies relative to the observations beyond the local Universe.

Compared to the observations, all three models shown here all strongly underpredict the abundance of galaxies above the break of the stellar mass function beyond the local Universe. The extreme end of the mass function must always be interpreted with care because of the potential for Eddington bias to artificially boost the population residing in the massive tail of the galaxy stellar mass distribution. On the other hand, the disagreement at the massive end could be related to the problem that all three models suffer from in failing to reproduce the rapid evolution in the specific star formation rates of massive star forming galaxies with $\log(M_\star/\mathrm{M}_\odot) = 11$ seen in Fig. 4.3.

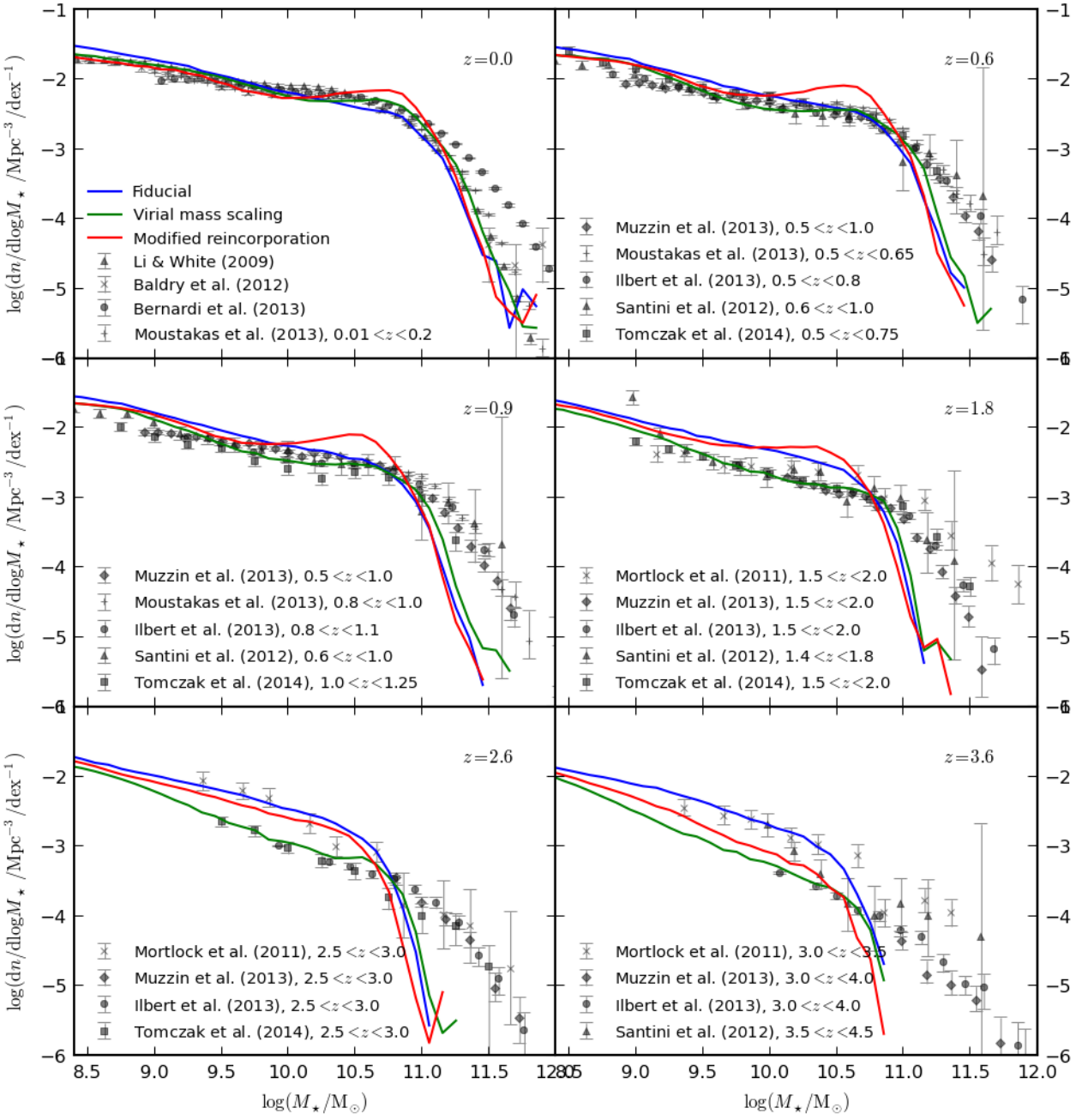


Figure D.1: Stellar mass functions predicted by the different GALFORM models for a selection of redshifts, as labelled in each panel. Blue lines show predictions from our fiducial model. Red lines correspond to the modified reincorporation model introduced in Section 4.5.2. Green lines correspond to a model using the virial mass scaling for the reincorporation timescale introduced by Henriques et al. (2013). Caption is continued on the following page.

Figure D.1: The grey points and error bars show observational estimates of the stellar mass function from Li & White (2009), Baldry et al. (2012), Ilbert et al. (2010), Mortlock et al. (2011), Santini et al. (2012), Bernardi et al. (2013), Ilbert et al. (2013), Moustakas et al. (2013), Muzzin et al. (2013b) and Tomczak et al. (2014). Where necessary we convert these observational results from a Salpeter to a Chabrier IMF using a $-0.24\,\mathrm{dex}$ correction (Ilbert et al., 2010; Mitchell et al., 2013).

At this stage, it is tempting to speculate whether it is possible to produce a model that can be consistent with the observed stellar mass function and star formation evolution simultaneously. One possibility that we did not fully explore in this study would be to search for a modified model which introduces a strong downsizing trend into the purely star forming population, such that low mass galaxies form very late, and yielding a star forming sequence with a slope of $\beta_{\mathrm{SF}} \approx -0.4$, compatible with current observations of the star forming sequence. In this case, it might be possible to reproduce the observed evolution in the low mass end of the stellar mass function while also predicting peaked star formation histories for star forming galaxies with $\log(M_{\star}/\mathrm{M}_{\odot}) = 10$ at $z = 0$. We defer any further exploration of this issue to future work.

Another consideration is that currently it is assumed in our model that all gas which is removed from galaxies by SNe feedback is added to a reservoir instead of being added straight back into the hot halo gas profile. In the case where the reincorporation timescale is of order the halo dynamical time, this is equivalent to assuming that the ejected gas moves in a ballistic fashion and escapes the halo virial radius before returning. In contrast, the models presented by Guo et al. (2011) and Henriques et al. (2013) assume that only a fraction of this gas is actually ejected from the halo. The remaining fraction is added back into the halo gas profile and is therefore able to inflow back onto the disk very rapidly when cooling timescales are short. In these models, the fraction of gas that is able to escape the halo is parametrised as a function of the halo circular velocity, $V_{\mathrm{vir}}$, such that a larger fraction of gas is ejected from the haloes of low mass systems. Depending on the set of chosen model parameters, this treatment of the gas affected by SNe feedback could

change the $z = 0$ stellar mass range over which a modification to the reincorporation timescale would be effective in changing the stellar mass assembly histories of star forming galaxies. Again, we defer any further exploration in this area to future work.

# Appendix E

# *Halo masses and satellite abundances*

In this appendix, we attempt to understand the reasons why abundance matching results from (Behroozi et al., 2013b) and (Moster et al., 2013) disagree with the SHM relation predicted by GALFORM at $z = 0$. Part of this disagreement simply reflects the fact that our reference model was not explicitly tuned to reproduce observational estimates of the local stellar mass function, but rather the local galaxy luminosity functions (see González et al., 2014, for details). However, another factor is the differing halo mass definitions used in different studies as well as differing assumptions about satellite halo abundances.

To explore these disagreements further, we have made use of an L-galaxies model which was run on the same MILLENIUM WMAP-7 simulation that was used in this chapter for our reference model (Guo et al., in prep). Compared to GALFORM, this Lgalaxies model uses the same SUBFIND subhalo catalogues as inputs but uses halo mass definitions and assumptions about satellites which are the same as those adopted by Moster et al. (2013). Specifically, the L-galaxies model uses a mean halo density of $200$ times the critical density ($M_{200}$) to define halo mass and a dynamical friction timescale is used to decide how long satellite galaxies survive after their subhalo can no longer be identified in the simulation (Guo et al., 2011; Moster et al., 2013). From here on, we refer to these orphan satellites as Type 2 satellites. We refer to satellites where the subhalo can still be identified in the simulation as Type 1 satellites. Combining the L-galaxies halo catalogue (split into central haloes, Type 1 and Type 2 satellites) with the SHM relationship (including scatter) from Moster et al. (2013), we can generate a stellar mass functions for central and satellite galaxies. To generate the stellar mass of satellite galaxies, we

use the infall redshift listed in the L-galaxies halo catalogue, consistent with the method of Moster et al. (2013).

To make a comparison with the results from Behroozi et al. (2013b), we follow the same procedure but rescale the central and satellite halo mass functions from the L-galaxies catalogue to reproduce the corrected Tinker et al. (2008) halo mass function and satellite fractions used by Behroozi et al. (2013b)[1]. Stellar masses are then assigned to each halo in the rescaled catalogue using the SHM relationship from Behroozi et al. (2013b). Behroozi et al. (2013b) define halo masses using the virial overdensity criterion predicted by the spherical collapse model (Bryan & Norman, 1998). Unlike GALFORM and Moster et al. (2013), Behroozi et al. (2013b) do not consider Type 2 satellites (satellite galaxies are considered to merge with the central galaxy once the subhalo can no longer be identified in the simulation). However, Behroozi et al. (2013b) use the Bolshoi simulation to compute satellite fractions which has a factor seven better mass resolution than the corresponding simulations used for our reference model and in Moster et al. (2013). As such, the number of satellite galaxies without identifiable subhaloes within a halo of a given mass should, in principle, be smaller for the results presented in Behroozi et al. (2013b).

To prove the validity of this "reverse-engineering" approach used to estimate the central/satellite halo/galaxy populations from abundance matching studies, we show in Fig. E.1 the resulting stellar mass functions at $z = 0$, compared to the observational datasets originally used as constraints in these studies. In all cases, it is apparent that our attempt to reverse engineer the abundance matching results is successful at reproducing the corresponding observational datasets. It is interesting to note that the corrections made by Behroozi et al. (2013b) to the observational estimates of the stellar mass function from Baldry et al. (2008) and Moustakas et al. (2013) have an appreciable impact relative to the original stellar

[1]We use this rescaling approach simply for convenience so that we can assign stellar masses to individual haloes in order to compute the stellar mass function. In this way we avoid the need to perform convolution integrals to include the effects of stellar mass errors and intrinsic scatter in the SHM relation.

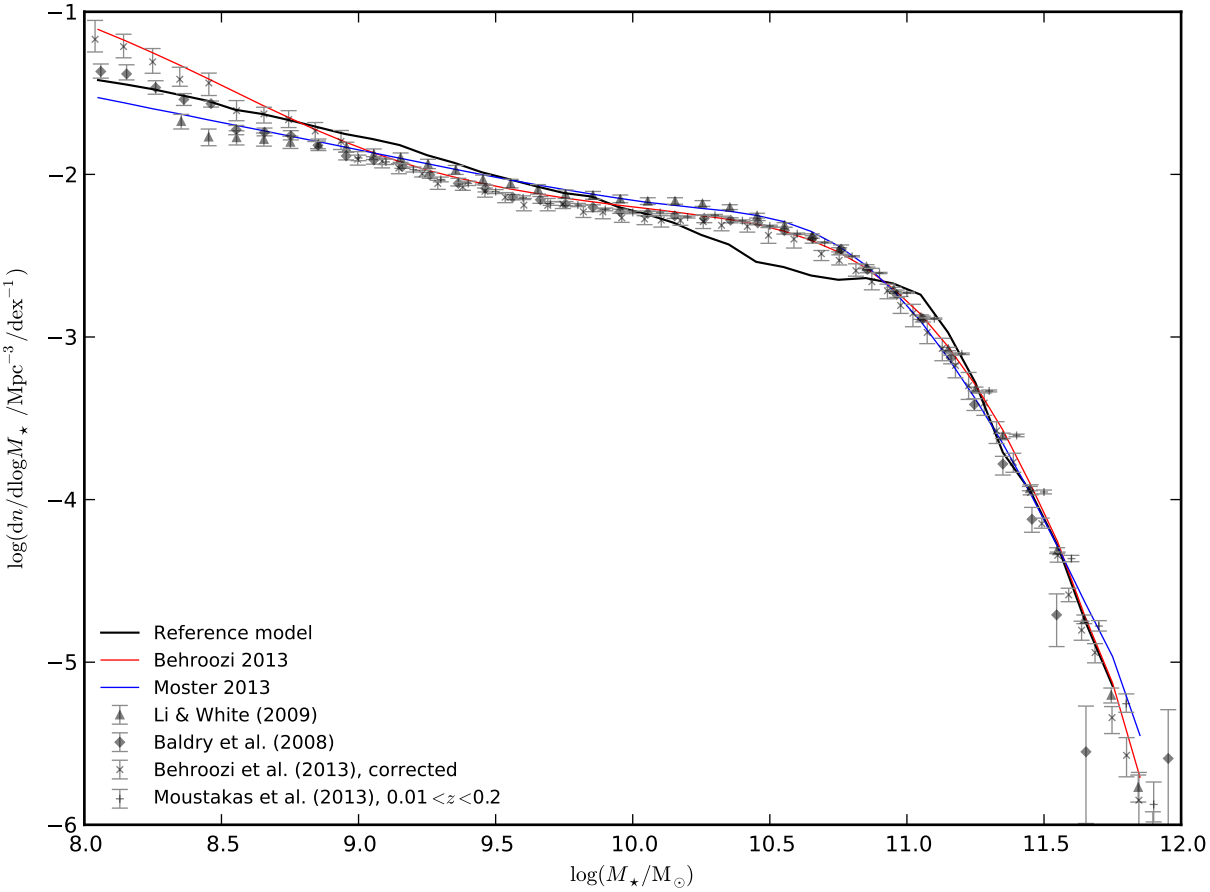


Figure E.1: Stellar mass functions at $z = 0$ for our reference model (black) and abundance matching empirical models based on Behroozi et al. (2013b) (red) and Moster et al. (2013) (blue). Points and associated errorbars show observational estimates of the local stellar mass function, taken from Baldry et al. (2008), Li & White (2009), Behroozi et al. (2013b) and Moustakas et al. (2013). The data points from Behroozi et al. (2013b) are based on a combination of results from Baldry et al. (2008) and Moustakas et al. (2013). Behroozi et al. (2013b) make corrections to these datasets for dust extinction, sample variance and surface brightness incompleteness effects. Behroozi et al. (2013b) use this corrected dataset to constrain their abundance matching model. Moster et al. (2013) use the uncorrected Baldry et al. (2008) and Li & White (2009) datasets to constrain their abundance matching model.

mass functions presented in those studies, particularly at the low mass end.

With this consistency check in place, we can now examine the halo mass function, satellite fractions and stellar mass functions, split into central and satellite galaxies. These are presented in Fig. E.2. Starting with the halo mass functions, it is clearly apparent that for the WMAP-7 cosmological parameters assumed here, there is an offset between the $M_{200}$ mass definition used by Moster et al. (2013) compared with the virial overdensity and DHalo[2] mass definitions used by Behroozi et al. (2013b) and GALFORM respectively. The offset is $\approx 0.16\,\mathrm{dex}$.

For the satellite fractions, much larger differences between the different models become apparent. The empirical model from Behroozi et al. (2013b) appears to contain significantly fewer satellite galaxies than GALFORM or Moster et al. (2013) in all but the highest halo mass bins. At $\log(M_{\rm H}/{\rm M}_{\odot}) = 12$, there is a $\approx 0.4\,\mathrm{dex}$ offset between the Behroozi et al. (2013b) satellite fractions, compared to Moster et al. (2013) and GALFORM. Although potentially coincidental, it is interesting to note that the Behroozi et al. (2013b) satellite fraction agrees fairly well with the GALFORM Type 1 satellite fraction down to a mass, $\log(M_{\rm H}/{\rm M}_{\odot}) = 12$ (recall that Behroozi et al., 2013b, do not include Type 2 satellites). While the total (Type 1 + Type 2) GALFORM and Moster et al. (2013) satellite fractions are similar, the relative contributions from Type 1 and Type 2 satellites are significantly different. At face value, this is puzzling given that the same SUBFIND input catalogues were used in both cases. However, in GALFORM, all satellites are allocated an analytically calculated dynamical friction merging timescale at infall, instead of when the subhalo is lost from the simulation [3] (as is the case for Moster et al., 2013). GALFORM and Moster et al. (2013) also use different parameters (albeit with effectively the same parametrisation) for the dynamical friction timescale. The effect of these differences is that GALFORM has a higher fraction of Type 2 satellites at a given mass

[2]We note that that the DHalo masses shown here are taken directly from GALFORM output. As such, they are distinct from the DHalo masses that are input into GALFORM because we impose mass conservation to ensure that all haloes most grow monotonically in mass.

[3]Consequently, it is possible in GALFORM for satellite galaxies to merge with the central galaxy before the associated subhalo actually disappears from the simulation.

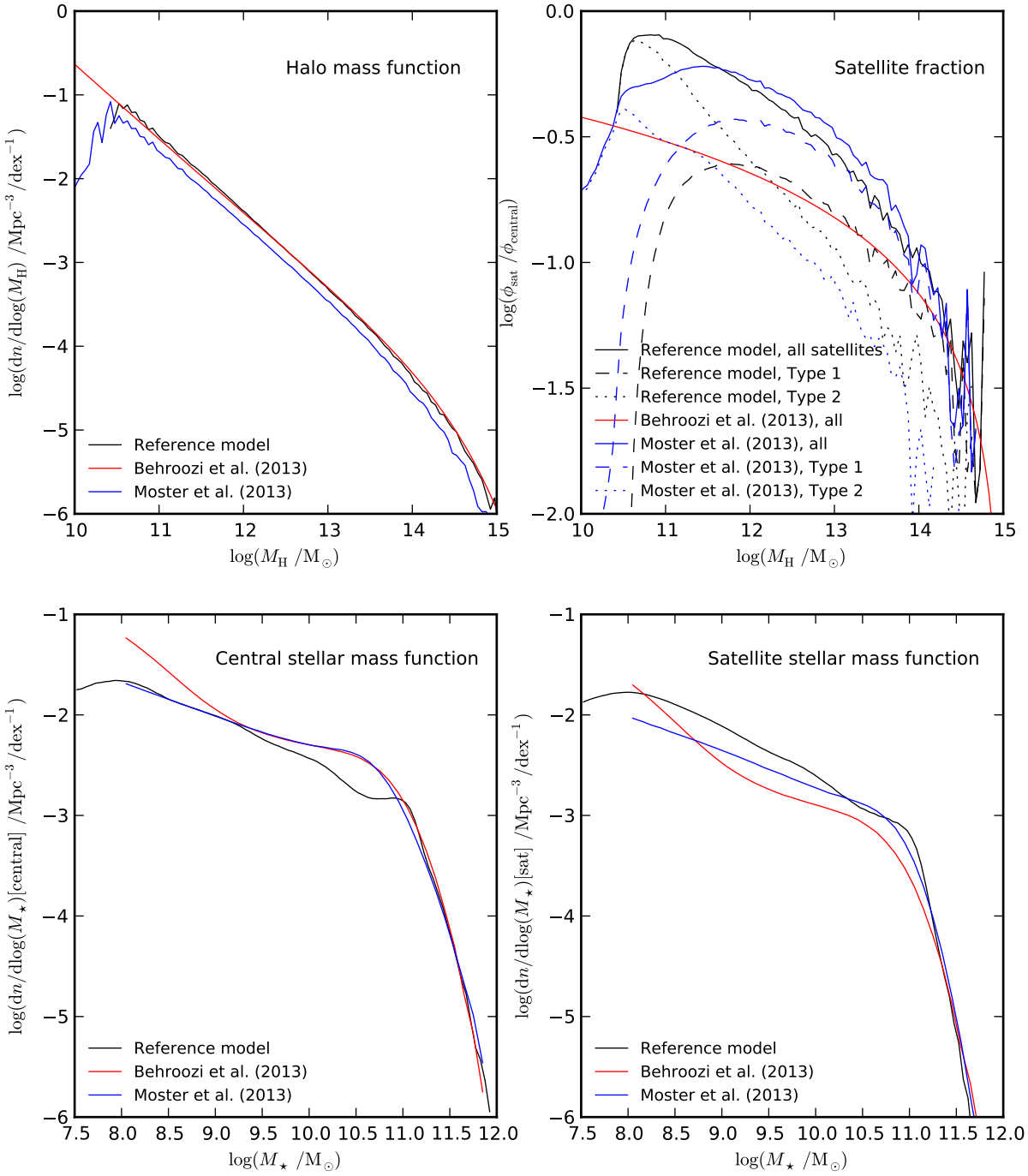


Figure E.2: Mass functions at $z = 0$ from our reference GALFORM model (black) and from applying the SHM relationship and satellite fractions from Moster et al. (2013) (blue) and Behroozi et al. (2013b) (red). *Upper left:* Halo mass functions, using the halo mass definitions used by each study to quantify the SHM relationship. *Upper right:* Satellite halo fractions as a function of halo mass. For satellite haloes, halo mass is taken as the subhalo mass at infall. *Lower left:* Central galaxy stellar mass functions. *Lower right:* Satellite galaxy stellar mass functions.

than Moster et al. (2013) who have a higher fraction of Type 1 satellites.

The differences between these satellite fractions are reflected in the stellar mass functions when split into central and satellite galaxies, shown in the bottom panels of Fig. E.2. Behroozi et al. (2013b) find fewer satellite galaxies at a given stellar mass down until the stellar mass range where their corrected Baldry et al. (2008) dataset significantly steepens the stellar mass function below $\log(M_{\rm H}/{\rm M}_{\odot}) = 12$. The satellite stellar mass functions also disagree between Moster et al. (2013) and our reference GALFORM model.

In summary, we find that there is an offset in halo mass definition between Moster et al. (2013) and GALFORM, and that there are significant differences in satellite fractions between Behroozi et al. (2013b), Moster et al. (2013) and GALFORM. This complicates the comparison of the SHM relation predicted by GALFORM with these abundance matching studies. While it would be straightforward to correct the Moster et al. (2013) SHM relation for the halo mass definition effect, the satellite fractions are much more problematic. Consequently, we have decided to simply present the SHM relations from Behroozi et al. (2013b) and Moster et al. (2013) in this chapter without applying corrections. We caution that quantitative disagreements in the SHM relation between GALFORM and abundance matching studies are therefore not necessarily caused by failings in the physics implemented within GALFORM.

# Appendix F

# *Criteria for a non-evolving SHM relation for star forming galaxies*

In this appendix, we explore the conditions required for a non-evolving SHM relation for star forming galaxies, based on the simplified analytical results presented in Chapter 5.4.1. There, we assumed that the instantaneous star formation efficiency, $\eta_{\rm SF} \equiv \dot{M}_\star/(f_{\rm B}\dot{M}_{\rm H})$, scaled as $\beta_{\rm ml}^{-1}$, where $\beta_{\rm ml}$ is the mass loading factor for SNe feedback. By also assuming that the disk circular velocity scales with the halo circular velocity for haloes hosting star forming galaxies, we arrived at the following relation:

$$\eta_{\rm SF} \propto M_{\rm H}^{\alpha_{\rm hot}/3}\,[\bar{\rho}_{\rm H}(a)]^{\alpha_{\rm hot}/6}\,. \tag{F.1}$$

For a non-evolving SHM relation, $\eta_{\rm SF}$ should be constant at a fixed halo mass. Eqn F.1 contradicts this requirement because the mean halo density, $\bar{\rho}_{\rm H}(a)$, depends on expansion factor, independent of halo mass. Integrating Eqn F.1 will therefore yield a SHM relation which depends on expansion factor at fixed halo mass.

In Chapter 5.4.1, we circumvented this problem by assuming that $\bar{\rho}_{\rm H}(a)$ was constant with expansion factor. In this case, integrating Eqn F.1 yields

$$M_\star \propto M_{\rm H}^{1+\alpha_{\rm hot}/3}\,[\bar{\rho}_{\rm H}]^{\alpha_{\rm hot}/6} \tag{F.2}$$

where, if $\bar{\rho}_{\rm H}$ is regarded as constant, we arrive at the non-evolving SHM relation given by Eqn 5.7. To test the regimes where this assumption is valid, we can invert

the process of integrating Eqn F.1 into Eqn F.2, differentiating Eqn F.2 to give

$$\dot{M}_\star \propto \left(1+\frac{\alpha_{\rm hot}}{3}\right) M_{\rm H}^{\alpha_{\rm hot}/3}\dot{M}_{\rm H}\left[\bar{\rho}_{\rm H}\right]^{\alpha_{\rm hot}/6} + \frac{\alpha_{\rm hot}}{6} M_{\rm H}^{1+\alpha_{\rm hot}/3}\dot{\bar{\rho}}_{\rm H}\left[\bar{\rho}_{\rm H}\right]^{\alpha_{\rm hot}/6-1}. \quad \text{(F.3)}$$

In order for this to be equivalent to Eqn F.1, we require that

$$\frac{|\dot{M}_{\rm H}|}{M_{\rm H}} \gg F(a) \equiv \frac{\alpha_{\rm hot}}{2(3+\alpha_{\rm hot})}\frac{|\dot{\bar{\rho}}_{\rm H}(a)|}{\bar{\rho}_{\rm H}(a)}. \quad \text{(F.4)}$$

In other words, given Eqn F.1, a non-evolving SHM relation requires that haloes are growing faster in mass than the rate with which they are changing in density. This equality will not be satisfied in general. However, it will be a satisfied for haloes of a particular mass over some redshift range.

In Fig. F.1, we show, for a range of halo masses, the redshift range for which the equality given by Eqn F.4 is satisfied. Here, we have selected haloes from our reference model that host star forming galaxies at a given redshift, and then computed $\dot{M}_{\rm H}$, averaged over bins in halo mass. To calculate $|\dot{\bar{\rho}}_{\rm H}(a)|$, we consider both $\bar{\rho}_{\rm H}(a)$ calculated using the spherical collapse model (solid lines) and calculated directly using halo circular velocities taken from our reference model (dashed lines).

Starting with halo densities computed from the spherical collapse model, Fig. F.1 shows that that the SHM relation should be non-evolving for star forming galaxies when $z > 1$. The exact redshift where Eqn F.4 is met depends on halo mass, such that the equality is met over a wider redshift range for more massive haloes.

Conversely, from Fig. F.1, we also expect that the SHM relation should evolve at lower redshifts ($z < 1$) if halo densities are computed using the spherical collapse model. However, significant evolution is not seen in the SHM relation over this redshift range (in the halo mass range associated with star forming galaxies) for our reference model in, for example, Fig. 5.10 of Chapter 5. This can partially be explaining by noting that for $z < 1$, star formation rates and halo mass accretion rates at a given halo mass have dropped dramatically relative to higher redshifts.

However, another very important consideration is that in our reference model, halo circular velocities (and hence the mean densities of haloes at fixed halo mass)

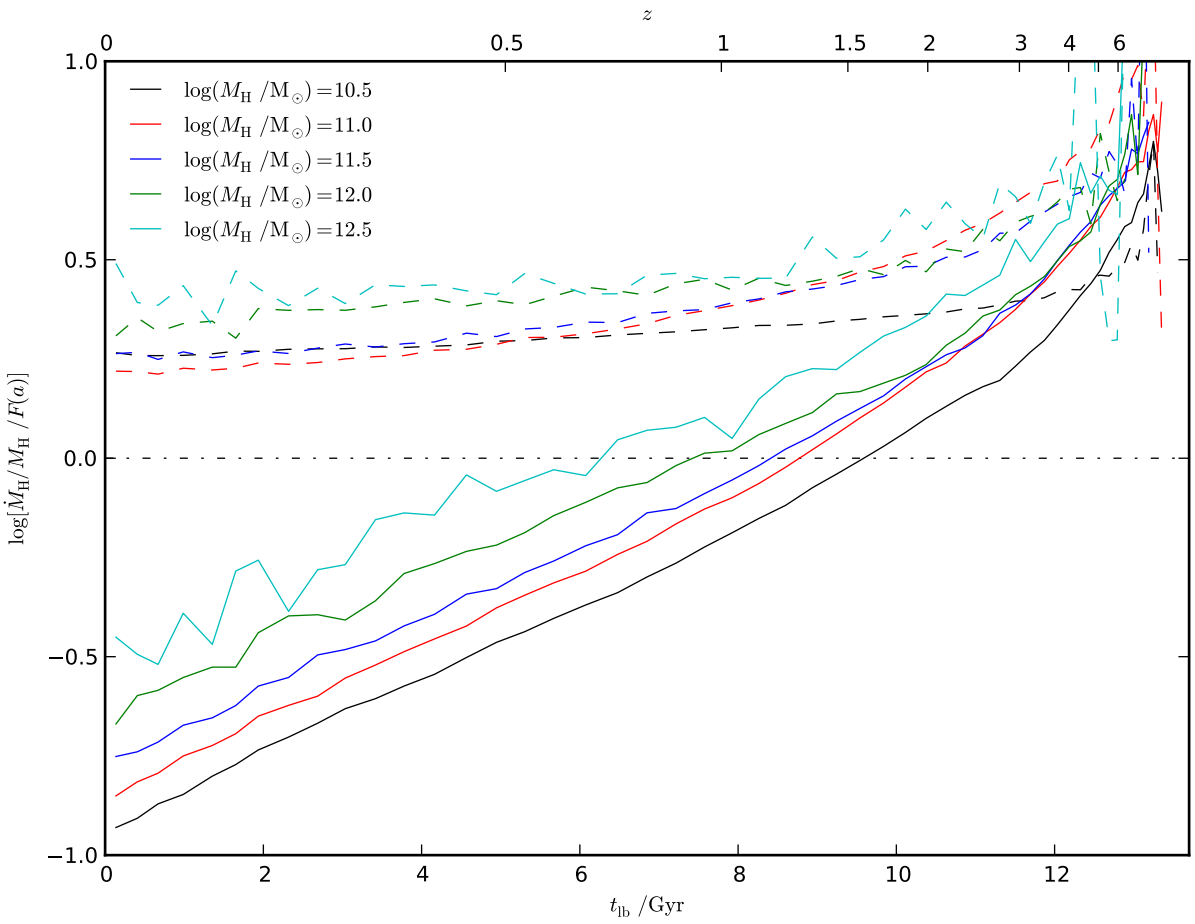


Figure F.1: Scaled ratio of average halo accretion rates to the rate with which the mean halo density, $\bar{\rho}_{\rm H}$, is changing with time, plotted as a function of lookback time. Average halo formation rates are taken from our reference model for haloes that host star forming central galaxies at a given redshift. The scaled rate of change in mean halo density, $F(a)$, is defined by Eqn F.4. Solid lines show $\dot{M}_{\rm H}/M_{\rm H}/F(a)$ when $F(a)$ is calculated using mean halo densities evaluated from the spherical collapse model. Dashed lines show$\dot{M}_{\rm H}/M_{\rm H}/F(a)$ when $F(a)$ is calculated by averaging over the mean halo densities taken directly from GALFORM. Each coloured line corresponds to a different halo mass bin, as labelled. The black dash-dotted horizontal line shows the line of equality, above which the conditions for a non-evolving SHM relation are met for star forming galaxies.

of individual haloes are only updated when haloes double in mass (see Chapter 2.8.2). While halo formation events are very frequent at high redshift when halo mass accretion rates are very large, they become very infrequent at low redshifts, for which halo mass accretion rates have dropped dramatically. Consequently, the average halo density for haloes from our reference model will evolve more slowly with time than if the halo densities followed exactly the spherical collapse model. This effect can be seen directly by considering the dashed lines in Fig. F.1, which show $F(M_{\rm H}, a)$ evaluated from the average of halo densities taken directly from our reference model. In this case, it is apparent that the equality given by Eqn F.4 is met for all haloes over all redshifts. This helps to explain why the SHM model does not evolve significantly in our reference model.

# Bibliography


Anderson, L., Aubourg, É., Bailey, S., et al. 2014, MNRAS, 441, 24

Aumer, M., White, S. D. M., Naab, T., & Scannapieco, C. 2013, MNRAS, 434, 3142

Avila-Reese, V., Colín, P., González-Samaniego, A., et al. 2011, ApJ, 736, 134

Baldry, I. K., Balogh, M. L., Bower, R. G., et al. 2006, MNRAS, 373, 469

Baldry, I. K., Glazebrook, K., & Driver, S. P. 2008, MNRAS, 388, 945

Baldry, I. K., Driver, S. P., Loveday, J., et al. 2012, MNRAS, 421, 621

Banerji, M., Glazebrook, K., Blake, C., et al. 2013, MNRAS, 431, 2209

Barnes, J., & Efstathiou, G. 1987, ApJ, 319, 575

Bauer, A. E., Hopkins, A. M., Gunawardhana, M., et al. 2013, MNRAS, 434, 209

Baugh, C. M. 2006, Reports on Progress in Physics, 69, 3101

Baugh, C. M., Lacey, C. G., Frenk, C. S., et al. 2005, MNRAS, 356, 1191

Behroozi, P. S., Conroy, C., & Wechsler, R. H. 2010, ApJ, 717, 379

Behroozi, P. S., Wechsler, R. H., & Conroy, C. 2013a, ApJ, 762, L31

—. 2013b, ApJ, 770, 57

Bell, E. F. 2002, ApJ, 577, 150

Bell, E. F., & de Jong, R. S. 2001, ApJ, 550, 212

Benson, A. J. 2010, PhysRep, 495, 33

Benson, A. J., & Bower, R. 2010, MNRAS, 405, 1573

—. 2011, MNRAS, 410, 2653

Benson, A. J., Bower, R. G., Frenk, C. S., et al. 2003, ApJ, 599, 38

Benson, A. J., Bower, R. G., Frenk, C. S., & White, S. D. M. 2000, MNRAS, 314, 557

Benson, B. A., de Haan, T., Dudley, J. P., et al. 2013, ApJ, 763, 147

Berlind, A. A., & Weinberg, D. H. 2002, ApJ, 575, 587

Bernardi, M., Meert, A., Sheth, R. K., et al. 2013, MNRAS, 436, 697

Bigiel, F., Leroy, A., Walter, F., et al. 2008, AJ, 136, 2846

Binney, J., & Tremaine, S. 2008, Galactic Dynamics: Second Edition (Princeton University Press)

Bîrzan, L., McNamara, B. R., Nulsen, P. E. J., Carilli, C. L., & Wise, M. W. 2008, ApJ, 686, 859

Blanton, M. R., & Roweis, S. 2007, AJ, 133, 734

Blitz, L., & Rosolowsky, E. 2006, ApJ, 650, 933

Blumenthal, G. R., Faber, S. M., Flores, R., & Primack, J. R. 1986, ApJ, 301, 27

Bogdán, Á., Forman, W. R., Vogelsberger, M., et al. 2013, ApJ, 772, 97

Böhringer, H., Chon, G., & Collins, C. A. 2014, A&A, 570, A31

Bolzonella, M., Miralles, J.-M., & Pelló, R. 2000, A&A, 363, 476

Bond, J. R., Cole, S., Efstathiou, G., & Kaiser, N. 1991, ApJ, 379, 440

Bouché, N., Dekel, A., Genzel, R., et al. 2010, ApJ, 718, 1001

Bouwens, R. J., Illingworth, G. D., Oesch, P. A., et al. 2012, ApJ, 754, 83

Bower, R. G., Benson, A. J., & Crain, R. A. 2012, MNRAS, 422, 2816

Bower, R. G., Benson, A. J., Malbon, R., et al. 2006, MNRAS, 370, 645

Bower, R. G., Vernon, I., Goldstein, M., et al. 2010, MNRAS, 407, 2017

Brinchmann, J., Charlot, S., White, S. D. M., et al. 2004, MNRAS, 351, 1151

Bruzual, G., & Charlot, S. 1993, ApJ, 405, 538

—. 2003, MNRAS, 344, 1000

Bryan, G. L., & Norman, M. L. 1998, ApJ, 495, 80

Buat, V., Noll, S., Burgarella, D., et al. 2012, A&A, 545, A141

Bullock, J. S., Kolatt, T. S., Sigad, Y., et al. 2001, MNRAS, 321, 559

Burke, C., Collins, C. A., Stott, J. P., & Hilton, M. 2012, MNRAS, 425, 2058

Calzetti, D., Armus, L., Bohlin, R. C., et al. 2000, ApJ, 533, 682

Calzetti, D., Kinney, A. L., & Storchi-Bergmann, T. 1994, ApJ, 429, 582

Cavaliere, A., & Fusco-Femiano, R. 1976, A&A, 49, 137

Charlot, S., & Fall, S. M. 2000, ApJ, 539, 718

Ciambur, B. C., Kauffmann, G., & Wuyts, S. 2013, MNRAS, 432, 2488

Clowe, D., Gonzalez, A., & Markevitch, M. 2004, ApJ, 604, 596

Coil, A. L., Newman, J. A., Kaiser, N., et al. 2004, ApJ, 617, 765

Cole, S., & Lacey, C. 1996, MNRAS, 281, 716

Cole, S., Lacey, C. G., Baugh, C. M., & Frenk, C. S. 2000, MNRAS, 319, 168

Cole, S., Percival, W. J., Peacock, J. A., et al. 2005, MNRAS, 362, 505

Conroy, C., Gunn, J. E., & White, M. 2009, ApJ, 699, 486

Conroy, C., Schiminovich, D., & Blanton, M. R. 2010a, ApJ, 718, 184

Conroy, C., Wechsler, R. H., & Kravtsov, A. V. 2006, ApJ, 647, 201

Conroy, C., White, M., & Gunn, J. E. 2010b, ApJ, 708, 58

Cousin, M., Lagache, G., Bethermin, M., Blaizot, J., & Guiderdoni, B. 2015, A&A, 575, A32

Cowie, L. L., Barger, A. J., & Hu, E. M. 2010, ApJ, 711, 928

Crain, R. A., Schaye, J., Bower, R. G., et al. 2015, ArXiv e-prints

Creasey, P., Theuns, T., & Bower, R. G. 2013, MNRAS, 429, 1922

Croton, D. J., Springel, V., White, S. D. M., et al. 2006, MNRAS, 365, 11

da Cunha, E., Charmandaris, V., Díaz-Santos, T., et al. 2010, A&A, 523, A78

Daddi, E., Cimatti, A., Renzini, A., et al. 2004, ApJ, 617, 746

Daddi, E., Dickinson, M., Morrison, G., et al. 2007, ApJ, 670, 156

Damen, M., Labbé, I., Franx, M., et al. 2009, ApJ, 690, 937

Davé, R. 2008, MNRAS, 385, 147

Davé, R., Oppenheimer, B. D., & Finlator, K. 2011, MNRAS, 415, 11

de Bernardis, P., Ade, P. A. R., Bock, J. J., et al. 2000, Nat, 404, 955

De Lucia, G., Kauffmann, G., & White, S. D. M. 2004, MNRAS, 349, 1101

de Vaucouleurs, G. 1948, Annales d'Astrophysique, 11, 247

Doroshkevich, A. G. 1970, Astrophysics, 6, 320

Drory, N., & Alvarez, M. 2008, ApJ, 680, 41

Durkalec, A., Le Fèvre, O., de la Torre, S., et al. 2014, ArXiv e-prints

Dutton, A. A., van den Bosch, F. C., & Dekel, A. 2010, MNRAS, 405, 1690

Dutton, A. A., van den Bosch, F. C., Dekel, A., & Courteau, S. 2007, ApJ, 654, 27

Efstathiou, G., Frenk, C. S., White, S. D. M., & Davis, M. 1988, MNRAS, 235, 715

Efstathiou, G., Lake, G., & Negroponte, J. 1982, MNRAS, 199, 1069

Eisenstein, D. J., Zehavi, I., Hogg, D. W., et al. 2005, ApJ, 633, 560

Eke, V. R., Cole, S., & Frenk, C. S. 1996, MNRAS, 282, 263

Eke, V. R., Navarro, J. F., & Frenk, C. S. 1998, ApJ, 503, 569

Eke, V. R., Navarro, J. F., & Steinmetz, M. 2001, ApJ, 554, 114

Elbaz, D., Daddi, E., Le Borgne, D., et al. 2007, A&A, 468, 33

Elbaz, D., Dickinson, M., Hwang, H. S., et al. 2011, A&A, 533, A119

Elmegreen, B. G. 1993, ApJ, 411, 170

Fadely, R., Keeton, C. R., Nakajima, R., & Bernstein, G. M. 2010, ApJ, 711, 246

Fakhouri, O., Ma, C.-P., & Boylan-Kolchin, M. 2010, MNRAS, 406, 2267

Fardal, M. A., Katz, N., Gardner, J. P., et al. 2001, ApJ, 562, 605

Ferrara, A., Bianchi, S., Cimatti, A., & Giovanardi, C. 1999, Astrophys. J. Suppl., 123, 437

Feulner, G., Goranova, Y., Drory, N., Hopp, U., & Bender, R. 2005, MNRAS, 358, L1

Firmani, C., Avila-Reese, V., & Rodríguez-Puebla, A. 2010, MNRAS, 404, 1100

Font, A. S., Bower, R. G., McCarthy, I. G., et al. 2008, MNRAS, 389, 1619

Font-Ribera, A., Kirkby, D., Busca, N., et al. 2014, JCAP, 5, 27

Freedman, W. L., Madore, B. F., Gibson, B. K., et al. 2001, ApJ, 553, 47

Frenk, C. S., White, S. D. M., & Davis, M. 1983, ApJ, 271, 417

Fukugita, M., & Peebles, P. J. E. 2004, ApJ, 616, 643

Furlong, M., Bower, R. G., Theuns, T., et al. 2014, ArXiv e-prints

Gabor, J. M., & Bournaud, F. 2014, MNRAS, 437, L56

Gallazzi, A., & Bell, E. F. 2009, Astrophys. J. Suppl., 185, 253

Genel, S., Vogelsberger, M., Springel, V., et al. 2014, ArXiv e-prints

Ghigna, S., Moore, B., Governato, F., et al. 1998, MNRAS, 300, 146

Giavalisco, M., Ferguson, H. C., Koekemoer, A. M., et al. 2004, ApJ, 600, L93

Goldader, J. D., Meurer, G., Heckman, T. M., et al. 2002, ApJ, 568, 651

Gonzalez, A. H., Sivanandam, S., Zabludoff, A. I., & Zaritsky, D. 2013, ApJ, 778, 14

González, V., Bouwens, R., Illingworth, G., et al. 2014, ApJ, 781, 34

Gonzalez-Perez, V., Lacey, C. G., Baugh, C. M., Frenk, C. S., & Wilkins, S. M. 2013, MNRAS, 429, 1609

Guennou, L., Adami, C., Da Rocha, C., et al. 2012, A&A, 537, A64

Gunn, J. E., & Gott, III, J. R. 1972, ApJ, 176, 1

Guo, Q., Cole, S., Eke, V., Frenk, C., & Helly, J. 2013a, MNRAS, 434, 1838

Guo, Q., White, S., Angulo, R. E., et al. 2013b, MNRAS, 428, 1351

Guo, Q., White, S., Boylan-Kolchin, M., et al. 2011, MNRAS, 413, 101

Hanany, S., Ade, P., Balbi, A., et al. 2000, ApJ, 545, L5

Hatton, S., Devriendt, J. E. G., Ninin, S., et al. 2003, MNRAS, 343, 75

Hearin, A. P., & Watson, D. F. 2013, MNRAS, 435, 1313

Heckman, T. M., Lehnert, M. D., Strickland, D. K., & Armus, L. 2000, Astrophys. J. Suppl., 129, 493

Heinis, S., Buat, V., Béthermin, M., et al. 2014, MNRAS, 437, 1268

Helly, J. C., Cole, S., Frenk, C. S., et al. 2003, MNRAS, 338, 903

Helmi, A. 2008, A&A Rev., 15, 145

Henriques, B., White, S., Thomas, P., et al. 2014, ArXiv e-prints

Henriques, B. M. B., White, S. D. M., Thomas, P. A., et al. 2013, MNRAS, 431, 3373

Henry, J. P., Evrard, A. E., Hoekstra, H., Babul, A., & Mahdavi, A. 2009, ApJ, 691, 1307

Hicken, M., Wood-Vasey, W. M., Blondin, S., et al. 2009, ApJ, 700, 1097

Hirschmann, M., Naab, T., Davé, R., et al. 2013, MNRAS, 436, 2929

Hogg, D. W., Cohen, J. G., Blandford, R., & Pahre, M. A. 1998, ApJ, 504, 622

Hopkins, A. M., & Beacom, J. F. 2006, ApJ, 651, 142

Hopkins, P. F., Cox, T. J., Hernquist, L., et al. 2013a, MNRAS, 430, 1901

Hopkins, P. F., Keres, D., Onorbe, J., et al. 2013b, ArXiv e-prints

Hopkins, P. F., Kereš, D., Oñorbe, J., et al. 2014, MNRAS, 445, 581

Hopkins, P. F., Richards, G. T., & Hernquist, L. 2007, ApJ, 654, 731

Howell, J. H., Armus, L., Mazzarella, J. M., et al. 2010, ApJ, 715, 572

Hoyle, F. 1949, Proceedings of the Symposium on the Motion of Gaseous Masses of Cosmical Dimensions, 1, 195

Hu, W., & Dodelson, S. 2002, ARA&A, 40, 171

Huang, S., Haynes, M. P., Giovanelli, R., & Brinchmann, J. 2012, ApJ, 756, 113

Iglesias-Páramo, J., Buat, V., Hernández-Fernández, J., et al. 2007, ApJ, 670, 279

Ilbert, O., Salvato, M., Le Floc'h, E., et al. 2010, ApJ, 709, 644

Ilbert, O., McCracken, H. J., Le Fèvre, O., et al. 2013, A&A, 556, A55

Jaffe, W. 1983, MNRAS, 202, 995

Jenkins, A., Frenk, C. S., White, S. D. M., et al. 2001, MNRAS, 321, 372

Jiang, L., Helly, J. C., Cole, S., & Frenk, C. S. 2014a, MNRAS, 440, 2115

—. 2014b, MNRAS, 440, 2115

Kahn, F. D., & Woltjer, L. 1959, ApJ, 130, 705

Kannan, R., Stinson, G. S., Macciò, A. V., et al. 2014, MNRAS, 437, 3529

Karim, A., Schinnerer, E., Martínez-Sansigre, A., et al. 2011, ApJ, 730, 61

Kauffmann, G., Colberg, J. M., Diaferio, A., & White, S. D. M. 1999, MNRAS, 303, 188

Kauffmann, G., White, S. D. M., & Guiderdoni, B. 1993, MNRAS, 264, 201

Kennedy, R., Frenk, C., Cole, S., & Benson, A. 2014, MNRAS, 442, 2487

Kennicutt, Jr., R. C. 1983, ApJ, 272, 54

—. 1998, ApJ, 498, 541

Kennicutt, Jr., R. C., Calzetti, D., Walter, F., et al. 2007, ApJ, 671, 333

Keres, D., Yun, M. S., & Young, J. S. 2003, ApJ, 582, 659

Kereš, D., Katz, N., Weinberg, D. H., & Davé, R. 2005, MNRAS, 363, 2

Khochfar, S., & Silk, J. 2011, MNRAS, 410, L42

Klypin, A. A., Trujillo-Gomez, S., & Primack, J. 2011, ApJ, 740, 102

Komatsu, E., Smith, K. M., Dunkley, J., et al. 2011, Astrophys. J. Suppl., 192, 18

Kormendy, J., & Richstone, D. 1995, ARA&A, 33, 581

Koyama, Y., Smail, I., Kurk, J., et al. 2013, MNRAS, 434, 423

Kregel, M., van der Kruit, P. C., & de Grijs, R. 2002, MNRAS, 334, 646

Kriek, M., Labbé, I., Conroy, C., et al. 2010, ApJ, 722, L64

Krumholz, M. R., & Dekel, A. 2012, ApJ, 753, 16

Labbé, I., González, V., Bouwens, R. J., et al. 2010, ApJ, 716, L103

Lacey, C., & Cole, S. 1993, MNRAS, 262, 627

Lacey, C. G., Baugh, C. M., Frenk, C. S., & Benson, A. J. 2011, MNRAS, 412, 1828

Lagos, C. D. P., Baugh, C. M., Lacey, C. G., et al. 2011a, MNRAS, 418, 1649

Lagos, C. d. P., Bayet, E., Baugh, C. M., et al. 2012, MNRAS, 426, 2142

Lagos, C. d. P., Lacey, C. G., & Baugh, C. M. 2013, MNRAS, 436, 1787

Lagos, C. D. P., Lacey, C. G., Baugh, C. M., Bower, R. G., & Benson, A. J. 2011b, MNRAS, 416, 1566

Lamastra, A., Menci, N., Fiore, F., & Santini, P. 2013, A&A, 552, A44

Larson, R. B. 1972, Nature Physical Science, 236, 7

Lee, K.-S., Ferguson, H. C., Wiklind, T., et al. 2012, ApJ, 752, 66

Lee, S.-K., Ferguson, H. C., Somerville, R. S., Wiklind, T., & Giavalisco, M. 2010, ApJ, 725, 1644

Lee, S.-K., Idzi, R., Ferguson, H. C., et al. 2009, Astrophys. J. Suppl., 184, 100

Leitner, S. N. 2012, ApJ, 745, 149

Leitner, S. N., & Kravtsov, A. V. 2011, ApJ, 734, 48

Leroy, A. K., Walter, F., Brinks, E., et al. 2008, AJ, 136, 2782

Li, C., & White, S. D. M. 2009, MNRAS, 398, 2177

Lilly, S. J., Le Fevre, O., Hammer, F., & Crampton, D. 1996, ApJ, 460, L1

Lin, L., Dickinson, M., Jian, H.-Y., et al. 2012, ApJ, 756, 71

Lo Faro, B., Franceschini, A., Vaccari, M., et al. 2013, ApJ, 762, 108

Longhetti, M., & Saracco, P. 2009, MNRAS, 394, 774

Loveday, J., Norberg, P., Baldry, I. K., et al. 2012, MNRAS, 420, 1239

Lu, Y., Mo, H. J., Lu, Z., Katz, N., & Weinberg, M. D. 2013a, ArXiv e-prints

Lu, Y., Mo, H. J., & Wechsler, R. H. 2014a, ArXiv e-prints

Lu, Y., Mo, H. J., Weinberg, M. D., & Katz, N. 2011, MNRAS, 416, 1949

Lu, Y., Wechsler, R. H., Somerville, R. S., et al. 2013b, ArXiv e-prints

Lu, Z., Mo, H. J., Lu, Y., et al. 2014b, MNRAS, 439, 1294

Madau, P. 1995, ApJ, 441, 18

Madau, P., Ferguson, H. C., Dickinson, M. E., et al. 1996, MNRAS, 283, 1388

Magdis, G. E., Rigopoulou, D., Huang, J.-S., & Fazio, G. G. 2010, MNRAS, 401, 1521

Magorrian, J., Tremaine, S., Richstone, D., et al. 1998, AJ, 115, 2285

Malbon, R. K., Baugh, C. M., Frenk, C. S., & Lacey, C. G. 2007, MNRAS, 382, 1394

Mantz, A. B., von der Linden, A., Allen, S. W., et al. 2015, MNRAS, 446, 2205

Maraston, C. 2005, MNRAS, 362, 799

Maraston, C., Daddi, E., Renzini, A., et al. 2006, ApJ, 652, 85

Maraston, C., Pforr, J., Renzini, A., et al. 2010, MNRAS, 407, 830

Marchesini, D., Stefanon, M., Brammer, G. B., & Whitaker, K. E. 2012, ApJ, 748, 126

Marchesini, D., van Dokkum, P. G., Förster Schreiber, N. M., et al. 2009, ApJ, 701, 1765

Marigo, P., Bressan, A., & Chiosi, C. 1996, A&A, 313, 545

Markevitch, M., Gonzalez, A. H., Clowe, D., et al. 2004, ApJ, 606, 819

Martin, A. M., Papastergis, E., Giovanelli, R., et al. 2010, ApJ, 723, 1359

Massey, R., Rhodes, J., Leauthaud, A., et al. 2007, Astrophys. J. Suppl., 172, 239

McCracken, H. J., Wolk, M., Colombi, S., et al. 2014, ArXiv e-prints

McNaught-Roberts, T., Norberg, P., Baugh, C., et al. 2014, MNRAS, 445, 2125

Mellier, Y., & Mathez, G. 1987, A&A, 175, 1

Merson, A. I., Baugh, C. M., Helly, J. C., et al. 2013, MNRAS, 429, 556

Meurer, G. R., Heckman, T. M., & Calzetti, D. 1999, ApJ, 521, 64

Michałowski, M., Hjorth, J., & Watson, D. 2010, A&A, 514, A67

Michałowski, M. J., Dunlop, J. S., Cirasuolo, M., et al. 2012, A&A, 541, A85

Mitchell, P. D., Lacey, C. G., Baugh, C. M., & Cole, S. 2013, MNRAS, 435, 87

Mo, H. J., Mao, S., & White, S. D. M. 1998, MNRAS, 295, 319

Mortlock, A., Conselice, C. J., Bluck, A. F. L., et al. 2011, MNRAS, 413, 2845

Moster, B. P., Naab, T., & White, S. D. M. 2013, MNRAS, 428, 3121

Moster, B. P., Somerville, R. S., Maulbetsch, C., et al. 2010, ApJ, 710, 903

Moustakas, J., Coil, A. L., Aird, J., et al. 2013, ApJ, 767, 50

Murphy, E. J., Chary, R.-R., Dickinson, M., et al. 2011, ApJ, 732, 126

Mutch, S. J., Poole, G. B., & Croton, D. J. 2013, MNRAS, 428, 2001

Muzzin, A., Marchesini, D., Stefanon, M., et al. 2013a, Astrophys. J. Suppl., 206, 8

—. 2013b, ApJ, 777, 18

Nakamura, O., Fukugita, M., Brinkmann, J., & Schneider, D. P. 2004, AJ, 127, 2511

Navarro, J. F., Frenk, C. S., & White, S. D. M. 1996, ApJ, 462, 563

—. 1997, ApJ, 490, 493

Neistein, E., & Weinmann, S. M. 2010, MNRAS, 405, 2717

Noeske, K. G., Faber, S. M., Weiner, B. J., et al. 2007a, ApJ, 660, L47

Noeske, K. G., Weiner, B. J., Faber, S. M., et al. 2007b, ApJ, 660, L43

Noll, S., Burgarella, D., Giovannoli, E., et al. 2009, A&A, 507, 1793

Norberg, P., Baugh, C. M., Hawkins, E., et al. 2001, MNRAS, 328, 64

—. 2002, MNRAS, 332, 827

Obreja, A., Brook, C. B., Stinson, G., et al. 2014, ArXiv e-prints

Oliver, S., Frost, M., Farrah, D., et al. 2010, MNRAS, 405, 2279

O'Meara, J. M., Tytler, D., Kirkman, D., et al. 2001, ApJ, 552, 718

Oort, J. H. 1940, ApJ, 91, 273

Overzier, R. A., Heckman, T. M., Wang, J., et al. 2011, ApJ, 726, L7

Pacifici, C., Kassin, S. A., Weiner, B., Charlot, S., & Gardner, J. P. 2013, ApJ, 762, L15

Pagel, B. E. J., & Patchett, B. E. 1975, MNRAS, 172, 13

Pannella, M., Carilli, C. L., Daddi, E., et al. 2009, ApJ, 698, L116

Papovich, C., Dickinson, M., & Ferguson, H. C. 2001, ApJ, 559, 620

Parkinson, H., Cole, S., & Helly, J. 2008, MNRAS, 383, 557

Patej, A., & Loeb, A. 2015, ApJ, 798, L20

Peacock, J. A., & Smith, R. E. 2000, MNRAS, 318, 1144

Peebles, P. J. E. 1969, ApJ, 155, 393

Peng, Y.-j., Lilly, S. J., Kovač, K., et al. 2010, ApJ, 721, 193

Penner, K., Dickinson, M., Pope, A., et al. 2012, ApJ, 759, 28

Pérez-González, P. G., Rieke, G. H., Villar, V., et al. 2008, ApJ, 675, 234

Perlmutter, S., Aldering, G., Goldhaber, G., et al. 1999, ApJ, 517, 565

Pforr, J., Maraston, C., & Tonini, C. 2012, MNRAS, 422, 3285

Pirzkal, N., Rothberg, B., Ly, C., et al. 2013, ApJ, 772, 48

Planck Collaboration, Ade, P. A. R., Aghanim, N., et al. 2014a, A&A, 571, A16

—. 2014b, A&A, 571, A20

—. 2015, ArXiv e-prints

Portinari, L., Chiosi, C., & Bressan, A. 1998, A&A, 334, 505

Press, W. H., & Schechter, P. 1974, ApJ, 187, 425

Rafferty, D. A., McNamara, B. R., Nulsen, P. E. J., & Wise, M. W. 2006, ApJ, 652, 216

Reddy, N. A., Erb, D. K., Pettini, M., Steidel, C. C., & Shapley, A. E. 2010, ApJ, 712, 1070

Reddy, N. A., Pettini, M., Steidel, C. C., et al. 2012, ApJ, 754, 25

Refsdal, S. 1964, MNRAS, 128, 307

Reid, B. A., Percival, W. J., Eisenstein, D. J., et al. 2010, MNRAS, 404, 60

Renzini, A. 2009, MNRAS, 398, L58

Riess, A. G., Filippenko, A. V., Challis, P., et al. 1998, AJ, 116, 1009

Rodighiero, G., Cimatti, A., Gruppioni, C., et al. 2010, A&A, 518, L25

Rodighiero, G., Daddi, E., Baronchelli, I., et al. 2011, ApJ, 739, L40

Rubin, V. C., Burstein, D., Ford, Jr., W. K., & Thonnard, N. 1985, ApJ, 289, 81

Rubin, V. C., & Ford, Jr., W. K. 1970, ApJ, 159, 379

Rubin, V. C., Ford, W. K. J., & . Thonnard, N. 1980, ApJ, 238, 471

Ruiz, A. N., Cora, S. A., Padilla, N. D., et al. 2013, ArXiv e-prints

Salim, S., Rich, R. M., Charlot, S., et al. 2007, Astrophys. J. Suppl., 173, 267

Santini, P., Fontana, A., Grazian, A., et al. 2009, A&A, 504, 751

—. 2012, A&A, 538, A33

Sargent, M. T., Béthermin, M., Daddi, E., & Elbaz, D. 2012, ApJ, 747, L31

Savage, B. D., & Mathis, J. S. 1979, ARA&A, 17, 73

Sawicki, M. 2012, MNRAS, 421, 2187

Schaerer, D., de Barros, S., & Sklias, P. 2013, A&A, 549, A4

Schaye, J., Crain, R. A., Bower, R. G., et al. 2015, MNRAS, 446, 521

Schrabback, T., Hartlap, J., Joachimi, B., et al. 2010, A&A, 516, A63

Scoville, N., Aussel, H., Brusa, M., et al. 2007, Astrophys. J. Suppl., 172, 1

Sehgal, N., Trac, H., Acquaviva, V., et al. 2011, ApJ, 732, 44

Shankar, F., Guo, H., Bouillot, V., et al. 2014, ApJ, 797, L27

Shapley, A. E., Steidel, C. C., Pettini, M., & Adelberger, K. L. 2003, ApJ, 588, 65

Sheth, R. K., Mo, H. J., & Tormen, G. 2001, MNRAS, 323, 1

Silva, L., Granato, G. L., Bressan, A., & Danese, L. 1998, ApJ, 509, 103

Slosar, A., Iršič, V., Kirkby, D., et al. 2013, JCAP, 4, 26

Smoot, G. F., Bennett, C. L., Kogut, A., et al. 1992, ApJ, 396, L1

Somerville, R. S., Gilmore, R. C., Primack, J. R., & Domínguez, A. 2012, MNRAS, 423, 1992

Somerville, R. S., Hopkins, P. F., Cox, T. J., Robertson, B. E., & Hernquist, L. 2008, MNRAS, 391, 481

Somerville, R. S., & Primack, J. R. 1999, MNRAS, 310, 1087

Sparre, M., Hayward, C. C., Springel, V., et al. 2015, MNRAS, 447, 3548

Springel, V. 2005, MNRAS, 364, 1105

Springel, V., White, S. D. M., Tormen, G., & Kauffmann, G. 2001, MNRAS, 328, 726

Springel, V., White, S. D. M., Jenkins, A., et al. 2005, Nat, 435, 629

Springel, V., Wang, J., Vogelsberger, M., et al. 2008, MNRAS, 391, 1685

Stark, D. P., Ellis, R. S., Bunker, A., et al. 2009, ApJ, 697, 1493

Stark, D. P., Schenker, M. A., Ellis, R., et al. 2013, ApJ, 763, 129

Stinson, G. S., Brook, C., Macciò, A. V., et al. 2013, MNRAS, 428, 129

Strateva, I., Ivezić, Ž., Knapp, G. R., et al. 2001, AJ, 122, 1861

Stringer, M., Cole, S., Frenk, C. S., & Stark, D. P. 2011, MNRAS, 414, 1927

Suyu, S. H., Marshall, P. J., Auger, M. W., et al. 2010, ApJ, 711, 201

Swinbank, A. M., Karim, A., Smail, I., et al. 2012, MNRAS, 427, 1066

Taylor, E. N., Hopkins, A. M., Baldry, I. K., et al. 2011, MNRAS, 418, 1587

Tinker, J., Kravtsov, A. V., Klypin, A., et al. 2008, ApJ, 688, 709

Tomczak, A. R., Quadri, R. F., Tran, K.-V. H., et al. 2014, ApJ, 783, 85

Tormen, G. 1997, MNRAS, 290, 411

Torrey, P., Vogelsberger, M., Genel, S., et al. 2014, MNRAS, 438, 1985

Trujillo-Gomez, S., Klypin, A., Colin, P., et al. 2013, ArXiv e-prints

van der Wel, A., Franx, M., van Dokkum, P. G., et al. 2014, ApJ, 788, 28

Vogelsberger, M., Genel, S., Springel, V., et al. 2014, MNRAS, 444, 1518

Wake, D. A., Whitaker, K. E., Labbé, I., et al. 2011, ApJ, 728, 46

Walcher, J., Groves, B., Budavári, T., & Dale, D. 2011, Ap&SS, 331, 1

Wang, L., Farrah, D., Oliver, S. J., et al. 2013, MNRAS, 431, 648

Warren, M. S., Quinn, P. J., Salmon, J. K., & Zurek, W. H. 1992, ApJ, 399, 405

Watson, D. F., Hearin, A. P., Berlind, A. A., et al. 2015, MNRAS, 446, 651

Weiner, B. J., Coil, A. L., Prochaska, J. X., et al. 2009, ApJ, 692, 187

Weinmann, S. M., Pasquali, A., Oppenheimer, B. D., et al. 2012, MNRAS, 426, 2797

Whitaker, K. E., van Dokkum, P. G., Brammer, G., & Franx, M. 2012, ApJ, 754, L29

Whitaker, K. E., Labbé, I., van Dokkum, P. G., et al. 2011, ApJ, 735, 86

White, S. D. M. 1976, MNRAS, 177, 717

—. 1984, ApJ, 286, 38

White, S. D. M., & Frenk, C. S. 1991, ApJ, 379, 52

White, S. D. M., Navarro, J. F., Evrard, A. E., & Frenk, C. S. 1993, Nat, 366, 429

White, S. D. M., & Rees, M. J. 1978, MNRAS, 183, 341

Wild, V., Charlot, S., Brinchmann, J., et al. 2011, MNRAS, 417, 1760

Wilkins, S. M., Gonzalez-Perez, V., Baugh, C. M., Lacey, C. G., & Zuntz, J. 2013, MNRAS

Williams, R. J., Quadri, R. F., Franx, M., van Dokkum, P., & Labbé, I. 2009, ApJ, 691, 1879

Wuyts, S., Franx, M., Cox, T. J., et al. 2009, ApJ, 696, 348

Wuyts, S., Labbé, I., Franx, M., et al. 2007, ApJ, 655, 51

Yang, X., Mo, H. J., & van den Bosch, F. C. 2003, MNRAS, 339, 1057

Yang, X., Mo, H. J., van den Bosch, F. C., et al. 2013, ApJ, 770, 115

Yang, X., Mo, H. J., van den Bosch, F. C., Zhang, Y., & Han, J. 2012, ApJ, 752, 41

York, D. G., Adelman, J., Anderson, Jr., J. E., et al. 2000, AJ, 120, 1579

Zehavi, I., Patiri, S., & Zheng, Z. 2012, ApJ, 746, 145

Zehavi, I., Weinberg, D. H., Zheng, Z., et al. 2004, ApJ, 608, 16

Zibetti, S., Charlot, S., & Rix, H.-W. 2009, MNRAS, 400, 1181

Zibetti, S., Gallazzi, A., Charlot, S., Pierini, D., & Pasquali, A. 2013, MNRAS, 428, 1479

Zwicky, F. 1933, Helvetica Physica Acta, 6, 110